Structure-Property Relationship of Comb Superplasticizers in Cement Pastes at Early Hydration investigated with Improved Rheo-FTIR

Zur Erlangung des akademischen Grades eines

Doktors der Naturwissenschaften
(Dr. rer. nat.)

von der KIT-Fakultät für Chemie und Biowissenschaften
des Karlsruher Instituts für Technologie (KIT)

genehmigte

Dissertation

von

M. Sc. Tamara Meyer
aus Markgröningen

Referent:	Prof. Dr. Manfred Wilhelm
Korreferent:	Prof. Dr. Patrick Théato
Tag der mündlichen Prüfung:	21. April 2026

Die vorliegende Arbeit wurde von Juni 2022 bis März 2026 unter der Betreuung von Herrn Prof. Dr. Manfred Wilhelm am Institut für Technische Chemie und Polymerchemie (ITCP) des Karlsruher Institut für Technologie (KIT) - Universitätsbereich angefertigt.

Ich versichere hiermit wahrheitsgemäß, die Arbeit selbstständig verfasst, alle benutzten Hilfsmittel vollständig und genau angegeben, und alles kenntlich gemacht zu haben, was aus Arbeiten anderer unverändert oder mit Abänderungen entnommen wurde, sowie die Satzung des KIT zur Sicherung guter wissenschaftlicher Praxis in der jeweils gültigen Fassung beachtet zu haben.

_____

Tamara Meyer

Karlsruhe, den

Kurzfassung

Diese Arbeit untersucht die Wirkung von Betonverflüssigern bzw. Fließmitteln in Zementleimen in frühen Hydrationsstadien, mit besonderem Fokus auf ihren Einfluss auf die rheologischen Eigenschaften und die Bildung von Ettringit. Die drei Hauptteile dieser Arbeit umfassen die Entwicklung eines Messprotokolls für eine reproduzierbare, rheologische Charakterisierung von Zementleimen, die Synthese einer Serie von Polycarboxylatmethyloxazolin (PCMOxa) Kammpolymeren als Alternative zum weit verbreiteten Fließmittel Polycarboxylatether (PCE) sowie die Anwendung des in dieser Arbeitsgruppe entwickelten Rheo-FTIR Aufbaus zur Untersuchung der frühen Hydratation von Zementleim in Gegenwart hochgeladener Polymere.

Die systematische Variation verschiedener Messgeometrien und Messparametern ergab ein Messprotokoll, welches zuverlässige und reproduzierbare Fließgrenzen liefert. In diesem Protokoll wird eine 50 mm Platte-Platte-Geometrie mit aufgeklebtem Schleifpapier der Körnung 600 als Geometrie verwendet, da diese für einen Zementleim mit einem Wasser-zu-Zement-Massenverhältnis von w/z = 0,4 eine Fließgrenze von 46 ± 7 Pa lieferte, welche am ehesten dem Referenzwert von 42 Pa entsprach, welcher auf der Basis des Ausbreitmaßes errechnet wurde. Die Reproduzierbarkeit wurde durch strenge Kontrolle des Probenalters (15 min), der Vorkonditionierung (IKA-Homogenisierung, 100 s^{-1} für 60 s), der Temperatur des Mischwassers (10 ± 1 °C) und der Umgebung (22 ± 1 °C) sowie durch eine Erhöhung der angerührten Probenmenge (100 g Zement) sichergestellt. Das Protokoll erfasste sowohl den erwarteten Zusammenhang mit der inversen fünften Potenz zwischen Fließgrenze und Ausbreitmaß über drei verschiedene w/z-Werte als auch die charakteristische S-Kurve der Fließgrenze mit zunehmender Konzentration von PCE-Fließmitteln. Aus diesem Grund wurde das entwickelte Protokoll in der gesamten Arbeit zur Bestimmung von Fließgrenzen angewendet.

Zur Untersuchung der Struktur-Eigenschafts-Beziehung von Kamm-Superplastifizierer wurde PCMOxa als mögliches Modellsystem für kommerzielle PCE Fließmittel entwickelt. Zwei Syntheserouten für PCMOxa wurden untersucht: eine Aufpfropfsynthese der Seitenketten auf ein vorsynthetisiertes Rückgrat sowie eine Copolymerisation eines zuvor synthetisierten PMOxa-Macromonomers mit Methacrylsäure. PCMOxa zeigte eine Reduktion der Fließgrenze der Zementleime, die in Trend und Konzentrationsabhängigkeit der Wirkung von PCE gleicht, und wies in DOC-Messungen ein vergleichbares Adsorptionsverhalten auf. Diese Ergebnisse bestätigen, dass PCMOxa die Fließgrenze mittels des gleichen Mechanismus wie PCE reduziert, nämlich durch eine Adsorption über das geladene Rückgrat an die Zementpartikel und die Erzeugung sterischer Hinderung zwischen den Partikeln durch die nicht-adsorbierenden Seitenketten. Zur systematischen der Struktur-Eigenschafts-Beziehung wurde über die Aufpfropfsynthese eine PCMOxa-Bibliothek aus acht Proben dargestellt, in der die Seitenkettendichte *N*, die Seitenkettenlänge *P* und die Rückgratlänge *B* systematisch variiert wurden. Dabei zeigte sich, dass PCMOxa eine ähnliche Struktur-Eigenschafts-Charakteristik wie PCE aufweist. Allerdings ist die maximale Dosierwirksamkeit σ_0/m bei PCMOxa zu niedrigeren P/N-Werten verschoben. Diese Verschiebung könnte auf die höhere Kettensteifigkeit und den dadurch erhöhten hydrodynamischen Radius der PMOxa-Seitenkette zurückzuführen sein. FRP-PCMOxa, welches über

die Macromonomer-Copolymerisation synthetisiert wurde, reduzierte die Fließgrenze bei einer Dosierung von 0,1 Gew.-% auf 10 Pa und entsprach damit den beiden Referenz-PCE-Proben. Diese Fließgrenzenreduktion von FRP-PCMOxa übertraf alle Grafting-onto-Produkte, was möglicherweise auf die niedrigere molare Masse zurückzuführen ist, die zu einer homogeneren Verteilung im Zementleim führen könnte. Die alternative Seitenkettenchemie von PCMOxa könnte den bei PCEs beobachteten Ton-induzierten Effizienzverlust abmildern und somit eine potenzielle zukünftige Anwendung in CO_2-reduzierten Betonformulierungen versprechen.

Abschließend wurde die im Arbeitskreis selbstgebaute Kombination aus Hochleistungsrheometer und kommerziellem Fourier-Transformations Infrarot (FTIR) Spektrometer, das sogenannte Rheo-FTIR, durch zentrale Modifikationen weiterentwickelt. Darunter waren die Neugestaltung des Spiegelringsystems, die Rekonstruktion des Detektortisches sowie die Verkürzung der oberen Geometrie. Durch die verbesserte Strahlführung und mechanische Stabilität konnte das Signal-zu-Rausch-Verhältnis im FTIR um einen Faktor von 63 erhöht und die Aufbauzeit von etwa einer Stunde auf 15 Minuten reduziert werden. Obwohl drei getestete Stickstoff-Spülkammern die atmosphärische Zusammensetzung innerhalb von 60 min nicht vollständig stabilisieren konnten, bietet das leistungsstärkste Full-Enclosure-Design (FE) eine vielversprechende Grundlage für einen vollständig eingehausten Rheo-FTIR-Aufbau. Zur Demonstration des Potenzials wurde das Rheo-FTIR eingesetzt, um die Ettringitbildung während des strukturellen Aufbaus von Portlandzementleim (OPC) zu verfolgen. Zur Nachbildung der Wirkung hochgeladener PCE-ähnlicher Polymere wurden ein lineares und ein sternförmiges Polymethacrylsäure (PMAA) Modellsystem synthetisiert und hinsichtlich ihres Einflusses auf die Ettringitbildung untersucht. In Gegenwart dieser stark geladenen Polymere deutet ein früherer und steilerer Anstieg von G′(t) ($\omega_1/2\pi$ = 1 Hz, γ_0 = 0,01 %) bei geringen Ettringitkonzentrationen auf die dominante Rolle physikalischer Wechselwirkungen, wie z.B. polymervermittelter Partikelbrücken in den ersten Minuten bis Stunde der Hydratation hin.

Abstract

This work addresses the effect of superplasticizers in cement pastes at early hydration states, with a focus on their influence on rheological properties and formation of ettringite. The three main parts concentrate on the development of a measurement procedure for a reproducible rheological characterization of cement pastes, synthesis of a series of Poly(carboxylate methyl-oxazoline) (PCMOxa) comb polymers as an alternative to the most prominent superplasticizer poly(carboxylate ether), and the application of a homebuilt Rheo-FTIR set-up to an investigation on the early hydration of cement paste in the presence of highly-charged polymers.

A systematic geometry and parameter screening yielded a measurement procedure that produced reliable and reproducible yield stress measurements. In this procedure, a 50 mm plate-plate geometry with 600-grit sandpaper is used as it provided a yield stress of 46 ± 7 Pa for a cement paste of w/c = 0.4, which closely matched the reference value of 42 Pa calculated from spread flow measurements. Reproducibility was secured by strict control of sample age (15 min), preconditioning (IKA homogenization, 100 s^{-1} for 60 s), temperature (water 10 ± 1 °C, ambient 22 ± 1 °C) and increased prepared sample batch size (100 g cement). The protocol captured the expected inverse-fifth-power relation between yield stress and spread diameter across three different water-to-cement ratios as well as the characteristic S-shaped yield stress decrease with PCE dosage and was used throughout this work.

To investigate the structure-property relationship of comb superplasticizers, PCMOxa was developed as a potential model system for the commercial superplasticizer poly(carboxylate ether) (PCE). Two synthetic strategies toward PCMOxa were explored, a grafting-onto and a grafting-through approach. PCMOxa demonstrated superplasticizer functionality comparable in trend to PCE by reducing the yield stress with similar concentration dependence and showing analogous adsorption by DOC analysis. These findings confirm that PCMOxa reduces the yield stress by the same mechanism as PCE, namely through an adsorption via the charged backbone to the cement particles and the creation of steric hinderance between the particles due to the non-adsorbing sidechains. To investigate the structure-property relationship, a library of eight PCMOxa comb polymers was synthesized via the grafting-onto synthesis while systematically varying the grafting density *N*, the sidechain length *P* and the backbone length *B*. Thereby, it was shown that PCMOxa exhibits a structure-property relationship of a similar archetype as PCE. However, the maximum dosing efficiency σ_0/m is shifted to lower *P*/*N* values for PCMOxa compared to PCE. This shift might be attributed to the higher chain stiffness and consequently the increased hydrodynamic radius of the PMOxa sidechain. FRP-PCMOxa, which was synthesized via the grafting-through synthesis, reduced the yield stress to 10 Pa at dosage of 0.1 wt.%, matching the two reference PCE samples. This yield stress reduction of FRP-PCMOxa outperformed all grafting-onto products, potentially due to its lower molar mass that might lead to a more homogeneous distribution within the paste. The alternative sidechain chemistry of PCMOxa might mitigate clay-induced efficiency loss observed for PCEs, thus promising a potential future application of PCMOxa in low-carbon concrete formulations.

Finally, the home-built combination of a high-end rheometer and a commercial Fourier-transform infrared (FTIR) spectrometer, the so-called Rheo-FTIR, was refined with key modifications including the redesign of the mirror ring system, the reconstruction of the detector table and the shortening of the upper geometry. By improving the beam alignment and the robustness of the set-up, these modifications lead to a substantial 63-fold signal-to-noise ratio improvement in the FTIR while reducing the set-up time from approximately one hour to 15 minutes. Although three tested nitrogen-purge enclosure concepts did not fully stabilize atmospheric composition within 60 minutes, the best performing full enclosure (FE) design provides a promising starting point for future designs of a fully enclosed Rheo-FTIR. To demonstrate its potential for the investigations of chemo-rheological relationships, the Rheo-FTIR was applied to monitor the formation of ettringite during the structural build-up of ordinary Portland cement (OPC) paste. To mimic the influence of highly charged polycarboxylate ether (PCE), two poly(methacrylic acid) (PMAA) model systems of a linear and a star topology were synthesized and their influence on the formation of ettringite was investigated. In the presence of highly charged polymers, an earlier and steeper von G′(t) ($\omega_1/2\pi$ = 1 Hz, γ_0 = 0.01 %) increase at low ettringite levels indicates a dominant role of physical particle interactions like polymer-mediated particle bridging within the first minutes to hour of hydration.

Table of Contents

1 Introduction

Concrete is besides water the second most consumed material in the world, with an annual production exceeding 30 billion tons [1]. This makes it the most important building material globally. Concrete is composed of binder, water and mineral aggregates such as sand or gravel. The most commonly used binder is cement which continues to dominate the market with a global production of approximately 4 billion tons in 2023 [2]. The environmental impact of cement production represents a major challenge. In recent years, cement production accounted for roughly 8 % of global anthropogenic carbon dioxide (CO_2) emissions [3]. This CO_2 is primarily released during the firing process of clinker, the main component of ordinary Portland cement (OPC). Efforts are made to reduce these emissions by replacing fossil fuels with renewable sources. In the EU, 58 % of the thermal energy was derived from circular waste fuels in 2022 [2]. However, these replacements cannot address the intrinsic process-related CO_2-release during the calcination of the limestone in clinker ($CaCO_3 \rightarrow CaO + CO_2$). Two principal strategies are currently being applied to reduce these emissions: carbon capture and storage (CCS) and the development of low-carbon concrete formulations. CCS is a technical process in which the CO_2 generated during industrial operations is captured, transported to a designated site and then stored deep underground in suitable geological formations [4, 5]. One of the first large-scale CCS facilities was inaugurated by Heidelberg Materials in Brevik, Norway, in 2025 [4]. However, critics describe CCS as a false solution, arguing that the process often requires energy-intensive CO_2 liquefaction and carries the risk of a potential CO_2 leakage, posing as a significant environmental hazard [5]. The alternative strategy is to develop new low-carbon concrete formulations that focus on reducing the cement content in concrete and partially replacing clinker with supplementary cementitious materials (SCMs) [6]. SCMs are often categorized depending on their reactivity. Inert materials, which do not partake in cement hydration, are usually referred to as filler. Reactive materials which contribute to the hydration of cement are called pozzolanic or latent-hydraulic if an activation is required. Pozzolanic SCMs are for example calcined clay or fly ash [6]. However, in many cases, low-carbon concrete formulations exhibit reduced workability, particularly when highly reactive SCMs with increased water demand are used [7].

To overcome the inferior workability of sustainable concrete formulations, admixtures can help to maintain the desired performance characteristics in their fresh as well as hardened material properties. To ensure suitable flow properties, water reducing agents or superplasticizers can be applied. Poly(carboxylate ether) (PCE) represents the most widely used superplasticizer. PCE is a comb copolymer consisting of a negatively charged poly(carboxylate) backbone, typically poly(acrylic acid) (PAA) or poly(methacrylic acid) (PMAA), and poly(ethylene oxide) (PEO) sidechains that remain uncharged in the highly alkaline environment of cement pastes [8]. Their performance can be tailored through modification of structural parameters such as sidechain length *P*, backbone length *B* and the grafting density *N*. These structural parameters directly influence macroscopic properties including the flow properties, the yield stress and the hydration retardation [9, 10]. Understanding this structure-property relationship of PCE-type superplasticizers, especially under early hydration conditions where the cement paste is highly dy-

namic, is therefore crucial for the design of future superplasticizers compatible with low-carbon binders. In this context, the present work investigates a novel PCE analogue featuring 2-methyl-2-oxazoline as an alternative sidechain monomer to act as a model system for comb-structured superplasticizers. These poly(carboxylate methyloxazolines) (PCMOxa, IUPAC: poly(2-methyl-2-oxazoline)-*graft*-poly(methacrylic acid)) can be synthesized via living aniconic and cationic polymerization, leading to a high-control over molecular parameters which makes them suitable for investigations on the structure-property relationship of comb superplasticizers.

The presence of polymer admixtures is known to influence the formation of early hydration products such as ettringite, thereby affecting the rheological evolution of cement pastes. To elucidate the microscopic origin of associated macroscopic behavior, different combinations of rheometers with additional analytical methods have been developed. These analytical methods involved dielectric spectroscopy (DES) [11–14], small angle x-ray scattering (SAXS) [15, 16] and nuclear magnetic resonance (NMR) [17–19] amongst others. Among these methods, the combined rheometry-infrared spectroscopy approach (Rheo-FTIR) which was developed in this working group allows simultaneous monitoring of macroscopic flow behavior and molecular-level chemical changes [20, 21]. Rheo-FTIR can be used to characterize a wide range of materials, e.g. bring new insights to hydrogel kinetics [25] or the formation of early hydration products in cement hydration [22]. A major part of this work is the redesign and enhancement of the existing home-built Rheo-FTIR set-up to achieve higher spectral sensitivity and to simplify operational handling. These upgrades significantly broaden the analytical capabilities of the technique and enable more precise insight into the correlation of chemical reactions. The potential of the Rheo-FTIR is demonstrated with an investigation of the rheological evolution during early cement hydration in the presence of highly charged poly(methacrylic acid) of different topologies.

Overall, this dissertation examines the role of superplasticizers in cement pastes during early hydration, with a particular focus on rheological behavior, ettringite formation and the underlying molecular mechanisms in these processes. The work is divided into three main parts: In chapter 3, a measurement protocol is developed which enables reproducible rheological characterization of cementitious materials. Chapter 4 summarizes the synthesis and rheological evaluation of the novel PCMOxa and explores its potential as a model system for the comb superplasticizer PCE. The Rheo-FTIR enhancement and the application of the improved Rheo-FTIR set-up to study the early formation of ettringite in the presence of highly charged polymers is described in chapter 5.

2 Theoretical Background and State of the Art

2.1 Polymerization Techniques

A polymerization is a reaction in which small molecules, the so-called monomers, react to form a polymer. There are two main types of polymerizations: step-growth and chain-growth polymerization [23–25]. In step-growth polymerizations, the monomers react in pairs at every stage to form macromolecules. The main representatives are polyaddition and polycondensation [23]. In chain-growth polymerization, monomers are added onto the reactive chain end, causing the polymer chain to grow in a continuous propagation [23–25]. The exact mechanism depends on the chemical nature of the reactive chain end. In the following, the mechanisms for chain growth polymerizations involving different reactive chain ends, namely radical polymerization, anionic and cationic polymerization are discussed. Moreover, different general grafting strategies towards comb polymers are presented.

2.1.1 Radical Polymerization of Methacrylic Acid

Free radical polymerization (FRP) is one of the most widely applied polymerization techniques. It is used for producing a broad range of commodity and specialty polymers, such as low-density polyethylene (LDPE), polyvinylchloride (PVC) or polystyrene (PS) [23–25]. FRP is central in the commercial production of large quantities of polymer due to its robustness, its tolerance towards functional groups and the applicability to a large variety of vinyl monomers. Typical monomers include styrene, (meth)acrylates, vinyl esters, acrylonitrile and various functional vinyl derivatives [23].

As for all chain growth polymerizations, the FRP is divided in three main reaction steps: initiation, propagation and termination. In the initiation, a radical is formed. Typically, the radical formation is achieved by thermal or photochemically induced decomposition of radical initiators like azo compounds (e.g. AIBN) or organic peroxides (DPO) in organic solvents [23] . In aqueous solution, typical initiators the water-soluble peroxide potassium persulfate ($K_2S_2O_8$) or the water-soluble azo-compounds like 4,4’-Azobis(4-cyanopentanoic acid) (ACPA, German abb.: ACVA) can be used [23, 26]. A third class of initiator systems are redox initiators, in which the radical is formed via a redox reaction. In this work, such a redox system consisting of tert-butyl hydroperoxide (TBHP) and sodium formaldehyde sulfoxylate (SFS) was applied (chapter 4.2.2, p. 76). SFS, also known as rongalite, acts as the reducing agent, reacting with the peroxide to form tert-butyloxyl radicals to initiate the chain reaction as shown in Figure 1 [27, 28]. As the radical is formed via a redox reaction, it is possible to conduct the synthesis at room temperature (~ 25 °C).

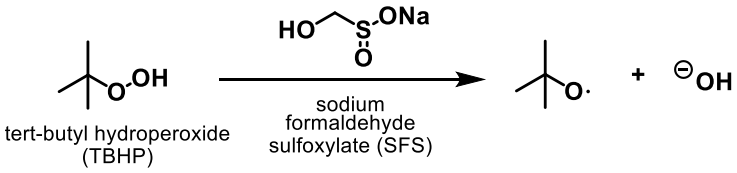

Figure 1: Reaction scheme of proposed decomposition tert-butyl hydroperoxide (TBHP) by the reducing agent sodium formaldehyde sulfoxylate (SFS), also known as rongalite. The formed tert-butyloxyl radical initiates the polymerization.

In the propagation reaction, monomers are added to the reactive chain end, which is a short-lived radical that determines both the polymerization kinetics and the achievable macromolecular structures [29]. The polymerization is stopped via two possible termination reactions: disproportionation and recombination. In recombination, the two radicals form a new covalent bond, effectively increasing the molecular weight of the resulting chain [23]. The disproportionation reaction is a proton transfer reaction resulting in a polymer chain and a macromolecule. Methacrylates seem to preferably react via disproportionation [30]. In FRP, all reaction steps (initiation, propagation and termination) occur in parallel. In the description of the kinetics, it is usually assumed that the radical polymerization reaches a steady-state after a few seconds in which the initiation reaction v_{st} is the same as the termination reaction v_{ter} ($v_{st} = v_{ter}$). Thus, the reaction speed mainly depends on the propagation.

In this work, methacrylic acid (MAA) was used as a monomer in FRP. In contrast to typical monomers like styrene or methyl methacrylate, the FRP of MAA is complicated by its acidic character ($pK_a \approx 4.5$) [31, 32]. In an aqueous solution, the carboxyl group can exist either in its protonated (-COOH) or deprotonated ($-COO^-$) form, depending on the pH. The deprotonation alters the electron distribution and the solvation of the carboxylic group, significantly affecting the reaction kinetics [31, 33]. As the pH increases and the degree of deprotonation rises, the polymerization rate decreases due to the reduced monomer reactivity and the increased electrostatic repulsion between the negatively charged carboxyl groups in both monomer and polymer [31, 33].

In general, a typical side reaction in FRP is the transfer of the radical to other molecules in the reaction mixtures [23]. The radical can be transferred to the monomer (M) which initiates a new active chain or to the already existing polymer chain (P) itself, causing long-chain branching. Other options are the transfer to a solvent or a specifically added "chain transfer agent" (CTA). All transfer reactions reduce the obtained degree of polymerization, as expressed by the general Mayo-equation [23]:

$$\frac{1}{P_n} = \frac{1}{P_0} + C_S \frac{[S]}{[M]} \tag{2.1}$$

P_n denotes the number-average degree of polymerization, P_0 is defined as the number-average polymerization degree in the absence of chain transfer, and [S] is the concentration of the molecule to which the radical is transferred. The symbol [M] denotes the monomer concentration,

whilst C_s signifies the chain transfer constant. If chain transfer occurs to several molecules, e.g. the polymer P and a CTA, then the individual contributions are expressed as a sum [23]:

$$\frac{1}{P_n} = \frac{1}{P_0} + C_{S,P}\frac{[P]}{[M]} + C_{S,CTA}\frac{[CTA]}{[M]} + \cdots \tag{2.2}$$

CTAs are small molecules which have at least one labile bond to facilitate the transfer of radicals to the molecule [23]. The newly formed radical then initiates a new polymer chain. Typical CTAs include thiols, commonly referred to as mercaptans, and halocarbons. CTAs are frequently used to deliberately reduce the degree of polymerization and, consequently, the molecular weight of the resulting polymer [23]. Their presence can also suppress undesired chain-transfer reactions to the polymer backbone, thereby reducing the degree of branching. In this work, 3-mercapto propionic acid (3-MPA) is applied in the FRP of MAA to lower the molecular weight and improve the architectural control [34]. The structure of 3-MPA is displayed in Figure 2 A).

A special type of CTA also plays a central role in the reversible-addition-fragmentation chain transfer (RAFT) polymerization, as shown in Figure 2. RAFT is one of several controlled radical polymerization (CRP) techniques which also include atom transfer radical polymerization (ATRP) and nitroxide-mediated polymerization (NMP). All of these CRP methods significantly reduce the termination reaction, enabling predictable molecular weights, narrow molecular-mass distributions, as well as the synthesis of complex architectures, e.g. block copolymers. However, irreversible chain termination is not completely suppressed, therefore the CRP reactions are usually referred to as *controlled* rather than *living* (compare chapter 2.1.2, p. 6).

In the RAFT polymerization, a dithio- or trithiocarbonate CTA is applied which regulates the chain growth through a reversible exchange between propagating radicals. This reversible activation-deactivation process ensures equal growth probability for all chains, as displayed in the main equilibrium in Figure 2 C). A suitable RAFT agent has to be chosen based on the monomer and the initiator. For methacrylates, typical RAFT agents are 2-cyano-2-propylbenzodithioat (CPDB) or 2-cyano-2-propyldodecyltrithiocarbonat (CDPT) [35].

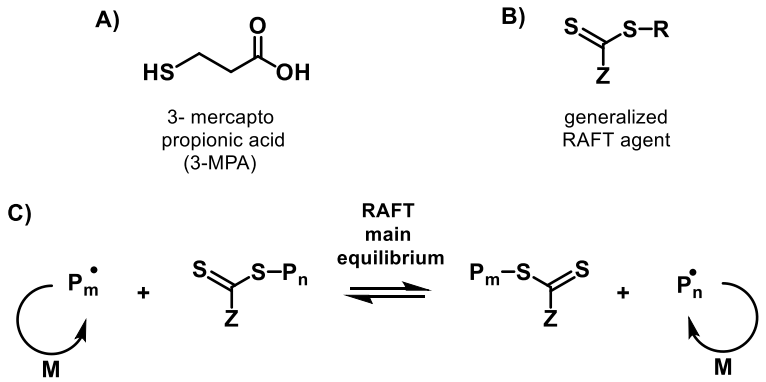

Figure 2: A) The chain transfer agent (CTA) 3-mercapto propionic acid (3-MPA) applied in this work in the FRP of MAA. B) generalized structure of a dithiocarbonate CTA which is used in RAFT polymerization. The substituent Z is needed to stabilize the formed intermediate, typically phenyl substituents. C) Main equilibrium of RAFT polymerization. The reversible addition-fragmentation ensures the same growth propagation probability for the two chains P_m and P_n.

2.1.2 Anionic Polymerization of Methacrylates

Anionic polymerization is a chain growth reaction that, under appropriate conditions, proceeds without chain termination or chain transfer [36]. Hence, it is called *living polymerization*, a concept first introduced in 1956 by Szwarc in the publication of the first anionic polymerization of styrene [37]. The term *living* describes systems in which the propagating species stays active after complete consumption of the monomer, allowing polymerization to resume upon subsequent addition of fresh monomer [38]. The retained reactivity of the chain end provides an easy access to end-functionalized polymers, block copolymers or more complex topologies [29]. To maintain the living character, anionic synthesis has to be conducted in the absence of protic substances, which would lead to premature termination. A comprehensive and detailed overview on the principles of anionic synthesis is given by Hadjichristidis and Hirao [36].

Anionic synthesis is limited to two types of monomers: cyclic monomers, which undergo anionic ring-opening or vinyl monomers with charge-stabilizing substituents [36]. Acrylates and Methacrylates fulfil the later requirement, as the -M-effect of the carbonyl group facilitates the stabilization of the anionic charge. Acrylates can be polymerized via anionic synthesis in principle. However, the reaction does not proceed in a living manner as acrylates can easily abstract the proton in the α-position which reduces the stability of the anionic propagating species during the polymerization and leads to side reactions, mainly uncontrolled termination [36]. This causes the loss of control over molecular weight and broadens the dispersity. For methacrylates like methyl methacrylate (MMA) or tert-butyl methacrylate (tBMA), the absence of an α-proton due to the methyl substituent makes living anionic polymerization possible if certain requirements are met [36]. In general, methacrylates display a “non-ideal” behavior compared to other monomers, e.g. styrene, as the carbonyl group introduces a second electron-deficient center to the monomer. The general mechanism of anionic polymerization and the measures to ensure a living polymerization for methacrylates are discussed in the following on the example of tert-butyl methacrylate, which was used in this work (see chapter 4, p. 61 and chapter 5.5.2, p. 119).

Reaction mechanism:

Initiation: In general, commercially available alkyl lithium compounds, especially the isomers of butyllithium, are used for the initiation of carbanionic polymerization [36]. They transfer a negative charge to the monomer forming new anionic species which react in the propagation reaction. However, the initiation of methacrylates with *sec*-BuLi is not as straight forward as for styrene. A significant portion of *sec*-BuLi attacks the carbonyl group forming a vinyl ketone and an unreactive alkoxide, as shown in Figure 3 A) [36]. The ketone can add to the reactive chain ends formed in regular initiation, which decreases the reactivity and slows down the reaction [36].

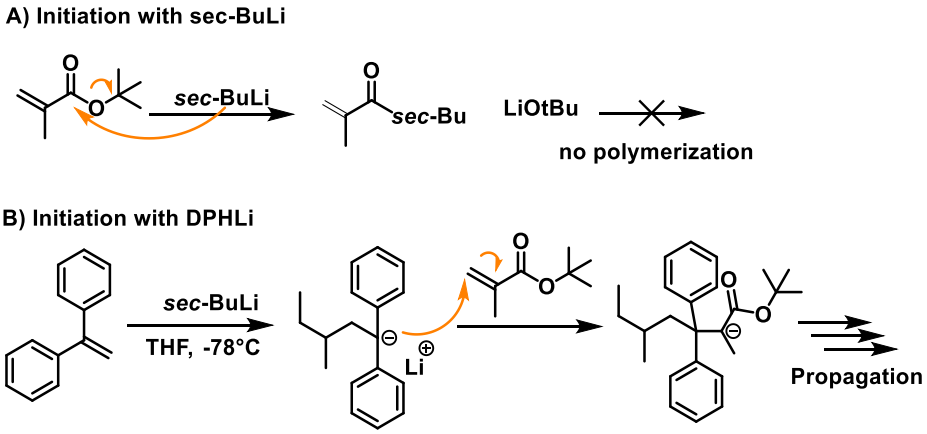

Figure 3: Initiation reaction of the anionic polymerization of methacrylates on the example of tert-butyl methacrylate (tBMA). A) In the initiation with alkyl lithium compounds, a significant portion of the initiator attacks the carbonyl group forming a vinyl ketone and a lithium alkoxide which both cannot initiate further polymerization. B) Initiation with 1,1 – diphenyl-3-methylpentyllithium (DPHLi) leads to the successful polymerization of methacrylates.

To avoid the nucleophilic attack of the initiator on the carbonyl group, the polymerization is usually initiated with bulky π-stabilized organolithium compounds, e.g. 1,1 – diphenyl-3-methylpentyllithium (DPHLi) [36]. This initiator is formed prior to the polymerization by the reaction of *sec*-BuLi with the not self-polymerizable 1,1-diphenylethylene (DPE). The phenyl groups introduce steric hinderance to the initiating species preventing the nucleophilic attack on the carbonyl group [36], as displayed in Figure 3 B).

Propagation: The propagation of anionic polymerization is the continuous addition of monomers to the reactive anionic chain end, as shown in Figure 4.

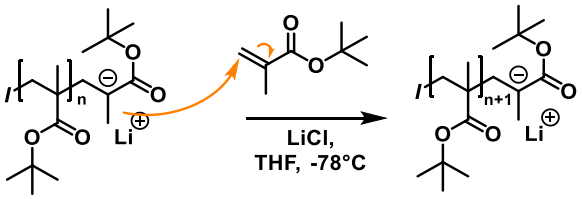

Figure 4: Propagation of anionic polymerization of tert-butyl methacrylate. I denotes the initiator, e.g. the diphenyl-3-methylpentyl-moiety of DPHLi.

Ideally, the growth of all chains propagates at the same rate independent of the chain length after a fast and quantitative initiation. Then, the final degree of polymerization P_n solely depends on the ratio of the initial monomer concentration $[M]_0$ to the initial initiator concentration $[I]_0$:

$$P_n = \frac{[M]_0}{[I]_0} \tag{2.3}$$

Consequently, the degree of polymerization and the molecular weight of the resulting polymer can be adjusted precisely by the monomer-initiator-ratio in the synthesis.

A typical side reaction in the anionic polymerization of methacrylates is the intramolecular Claisen-type condensation between the propagating enolate anion and a carbonyl group in the same polymer chain, the so-called back-biting reaction [38, 39]. This backbiting-reaction is displayed in Figure 5. To reduce the reactivity of the anions, the polymerization is typically conducted in at -78 °C in polar, aprotic solvents, usually THF [40]. Non-polar hydrocarbon solvents, such as cyclohexane, cannot dissolve methacrylates. Moreover, the addition of a 3- or morefold excess of LiCl can further decrease the reactivity of the carbanions. LiCl is a μ-type ligand which forms a complex with the reactive chain end, reducing the tendency towards intramolecular nucleophilic attack [36].

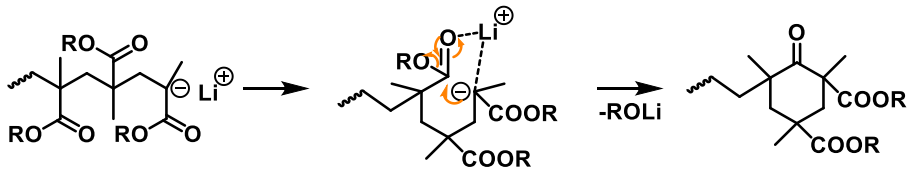

Figure 5: Intramolecular backbiting reaction of the carbanion on the carbonyl functionality. The wavy line symbolizes a polymer chain of arbitrary length. The nucleophilic attack can also occur intermolecularly. This side reactions is typically suppressed at low reaction temperatures and the presence of LiCl, which stabilizes the reactive chain end.

Termination: The negative charges of the anionic propagating species repel each other. Thus, no spontaneous termination occurs. To terminate the polymerization reaction in a controlled manner, a terminating agent is added. If end-group functionalization is not intended, the reaction is terminated by adding a protic agent, typically degassed methanol, which deactivates the living chain through a proton transfer reaction. The degassing of the methanol is necessary as the presence of gaseous impurities can lead to side reactions. Oxygen (O_2) impurities lead to the formation of peroxides which decompose to form radicals that recombine. Consequently, the presence of O_2 in the terminating agent doubles the intended molecular weight. CO_2 can lead to the formation of a carboxyl end group [36].

A commercial application of the carbanionic polymerization is for example the synthesis of thermoplastic elastomers based on block-copolymers. Prominent examples are the PS-PI-PS (SIS) and PS-PB-PS (SBS) copolymers which are sold by the company Kraton [38]. These block copolymers were originally designed to be used in tire industry, but are now also applied in footwear, automotive, wire and cable, as well as lubricants, adhesives and gels [38]. Another prominent commercial application of living anionic polymerization is the synthesis of poly(ethylene oxide) (PEO) from gaseous ethylene oxide. A second name for PEO is poly(ethylene glycol) (PEG), which is typically used for lower molar mass PEO oligomers and is the generally preferred term in the biomedical research field. PEO is utilized in various applications such as cosmetics, medical applications or the manufacturing of PCE superplasticizers [8, 41].

2.1.1 Cationic Polymerization of Methyloxazoline

The living cationic ring opening polymerization (CROP) of 2-alkyl-2-oxazoline to form poly(2-akly-2-oxazoline) (POxa) was discovered simultaneously by four different research teams in 1966 [42]. Since then, this class of polymers has been extensively studied, giving rise to a manifold of polymeric materials for potential applications [43–45]. In the last few decades, POxa has gained significant interest, especially driven by their high potential for biomedical applications and the potential substitution of PEO. Their biocompatibility most likely arises from their structure which is often referred to as amino-acid analogues or as pseudo-polypeptides, since each repeating unit contains a peptide-bond in the side group [46]. This work focuses on the potential of PMOxa as a PEO alternative in the comb superplasticizers used in cementitious materials (see chapter 4, p. 61).

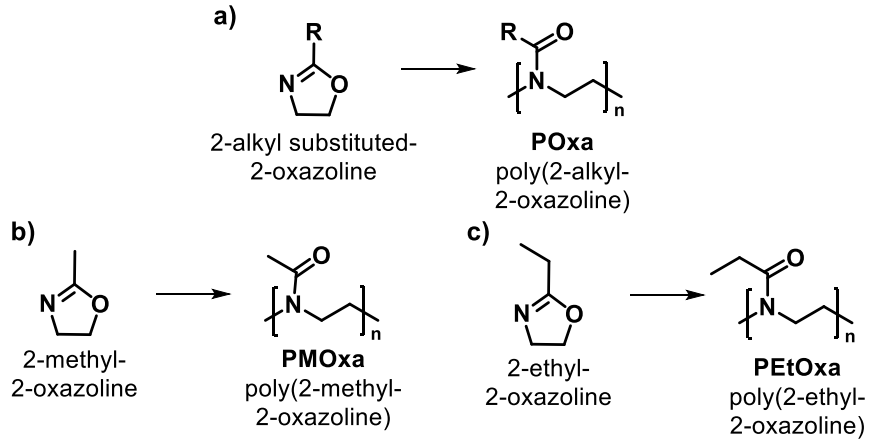

Figure 6: a) Generalized oxazoline monomer and its respective polymer. In addition, the two specific oxazoline monomers and their respective polymers are displayed: b) 2-methyl-2-oxazoline and c) 2-ethyl-2-oxazoline.

As displayed in Figure 6, 2-Oxazolines represent a special class of 5 membered cyclic imino-ethers. The alkyl substituent allows to tune the material properties of the resulting polymer, like the glass transition temperature or the solubility [47]. Poly(2-methyl-2-oxazoline) (PMOxa) is very hydrophilic and is fully water-soluble from 0 °C to 100 °C independent of the molecular weight. POxa with longer alkyl sidechains exhibit a lower critical solution temperature (LCST) [46, 47]. The cloud point temperature (T_{CP}) decreases with increasing hydrophobicity. Poly(2-ethyl-2-oxazoline) (PEt-Oxa) of high molecular weight displays $T_{CP} \approx 66$ °C, while Poly(2-isopropyl-2-oxazoline) (P*i*-PrOxa) shows $T_{CP} \approx 35$ °C. A detailed and comprehensive overview on the solution behavior of POxa is given elsewhere [47, 48].

Although POxa was intensively studied in the last few decades, only a limited number of commercial applications emerged. To date, PEtOxa is the only POxa which is commercially available and finds application as a viscosity modifier and surfactant for paint or cosmetics. It is marketed under the tradename Aquazol [43, 49]. Moreover, PEtOxa is used as a precursor in the synthesis of linear poly(ethylene imine) (PEI). Linear PEI is prepared via hydrolysis of linear PEtOxa after polymerization [46]. The direct synthesis of PEI via ring opening polymerization

of aziridine results in a high degree of branching [46]. PEI is used in many biomedical applications, e.g. as DNA compacting material [50]. In the following the mechanism of the CROP of POxa is discussed with a focus on 2-methyl-2-oxazoline.

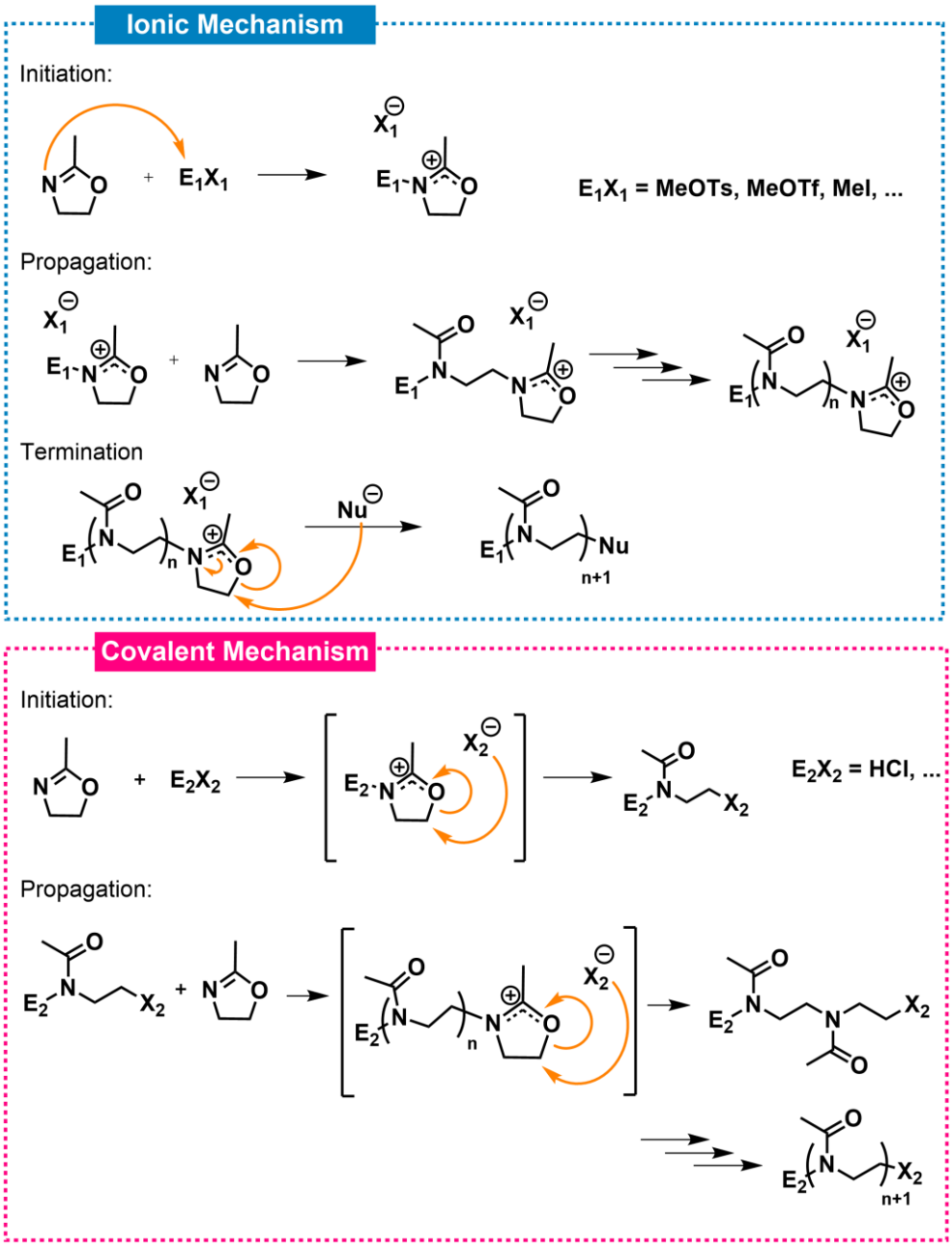

Figure 7: Ionic and covalent reaction mechanism of oxazoline polymerization. The ROP of 2-oxazolines can be initiated by various reagents including Lewis acids (BF_3, $AlCl_3$,), strong protic acids ($HClO_4$, HBr, H_2SO_4,), or more generally an electrophile EX, where the X typically stands for p-toluenesulfonate (OTs), trifluoromethane-sulfonate (OTf), bromide (Br), chloride (Cl) or iodide (I). The nucleophilic character of the counter ion and the chosen 2-alkyl oxazoline determine the reaction mechanism. The polymerization of 2-MeOxa with MeOTf proceeds via a true cationic reaction mechanism. Adapted from [51]

Reaction Mechanism:

The polymerization of oxazolines can proceed via two mechanisms as shown in Figure 7: a living cationic polymerization and a covalent type polymerization. In the cationic polymerization, an electrophilic species initiates the reaction, creating a cationic oxazolinium propagating species. In the covalent reaction mechanism, the counter ion is covalently bound to the propagating end. The polymerization propagates via a dipole-dipole S_N2-reaction [46]. The propagating species in the reaction mechanism is determined by the monomer-initiator combination. It results mainly from the alkyl substituent at the monomer, the nucleophilicity of the initiator and the stability of the resulting counter ion [47]. For the polymerization of 2-methyl-2-oxazoline initiated by methyl triflate (MeOTf), the reaction proceeds via a true cationic polymerization [52]. After complete monomer conversion, the reaction is terminated by the addition of a nucleophilic compound, e.g. water or alcohol [46]. The termination reaction can also be used to end-group functionalize the polymer and to synthesize macromonomers [47, 53]. Since the reaction proceeds in a living manner, the polymerization results in defined molecular weight (equation (2.3), p. 7, applies here as well) and narrow dispersity. However, the synthesis of PMOxa of defined molecular weight is limited to molar masses < 10 kg mol^{-1} due to extensive chain transfer and chain coupling side reactions [52]. PMOxa of higher molecular masses can be synthesized by acetylation of well-defined linear PEI prepared by sidechain hydrolysis of defined high molar mass PEtOxa [52].

2.1.2 Grafting Methods

Branched architectures like comb polymers can be synthesized in general via three basic grafting strategies: grafting-onto, grafting-from and grafting-through [29]. All of these strategies are illustrated in Figure 8. In the grafting-onto synthesis, terminal functional groups of the sidechains attach to functional groups at the backbone. This synthetic approach is often used in anionic polymerization due to high nucleophilicity of the propagating anion, but is also applied with other reactive chain ends e.g. in cationic polymerization [54]. For the grafting-from synthesis, functional sites on the backbone are used to start the polymerization process which leads to the simultaneous growth of sidechains directly from the backbone. The grafting-from approach was applied for example in the synthesis of a super H polymer with poly(lactic acid) sidechains [55]. In the grafting-through synthesis, prepolymerized sidechains with a terminal vinyl unit are copolymerized with a monomer to form combs or stars. As the sidechain is a macromonomer, this synthesis strategy can also be referred to as macromonomer route. The grafting-through synthesis is for example applied in the industrial synthesis of poly(carboxylate ether) superplasticizers (compare chapter 2.4, p. 29) [8, 56].

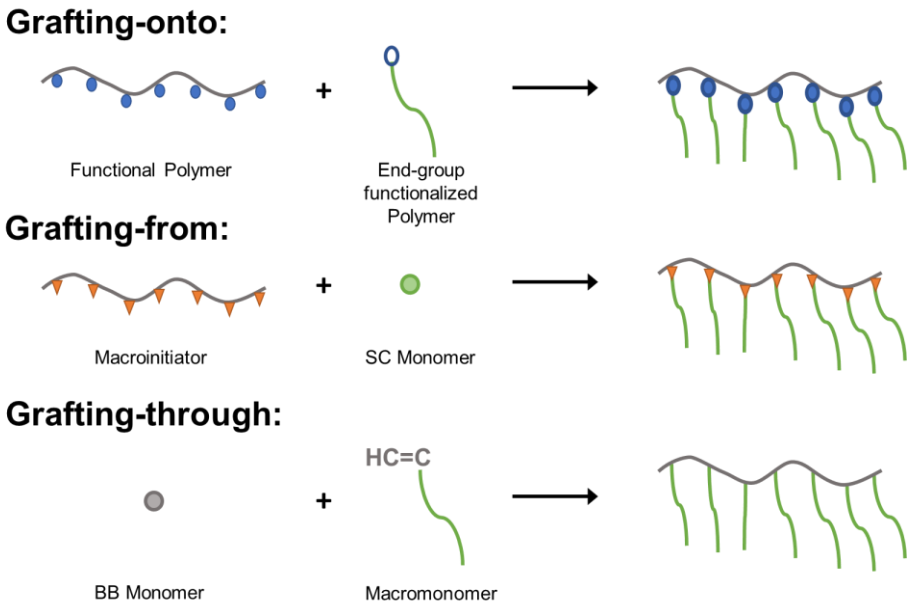

Figure 8: Grafting strategies used for the synthesis of combs or other branched structures. Adapted from [29].

2.2 An Introduction to the Chemistry of Cement Pastes

Cement is the most important binder in construction materials [57]. Upon contact with water, a series of hydration reactions occur which lead to the transformation of the liquid suspension to a rigid, load-bearing solid. In a simplified view on the complex hydration reaction, the cement particles begin to dissolve immediately when in contact with water, releasing ionic species into the solution. Hydrates start to form from these ions and precipitate onto the surface of the remaining cement grains. These hydrates continue to grow into a continuous solid matrix, macroscopically forming a new solid [8]. This simplified reaction mechanism is illustrated in Figure 9.

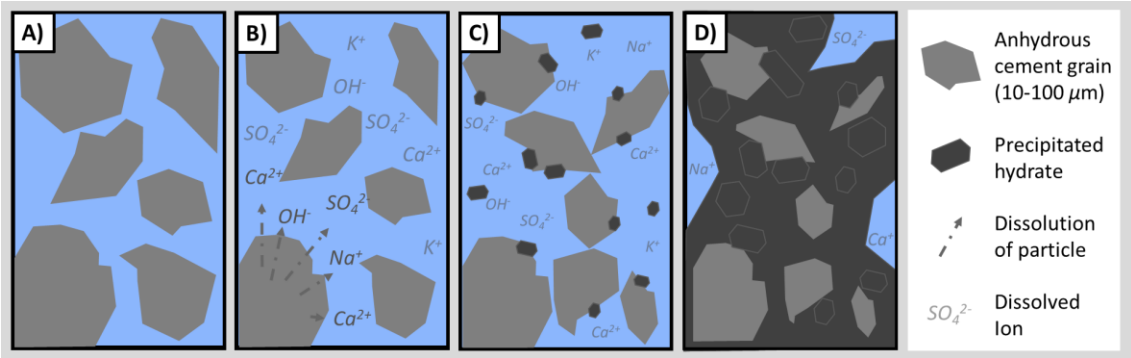

Figure 9: Simplified view on cement hydration. A) Mixing cement particles in water results in the formation of a suspension. B) The cement particles start to dissolve immediately and various ions are released into the solution, as indicated by the arrows. C) Within a few seconds to a few minutes, hydrates start to form and precipitate, mainly on the surface of the unhydrated particles. D) Within approximately eight hours, the hydrates grow to form a new solid which macroscopically leads to hardening of the material. The hydration is completed approximately 28 days after the first water to cement contact. Adapted from [8].

On closer inspection however, cement is not a simple, pure substance but a complex, multimineral material. Its composition strongly depends on the geological origin and the mineralogical composition of the raw materials. The different cement types are distinguished by their mineral contents. The most widely used cement type in construction industry is ordinary Portland cement (OPC) which is primarily composed of clinker, mixed with a small amount of gypsum to control the setting time [57]. In the European standard DIN EN 197-1, OPC corresponds to CEM I, the first of five different cement types defined in the standard [58]. The designation of cement types in this standard follows the structure “CEM II 52.5 L”. The number following the cement type denotes the minimum 28 – day compressive strength in MPa. The standard defines three strength classes: 32.5, 42.5 and 52.5 (MPa). The subsequent letter indicates the early strength class, with L, N and R referring to low, normal and rapid strength development [58]. The early strength can be an indicator for the cement powder’s mean particle size, with small particles providing a larger surface area and thus exhibit an accelerated hydration. The cement used in this work, CEM I 42.5 R is an OPC characterized by rapid strength development and a final compressive strength of at least 42.5 MPa.

Clinker is the main component in OPC. It consists of four major clinker phases: alite (Ca_3SiO_5), belite (Ca_2SiO_4), tricalcium aluminate ($Ca_3Al_2O_6$) and ferrite ($Ca_4Al_2Fe_2O_{10}$) [59]. Typical compositions reported for clinker additionally include small amounts of several secondary phases like alkali sulfates [59]. In cement chemistry, the different mineral phases are usually abbreviated using the oxide notation common in ceramic science with CaO = **C**, SiO_2 = **S**, Al_2O_3 = **A**, Fe_2O_3 = **F**, SO_4^{2-} = **$** and H_2O = **H** [8, 60]. Accordingly, the clinker phases alite, belite, tricalcium aluminate and ferrite are denoted as C_3S, C_2S, C_3A and C_4AF. In this work, the phases are primarily referred to by their oxide notation. It should be noted that sometimes a differentiation is made between the oxide notation, e.g. C_3S and the mineral name, e.g. alite, with C_3S referring to the pure, laboratory-synthesized substance while alite refers to the naturally occurring mineral potentially containing impurities. In this work, the mineral names and the oxide notation are used interchangeably.

Table 1: Four phases of clinker, their chemical composition, abbreviation and amount in percent [8].

Phase	Abbreviation	wt.%	Compound name	Chemical Formula
Alite	C_3S	55 - 65	tricalcium silicate	Ca_3SiO_5
Belite	C_2S	15 - 25	dicalcium silicate	Ca_2SiO_4
Aluminate	C_3A	8 - 12	tricalcium aluminate	$Ca_3Al_2O_6$
Ferrite	C_4AF	8 - 12	tetracalcium aluminoferrite	$Ca_4Al_2Fe_2O_{10}$

2.2.1 The Importance of the Water to Cement Ratio

In the hydration reaction, the stoichiometry of the water in relation to the amount of cement plays a central role. This ratio is usually given as the water-to-cement mass ratio (w/c-ratio), whereby the cement mass refers to the mass of dry cement powder. The w/c-ratio governs both the fresh state properties as well as the microstructure that develops during hydration. Therefore, it determines the final mechanical strength as well as the durability of hardened cementitious materials [8]. The w/c-ratio has an inverse relationship with the final compressive strength and is therefore one of the most important parameters in the design of concrete mixtures [8]. In cement pastes, a stochiometric minimum w/c-ratio of approximately 0.42 is needed to reach full hydration, meaning that the water and (non-hydrated) cement are fully consumed [8]. However, the w/c = 0.42 only represents the chemical water demand. In practice, concrete mix designs often require significantly higher w/c-ratios of up to 0.6 to achieve a sufficient workability. In these mixtures, only part of the mixing water reacts in the hydration, while the remaining fraction acts as free water that ensures flowability [8, 61]. For cement pastes with w/c < 0.42, the available water is insufficient to reach full hydration. Some unreacted cement particles remain, which can be considered as hard inclusions that increase the final compressive strength relative to the fully hydrated material [8]. In practice, complete hydration is rarely achieved even for

w/c $\geq$ 0.42 in real systems due to self-desiccation, evaporation of water and restricted ion transport within the microstructure.

The w/c-ratio strongly influences the pore structure of the hardened material. At w/c ratios above 0.42, the presence of excess water promotes the formation of additional capillary pores compared with pastes at w/c $\leq$ 0.42 [8]. These additional pores govern the permeability and mechanical performance of the hardened material [8]. A higher porosity allows aggressive agents, such as chlorides, to penetrate the hardened cementitious material more easily, where they can attack both the cementitious material as well as the reinforcing steel in reinforced concrete. Consequently, the durability of the concrete is compromised. In summary, the increased porosity for mixtures of w/c $\geq$ 0.42 reduces the compressive strength, decreases the durability and affects the resistance to chloride ingress, carbonation and sulfate attack [8].

Furthermore, the w/c-ratio significantly influences the rheological behavior of cement pastes during the early stages of hydration, as it correlates directly to the solid volume fraction ϕ [62]. The relationship between ϕ and rheological properties, such as the yield stress and the viscosity, is further explained in chapter 2.3 (p. 19).

2.2.2 Hydration of Cement Pastes

This chapter gives a brief and focused introduction to the key reactions in the hydration process of cement pastes. For more comprehensive and detailed discussions, the reader is referred to the relevant literature [8, 59, 63–65].

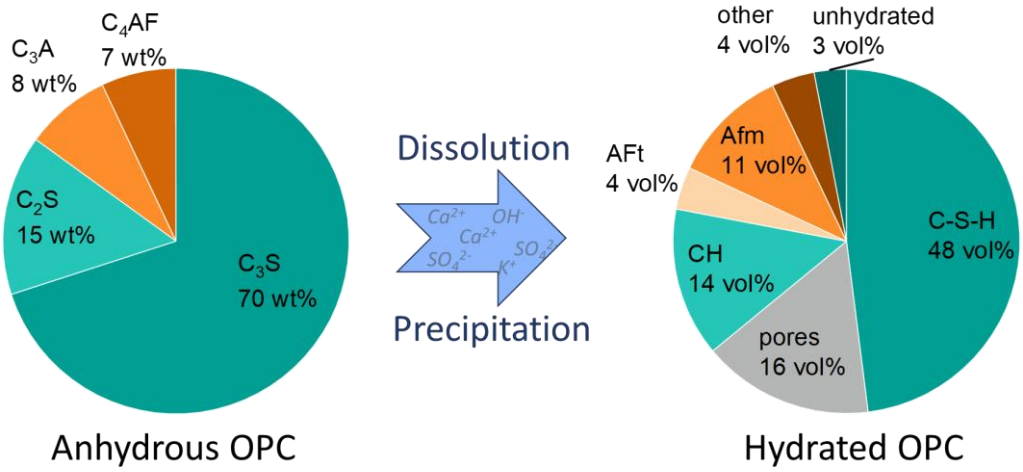

Figure 10: Qualitative description of the reactions of cement upon contact with water. Within 28 days of hydration, the multiphase clinker being composed of tricalcium silicate (C_3S), dicalcium silicate (C_2S), tricalcium aluminate (C_3A) and calcium aluminoferrite (C_4AF) reacts to form Calcium silicate hydrate (C-S-H), portlandite (CH = CaOH), trisulfoaluminoferrite hydrates (AFt) and monosulfoaluminoferrite hydrates (AFm). It should be noted that the compositions are given in wt.% and vol.%, as this corresponds to experimentally obtainable units and is in agreement with standard textbooks. Adapted from [8].

The hydration process of OPC is highly complex, involving a multitude of different reactions which include the dissolution of different cement phases and the precipitation of new, less soluble hydrate phases [60]. These reactions proceed both in parallel and subsequently to each other. The fundamental mechanisms of these reactions and their influence on the macroscopic properties are not fully understood yet and are still a prominent subject in current research [64, 65]. Figure 10 gives a qualitative overview on the hydration reaction of OPC. The multiphase clinker being composed of tricalcium silicate (C_3S), dicalcium silicate (C_2S), tricalcium aluminate (C_3A) and calcium aluminoferrite (C_4AF) reacts to form calcium silicate hydrate (C-S-H), portlandite (CH), trisulfoaluminoferrite hydrates (AFt) and monosulfoaluminoferrite hydrates (AFm). The most important phase in the AFt family is ettringite [60]. In Figure 8, it is indicated that the formation of hydrates happens in solution and in parallel. Thus, for example, a calcium ion bound in C-S-H does not necessarily originate from C_3S as the formal reaction equation might suggest (see Figure 11) but could have been released into solution from any calcium containing clinker phase like e.g. C_3A.

The hydration of OPC is formally divided in two main reactions: the silicate and the aluminate reaction [59, 63]. The silicate reaction involves the dissolution of the silicate containing phases C_3S and C_2S, and the subsequent precipitation of amorphous C-S-H and crystalline portlandite (CH). C_3S and C_2S differ strongly in their reactivity. C_3S is consumed first within 8 hours while the hydration of C_2S only becomes significant after 10 days [66]. The notation C-S-H with hyphens indicates the variable composition of the calcium silicate hydrate phase. The gel-network fluctuates in its Ca/Si ratio between 1.2 and 2.3 depending on the reaction conditions, e.g. dissolved ion concentrations and the reaction temperature [67]. Since C-S-H is the main phase in hydrated cement paste, it mainly governs the final compressive strength [60, 61]. The silicate reactions can be written in the following simplified reaction equations:

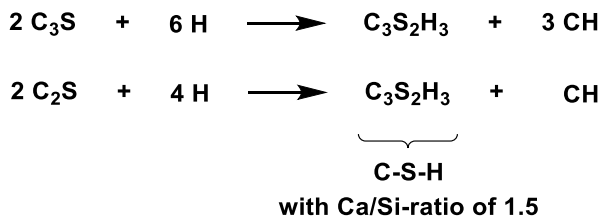

Figure 11: Formal reaction scheme of the silicate reaction in cement hydration [60]. The Ca/Si-ratio of C-S-H is variable and depends on the reaction conditions, e.g. the ion concentration and the reaction temperature [67].

The dissolution of aluminum containing phases and sulfate carriers leads to the precipitation of ettringite Aft, which is referred to as the aluminate reaction. The reaction scheme for the aluminate reaction is given in Figure 12. Despite C_3A only making up about 8 wt.% in clinker, it has a significant effect on the hydration of OPC, especially at early hydration stages. C_3A is by far the most reactive clinker phase. In the absence of sulfates, C_3A hydrates rapidly within a few minutes, known as *flash set* which is a macroscopic rapid hardening. This flash set impairs the workability and is therefore usually undesired. The addition of sulfate carriers, like gypsum, alters the C_3A reaction to the formation of ettringite, which is a much slower reaction. The sulfate concentration decreases with progressing hydration. At low residual sulfate concentra-

tions (≤ 2.85 mg L^{-1}), the remaining C_3A reacts with ettringite to form monosulfoaluminate. To ensure the complete conversion of the aluminate phase to ettringite, the amount and solubility of the sulfate carriers have to be adjusted precisely to the composition of the available clinker [61].

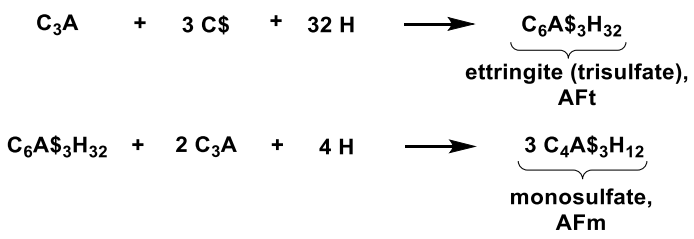

Figure 12: Formal reaction scheme of the aluminate reaction. In the presence of sufficiently high SO_4^{2-} concentration, ettringite ($C_6A\$_3H_{32}$, 3 CaO · Al_2O_3 · 3 $CaSO_4$ · 32 H_2O) which is the most prominent trisulfate (AFt), is formed. As the sulfate concentration decreases over time during the hydration and drops below ~ 2.85 mg L^{-1}, the ettringite begins to react with remaining C_3A to form monosulfate (AFm) [61].

Evolution of hydration reaction according to heat flow curve

The complex, time-dependent mechanisms of cement hydration are often difficult to access. Typical measurements which can give an insight to the reaction kinetics are heat flow calorimetry, in-situ x-ray diffraction (XRD) and electron microscopy (SEM) [68, 69]. Since the hydration of OPC is mainly an exothermic process, heat flow calorimetry constitutes the state-of-the-art method to resolve the hydration process. On the basis of a typical heat flow curve, the hydration reaction can be divided into five different stages [8, 60, 61, 68], as displayed in Figure 13.

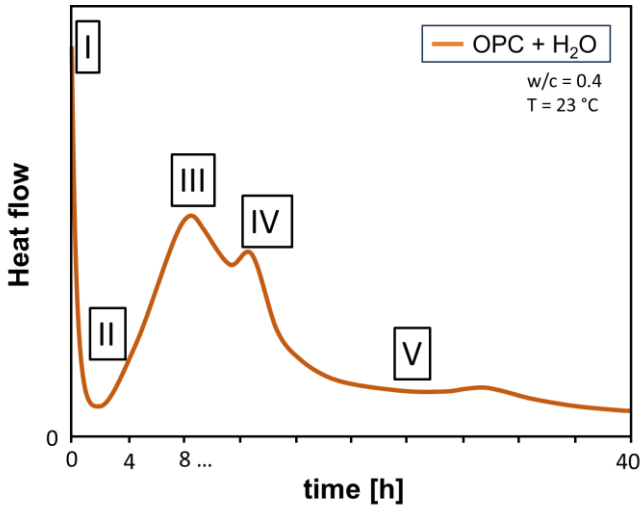

Figure 13: Hydration reaction of OPC with w/c = 0.4 at T = 23 °C monitored by isothermal heat flow calorimetry. The time-dependent heat flow can be divided into five stages: I: Initial dissolution, II: Induction period, III: Acceleration period and alite peak, IV: Deceleration period and aluminate peak and V: Slowed down reaction and formation of AFm. Redrawn from [70].

I) Initial dissolution

The initial, substantial heat release within the first minutes is primarily caused by the initial dissolution of C_3A, C_3S and the complete dissolution of readily soluble sulfates. The dissolution is followed by an immediate onset of ettringite precipitation [61].

II) Induction period

After the initial dissolution, the heat flow drops to a low, but still detectable level until the acceleration period sets in approximately three hours after first water-to-cement-contact. This time frame of reduced heat flow is referred to as the induction period [8, 60, 61]. It is commonly interpreted as a period during which little to no hydration occurs. The induction period is crucial for the workability of the material. Since the material largely remains in its suspension state, it can easily be processed and, for example, be pumped to its designated location. However, the reaction does not completely stop, but it is merely slowed down drastically. Ettringite precipitates at a low, but constant rate while calcium sulfates continue to dissolve [71, 72]. The existence of the induction period is mainly attributed to a temporary slowdown in C_3S dissolution. The cause of this slowdown is and has been the subject of many hypotheses and discussions [65]. It appears that the hypothesis suggesting the dissolution to be controlled by undersaturation has prevailed against the protective membrane theory [64]. However, the undersaturation theory cannot provide a satisfactory explanation for the onset of the acceleration period of the silicate reaction yet. For a more detailed discussion on the different hypotheses, the reader is referred to literature [64, 65].

III) Acceleration period and alite peak maximum

In the third time period, the heat flow increases significantly. This increase and the following peak maximum correlate to the accelerated dissolution of C_3S and the synchronous precipitation of C-S-H and CH [8]. The cause for the onset of this acceleration period is still under debate [64].

IV) Deceleration period and aluminate peak maximum

The alite peak maximum is followed by a slowdown in the reaction due to the decreasing dissolution rate of C_3S (deceleration period). The following heat flow maximum is the aluminate peak. Its onset is defined by the so-called “sulfate depletion” which is caused by the final consumption of the available calcium sulfates. This leads to the reinitiation of C_3A dissolution and an acceleration of the exothermic ettringite precipitation [60, 72, 73]. The position of the aluminate peak in relation to the silicate peak therefore strongly depends on the amount of sulfate carriers in the mixture.

V) Slowed down reaction and formation of AFm

The two main reactions in period III and IV are followed by the last period, which is characterized by slow diffusion processes in the hardening material. It contains a small peak at approximately 24 - 48 h after the first water-to-cement-contact. The small peak maximum marks the reaction of C_4AF and the conversion of ettringite to the monosulfate phases (AFm) [8, 60].

2.3 Rheological Characterization of Cement Pastes

Rheology is the science of deformation and flow of materials under an applied stress or strain [74–78]. Different types of deformation can be applied, including compression, elongation and simple shear. In simple shear, the applied force is in-plane with the direction of deformation. All types of shear behavior can be described within two boundary cases: the flow of a linear viscous liquid, described by Newton's law, and the deformation of an ideal elastic solid, described by Hooke's law. The behavior of most materials, like polymers and suspensions, falls in between these limiting cases, making them *viscoelastic*. Concentrated suspensions, for example, show viscoelastic behavior due to collective particle movements. Rheology has a broad range of applications, e.g. in material science, engineering, geophysics, cosmetics, human biology and polymer processing as rheological measurements can provide insights into structure – property relationships and processing behavior. Moreover, it can be used to characterize the performance of materials in applications such as coatings, adhesives, biomedical formulations, and soft matter engineering. For a fundamental introduction to the field of rheology, the reader is referred to standard textbooks [74–78].

This work focuses on the rheological characterization of cement pastes at early hydration states. Cement paste is an aqueous, concentrated suspension, which displays several non-Newtonian behaviors such as shear-thinning, shear-thickening, yield stress and thixotropy. Therefore, chapter 2.3.1 gives a short introduction into basic rheological concepts describing the shear behavior of suspensions including the concepts of these non-linear phenomena. Chapter 2.3.2 (p. 23) gives a short introduction to the rheological experiments applied to cementitious materials.

2.3.1 Rheological Concepts for Suspensions

Suspensions are disperse systems consisting of solid particles distributed within a liquid medium [79]. The behavior of suspensions is often classified by the size of the dispersed particles. According to the IUPAC definition, colloidal suspensions contain particles with diameters between roughly 1 nm to 1 µm [80]. However, the actual limits applied in literature can differ. Liquids containing particles with diameters of < 1nm are considered solutions, whereas liquids containing particles with diameters of > 1µm are referred to as suspensions, but not as colloidal suspensions. The lower limit of 1 nm ensures that the dispersed particles are considerably larger than the solvent molecules, allowing the surrounding fluid to be treated as a continuum. The key criterium for colloidal suspensions is that the particles undergo Brownian motion due to thermal forces, counteracting gravitational settling, which is given for particles with diameters < 1µm. Particles of diameters > 1 µm are not subjected to substantial Brownian motion and therefore sediment or cream more readily [79].

Effect of Solid Volume Fraction ϕ on the Rheological Properties of Suspensions

The rheological properties of suspensions (viscosity, critical strain, yield stress, etc.) are functions of the solid volume fraction ϕ occupied by the particles [81], which is calculated as the ratio of the volume V_P occupied by the particles to the total volume V_{total}:

$$\phi = \frac{V_p}{V_{total}} \tag{2.4}$$

Suspensions are categorized by their solid volume fraction ϕ as *dilute* (ϕ << 1 %), *semi-dilute* (0.01 [82] or 0.05 [83] < ϕ < ϕ_c), *concentrated* (ϕ_c < ϕ < ϕ_m) and *compact* ($\phi \rightarrow \phi_m$), as illustrated in Figure 14 [79, 81, 82].

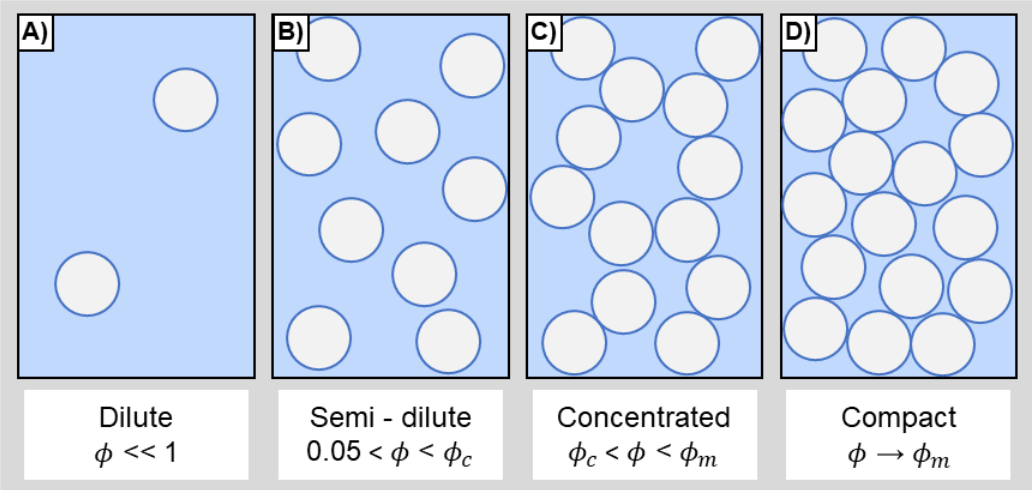

Figure 14: Graphic illustration of concentration regimes for suspensions. Suspensions are categorized by their solid volume fraction ϕ as dilute (ϕ << 1 %), semi-dilute (0.01 [82] or 0.05 [83] < ϕ < ϕ_c), concentrated (ϕ_c < ϕ < ϕ_m) and compact (ϕ → ϕ_m) [79, 81, 82]. Adapted from [82].

However, exact definitions of the limits between these regimes do not exist and thus the classifications differ between textbooks [79, 82, 83]. For dilute suspensions, the particle concentration is sufficiently small so that particle interactions are minimized and can be neglected in the description of the macroscopic behavior [82]. In the case of non-colloidal particles in a Newtonian suspension fluid, the dependence of the relative zero shear viscosity $\eta_{0,rel}$ on ϕ is given by the Einstein equation [84, 85] :

$$\eta_{0,rel} = 1 + 2.5 \cdot \phi \tag{2.5}$$

This equation represents a close approximation of reality for ϕ < 2% [81]. For higher solid volume fractions, the proportion of space is excluded in terms of occupancy by any single particle. Consequently, the probability of particle–particle interaction increases, wherefore a quadratic term is added to the equation (e.g. Batchelor equation) [79, 83]. Further increasing the volume fraction to $\phi > \phi_c \approx 0.15$ leads to a state, where the macroscopic behavior is mainly governed by collective particle interactions [79]. The relative zero shear viscosity of those

concentrated suspensions can be expressed by different phenomenological models, such as the Quemada, Marcon-Pierce or the Krieger Dougherty equation [79, 81, 82]. The Krieger-Dougherty equation describes the relative zero shear viscosity as:

$$\eta_{0,rel} = \left(1 - \frac{\phi}{\phi_m}\right)^{-[\eta]\cdot\phi_m} \tag{2.6}$$

With the maximum solid volume fraction ϕ_m and the intrinsic viscosity $[\eta]$, which is defined as the limit of the reduced viscosity $\eta_{red}(c)$ as the concentration c approaches zero:

$$[\eta] = \lim_{c\to 0} \eta_{red} \tag{2.7}$$

The Krieger-Dougherty equation introduces the maximum solid volume fraction or maximum packing fraction ϕ_m. For uniform spheres, the maximum packing density obtained by an unordered state resulting from pouring the suspension into a container is ϕ_m = 55 %. By vibration of the container, random close packing increases ϕ_m to 64 %. For a crystalline monodisperse system, ϕ_m = 74 % which corresponds to the maximum packing fraction of face-centred cubic packing [77]. Suspensions with broad particle size distributions can reach much higher maximum packing fractions of up to 90 - 95%, as smaller particles can fill up the gaps between bigger particles [82].

Yield Stress

Many materials such as dense suspensions, colloidal gels, microgel suspensions, concentrated emulsions or foams behave as yield stress fluids, meaning they behave like solids under rest and start to flow above a critical stress, the so-called yield stress σ_0 (see Figure 15) [82]. Many "real-life" materials display a yield stress which is not uncommonly key to their application. Examples are the decoration of a cake with cream or toothpaste on a toothbrush. Both of these materials are transported via flow under applied stress (pressure on the tube) to their designated place and then maintain their shape once the flow stopped [82]. Although the existence of true yield stress behavior has been under debate [86], it can be concluded that in any event the yield stress is an engineering reality [87].

Microscopically, the yield stress σ_0 manifests due to the formation of interparticle networks formed by interparticle forces and percolation. If an external stress higher than the yield stress is applied, the network collapses and the material starts to flow. Yield stress materials usually display two yield stresses: the static and the dynamic yield stress. The static yield stress is the stress required to initiate flow, while the dynamic yield stress is the stress needed to maintain flow when the network structure is already broken. It takes more stress to destroy the network structure than to maintain flow, consequently:

$$\sigma_{0,s} > \sigma_{0,d} \tag{2.8}$$

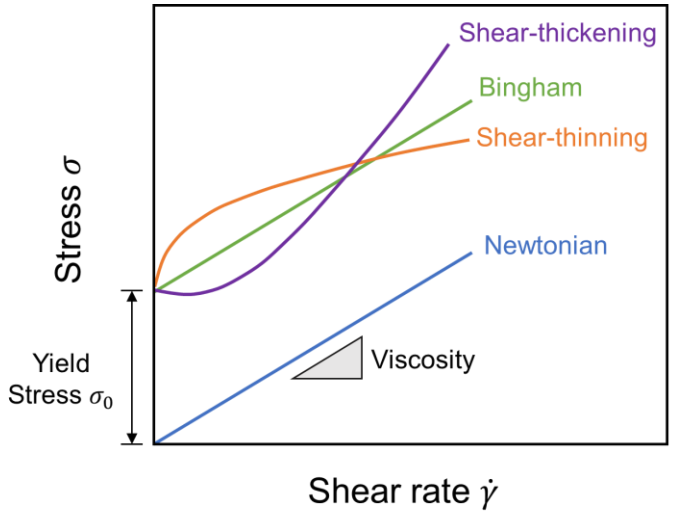

Figure 15: Illustration of different rheological behaviors. The yield stress σ_0 is the minimum shear stress which has to be applied for a yield stress material to transition from a solid-like to a liquid like state. Adapted from [8].

The shear-rate dependent viscosity of yield stress materials can be described by different phenomenological models. The simplest model is the Bingham-model [79]:

$$\sigma = \sigma_0 + \eta_p \cdot \dot{\gamma} \tag{2.9}$$

with the yield stress σ_0, the plastic viscosity η_p and the shear rate $\dot{\gamma}$. According to this model, Bingham-plastics show a linear flow behavior above the yield stress [79]. However, many materials display shear-thinning or shear-thickening behavior above the yield stress [79]. This can be described by the Herschel-Bulkley model [82]:

$$\sigma = \sigma_0 + k \cdot \dot{\gamma}^n \tag{2.10}$$

The consistency index *k* and the exponent *n*, which is usually negative, are both material parameters [81]. With n < 1 shear thinning and n > 1 shear-thickening behavior can be described. With n = 1, the Bingham model is obtained [75]. To describe more complex yield stress material behaviors a multitude of models such as the modified Bingham-model, the Casson model, the De Kee-Turcotte or the Papanastasiou-Model exist [78]. The modified Bingham-model, introduces a second order term of $\dot{\gamma}$ and is quite prominent in the rheological characterization of cementitious materials [88, 89]:

$$\sigma = \sigma_0 + \eta_p \cdot \dot{\gamma} + c \cdot \dot{\gamma}^2 \tag{2.11}$$

It can be considered to be an extension of the Bingham model with a second order term or as a second order Taylor development of the Herschel-Bulkley equation [90]. The relation of the two proportionality constants describes the behavior, with $c/\eta_p < 0$ occurring for shear-thinning and $c/\eta_p > 0$ for shear-thickening. For c = 0, the Bingham model is obtained [90].

Thixotropy

Thixotropy refers to the time-dependent decrease in viscosity under external influences such as shear stress, followed by a gradual recovery of viscosity once the applied stress is removed or reduced [91], as illustrated in Figure 16. The fluidization of the material results from the breakdown of its internal network structure due to the applied deformation. When the material is at rest or subjected to very low shear rates, the network is rebuilt over time, and the original viscosity can be recovered after a sufficient resting time. By definition, thixotropy is a reversible process [82, 91]. This behavior causes rheological parameters – such as the yield stress or the plastic viscosity – to be dependent on the applied shear rate and the duration of shear [81].

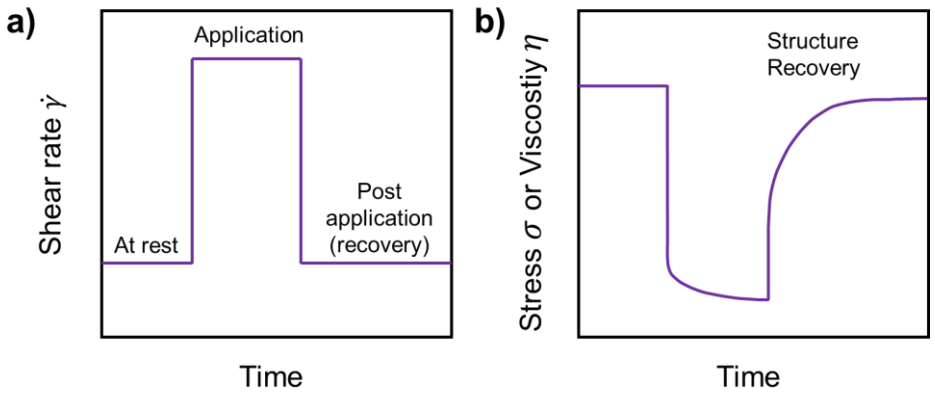

Figure 16: Schematic graphs illustrating thixotropic behavior. Thixotropy refers to the loss of a material's internal structure under external deformation, such as an applied shear rate as illustrated in a), which leads to a temporary decrease in viscosity, as illustrated in b). Once the applied shear rate is removed or reduced, the initial viscosity gradually recovers as the internal network structure rebuilds (see b)). Adapted from [92].

2.3.2 Rheological Characterization of Cementitious Materials

Rheometry is a key method for assessing the processability of cementitious materials, i.e. all materials containing cement across all relevant length scales from cement paste to mortar to concrete. The particle sizes vary significantly between these materials. Since the gap size typically should be ten times larger than the largest particle, very different rheological techniques must be applied. For cement pastes, with typical particle sizes of approximately 10 µm, "standard" rotational rheometers with typical geometries and a gap height of 1 mm can be applied. For mortar and concrete, which contain aggregates of up to 20 mm in diameter, various custom rotational rheometers with gap sizes of 50 – 100 mm and several alternative rheological experiments like the L-box or image-based analysis of flow behavior have been developed [81, 93]. A detailed review of concrete rheology is beyond the scope of this work, thus the reader is referred to literature [81]. This chapter focuses on the variety of rheological experiments applied to cementitious materials of small particle sizes (< 4 mm) with a strong focus on cement paste.

Generally, cementitious materials undergo a hydration reaction which leads to the macroscopic transition from a liquid to a solid [8]. The relevant time frame in which the material flows and is therefore characterizable via rotational rheometry, is approximately three to four hours after first water-to-cement contact [81]. This corresponds to the induction period (compare chapter 2.2.2, p. 15). Although the heat flow in calorimetry drops to a low level in this time period (see Figure 13, p. 17), the material continuously evolves by the dissolution of clinker phases and sulfate carries, and the simultaneous precipitation of hydrates [60, 61]. Consequently, the rheological properties of cement paste are time-dependent [8, 68, 81, 94]. The yield stress, for example, increases with time [8]. However, since the exact reaction mechanisms in the induction period are still under debate, the correlation between the ongoing hydration and the macroscopic stiffening or hardening of the material are a central topic in current research [94, 95]. In summary, when rheological measurements on cement pastes are conducted, the time-dependent microscopic change needs to be considered.

Cement paste at early hydration states (< 4 h) is a concentrated suspension of non-spherical, non-colloidal particles with a broad particle size distribution ranging from a few microns to a few hundreds of microns [81, 82]. Consequently, $\phi_m \geq 64\,\%$ can be assumed [96]. Moreover, due to the ongoing dissolution and precipitation, the number, shape, and distribution of particles is time-dependent. This makes the solid volume fraction an unknown function of time: $\phi(t)$ [96].

Thixotropy and Structural Build-up

Cementitious materials generally display thixotropic behavior. During rest, a percolation network is formed which is destroyed by an applied shear deformation, leading to a macroscopic reduction of the viscosity. If the material is left to rest and then subjected to shear again at a higher sample age, less shear-thinning is observed due to the ongoing hydration reaction, that can lead to the formation of permanent bridges between particles [97]. Consequently, the thixotropy of cementitious material is not a reversible process, as illustrated in Figure 17. Thus, the network formation is usually described as *structural build-up* [97–99]. The term “structural build-up” is not clearly defined, but it usually refers to the formation of a percolation network including both the physical agglomeration of particles as well as the ongoing hydration reaction and formation of hydrates which potentially act as interparticle bridges. The extend of the contribution of the hydration as well as the question whether the C-S-H or the ettringite formation contribute more to the structural build-up, is the topic of current research [95, 97, 99].

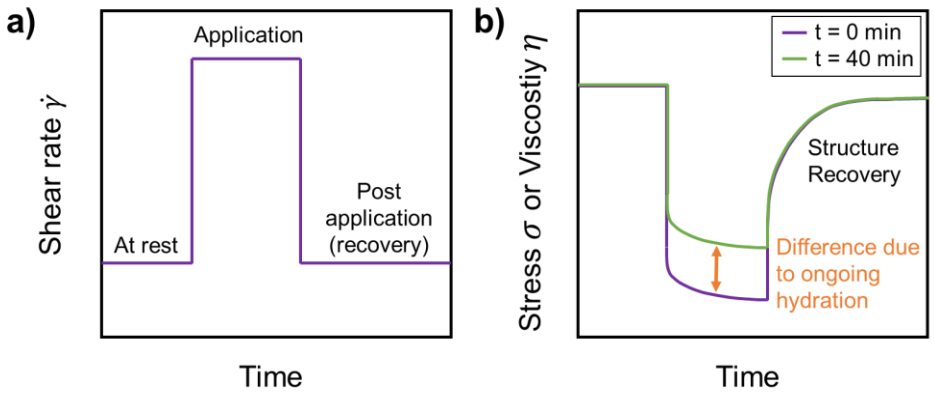

Figure 17: Illustration of the time-dependent thixotropic behavior of cementitious materials. The material's internal structure is destroyed under an applied shear rate (illustrated in a), which leads to a temporary decrease in viscosity (illustrated in b) in violet). The network rebuilds under rest, which leads to the gradual recovery of the initial viscosity. When subjected to shear again at a higher sample age (green), the viscosity under shear is higher due to the progressed hydration reaction which leads to the formation of permanent interparticle bridges. Consequently, the thixotropy of cementitious materials is not a reversible process. The network formation caused by both physical agglomeration as well as the ongoing hydration is referred to as 'structural build-up'.

Spread Flow or Slump Flow

The most common technique to characterize the flow properties of cementitious materials is the spread flow or slump flow test, which is shown in Figure 18. In this standardized test, a cone of defined size is completely filled with cementitious material and, if required by the particular standard, the material is compacted by vibration. As the cone is lifted, the material flows to ideally form a symmetrical, round puddle whose diameter, usually in [cm], is the so-called *spread*. Sometimes it is also referred to as *slump flow*. If the difference in height between the cone and the material is measured, then this value is referred to as *slump*. The used cone size depends on the particle sizes of the material. The smallest material scale covered by flow-based consistency tests according DIN standards is mortars (aggregate sizes < 4 mm), as described in DIN 1015-3 [100]. Spread flow tests of cement pastes without aggregates are not covered by German standards. In the scientific literature on cement paste rheology, the Haegermann cone (r_1 = 35 mm, r_2 = 50 mm, h = 60 mm; compare DIN 1015-3) [100, 101] or the Vicat cone (r_1 = 35 mm, r_2 = 40 mm, h = 40 mm) [102] are frequently applied. A picture of a spread flow test conducted with a Vicat cone is given in Figure 84 (SI, p. 163). However, these cones require rather large volumes of cement paste with V(Haegermann) = 344 mL and V(Vicat) = 177 mL, which can be a disadvantage especially when laboratory-synthesized admixtures only available in small quantities are to be characterized. Thus, smaller cones, like the mini cone (r_1 = 9.5 mm, d_2 = 19 mm, h = 57 mm, V = 37 mL), as displayed in Figure 18, can be used as an alternative to obtain the spread of cement pastes, especially in the presence of superplasticizers (chapter 2.4, p. 29) [103–105]. However, with decreasing cone size, the obtained spread values increasingly depend on the speed and the direction of the lifting motion and thus become user dependent [106]. Therefore, spread values obtained with the mini cone, smaller

cones or cylinders should only be interpreted relatively within the same measurement series conducted by the same user. The resulting spread flow does not only depend on the investigated cementitious material and the cone geometry, but also on the surface on which the experiment is performed. In practice, spread flow tests of cement pastes are carried out either on acrylic plates (plexiglass) or glass plates, depending on the laboratory set-up or research methodology. Regional laboratory practices can influence this choice, with North American laboratories preferring acrylic plates, while European laboratories often employ glass plates. However, this distinction is not defined by any of the respective standards. In addition to the type of surface, the pretreatment of the surface prior to the experiment also needs consideration. Whether the surface is dry or pre-wetted influences the obtained spread value and should therefore be kept consistent within a measurement series.

Figure 18: Picture of a spread flow test conducted with a mini cone. In a spread flow test in general, a cone of a defined size is filled completely with cementitious material. As the cone is lifted, the material flows to ideally form a symmetrical, round puddle whose diameter is the so-called spread. The experiment shown on this picture was conducted using a mini cone (r_1 = 9.5 mm, d_2 = 19 mm, h = 57 mm, V = 37 mL), which in this case was a negative mould inside an acrylic cylinder. The cone inside the cylinder is highlighted with orange lines as guide to the eye. In this experiment, the spread flow test was conducted on a dry acrylic plate in the laboratory of Prof. Ammar Yahia, Sherbrooke, Canada.

In summary, the spread flow test is a robust, widespread, and simple rheological experiment, that does not require any understanding of rheology and can be performed for all cementitious materials from cement pastes to concrete. The standardized cones and procedures make the obtained values for mortar and concrete easily comparable between different laboratories or construction sites. However, the reduction to a single diameter value cannot cover all aspects of the complex rheological properties of cementitious materials, like their thixotropic behavior. Thus, more sophisticated rheological procedures are required to fully characterize these materials.

Yield Stress in Steady-Shear Rheometry

The dynamic yield stress $\sigma_{0,d}$ obtained via rotational rheometry is a very central property in the characterization of cementitious materials as it is closely tied to the spread flow test. It is assumed that the material in the spread-flow tests stops to flow when the dynamic yield stress is reached, thus $\sigma_{0,d}$ defining the resulting spread value. Different mathematical correlations between $\sigma_{0,d}$ and the spread have been proposed, with the most commonly used being [101, 107, 108]:

$$\sigma_{0,d} \approx \frac{225 \cdot \rho \cdot g \cdot V^2}{128 \cdot \pi^2 \cdot R^5} \tag{2.12}$$

including the density ρ (typically ρ = 2 kg m^{-3} for cement paste), the earth gravity g (9.81 m s^{-2}), the volume of the cone V and the radius of the spread R. Different rheological experiments can be used to obtain the dynamic yield stress [76, 82, 87]. In rotational rheometry, the most common technique, a flow curve is obtained by a descending series of shear rates. The yield stress is determined via fitting of the stress data with a suitable model (compare chapter 2.3.1, p. 19). As described in the previous chapter, different models can be used to calculate the yield stress with Bingham and Herschel-Bulkley being the most prominent models for cementitious materials [81, 104, 109]. Yahia et al. compared different models, including the Bingham, the Herschel-Bulkley model and the modified Bingham, and their fit for a series of different cementitious materials. The value obtained by a Herschel-Bulkley fit gave the lowest estimates for shear-thinning and the highest estimates for shear-thickening materials [88]. For cement pastes, similar studies on the rheological models show that the Bingham-Fit yields the most stable results, while the Herschel-Bulkley model is a better representation of the non-linear behavior [104, 110, 111]. It should be noted that the yield stress in general is a fit parameter, that strongly depends on the rheological experiment, the fit function and the fitted shear rate range. Therefore, care should be taken in the comparison of different studies, especially when the numerical values are being discussed.

The static yield stress $\sigma_{0,s}$ can also be of interest, especially when studies on the structural build-up are being conducted [104, 109, 112, 113]. Nicia et al., for example, used the time-dependent growth of $\sigma_{0,s}$ to quantify the thixotropic structural build-up [113]. The static yield stress is often obtained by applying a constant shear rate in a simple shear measurements [104].

As the rheological behavior of cementitious materials strongly depends on the state of the ongoing hydration reaction, experiments to determine the dynamic yield stress need to be sufficiently short, typically less than five to ten minutes, to ensure that the chemical changes are negligibly slow in comparison to the duration of the experiment.

Oscillatory Shear

Oscillatory shear rheometry can be conducted in two amplitude regimes: Small amplitude oscillatory shear (SAOS) probes the linear viscoelastic response of a material, whereas large amplitude oscillatory shear (LAOS) explores its nonlinear behavior under progressively greater

deformation. In oscillatory time sweep experiments, an amplitude in the SAOS regime is applied and the time-dependent evolution of the shear modulus G'(t) and the loss modulus G''(t) is monitored. In these experiment, G'(t) usually increases and reaches a plateau within ten to twenty minutes, a time frame which is by far too small to correspond to the liquid to solid transition of cement pastes (compare chapter 2.2.2, p. 15). Therefore, the G'(t) evolution is usually attributed to the structural build-up caused both by interparticle interactions and the ongoing hydration reaction [99, 114]. Michel et al. recently suggested the structural build-up monitored by the G' evolution to be directly caused by C-S-H formation [115], while the findings of Jakob et al. suggest ettringite to be the main contributor to the observed stiffening [95]. According to Mostafa and Yahia, the linear increase in G' can be described by the rigidification rate of the percolation network [114]. Although the static yield stress also probes the formed percolation network, it has been found that the G'(t) increase does not necessarily coincide with the time-dependent increase in $\sigma_{0,s}$ [99].

Oscillatory strain sweeps are also an important tool in the investigation of the structural build-up of cement pastes [112, 116–118]. Two critical strains are identified in these tests: the strain that marks the transition from the linear to the non-linear regime, and the strain at which G' = G'' [97]. These critical strains have often been correlated to the static yield stress [112]. LAOS experiments have also been conducted for cement pastes [119, 120], but are beyond the scope of this work.

2.4 Poly(carboxylate ether)s – the Most Prominent Cement Admixtures

Concrete is an engineering material. Its properties are mainly governed by its mix design, primarily the chosen aggregate sizes and the water content [8]. In addition, a broad range of admixtures can be used to fine-tune the final concrete properties both in fluid and solid state. These admixtures include e.g. *viscosity modifiers*, like carboxymethylcellulose (CMC), which are used to increase the viscosity and stabilize the mixture against segregation, and *retarders*, often mono- or polysaccharides, which are used to prolong the induction period [8].

The group of admixtures that are used to increase the flowability and thus improve the workability, are *water reducers* [8]. Water reducers are molecules which either improve the flowability at a given w/c ratio or allow decreasing the water content by at least 5% while maintaining good workability. The water content determines the final solid properties of the hardened cementitious material (see chapter 2.2.1, p. 14). Reducing the water content increases the resulting final compressive strength. This relationship is used, for example, in ultra-high performance concrete (UHPC), which is characterized, amongst other properties, by a very high final compressive strength exceeding 150 MPa resulting from its extremely low water-to-cement ratio of w/c < 0.2 [121]. The most commonly used water reduces are lignosulfonates, which electrostatically stabilize the cement suspension [8]. In the 1980s, synthetic polymers emerged as water reducers which allowed such a high water reduction, that they opened up a new category within the water reducers: *superplasticizers*, also referred to as *high-range water reducers* (HRWR) [8, 56]. Superplasticizers usually allow a water reduction of at least 12% [8].

With an annual production of about 15 million tons [122], the most important type of superplasticizers are the poly(carboxylate ether)s (PCEs). The great water-reducing effect of PCEs relies on their unique molecular architecture [8]. The term *poly(carboxylate ether)s* describes a group of comb copolymers which share the characteristics of a charge-carrying backbone and poly(ethylene) (PEO) sidechains. As illustrated in Figure 19, the negatively charged backbone allows the combs to adsorb to the positively charged surfaces of cement particles. The non-adsorbing sidechains extend to the pore solution and create steric hindrance between the particles, resulting in the macroscopic reduction of the yield stress σ_0 and thus an enhancement in workability [8]. In the most common PCE structure, the backbone is made from a polycarboxylate, usually poly(acrylic acid) (PAA) or poly(methacrylic acid) (PMAA) in which the carboxylic acid functions bear negative charges in the strongly basic environment of cement pastes of pH ≈ 12 - 14. The term *PCEs* is also used for comb structures with e.g. alternative anchoring groups such as phosphate ($-PO_4^{2-}$) or sulfonate ($-SO_3^-$). For an overview of possible PCE architectures and their influence on the macroscopic properties of cement pastes, the reader is referred to recent review articles [56, 123–125]. Unless stated otherwise, the term *PCE* in this work refers to comb polymers with a polycarboxylate backbone ($-CO_2^-$) and PEO sidechains. In addition to their fluidizing effect, PCEs typically exhibit a retarding effect, meaning they extend the induction period of the cement hydration [8]. Different hypotheses as to why PCEs act as a retarder have been developed and are still under debate [8, 9, 126].

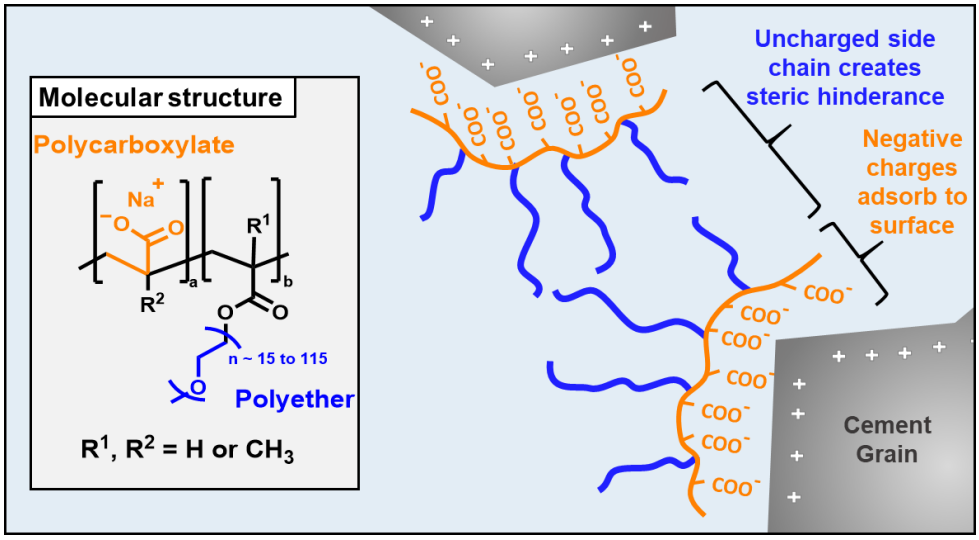

Figure 19: Schematic illustration of working principle of poly(carboxylate ether) (PCE) superplasticizer, adapted from [8]. Its comb-copolymer architecture is key to its functionality. The negatively charged backbone allows the combs to adsorb to the positively charged surfaces of the simplified cement particles. The non-adsorbing sidechains extend to the pore solution and create steric hindrance between the particles, resulting in the macroscopic reduction of the yield stress σ_0 and thus an enhancement in workability.

As PCE increases the flowability of cement pastes, the spread value increases accordingly, which correlates to a reduction in the dynamic yield stress (compare chapter 2.3.2, p. 23). The macroscopic spread increase induced by PCE is concentration-dependent and follows the so-called S-curve [127, 128], illustrated in Figure 20. The S-curve displays the spread plotted against the PCE dosage, expressed in wt.% relative to the mass of dry binder (typically cement). The plotted spread values correspond to the initial fluidity during the first thirty minutes after mixing [8]. A critical dosage must be exceeded before any significant increase in spread flow is observed. Above this threshold, the spread flow increases linearly with dosage until the saturation dosage is reached. The saturation denotes the point beyond which a further concentration increase no longer enhances the spread values significantly. Dosages above the saturation may lead to segregation or bleeding. The maximum PCE dosage is typically below 2 wt.% of solid polymer in relation to mass of dry binder [8]. However, most studies employ substantially lower dosages, with PCE commonly used in the range of 0 – 0.5 wt.% [129]. Rheological characterization along the S-curve can be challenging because the reference paste without PCE is very stiff due to its low w/c-ratio, while pastes near the saturation dosage are highly flowable and exhibit very low yield stresses and viscosities [130]. Mantellato et al. recently proposed the so-called shifting factor, under the assumption, that the presence of superplasticizer increases the percolation threshold ϕ_{perc}. The shifting factor is meant to enable measurements to be performed at different solid volume fractions and subsequently be superimposed to a single master curve [96, 130].

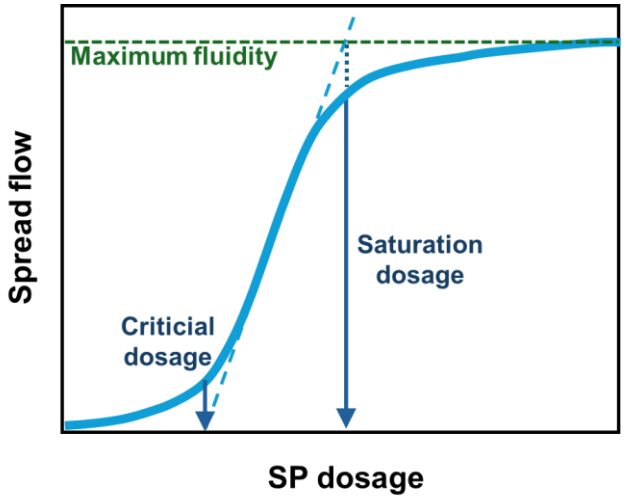

Figure 20: Typical S-curve in the spread vs. SP dosage diagram. Above the critical dosage, the spread flow increases linearly with the added mass of SP until the saturation dosage is reached. The saturation denotes the point beyond which a further addition no longer linearly increases the spread values. Adapted from [127, 128, 131].

As described in the previous chapter, the yield stress of cementitious materials increases with hydration time (compare chapter 2.3.2, p. 23). The addition of PCE slows down this time-dependent evolution, but a progressive loss of workability is usually observed nevertheless. The capability to maintain a low yield stress for a prolonged time period is called yield stress retention or slump retention, and it is a critical parameter for the practical performance of PCE superplasticizers [8]. However, the studies in this work only focus on the initial fluidity thus the slump retention is not further discussed. The saturation dosage in the S-curve is generally associated with the maximum possible surface coverage, as determined by the adsorption equilibrium and competitive adsorption [9, 132]. Thus, it is essential to examine the adsorption behavior of PCE molecules in more detail. The most influential work on the adsorption of PCEs has been developed by Flatt and co-workers, based on the solution theory of comb polymers originally proposed by Gay and Raphaël [9, 10, 126, 133, 134]. Gay and Raphaël extended classical polymer solution theory to comb polymers and identified distinct conformational regimes depending on their structural parameters [133]. They propose the combs to be characterized by three parameters: the number of structural repeating units n, the number of backbone monomers per repeating unit N and the sidechain length P. The ratios between these structural parameters can be used to describe the polymers in solution as shown in Figure 21, which can fall into one of the following structural regimes: decorated chain (DC), flexible backbone worm (FBW), stretched backbone worm (SBW), stretched backbone star (SBS), and flexible backbone star (FBS) [133]. Most PCE combs fall into the FBW regime, with the SBW being second most common [129].

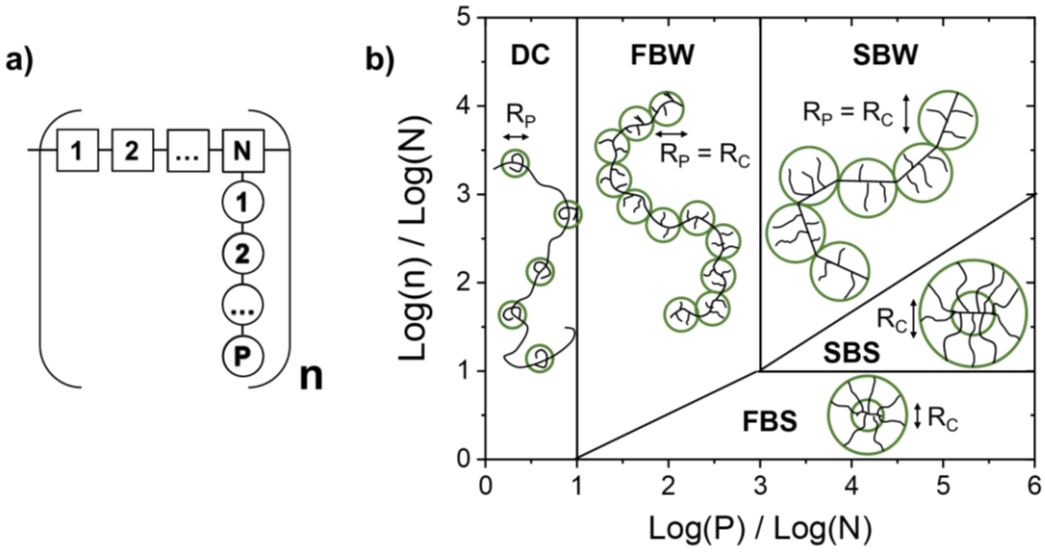

Figure 21: A) Schematic representation of one of the n structural repeating units of comb polymer with the sidechain length P and the number of backbone monomers N. B) Structural regimes of comb polymers. The different domains are the following: decorated chains (DC), flexible backbone worm (FBW), stretched backbone worm (SBW), stretched backbone star (SBS), and flexible backbone star (FBS). The sidechain length is denoted R_P and the core size is R_C. Redrawn from [10, 133].

For FBW type molecules, the equilibrium adsorption constant has been shown to scale with the structural parameters *P*, *N* and *n* of the polymer according to:

$$K_A = \frac{k_{ads}}{k_{des}} \sim \frac{(N-1)^2 \cdot z^2}{P^{\frac{9}{5}} \cdot N^{\frac{3}{5}} \cdot n} \tag{2.13}$$

with the adsorption and desorption rate constants k_{ads} and k_{des}, and the unitless effective charge density *z*. This expression links the molecular architecture of the comb polymer directly to its adsorption affinity. The derivation of equation (2.13) is based on several simplifying assumptions [134]:

1. The PCE combs follow a Langmuir type adsorption isotherm. The Langmuir adsorption isotherm describes a monolayer adsorption onto a finite number of identical surface sites, assuming that no interaction occurs between molecules. For an introduction to adsorption isotherms, the reader is referred to literature [135].
2. The driving force for adsorption is attributed to the electrostatic interaction between the charged polymer and the charged surface, which is driven by the number of charges carried by the polymer. Competitive adsorption should be expressed with respect to the surface charge sites.
3. The polymer combs are considered to compete with small ions for the available adsorption sites.
4. The adsorption and desorption rates are expressed solely in terms of the total number of charges on the polymer in relation to the total number of free adsorption sites, thereby

neglecting the role of the polymer structure. The polymer structure is incorporated into the kinetic pre-factors.

The FBW structure describes the polymer as a chain of spherical blobs, each characterized by a core radius R_c [10]. When adsorbed to the surface, this sequence becomes a chain of hemispherical blobs. The characteristic size of these hemispherical blobs was derived based on free-energy minimization following a Flory-Huggins type approach [10]:

$$R_{AC} = (2\sqrt{2}\,\frac{a_P}{a_N}(1-2\chi))^{\frac{1}{5}} a_p P^{\frac{7}{10}} N^{-\frac{1}{10}} \tag{2.14}$$

With the gyration radius of a single adsorbed hemispherical core R_{AC}, the length of the backbone monomer a_N, the length of the sidechain monomer a_P and the Flory-Huggins parameter χ of the PEO sidechain in the respective solution. For their calculations, Flatt et al. use a_N = 0.25 nm for methacrylic acid, a_P = 0.36 nm for ethylene oxide and χ = 0.37 for PEO, determined for D_2O at 25 °C [10]. The gyration radius of a hemisphere R_{AS} is assumed to correspond to the layer thickness, also often referred to as the brush height *h*, created by the non-adsorbed sidechains [10].

The overall surface area covered by the FBW polymer, including the lateral space required by the backbone, can be expressed by the following scaling law [10]:

$$S_A = \frac{\pi}{\sqrt{2}} a_N\, a_P \left(2\sqrt{2}(1-2\chi)\frac{a_P}{a_N}\right)^{\frac{2}{5}} P^{\frac{9}{10}} N^{\frac{3}{10}} n \tag{2.15}$$

Although equation (2.13) provides a useful conceptual link between polymer architecture and adsorption capability, a few key limitations require consideration. As discussed in the chapters 2.2 (p. 13) and chapter 2.3 (p. 19), cement pastes evolve rapidly during hydration by dissolution of clinker phases and precipitation of hydrate phases, which ultimately rapidly changes the available surface, thus limiting the time for PCE - surface interactions. Thus, it is questionable if a true equilibrium state can be reached. Additionally, PCEs do not adsorb uniformly on the various cement phases. They exhibit a higher affinity for aluminate phases than for silicate phases [124, 136]. Moreover, in recent studies on the effect of addition time of PCE, it was observed that PCE seemed to be “lost” when added directly to the mixing water [137], thus raising questions regarding the reversibility of the adsorption process. In the study, this apparent loss has been attributed to the enhanced formation of ettringite, which increases the available surface area and may therefore demand higher PCE dosages to achieve the same level of fluidity [137].

2.5 Principles of Infrared Spectroscopy

Infrared Spectroscopy is a standard tool in chemical laboratories for qualitative and quantitative analysis, such as the identification of chemical substances, the determination of molecular structures and the monitoring of reaction kinetics [138].

The infrared portion of the electromagnetic spectrum lies directly below the wavenumber region of visible light and is usually divided into three regions: near-, mid- and far infrared, as displayed in Figure 22. They are differentiated by their wavelengths and the related energy (see equation (2.16)). Therefore, different transitions are excited in the different electromagnetic regions, as written in Figure 22.

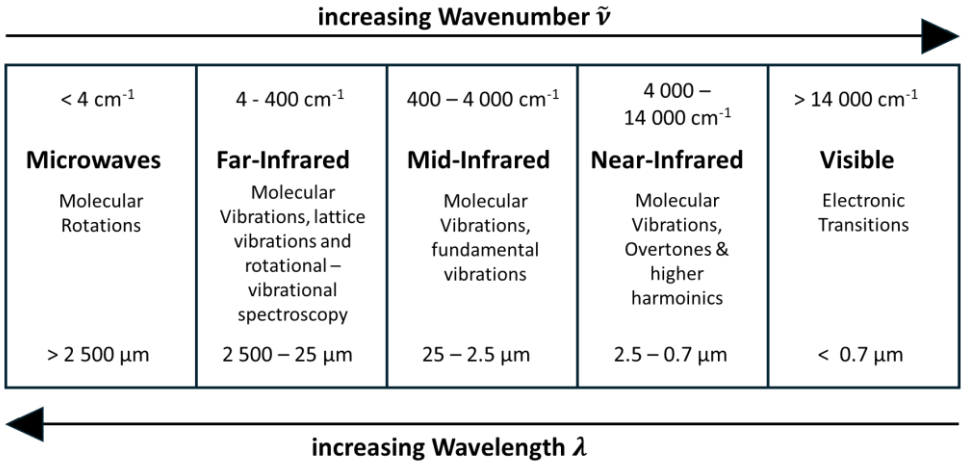

Figure 22: Infrared portion of the electromagnetic spectrum. The wavenumber increases from left to right, while the wavelength increases from right to left. Since the energy is proportional to the wavenumber, it also increases from left to right. Adapted from [138]

Most industrial applications of infrared spectroscopy are based on near - infrared (NIR) spectroscopy, as it is fast, penetrates bulk materials and uses inexpensive, robust hardware [139]. NIR analysis is for example applied in the sorting of waste prior to recycling. However, NIR mostly excites overtones, which makes the spectra difficult to interpret. Thus, chemometrics are usually needed to identify substances from the weak, broad and overlapping overtone bands [139]. Therefore, MIR spectroscopy is preferred in analytical laboratories because it probes fundamental molecular vibrations leading to sharp absorption bands, making the spectra easier to interpret. The basic working principle of infrared spectroscopy is the absorption of infrared light by vibrational modes of molecules energies match the energy of the incident radiation. This general concept is illustrated in Figure 23. In quantum theory, radiation is emitted from a source in discrete units called photons [140]. The photon energy *E* is expressed by:

$$E = h \cdot \nu = h \cdot \frac{c}{\lambda} \tag{2.16}$$

with the Planck's constant h, the photon frequency ν, the speed of light c, and the wavelength of the photon λ. If the photon energy corresponds to the energy of a vibrational mode of a molecular bond in the sample's molecule, the corresponding portion of the radiation is absorbed and therefore missing from the light reaching the detector. The remaining transmitted radiation is measured and the spectrum is obtained. IR spectra can be displayed in two ways: as transmittance or absorbance spectra. In the transmittance spectrum, the transmittance T is plotted against the wavenumber $\tilde{\nu}$, with the wavenumber $\tilde{\nu}$ being the inverse of the wavelength λ:

$$\tilde{\nu} = \frac{1}{\lambda} \tag{2.17}$$

and the transmittance T being defined as:

$$T = \frac{I}{I_0} \tag{2.18}$$

where I_0 is the incident intensity and I the transmitted intensity. Transmittance is usually expressed in percent: if no light of a given wavelength portion is absorbed, the transmittance is 100 %. If all light is absorbed, it is 0 %. For quantitative analysis, absorbance spectra are preferred. The absorbance A is calculated as:

$$A = -\log T = \log \frac{I_0}{I} \tag{2.19}$$

The absorbance is directly proportional to the concentration, as given by the Lambert-Beers law:

$$A = \varepsilon \cdot c \cdot l \tag{2.20}$$

with the molar extinction coefficient ε, the concentration c and the optical path length l.

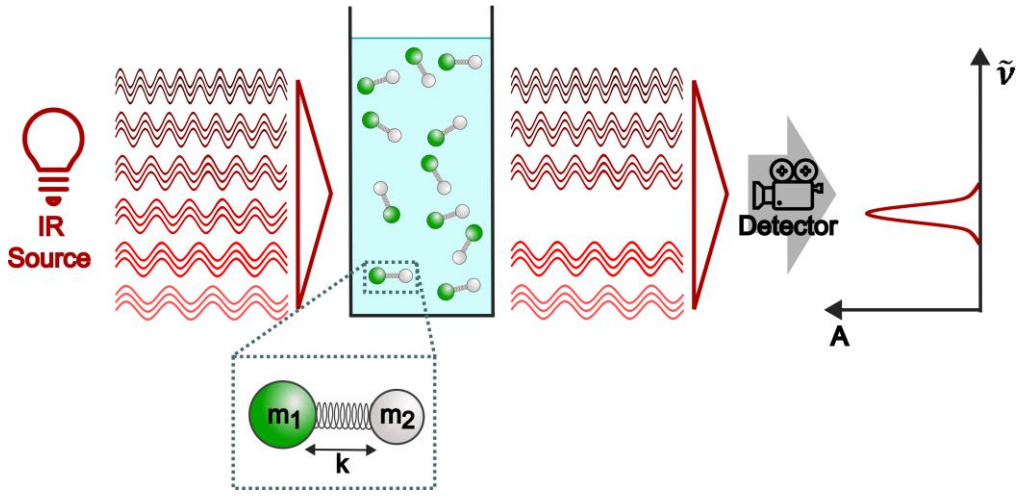

Figure 23: Scheme of the principle of IR spectroscopy. IR radiation of different wavelengths (indicated by the different shades of red) is used to irradiate the sample. The sample absorbs the infrared light if vibrational modes of the molecule match the energy of the incident radiation. The peaks in the absorbance spectrum mark the absorbed wavenumber regions. The molecule can be described as two masses m_1 and m_2 connected by a spring with the spring constant k.

As stated above, the infrared radiation is absorbed when its energy matches one of the vibrational modes of the molecules in the sample. The characteristics of a stretching vibration can be approximated by a mechanical model consisting of two point masses connected with a spring, as displayed in Figure 23 (p. 36). In this analogy, the atoms correspond to the point masses while the spring represents the chemical bond. A diatomic system can be described with a concept from classical mechanics: the *harmonic oscillator*. The classical vibrational frequency of a diatomic molecule is given as

$$\nu = \frac{1}{2\pi}\sqrt{\frac{k}{\mu}} \tag{2.21}$$

with the force constant *k* and the reduced mass μ, which is defined as:

$$\mu = \frac{m_1 m_2}{m_1 + m_2} \tag{2.22}$$

The force constant *k* corresponds to the bond strength of different bond types. For a C-C single bond, $k_1 \approx 300$ - 600 N m^{-1}, while $k_2 \approx 1\,000 - 1\,200$ N m^{-1}for a C=C double bond [140]. The potential energy of the classical harmonic oscillator is a function of the displacement *x*, as given by:

$$V(x) = \frac{1}{2}kx^2 \tag{2.23}$$

Molecular vibrations require a quantum-mechanical description. In quantum mechanics, the vibrational energy levels are quantized, and the energy of the harmonic oscillator is given by:

$$E = \left(n + \frac{1}{2}\right)h\nu, \quad with\ n = 1, 2, \ldots \tag{2.24}$$

Here, ν is the classical vibrational frequency of the oscillator and n is the vibrational quantum number. In the harmonic approximation, transitions are only allowed when the quantum number changes by Δn ± 1. All other transitions are forbidden. For a more detailed introduction to the concepts of the harmonic and anharmonic oscillator and the quantum-mechanical treatment of molecular vibrations, the reader is referred to [135, 138, 141, 142].

2.5.1 FTIR Instrumentation and Calculation of Spectra

The first infrared spectrometers were dispersive instruments in which each wavelength was measured individually. This was achieved by splitting the broadband infrared radiation with a prism or a grating into its spectral components and sequentially selecting wavelengths using a movable slit [141]. These instruments have been replaced by the much faster and more robust Fourier-Transform Infrared (FTIR) spectrometers. In FTIR, the sample is irradiated with modulated light containing all wavelengths at the same time. The measured intensity at the detector is Fourier-transformed to obtain the spectrum [141].

This chapter provides a brief and fundamental introduction to the operating principles of FTIR instruments and to the calculation of FTIR spectra. For a more theoretical and technical background, the reader is referred to the book by Griffiths and de Haseth [142]. For a comprehensive guide to obtaining high-quality FTIR spectra, the reader is referred to the book by Smith [138].

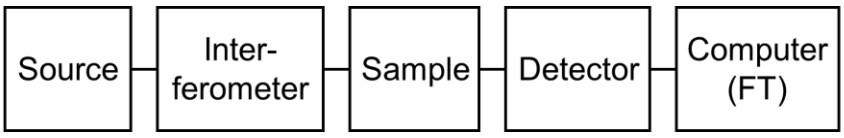

Figure 24: Simplified FTIR instrument, adapted from [141].

In a simplified FTIR instrument, the IR beam follows the general path displayed in Figure 24: An infrared source produces infrared light, which is modulated in the interferometer. Subsequently, the modulated light is guided to sample where parts are absorbed. The remaining light is detected by the detector, which is connected to a computer that conducts the Fourier transform (FT) to obtain the spectrum. In the following, the different parts of the instrument are discussed along the beam path. Sources in FTIR instruments are usually blackbody radiators that emit IR radiation. The most commonly used IR source is the Globar, a material based on silicon carbide [141]. It is usually preferred over other IR sources due to its high emissivity and the comparatively long life time [141]. Alternative sources are the Nernst Stick or metallic coils made from chrome-nickel alloys or tungsten [141].

The core of the FTIR instrument is the interferometer. There is a number of various interferometer designs used by FTIR manufacturers. The Michealson Interferometer is commonly used to introduce the concept of interferometers and is displayed in Figure 25. The IR beam irradiated by the source is parallelized by a collimating mirror before the beam reaches the beam splitter. The beam splitter is a semi-transparent mirror which ideally divides the beam in two halves. The reflected half travels to the moving mirror while the passing light travels to the fixed mirror. Both mirrors reflect the beam back to the beam splitter, where again half passes while half is reflected. This results in one beam passing towards the sample while the second travels back to the source.

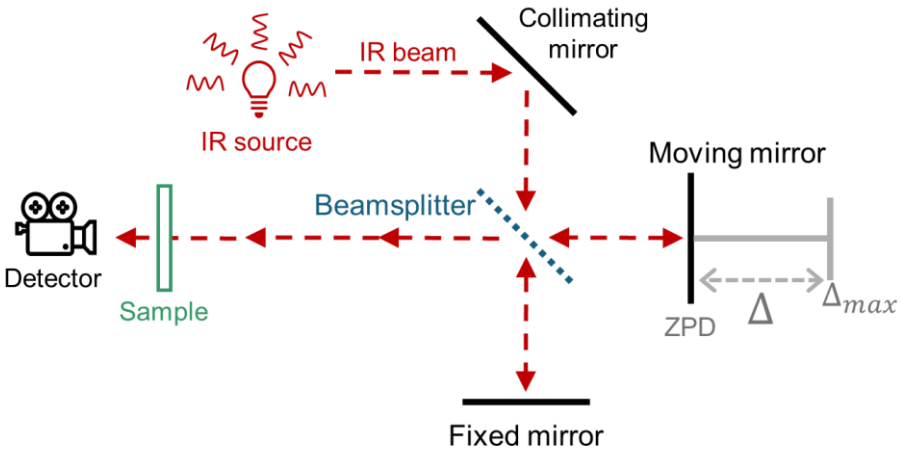

Figure 25: Schematic drawing of a Michelson interferometer. The collimated IR beam is split into two perpendicular paths using a beam splitter (ideally 50 % reflectance, 50 % transmission), directing one beam to a fixed mirror and the other to a mirror displaced by the mirror position Δ. The maximum mirror displacement is indicated as Δ_{max}. The beams reflect back to the beam splitter, where they recombine and interfere depending on the optical path difference $\delta = 2\,\Delta$. The position at which the optical path difference equals zero as the distance between the beam splitter to the fixed and to the moving mirror is the same, is referred to as zero path difference (ZPD). As the moving mirror changes its position, the interference pattern is modulated resulting in an interferogram (see Figure 26, p.41). Adapted from [138].

Depending on its displacement Δ, the moving mirror introduces an optical path difference δ (OPD), which is given by:

$$\delta = 2\Delta \tag{2.25}$$

If the moving mirror is placed at the same distance to the beam splitter as the fixed mirror, the optical path difference is zero ($\delta = 0$). Therefore, this position is usually referred to as zero path difference (ZPD). When the beams of the two interferometer arms recombine, their path-length difference produces an interference pattern, the so-called interferogram, which contains the full spectral information. The interferogram is a function of the optical path difference and has a very distinctive form, as displayed in Figure 26 (p. 41). It has a high peak of intensity at the ZPD, the so-called center burst, which is the result of the light of all wavelengths contained in the spectral range constructively interfering. The low intensity regions of an interferogram are referred to as its wings. These wings show reduced intensity because, as the optical path difference increases the various Fourier frequencies, they increasingly fall out of phase with one another, leading to destructive interference [138]. For a single, specific wavelength $\tilde{\nu}_0$, the modulated intensity can be written as [142]:

$$I_{\tilde{\nu}_0}(\delta) = 0.5\, I_{0,\tilde{\nu}_0} \cos(2\pi\tilde{\nu}_0\delta) \tag{2.26}$$

$I_{0,\tilde{\nu}_0}$ is the intenstiy of the source for the wavenumber $\tilde{\nu}_0$. In commercial rapid scan spectrometers, the movable mirror is varied at a constant velocity *V'* in [cm s^{-1}] [142]. Consequently, the retardation which is reached *t* seconds after the ZPD is given by:

$$\delta = 2V' \cdot t \tag{2.27}$$

A higher mirror velocity increases the rate of change of the optical path difference, causing each wavenumber component to oscillate faster in the interferogram. For a single wavenumber, the intensity can thus be expressed as a function of time:

$$I_{\tilde{\nu}_0}(t) = 0.5\, I_{0,\tilde{\nu}_0} \cos(2\pi\tilde{\nu} \cdot 2V't\,) = 0.5\, I_{0,\tilde{\nu}_0}\, \cos(2\pi f_{\tilde{\nu}} t\,) \tag{2.28}$$

with the modulation frequency $f_{\tilde{\nu}}$, which is directly proportional to the mirror speed:

$$f_{\tilde{\nu}} = 2V' \cdot \tilde{\nu} \tag{2.29}$$

Most FTIR spectrometers have the option to vary the mirror velocity, also referred to as scan speed or scanning velocity. For a constant physical mirror speed, the modulation frequency is wavelength dependent as stated by equation (2.29). Therefore, the scan speed is conventionally given as frequency in reference to the HeNe laser, which is integrated in most interferometers to precisely determine the mirror position of the movable mirror. The wavelength of the HeNe laser is 632.8 nm, which corresponds to $\tilde{\nu}$ = 15 800 cm^{-1}. Consequently, a physical scan speed of V' = 0.16 cm s^{-1} generates a HeNe frequency of 5 kHz, which is a typical scan speed for the deuterated triglycine sulfate (DTGS) pyroelectric detector. The mercury-cadmium telluride (MCT) detector requires faster optical velocities of ≥ 10 kHz for a sufficient sensitivity [142].

The DTGS and the MCT are the most common FTIR detectors. The DTGS is a pyroelectric detector, meaning it relies on the electrical signal induced in the pyroelectric crystal by increasing temperature. It is widely used in FTIR due to its broad spectral range, its low cost and because it can be operated at room temperature. The MCT detector is photoelectric detector, in which the incident infrared light changes the electrical conductivity of the semiconductor element. It requires cooling to reduce thermal noise, i.e. with liquid nitrogen (LN2). The MCT detector provides up to 10 times higher sensitivity in comparison to the DTGS detector [142]. However, the higher sensitivity comes at the cost of spectral range. A typical DTGS detector covers the whole mid-IR range while MCT detectors have a cut-off at 800 – 500 cm^{-1}, depending on their bandwidth [142]. The detector records the intensity as a function of the OPD. This results in the interferogram, which is displayed in Figure 26. To calculate the spectrum, half of the interferogram is Fourier transformed to obtain the single channel spectrum. As a magnitude Fourier transform is applied, the x-axis becomes inverted. Thus, the optical path difference in [cm] is converted to the wavenumber in [cm^{-1}], as shown in Figure 26.

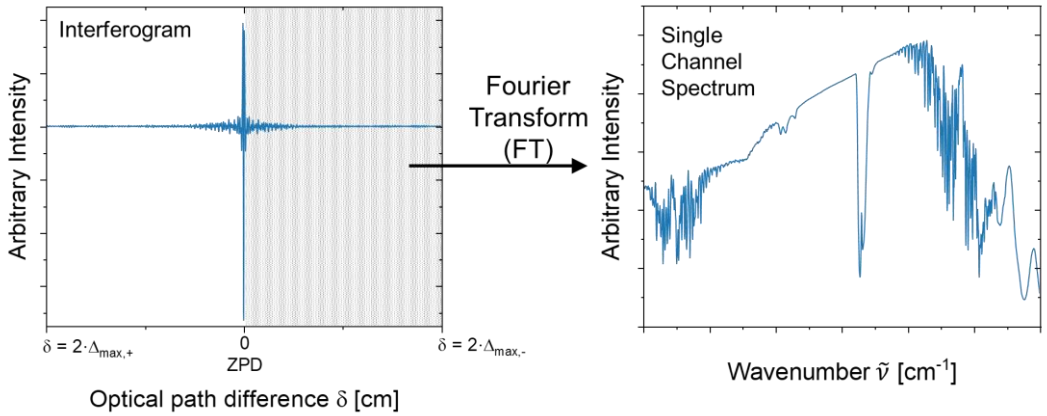

Figure 26: The interferogram is a plot of arbitrary infrared intensity obtained at the detector versus the OPD δ. The mirror moves from the maximum displacement through the ZPD back to the maximum displacement. In the interferometer drawn in Figure 25, this would correspond to a forward-backward motion which is indicated in the interferogram with the indices + (forward) and – (backward). The recorded intensity is maximum at the ZPD, which is the so-called center burst. The low intensity regions of an interferogram are referred to as its wings. Magnitude Fourier-transform (FT) of half of the interferogram (gray background) results in a single channel spectrum (SC), which is an arbitrary infrared intensity plotted against the wavenumber. As the FT is applied, the x-axis is inverted (cm → cm^{-1}).

In two beam FTIR instruments, the IR beam is split after the interferometer, with one beam traveling directly to the detector while the second passes the sample. Thus, the absorbance is calculated by equation (2.19) (p. 36) with the initial intensity I_0 of the undisturbed beam and I the intensity of the beam which passed the sample. However, most commercial FTIR instruments are single channel FTIR, meaning they only have one beam. Consequently, to obtain the final spectrum, two single channel spectra are required: one background single channel spectrum (BGSC) without any sample, corresponding to I_0, and a sample single channel spectrum (SSC) with the sample, corresponding to I. The absorbance spectrum is then calculated from the BGSC and the SSC following equation (2.19) (p. 36) as displayed in Figure 27.

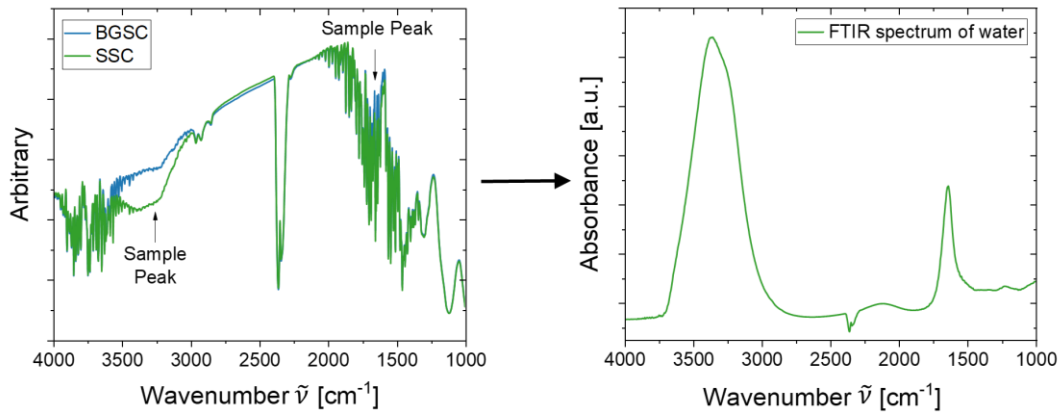

Figure 27: To obtain one FTIR spectrum, two single channel spectra are needed: a background single channel spectrum (BGSC) and a sample single channel spectrum (SSC). Using equation (2.19) (p. 36), the final absorbance spectrum is calculated as the ratio of BGSC and SSC.

2.5.2 Attenuated Total Reflectance (ATR)

FTIR can be carried out using various sampling techniques. An important alternative to the standard transmission measurements is attenuated total reflectance (ATR) spectroscopy: In ATR FTIR, infrared light is directed through an internal reflection element (IRE), usually a high refractive-index ATR crystal. A distinction is made between external reflection, where IR light is reflected from the sample surface as for example in diffuse reflectance infrared Fourier transform spectroscopy (DRIFTS) and internal reflection, which refers to the reflection of the IR beam inside the IRE.

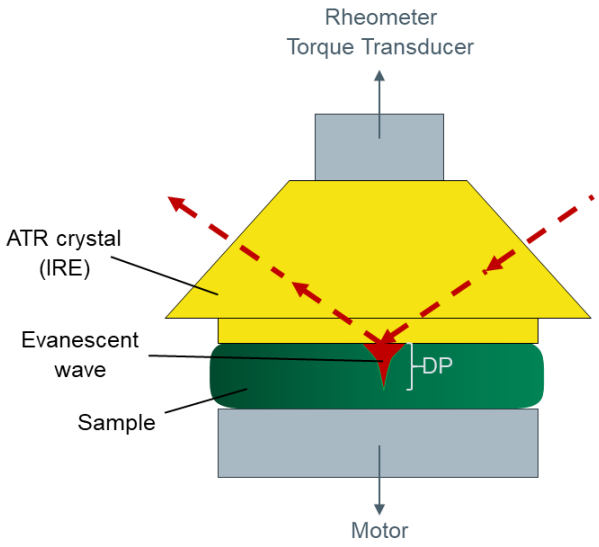

Figure 28: Schematic representation of ATR FTIR on the example of the Rheo-FTIR (see chapter 5, p. 87), including the IR beam and the evanescent wave. For improved clarity, the schematic is intentionally not drawn on scale. The evanescent wave probes the sample at the wavelength-dependent depth of penetration DP. *Adapted from [20]*

At the interface between the IRE and the sample, the totally reflected IR beam generates an evanescent wave that probes the sample within a short distance as illustrated in Figure 28. This penetration depth *DP*, which is in the µm – range, is wavelength-dependent:

$$DP = \frac{\lambda}{2\pi n_c \sqrt{sin^2\theta - \left(\frac{n_s}{n_c}\right)^2}} \tag{2.30}$$

with the refractive index of the sample n_s (typically $n_s \approx 1.3$ for polymers) and the refractive index of the ATR crystal n_c. Typical ATR crystal materials are Zinc selenide (ZnSe, $n_c = 2.43$), germanium (Ge, $n_c = 4.01$), silicon (Si, $n_c = 3.41$) or diamond ($n_c = 2.42$) [143]. In general, diamond is the most commonly used ATR crystal material due to its durability, chemical resistance and the highest penetration depth [143]. Typical values for the depth of penetration are given in Figure 29.

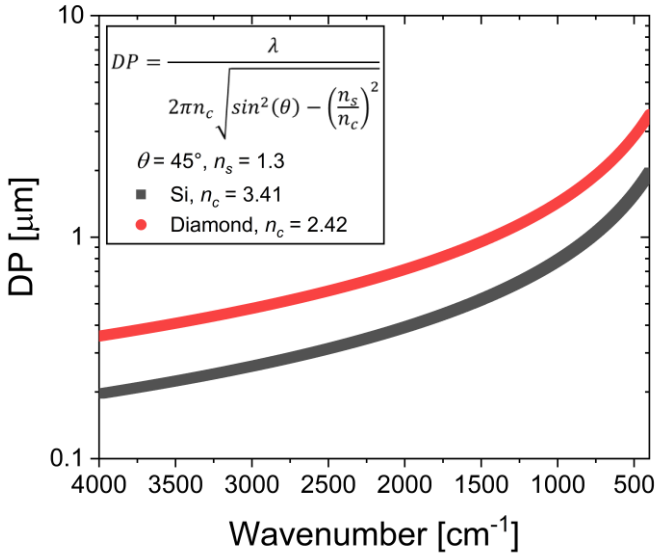

Figure 29: Depth of penetration DP calculated for the two ATR crystal materials diamond and silicon. For the calculation, an incident angle of θ = 45 ° was assumed. As sample refractive index, the value n_s = 1.3 was chosen which is typical for polymers. At 1 000 cm^{-1}, DP = 0.78 µm for Si and DP = 1.43 µm for diamond.

ATR FTIR comes with a few limitations in comparison to transmission spectroscopy. Since the evanescent wave penetrates only a few micrometers into the sample, ATR primarily probes near-surface regions whereas transmission techniques capture bulk properties. The rather shallow penetration depth of < 4 µm of ATR FTIR reduces the effective number of absorbing bonds and thus the overall sensitivity. In addition, intrinsic phonon absorptions of the ATR crystal can reduce the transmitted intensity in certain spectral regions [141]. Nevertheless, ATR is one of the most common sampling techniques as it offers significantly simpler handling than transmission spectroscopy. While transmission techniques often rely on thin films or pressed KBr pellets, samples in ATR can be examined by directly placing them onto the crystal surface. ATR also facilitates practical use and enables convenient *in-situ* FTIR measurements with fiber-coupled ATR probes. In addition, the sensitivity of ATR can be increased by introducing multiple reflections [141].

3 Development of a Procedure for the Rheological Characterization of Cement Pastes

While the adjustment of flowability of cementitious materials has always been of importance, the use of rotational rheometers is a comparatively young research field in cement and concrete science [81]. Traditionally, the most prominent methods to characterize the flowability of cementitious materials have been, and still are, spread flow and slump flow tests (see chapter 2.3.2, p. 23). However, following the fundamental works of researchers like Roussel, Feys and Wallevik as well as the introduction of rheometers to standards, as e.g. in ASTM C1874-20, rotational rheometery has increasingly been applied to investigate viscosity, yield stress and other complex rheological properties such as the thixotropy of cementitious materials [81]. Nevertheless, due to the complex material behavior of cement paste, the rheological characterization remains challenging. Consequently, the question on how to properly conduct reliable rheological measurements has been a recurring research question over the past decades [89, 103, 144]. For this reason, in this chapter, a rheological procedure is developed to ensure reproducible and reliable results in the determination of the yield stress of cement pastes. For this purpose, different geometries were first tested and are discussed. Second, the measurement parameters for the chosen geometry were optimized to enhance the reproducibility of the measurements. Finally, the validity of the developed procedure is confirmed via comparison of the obtained data to spread flow measurements.

3.1 Choice of a Suitable Geometry

In general, a large variety of different geometry shapes, sizes and functionalities are available for rheological characterizations [76, 77]. Therefore, when a rheological protocol is to be developed, the first choice that has to be made is the selection of a proper geometry. In this work, five geometries are compared on their suitability for cement paste characterization: a 25 mm Plate-Plate (PP) geometry with smooth surfaces, a 25 mm PP geometry with sandpaper glued to the surface, a 50 mm PP geometry also with sandpaper, a helix-cup and a vane-cup geometry, as shown in Figure 30 (p. 46). Cone-Plate geometries were excluded, since the gap is too small in comparison to the particle size. The chosen geometries were based on the selection of geometries in the interlaboratory study carried out within the framework of the Priority Programm SPP2005 ‘Opus Fluidum Futurum – Rheology of reactive, multiphase construction materials’ (abb.: SPP2005) [101, 145]. While this study already provides some insight on the effect of different geometries, the use of a variety of different rheometers complicates the absolute comparison of the obtained yield stress values. Moreover, the choice to compare flow curves at the same rotational speeds instead of the same shear rates makes the results depend heavily on the gap sizes. Therefore, the protocol probes different ranges of deformation depending on the used

geometry, making a comparison almost impossible. Consequently, a definite optimum choice of geometry cannot be concluded from the interlaboratory study conducted within SPP2005.

For this reason, in this thesis, a comparison of geometries was conducted similarly as proposed in [101] with the difference that all flow curves were obtained with the same rheometer, the ARES G2, and the sample was characterized at the same shear rates instead of the same rotational speeds. The applied rotational spreads are converted to shear rates by the rheometer software based on the geometric dimensions of the measurement systems. These conversions are standard and therefore were not further investigated. An overview on these conversions is given elsewhere [76].

Figure 30: Pictures of different upper geometries tested for the characterization of cementitious materials. From left to right: 25 mm Plate-Plate geometry with smooth surface, 25 mm PP geometry with sandpaper, 50 mm PP with sandpaper, a helix with smooth surface and a four-blade vane with a smooth surface. In the PP configurations the lower geometry matches the upper one. The helix and vane are paired with a Couette (cup) geometry as their counterpart.

The compared geometries are displayed in Figure 30 and can be categorized in two groups: Plate-Plate (PP) measurement systems (MS), in which both the upper and the lower geometry are flat plates, and cup systems, in which different upper geometries are combined with a cup in the lower geometry. The definition of a cup measurement system is specific to this thesis. The rheology handbook of Mezger classifies the helix and the vane as “spindle” measurement systems [76]. PP geometries are widely used in many fields of rheology, e.g. in the characterization of hydrogels or polymer melts [76, 113]. These systems have different advantages, such as that only a comparatively small sample amount is needed if the standard gap height of 1 mm is applied, that they ensure steady laminar flow and that the shear rate and strain can be altered by changing the gap height [89]. Three different PP were compared in this study: A 25 mm PP with smooth surfaces was chosen as reference to previous works conducted in this working group by N. W. Radebe and T. Meyer [21, 146]. Several studies in literature suggest that smooth geometry surfaces lead to pronounced slippage effects, most probably by formation of a water layer between the cement paste and the geometry [110, 147]. Therefore, the other two chosen PP of the diameters 25 mm and 50 mm were treated by attaching water-resistant sandpaper (abbreviated SP, 600 grit) with cyanoacrylate glue to stainless steel disposable plates. The standard aluminum disposable plates were not used due to the significant corrosion by the strongly basic cement pastes. The two cup systems are a helix-cup combination designed for complex fluids

and a vane geometry similar to versions tested in the reference study [101]. The vane can also be described as a reduced concentric cylinder. As cement is confined within the rotor blades in rotational tests, the geometry basically acts as a cement bob in cement paste. Therefore, it is assumed that slippage between the geometry and cement paste is reduced in comparison to other geometries. Moreover, both the helix and the vane have a lower surface-to-volume (S/V)-ratio than PP MS and are thus more stable against surface drying effects.

To test the suitability of the different geometries, the preparation of cement pastes of w/c = 0.4 as well as the rheological procedure were adapted from [101]. After placing the paste in the respective geometry, a series of descending shear rate steps in the range of $\dot{\gamma}$ = 100 – 0.1 s^{-1} was applied, as illustrated in Figure 31. Starting at 100 s^{-1}, every shear rate step was applied for 20 s, which was sufficient to reach a steady-state. For time-independent materials, the shear rate steps can be applied as long as necessary to reach steady-state. However, as the rheological behavior of cement paste strongly depends on the state of the ongoing hydration reaction, experiments to determine the dynamic yield stress need to be sufficiently short, typically less than five to ten minutes, to ensure that the chemical changes are negligibly slow in comparison to the duration of the experiment. Therefore, the step time has to be a compromise between a sufficiently long-time span to reach steady-state and a sufficiently short time span to minimize chemical changes. In the experiments in this work, this compromise was a step time of 20 s.

Prior to the comparison of the different geometries, the data evaluation of the typical stress-time curves to obtain the yield stress is discussed in the following. The data evaluation was conducted accordingly for all further yield stress measurements reported in this work.

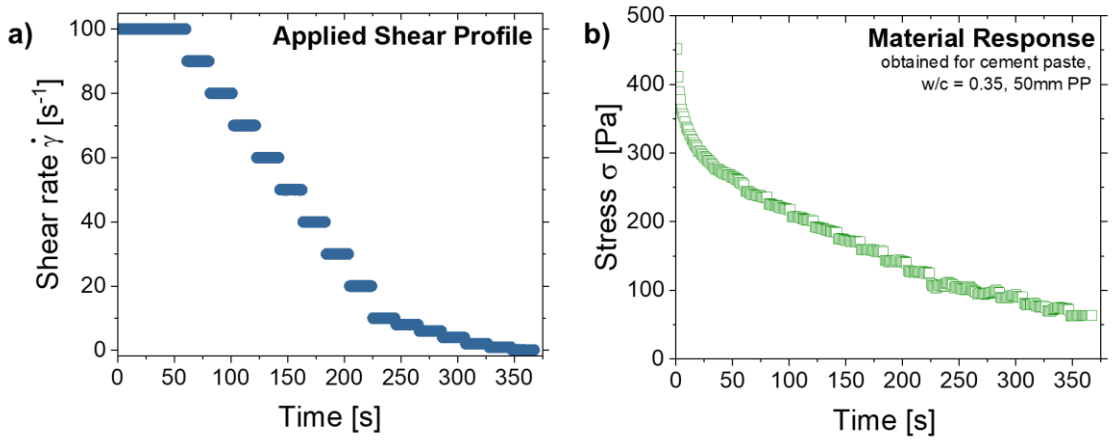

Figure 31: a) Applied shear rate profile to obtain flow curve of cement pastes. A series of descending shear rates in the range of $\dot{\gamma}$ = 100 – 0.1 s^{-1} is applied. The pre-shear at 100 s^{-1} is applied for 60 s, while all other shear rate steps are applied for 20 s. In this graph, the final shear profile after optimization is shown (see chapter 3.2, p.51), which was used for all experiments in the following chapters. As the geometry selection discussed in the present chapter was conducted prior to procedure optimization, the pre-shear at 100 s^{-1} was only applied for 20 s in the experiments reported in this chapter 3.1. b) Typical set of raw data stress-time curve for cement pastes of w/c = 0.35 obtained with the shear rate profile displayed in a). The material reaches a steady state when the stress response is time-independent.

To obtain the final flow curve, the stress obtained for the individual shear rate steps is averaged over the steady-state region. For most samples, steady state was obtained immediately at applying the shear rate (see Figure 31 b)). Therefore, the stress was averaged over the whole step time of 20 s and plotted against the respective shear rate to obtain the flow curve, as shown in Figure 32. To obtain the apparent yield stress, a linear Bingham (BG) regression (equation (2.9), p. 22) is made between 90 s^{-1} and 20 s^{-1}. The yield stress is obtained as the y-intersection.

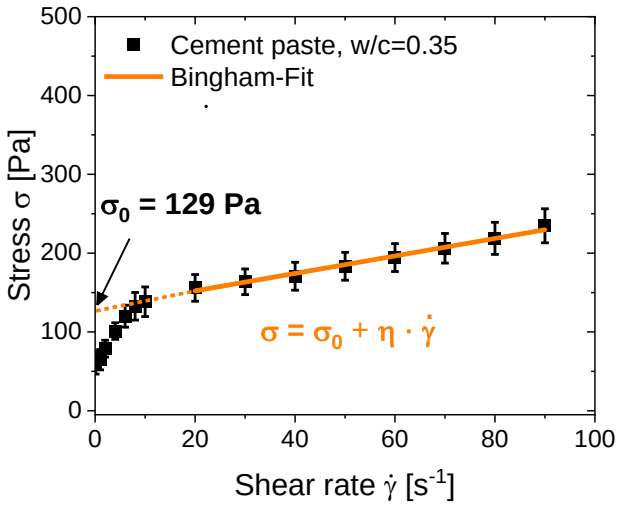

Figure 32: Exemplary flow curve for cement paste of w/c = 0.35. This flow curve was obtained for the optimized procedure (see chapter 3.2, p. 51), but is representative for all flow curves discussed in this work. A Bingham regression is applied to the shear rate range of 90 s^{-1} to 20 s^{-1}. The yield stress is obtained as the intersection of the Bingham-Fit with the y-axis.

For the comparison of the different geometries, a spread-flow test was performed as a reference using a Vicat cone (r_1 = 35 mm, r_2 = 40 mm, h = 40 mm, V = 177 mL) on a dry glass plate surface, staying close to DIN EN 1015-3 [100]. The resulting spread-flow diameter was converted to a yield stress $\sigma_{0,SF}$ value by using the following relation [107, 108]:

$$\sigma_{0,SF} = \frac{225 \cdot \rho \cdot g \cdot V^2}{128 \cdot \pi^2 \cdot R^5} \tag{3.1}$$

With the paste density $\rho \approx 2$ kg m^{-3}, the gravitational constant g = 9.81 m s^{-2}, the cone volume V = 177 mL, and the spread flow radius R. The obtained reference yield stress of $\sigma_{0,SF}$ = 42 Pa is in agreement with the reference study [101]. A tolerance of ± 10 Pa, equivalent to a 25 % deviation, is defined as the range within which an obtained yield stress is considered as to meet the expected value.

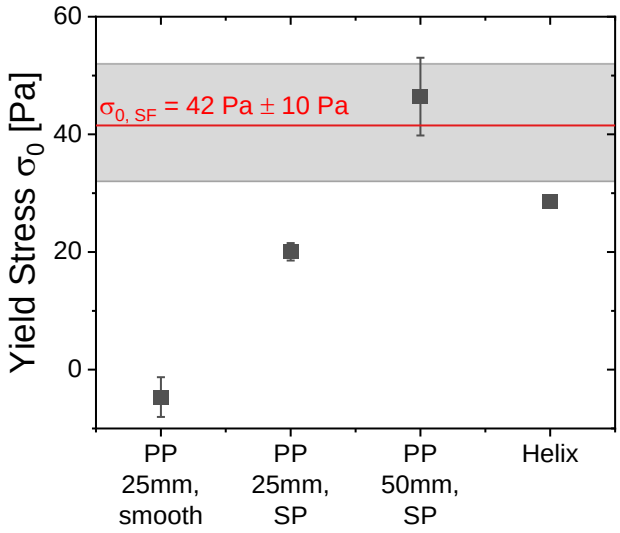

Figure 33: Comparison between yield stress σ_0 obtained with different geometries for cement paste of w/c = 0.4, referenced to the yield stress obtained by spread-flow tests $\sigma_{0,SF}$. The reference $\sigma_{0,SF}$ was calculated from the spread diameter using equation (3.1). The stress response of cement pastes is in the non-linear regime during steady shear, consequently differences emerge in the yield stress for different PP diameters. For deformations in the linear regime, the stress response would be independent of the PP diameter.

Figure 33 displays the yield stress σ_0 which was obtained with the different geometries. The reference $\sigma_{0,SF}$ calculated from the spread flow values is incorporated as a horizontal line. With the smooth PP geometry, no yield stress could be measured for the cement paste, which is not in agreement with the observed material behavior. This yield stress value of $\sigma_0 \approx 0$ Pa is most likely caused by the formation of a thin water layer at the surface of the cement paste, which potentially results in wall slip [21, 144]. In suspensions, there is a natural depletion of particle concentration close to the geometry-sample interface, since the suspended particles cannot be centered at a distance shorter than their characteristic length. Consequently, the mean concentration of particles is decreasing with decreasing distance to the sample-geometry interface, which leads to the formation of a thin water layer at the surface of the paste [92, 144]. Therefore, smooth geometries in general, and in this study specifically the smooth PP geometry, are not suitable to characterize cement pastes. For the 25 mm PP with sandpaper, the Bingham regression results in a yield stress, which is approximately 50 % smaller than $\sigma_{0,SF}$, while the 50 mm PP with sandpaper provides a reasonable σ_0 close to the reference value. For deformations in the linear regime, the stress response would be expected to be independent of the PP diameter. However, the stress response of cement pastes is in the non-linear regime during steady shear, consequently differences emerge in the yield stress for different PP diameters. It is assumed that the bigger diameter of the 50 mm PP increases the sheared volume and thus represents the bulk yield stress more properly. The helix provides a σ_0 value, which underestimates the spread-flow reference by about 32 %. Moreover, the shear rate is not well defined with the helix geometry since no narrow gap exists. Therefore, homogeneous shear conditions throughout the entire sample are not given. For this reason, geometries such as the helix or other spindle type geometries are producing more incalculable edge effects, and therefore, more turbulent flow conditions showing vortices, than laminar flow conditions [76]. The PP opposes a defined, laminar shear

field on the sample. For this reason, and more importantly the determination of a yield stress close to the reference value, the 50 mm PP geometry with SP was identified as the most suitable geometry for yield stress measurements of cement pastes in this study.

The vane geometry is one of the most widely used geometries in the characterization of cement pastes [103, 148]. Its suitability was tested in a later, separate study conducted within the master thesis of Klaus Beier [149]. In this study, the geometry comparison was conducted using a cement paste of w/c = 0.35 containing 0.03 wt.% of the commercial PCE superplasticizer BASF VP14.1 added via delayed addition [149] (for characterization of BASF VP14.1 see chapter 'Materials' in SI, p. 151). The rheological procedure was the same as for the other measurements described in this chapter. The yield stress obtained with the vane geometry is compared to the reference 50 mm PP (SP) in Table 2.

Table 2: Comparison of the results for the yield stress σ_0 of cement paste containing 0.03 wt.% BASF 14.1 obtained with the vane and the 50 mm PP (SP) geometry, reproduced from [149].

	Vane	**50 mm PP (SP)**
Yield stress σ_0	36.0 ± 1.8 Pa	97.8 ± 15.4 Pa

The determination of the yield stress using the vane geometry results in a value that is about a factor three reduced relative to the value obtained with the PP geometry. In combination with the observed deposition of sample at the cup walls after the measurement (see Figure 34), it is presumed that shear band formation occurs. Under simple shear conditions some complex fluids can separate into bands of a different viscosities, the so called shear bands [150]. For cement paste in a concentric cylinder, the formation of shear bands has been observed via x-ray tomography [151]. For cement paste of w/c = 0.41 (φ = 0.44) at the shear rate of 0.01 s^{-1}, the shear was concentrated in a single, small band of a few µm in close vicinity to the inner cylinder [151]. In this region, the particle content is visibly reduced [151]. Due to the underestimation of the yield stress as well as the high probability of shear band formation, the PP geometry was preferred over the vane.

Figure 34: Cement sample after a flow curve was recorded. The grey cross indicates the position of the vane during measurement. The material sticking to the side and the hole at the vane position indicates shear band formation and plug flow. Reproduced from [149].

In summary, there is no single geometry which is suitable for all types of cement pastes and rheological experiments [76, 89]. In the rotational experiments conducted here, shear band formation led to an underestimation of the yield stress for the vane and the helix geometry. This type of flow instability is expected to be reduced in oscillatory shear, particularly in SAOS experiments. Since these cup systems are less prone to drying, the helix and the vane are well suited for long-term, oscillatory measurements like investigations on the structural build-up. For yield stress measurements however, the 50 mm PP with sandpaper resulted in a yield stress value of 46 ±7 Pa, matching the reference spread-flow result of 42 Pa the closest while maintaining laminar flow conditions. Therefore, this geometry was used in all further experiments in this work. However, since it is known to be prone to drying, especially in the region of high shear rates at the outer rim [89], all experiments were designed with a duration of maximum five minutes. It should be noted, that in PP geometries flow instabilities and shear band formation can occur as well [76, 103].

3.2 Optimization of the Measurement Procedure

While the yield stress values obtained for the 50 mm PP with sandpaper were close to the reference $\sigma_{0,\,SF}$, the yield stress results lacked reproducibility. This is represented by the comparatively large standard deviation in Figure 33 (p. 49). To improve the reproducibility of the flow measurements, a procedure for the sample preparation was developed based on [101]. For this purpose, cement paste of w/c = 0.35 was prepared and a number of different measurement parameters were systematically varied. For each set of parameters, three flow curves with freshly prepared samples were recorded and the flow curve shape was compared. The resulting optimized procedure is shown in Table 3. With this procedure, both the stress-shear rate curve as well as the resulting yield stress could be measured reproducibly at separate measurement days, as shown Figure 35. Before the optimization, the shape of the stress-shear rate curve changed in between measurement runs, indicating poor reproducibility. After optimization, the curve shape curve was observed to be similar in all measurements over several measurement days, indicating a good reproducibility.

Table 3: Optimized Procedure for the preparation of cement paste for rheological characterization.

0:00 - 0:15 min	**Addition of water to cement powder at 200 rpm**
0:15 - 0:30 min	**Continue at 200rpm**
0:30 – 1:00 min	**Pause**
1:00 – 3:00 min	**Mixing at 550rpm**
3:00 - 12:00 min	**Pause**
12:30 – 13:30 min	**Homogenization at 550rpm**
13:30 - 15:00 min	**Sample Loading**
15:00 min	**Start of measurement**

The following parameters were considered and varied in the optimization procedure:

Slippage of Sample: As already described in the previous subchapter, roughened geometry surfaces should be used for cement pastes to reduce slippage. Therefore, sandpaper (for wet-sanding) was attached to the PP surface with a cyanoacrylate glue (superglue) to introduce surface roughness. In the process of procedure optimization, two different sandpapers were tested, one with 600 grit and one with 120 grit. No significant influence on the measured stress or the reproducibility could be observed for the two tested sandpaper grits. For all experiments in this work, the 600 grit SP was used.

Sample Age: Literature reports that the yield stress evolves rapidly in the first minutes after the initial water-to-cement contact, and that this evolution slows down after 10 - 15 min [103]. This can be explained by the cement reaction (see chapter 2.2.2, p.15). In the first minutes after water-to-cement contact, the cement particles start to dissolve. Dissolution heat is released and the first hydrates start to nucleate [8, 152]. This initial dissolution is governed by many different factors, e.g. temperature and the available surface. These factors can vary in between measurements, which leads to variations in the early stage yield stresses during reaction times shorter than 10 min. Approximately 10 to 15 min after initial water-to-cement-contact, an equilibrium is reached which creates more stable conditions, thus increasing the reproducibility. In this study, the used sample ages was changed from 3 min as used in the previous studies [21, 146] to 15 min to increase the reproducibility of the yield stress.

Pre-shear: To achieve high reproducibility in measurements of concentrated suspensions, the state of the sample before the measurement has to be reproducible. Varying numbers and sizes of particle agglomerations change the rheological behavior in the measurement. Therefore, the sample has to be treated to destroy agglomerates prior to the measurement. This is usually achieved by a pre-shear prior to the rheometer. In previous studies conducted in this working group, the sample was mixed by hand with a spatula [21, 146]. However, the force applied to the sample during hand-mixing is not sufficient to destroy agglomerates. In this study, we found that the use of an IKA stirrer with 550 rpm for 2 min to be sufficient, especially for rather liquid pastes containing dispersing agents. An IKA stirrer is a mechanical overhead stirrer commonly used in laboratories for mixing high-viscosity materials and is shown in Figure 83 (SI, p 155). The use of an IKA stirrer and an applied mixing rate of 550 rpm for 2 min is in agreement with other cement paste preparations in literature [151, 153]. In addition, a pre-shear in the rheometer was used to homogenize the sample and to erase the shear history imposed through sample loading. Initially, the highest shear rate was applied for 20 s. The raw data showed that no steady state could be reached, as shown in Figure 86 (SI, p.164). Consequently, the pre-shear at 100 s^{-1} was prolonged to 60 s, which was sufficient to reach a steady state for the samples investigated.

Temperature: A key to reproducibility is to control the temperature. To keep the cement kinetics similar in separate experiments, the temperature has to be constant. Two temperatures have to be considered here. The room temperature has to be set to a constant value. In this study, it was adjusted to 22 ± 1 °C. The second important temperature is the temperature which the paste experiences. This can be adjusted by controlling the temperature of the mixing water. Although this factor is often either not specified or overlooked in rheological studies, maintaining precise temperature control is critical. Elevated temperatures ($T \geq 30$ °C) produce a markedly more stiff material that is challenging to characterize reliably [154]. Lower water temperatures ($T < 15$ °C)

slow down the reaction and lead to a lower viscosity macroscopically [154], and enhances the reproducibility of the rheological measurements. Accordingly, to prevent excessive stiffening and to moderate the hydration rate while improving measurement reproducibility, a mixing water temperature of T = 10 ± 1 °C was employed. This temperature deviates from the room temperature conditions (T = 22 – 25 °C) applied in the previous studies conducted in this working group [21, 146]. To ensure that the temperature evolution is similar for separate sample preparations, the temperature of the paste was taken prior to sample loading and the sample was discarded if the temperature was outside of a range of T = 22 ± 1 °C. Ideally, the humidity in the laboratory should be controlled to a constant value in addition to the room temperature control if the necessary infrastructure is available.

Sample Size: Sample batch size also has an influence on the reproducibility of measurements. It was observed that a larger batch size improved the reproducibility of measurements drastically. A larger sample size lowers the S/V-ratio of the sample and therefore makes the sample temperature more dependent on the mixing water than room temperature fluctuations or slight temperature increases due to holding the container. As the aim was to study self-synthesized superplasticizers which are only available in small quantities, a compromise between an adequately large sample size for temperature stability and small sample size for minimal superplasticizer demand had to be found. Therefore, in most presented experiments, a sample batch size of 100 g dry cement was used in contrast used to the 10 – 20 g used in the previous studies [21, 146].

Other factors influencing the early hydration reaction kinetics: In this study, only cement of the type CEMI 42.5R was used. Therefore, other factors influencing the cement reactivity such as the particle size distribution were not considered.

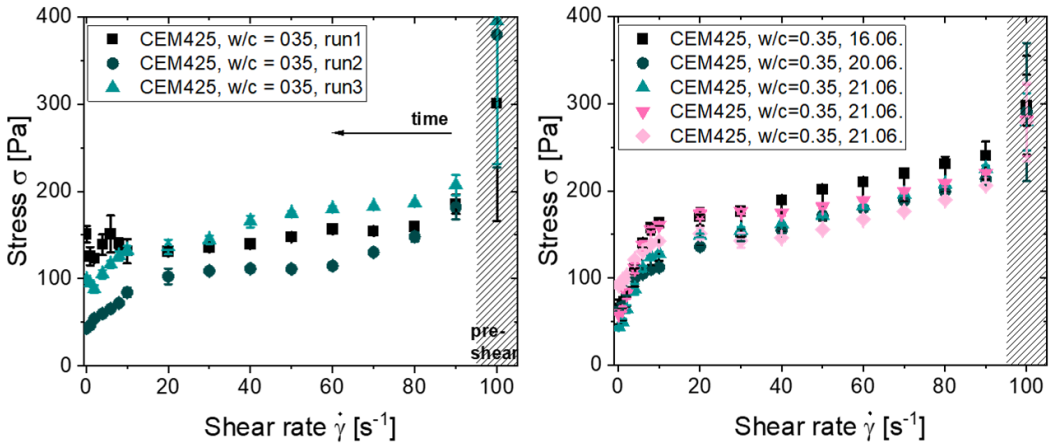

Figure 35: Both figures display flow curves obtained for cement paste of w/c = 0.35. The pre-shear at 100 s^{-1} was applied for 60 s; all other shear rate steps were applied for 20 s. The stress measured at each shear rate step was averaged over the complete duration. The stress value corresponds to the averaged stress measured at each shear rate step, the error bar corresponds to the respective standard deviation during one run. Left: flow curve data obtained in three subsequent runs on the same measurement day. The stress curves and therefore the obtainable yield stress are not reproducible. Right: Flow curve data obtained on separate runs on three different measurement days. Both the stress-shear rate relation and the obtained yield stress are reproducible.

3.3 Validation of the Optimized Measurement Procedure

The procedure developed in chapter 3.2 was initially validated only by assessing the reproducibility of the recorded flow curves. Although reproducibility is a fundamental requirement when establishing a measurement procedure, it should not serve as the only validation criterion. For instance, the vane geometry underestimated the yield stress value (see Table 2, p. 50) highly reproducibly with a standard deviation σ of only σ = 1.77 Pa across three measurements. This example shows that shear band formation and other shear flow instabilities can also produce highly reproducible results, and therefore reproducibility alone does not guarantee physical correctness. Consequently, three additional criteria were used to validate the data obtained using the optimized procedure.

First criterion: flow curve shape for blank cement paste. The obtained stress-strain curve should resemble other flow curves obtained for cement paste. At medium to high shear rates ($\dot{\gamma} \geq 20$ s^{-1}), the stress correlates linearly on the shear rate. At low shear rates $\dot{\gamma} < 20$ s^{-1}, shear-thinning behavior with decreasing shear-rates is observed. This deviation from the linear relation is usually understood as elastic behavior caused by particle-particle interactions [110]. Wall slip might also contribute to the observed behavior [103]. This shape of the flow curve has been observed in several studies on the flow behavior of cement [101, 110] and could be reproduced with the optimized procedure, as shown in Figure 36.

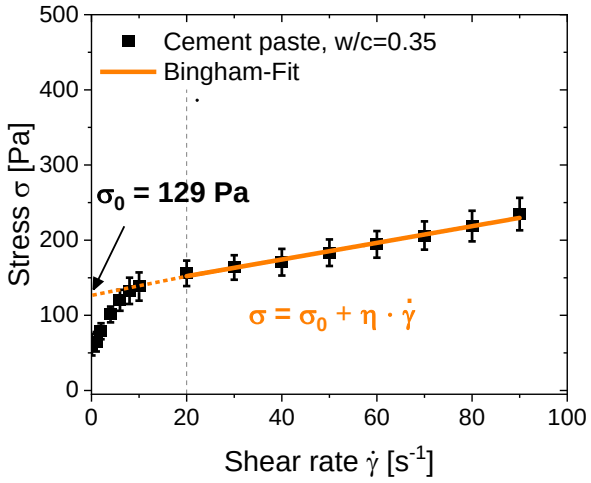

Figure 36: Exemplary flow curve data averaged for 10 measurements with a Bingham Regression. This data was obtained after full optimization of the measurement procedure for a cement paste of w/c = 0.35. The flow curve shows shear-thinning at low shear rates $\dot{\gamma} < 20$ s^{-1} as typical for cement pastes.

Second criterion: spread flow trends correspond to yield stress trends. The yield stress is extremely dependent on both the experimental procedure as well as the used data evaluation. Therefore, absolute values can be difficult to be reproduced or to be compared between studies [92]. However, relative yield stress trends obtained via rotational rheometry should qualitatively

reflect the trends observed by spread flow tests [107]. To correlate the obtained yield stress with spread flow tests, cement pastes with three different water-to-cement ratios were prepared. The chosen ratios were w/c = 0.35, w/c = 0.4 and w/c = 0.45. The yield stress values were determined via flow curves and the same samples were also characterized using spread flow tests. The results are displayed in Figure 37.

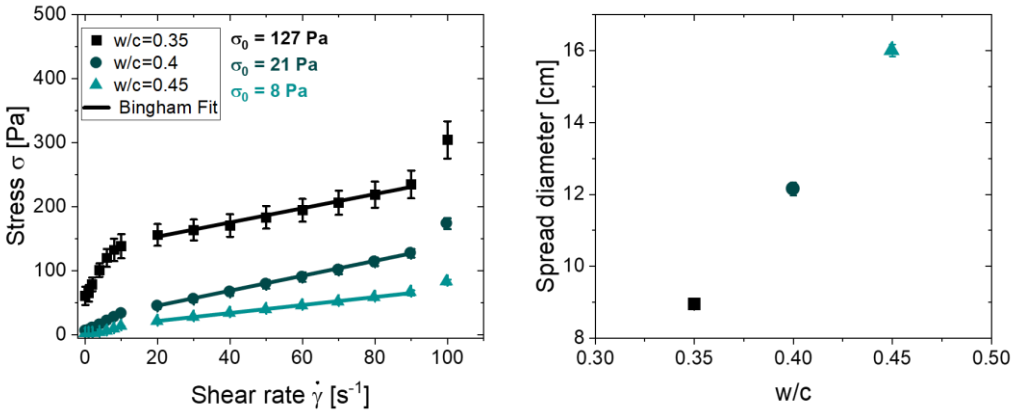

Figure 37: Left: Averaged flow curves of cement samples with w/c = 0.35, w/c = 0.4 and w/c = 0.45 averaged for three individually prepared sample per w/c-ratio. The Bingham-Fit was used for the yield stress evaluation. The obtained yield stress values are given in the graph. Right: Spread flow diameters for w/c = 0.35, w/c = 0.4 and w/c = 0.45 obtained for the same samples as used in rotational rheometry. The values are averaged for three individually prepared sample batches per w/c-ratio.

With increasing w/c-ratio and therefore increasing water content, the flowability of the paste is increased. This is confirmed both by the decreasing yield stress in the rotational rheometry experiments as well as the increasing diameter obtained by the spread flow experiments. According to the prominent works of Murata and Roussel [107, 108], the relation between the yield stress and the spread flow can be expressed as stated in equation (3.1) (p. 48). Therefore, to validate the obtained data, the yield stress was plotted against the spread flow values and a function of the form $y = A \cdot x^{-5}$ was added to the graph. As Figure 38 shows, the obtained data correlates well with the expected x^{-5} - dependency. This validates the obtained yield stress data and confirms the representability of the obtained trends.

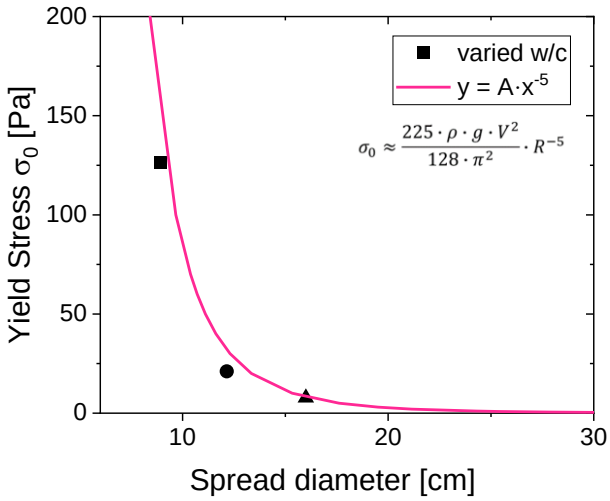

Figure 38: Correlation of obtained yield stress and spread flow for three samples of varied w/c-ratio. The pink line corresponds to A x^{-5}-correlation following equation (3.1) (p. 48).

Third criterion: Suitability for superplasticizer (SP) characterization. Superplasticizers (see chapter 2.4, p. 29) increase the flowability and thereby decrease the yield stress, depending on their molecular structure and the dosage [8]. In the rheological characterization of these effects, it can be challenging or impossible to measure the yield stress values with the same experimental procedure over the wide range of dosage-dependent flowability of the material [96, 130]. A suitable measurement procedure for superplasticizer should a) represent the macroscopically observed material behavior and b) work over the total range of superplasticizer dosage.

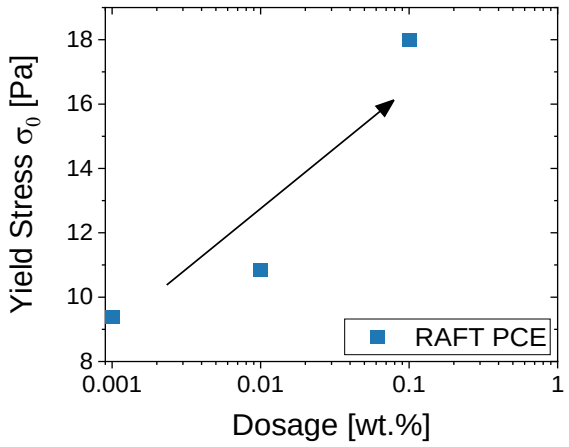

Figure 39: Example for a yield stress – PCE dosage curve that does not fulfill the third criterion as it does not reflect the material behavior, which was observed with increasing PCE dosage. This data was obtained with grooved concentric cylinders (picture given in the Appendix, p. 163) and therefore departs from the optimized procedure. The increasing PCE dosage increased the flowability of the cement paste and thus should have given decreasing yield stress values. The arrow is a guide to the eye which highlights that the inverse trend was observed. The PCE sample was synthesized via RAFT polymerization. The yield stress value at 0.001 wt.% corresponds to the yield stress of blank cement paste.

Figure 39 shows a yield stress – concentration curve which does not fulfill these requirements. This data was obtained with grooved concentric cylinders (picture given in the Appendix, p. 163) and therefore departs from the optimized procedure. It is observed that with an increasing superplasticizer dosage, the measured yield stress increases which is contradictory to the observed increase in flowability during sample preparation. This can be explained by the choice of the measurement system. The grooved concentric are prone to plug flow and shear band formation [151]. It is assumed that the stiff paste was pressed to the walls during the pre-shear and was too stiff to flow back towards the center of the cup. Consequently, the shear was concentrated in a small shear band of reduced solid content. With addition of the superplasticizer, the fluidity of the paste is increased. Consequently, the material is less stiff and the size of the sheared areas are increased. As larger parts of the sample are opposed to shear, the measured stress increases although the macroscopic material seems to flow more easily.

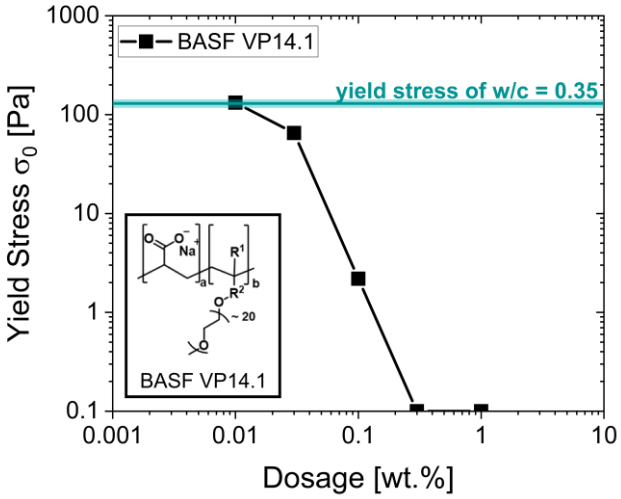

Figure 40: Yield stress in dependency of superplasticizer BASF VP14.1 dosage, which fulfills the third criterion. The data displays the typical S-curve shape [8]. At low concentrations, no yield stress reduction can be observed. When a critical concentration is reached (here ~ 0.02 wt.%), the yield stress depends directly on the superplasticizer dosage. Above the saturation dosage (here ~ 0.3 wt.%), the yield stress cannot be decreased further with adding more superplasticizer.

The flow curve data obtained with the optimized procedure involving the 50 mm PP (SP) is shown in Figure 40. The yield stress-concentration curve of BASF VP 14.1 displays the typical S-curve shape expected for PCE superplasticizers [8, 127]. At low concentrations, no yield stress reduction can be observed. When a critical concentration is reached (here ~ 0.02 wt.%), the yield stress depends directly on the superplasticizer dosage. Above the saturation dosage (here ~ 0.3 wt.%), the yield stress cannot be decreased further with adding more superplasticizer. Therefore, this data proves that the optimized procedure presented in chapter 3.2 (p. 51) fulfils the requirements of the third criterion as it a) represents the macroscopically observed material behavior and b) works over the total range of superplasticizer dosage.

3.4 Conclusions

In this chapter 3, a rheological procedure was developed to ensure the reproducibility and reliability of the results obtained via rotational rheometry. For this purpose, a geometry was selected. Subsequently, a procedure for the sample procedure was optimized. The obtained results were validated via comparison to values obtained via spread flow tests. Five different geometries were selected and compared a 25 mm Plate-Plate (PP) geometry with smooth surfaces, a 25 mm PP geometry with sandpaper glued to the surface, a 50 mm PP geometry also with sandpaper, a helix-cup and a vane-cup geometry. Among the five tested systems, the 50 mm plate-plate (PP) geometry with a 600-grit sandpaper glued to the surface delivered a yield stress value of σ_0 = 46 ±7 Pa, which was closest to the reference spread-flow reference of $\sigma_{0,SF} \approx 42$ Pa while maintaining laminar shear conditions. In the optimization of the preparation procedure in chapter 3.2 (p. 51), many parameters were considered. The final procedure was obtained by extending the sample age from 3 min to 15 min, using an IKA stirrer to homogenize the sample prior to the measurement instead of hand mixing, applying a pre-shear of 100 s^{-1} for 60 s instead of 20 s^{-1} and reducing the water temperature to 10 ± 1 °C from the initially used 22 – 25 °C. Moreover, the room temperature was set to a constant value of 22 ± 1 °C and the sample batch size was increased from 10 – 20 g to 100 g of dry cement per measurement. The validity of the yield stress results obtained with this optimized procedure was checked in 3.3 (p. 54). The optimized procedure was able to reproduce the characteristic cement-paste flow curve. Moreover, the inverse-fifth-power correlation between yield stress and spread-flow diameter [107, 108] could be confirmed for a series of different w/c-ratios. In addition, the expected S-curve with increasing superplasticizer dosage was successfully captured. In summary, it can be concluded that the optimized rheological protocol using a 50 mm plate-plate geometry with sandpaper provides reproducible, accurate yield-stress measurements for cement paste and is suitable for investigations on the influence of superplasticizers and their structure-property relationship on the yield stress of cement pastes.

4 PCMOxa – an Approach Toward a PCE Model System with an Alternative Sidechain

The use of polycarboxylate ether (PCE) as superplasticizers (SP) has increased significantly in recent decades to an annual production of 15 million tons [122], primarily due to their high dispersing efficiency [8, 9]. The working mechanism of PCEs relies on their comb copolymer architecture. The charged backbone (BB) allows the combs to adsorb to the surfaces of cement particles while the non-adsorbing sidechains (SC) create steric hindrance between cement particles, which macroscopically reduces the yield stress σ_0 and therefore enhances the macroscopic workability (see chapter 2.4, p. 29) [8]. In conventional PCEs, the backbone is made from a polycarboxylate, usually poly(acrylic acid) (PAA) or poly(methacrylic acid) (PMAA) where the carboxylic acid functions bear negative charges in the strongly basic environment of cement pastes with a pH of 12 - 14. Poly(ethylene oxide) (PEO) is conventionally used for the uncharged, non-adsorbing sidechains [8].

The functionality of these PCE structures can be tuned in many ways. Investigated modifications involve exchanging the ionic moieties in the backbone from CO_2^- to e.g. SO_3^-, PO_4^{3-} or silanol groups [155, 156], variation of the reactive group on PEO macromonomers to e.g. vinyl-terminated (VPEG) or isoprenyl-terminated PEO (IPEG) [56] or changing the topology from a comb to other polymer architectures such as stars [157]. However, even in conventional PCE structures simply made from a polyacid and PEO sidechains, the macroscopic properties can be tuned on the microscopic scale by adjusting the structural parameters namely the number of backbone monomers per repeating unit *N*, the SC degree of polymerization *P*, and number of repeating units *n* (compare Figure 42) [9, 10]. The BB degree of polymerization *B* corresponds to the product of $N \cdot n$. The aim to tailor macroscopic properties such as the yield stress and the retardation by adjusting the molecular structure has provided different theoretical and semi-empirical relations between *P*, *N* and *n* and their functionality, e.g. their adsorption properties [9, 10]. These structure property relations are derived from general solution theory and should be applicable to all comb polymers in solution independent of their chemical composition.

To date to the best of our knowledge, no systematic study has been reported on comb polymers that replace the PEO sidechains with an alternative water soluble polymer, nor on how such a substitution reshapes the structure-property relationships that governs cement paste rheology. The number of suitable polymers and monomers for this exchange is limited. The sidechains have to be water-soluble and uncharged, in order not to adsorb onto the cement grain surfaces. For this reason, poly(2-methyl-2-oxazoline) (PMOxa) was chosen in this work as it is highly water-soluble and uncharged under basic conditions [158]. Moreover, it can be synthesized via cationic ring opening polymerization (CROP) which provides high control over the molecular weight in combination with low dispersity ($Đ < 1.2$). Two different synthetic strategies towards the comb polymers with PMOxa-sidechains were investigated: a grafting-onto synthesis, pre-

sented in the subchapter 4.1, and a grafting-through strategy, presented in the subchapter 4.2. The grafting-through approach is also referred to as macromonomer route.

4.1 Structure-Property Relationship of PCMOxa investigated via Grafting-Onto Synthesis

The results presented in the following subchapter 4.1 are part of a publication [159]. In this subchapter, the influence of the sidechain chemistry on the structure-property relationship is investigated by (i) developing a grafting-onto synthetic strategy involving the living anionic polymerization of a poly(tert-butylmethacrylate) (PtBMA) backbone precursor combined with CROP of Moxa to obtain defined sidechains, thereby delivering a library of well-defined PCMOxa comb polymers with narrow dispersity ($Đ \leq 1.30$) and precisely controlled molecular parameters; (ii) validating the concept of PCMOxa superplasticizers and (iii) establishing structure-property relationships by investigating the influence of the structural parameters sidechain length *P*, grafting density represented by *N*, and backbone length *B* on the yield stress of OPC pastes.

4.1.1 Grafting-Onto Synthesis of PCMOxa combs

Synthesis of the PMAA Backbone

The synthesis of the PMAA backbone is a two-step process. In the first reaction step, a PtBMA BB-precursor is synthesized via living anionic polymerization following an established procedure [36, 160] as shown in Figure 1 A). The molecular weight and dispersity of the BB-precursor were characterized by SEC in THF (see SI, Figure 87, 165), since polyesters do not exhibit a pH-dependent hydrodynamic radius like polyacids and therefore the SEC provides more reliable results. Typically, the dispersity of PtBMA from anionic synthesis is $Đ < 1.1$ [36]. The backbone with $B = 100$ has a slightly higher dispersity with $Đ = 1.25$ due to the comparatively large batch size of 30 g tBMA. In the second reaction step, the PtBMA BB-precursor is hydrolyzed with TFA in DCM to receive the PMAA BB. The NMR spectrum confirmed quantitative hydrolysis (see SI, Figure 88, p. 165). An alternative hydrolysis strategy involving reflux in HCl in dioxane and subsequent neutralization with NaOH was also tested, following the synthetic procedure published in [161]. However, the obtained PMAA natrium salt could not be dissolved in the DMF necessary for the grafting-onto reaction step.

Synthesis of PMOxa SC and grafting to BB

The PMOxa SCs were synthesized via CROP of Methyl(2-oxazoline) (MOxa) in a procedure adapted from literature [54, 162]. The PMOxa SCs are polymerized in ACN at 80 °C resulting in a narrow dispersity $Đ < 1.1$ (compare Table 4). The living PMOxa cations are grafted onto the deprotonated PMAA backbone, as shown in Figure 1 a). The anionic carboxylate units can act as a nucleophile and attack the ring in the 2-position, terminating one SC by formation of an ester group [54]. The successful grafting of the PMOxa SCs to the PMAA BB is indicated by a shift of the main peak in SEC measurements (DMAc + 0.316 g L^{-1} LiBr) to smaller elution volumes, shown exemplary for one comb in Figure 41 B). Under the assumption that the refrac-

tive index increment dn/dc(PMOxa-comb) equals dn/dc(PMOxa-SC), the remaining SC peak is integrated to obtain the amount of remaining sidechains and calculate the actual grafting density. The area of the remaining SC peak is below 10 % for all samples, indicating a high grafting efficiency of the reaction.

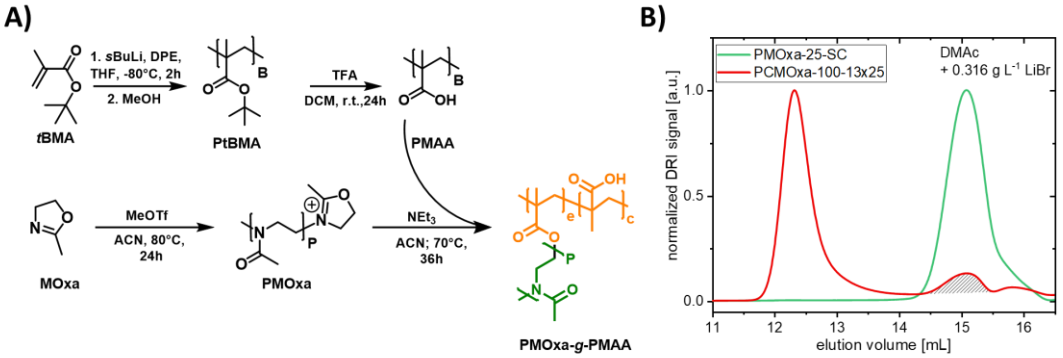

Figure 41: A) Synthesis Scheme of Comb Polymerization. The upper line describes the BB synthesis. The bottom line displays the SC synthesis as well as the grafting reaction. B) SEC curves of a PMOxa-25-SC (green) and the corresponding comb PMOxa-100-13x25 (red). The hatched area in the comb SEC corresponds to the integrated area of the unreacted sidechains.

Applying this synthesis strategy, a library of eight combs with a systematical variation of structural parameters was synthesized. This library is structured in three different series, as shown in Table 4 and Figure 43 . In series I), the grafting density is varied. The grafting density corresponds to the number *N* of BB monomers per SC, which is varied between *N* = 5.5, *N* = 7.7 and *N* = 11. Series II) is synthesized from three different BB polymerization degrees, *B* = 25, 100 and 300. In series III), the BB length *B* is kept constant while the sidechain length is increased from *P* = 12.5 to *P* = 100. PCMOxa-100-18x25 is incorporated in all three series as a reference. The comb parameters were chosen to cover typical parameter values for PCE [129].

The synthesized combs were characterized via SEC and ^{1}H-NMR. The obtained molecular weights and dispersity are summarized in Table 4. In analogy to the PCE nomenclature, where the E stands for ether (PEO), all poly(2-methyl-2-oxazoline)-*g*-poly(methacrylic acid) comb polymers in this work are called PCMOxa. The samples are named e.g. *PCMOxa-B-nxP* indicating *n* PMOxa sidechains of the degree of polymerization *P* are attached to a backbone with a degree of polymerization *B*. The definitions of the parameters *P*, *N* and *n* are displayed in a schematic repeating unit in Figure 42 A). Figure 42 B) shows an exemplary comb polymer with the respective nomenclature.

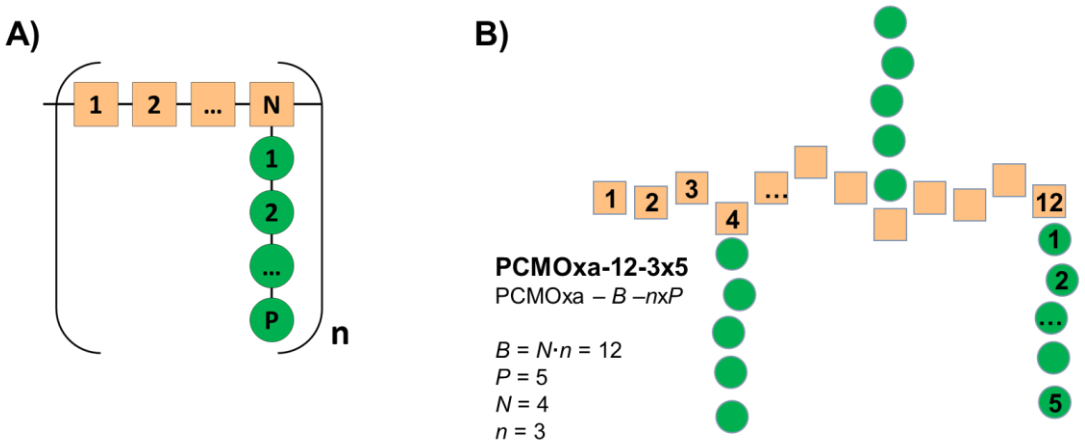

Figure 42: A) Schematic representation of one of the n average repeating structural units of the investigated comb copolymers. This terminology is adapted from [10, 163]. Per repeating unit, one sidechain of the polymerization degree P is attached in average to the N^{th} BB monomer. B) Schematic comb polymer to explain the used nomenclature. In the sketched comb polymer, 3 sidechains of the polymerization degree P = 5 are attached to a BB of B = 12. Therefore, the corresponding comb would be called PCMOxa-12-3x5.

Table 4: Structural parameters, molecular weights and dispersity of the synthesized comb library. In series I), the grafting density is varied by changing the number of BB monomers per SC from N = 5.5 to N = 11. Series II) is synthesized from three different BB polymerization degrees, B = 25, 100 and 300. In Series III), the BB length B is kept constant, and the sidechain length is increased from P = 12.5 to P = 100. The comb PCMOxa-100-18x25 is incorporated in all three series. The SEC data was obtained in DMAc with 0.316 g L^{-1} LiBr with a PMMA calibration for the combs and the SC. The N and n were calculated from integration of the remaining sidechain peak. The BB molecular weight was calculated from the SEC in THF of the PtBMA BB precursor. The BB dispersity is equivalent to the PtBMA BB precursor dispersity.

	Comb							BB		SC	
Name	**B**	**P**	**N**	**n**	**M_n [g mol^{-1}]**	**M_w [g mol^{-1}]**	**Đ**	**M_n [g mol^{-1}]**	**Đ**	**M_n [g mol^{-1}]**	**Đ**
I)											
PCMOxa-100-18x25	100	25	5.5	18	47 000	60 000	1.26	8 500	1.25	2 300	1.09
PCMOxa-100-13x25	100	25	7.7	13	57 000	57 000	3.63	8 500	1.25	2 500	1.07
PCMOxa-100-9x25	100	25	11	9	40 000	53 000	1.34	8 500	1.25	3 000	1.09
II)											
PCMOxa-25-3x25	25	25	8.5	3	33 000	49 000	1.46	2 300	1.09	2 400	1.12
PCMOxa-100-18x25	100	25	5.5	18	47 000	60 000	1.26	8 500	1.25	2 300	1.09
PCMOxa-300-64x25	300	25	4.7	64	130 000	150 000	1.17	26 000	1.07	2 600	1.09
III)											
PCMOxa-100-25x13	100	13	4	25	35 000	54 000	1.56	8 500	1.25	1 000	1.11
PCMOxa-100-18x25	100	25	5.5	18	47 000	60 000	1.26	8 500	1.25	2 300	1.09
PCMOxa-100-16x50	100	50	6.3	16	87 000	99 000	1.14	8 500	1.25	5 300	1.07
PCMOxa-100-15x100	100	100	6.6	15	150 000	110 000	1.23	8 500	1.25	9 600	1.21

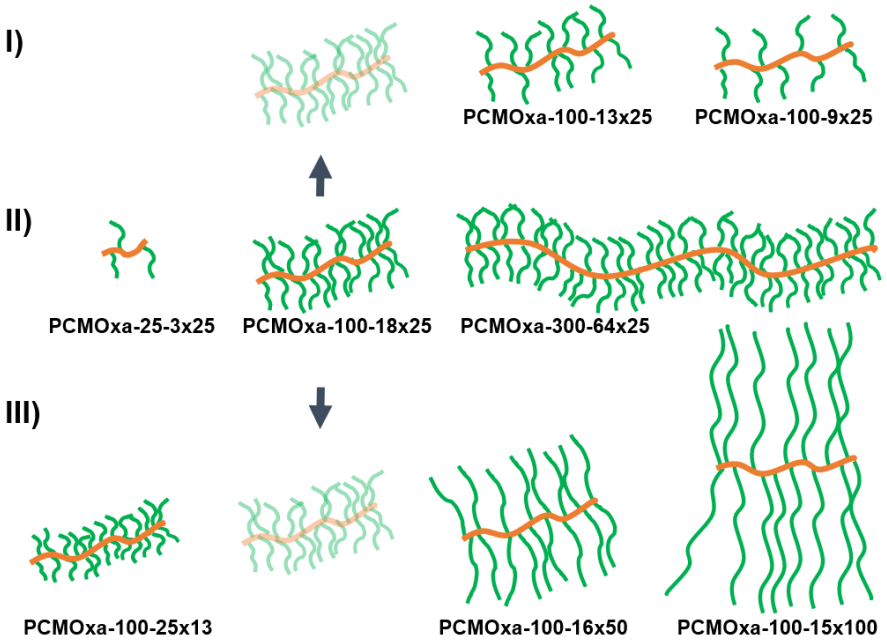

Figure 43: Qualitative overview on synthesized PCMOxa library. In series I), the grafting density is varied by changing the number of BB monomers per SC from N = 5.5 to N = 11. Series II) is synthesized from three different BB polymerization degrees, B = 25, 100 and 300. In Series III), the BB length B is kept constant, and the sidechain length is increased from P = 12.5 to P = 100. A quantitative overview on the structural parameters and molecular weights is given in Table 4. The comb PCMOxa-100-18x25 is incorporated in all three series, but was only synthesized once which is indicated by the arrows and the transparent colour.

4.1.2 Concept Validation for PCMOxa Superplasticizers

The effect of the synthesized PCMOxa combs on the initial fluidity of cement pastes was characterized via rotational rheometry. Superplasticizers can be dosed via direct or delayed addition, meaning they either get added directly to the mixing water or are added a few minutes after the initial water to cement contact. Typical delay times are 2 – 10 min [137, 164]. In this study, delayed addition was chosen, since it leads to a higher yield stress reduction and potentially reduces polymer induced changes of the nucleation and growth of early forming hydrates like ettringite [113, 164, 165]. A strain-controlled TA Instruments ARES G2 equipped with 50 mm parallel plates with wet-sanding sandpaper (600 grit) glued to the surface are used to characterize the SP modified cement pastes. The rheological procedure was adapted from [101]. Steady shear experiments were performed by applying shear rates starting from $\dot{\gamma}$ = 100 s^{-1} to 0.1 s^{-1}. A Bingham regression (see eq. (1)) is applied to the flow curves in the shear rate range of 90 s^{-1} to 20 s^{-1} to obtain the yield stress σ_0.

$$\sigma = \sigma_0 + \eta_p \cdot \dot{\gamma} \tag{4.1}$$

with the measured shear stress σ, the plastic viscosity η_p, and the applied shear rate $\dot{\gamma}$. Exemplary flow curves are shown for different concentrations of PCMOxa-100-8x25 in Figure 44. For increasing comb concentration, both σ_0 and η_p are decreased (see SI Table 28, p. 166). This trend is typical for conventional PCEs [8].

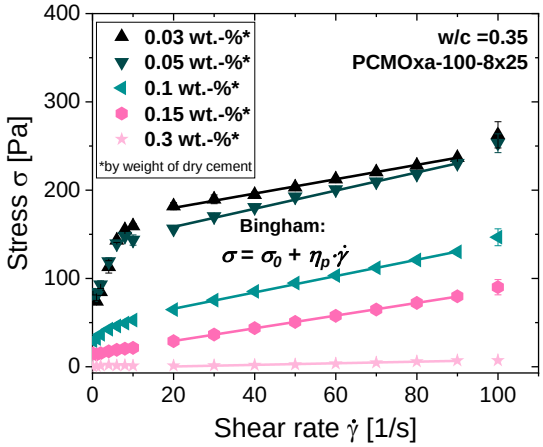

Figure 44: Exemplary flow curves for PCMOxa comb. The yield stress σ_0 is obtained by assuming Bingham behavior in the shear rate range of 20 s^{-1} to 90 s^{-1}.

The commercial PCE compound BASF VP14.1 was chosen as a reference material [166]. A short characterization of BASF VP14.1 is given in the chapter 'Materials' (SI, p. 151). The aim of the comparison to a commercial reference is to evaluate if the σ_0 reduction observed for PCMOxa-100-8x25 is in the same range as for commercial PCEs. Three flow curves for each additive concentration were measured and the yield stress was arithmetically averaged and the standard deviation was determined. The averaged σ_0 and its standard deviation is shown as a function of the polymer concentration c in Figure 45 A). PCE typical S-curves could be observed for both admixtures. At low concentrations, the addition of comb polymer does not influence the macroscopic yield stress. Above a critical concentration, σ_0 is reduced proportionally to the concentration. At high concentrations, above the saturation dosage, σ_0 cannot be further reduced by the addition of polymer [8]. Figure 45 A) shows that the PMOxa-comb PCMOxa-100-8x25 leads to a similar yield stress reduction at similar molar concentrations as the conventional PCE BASF VP14.1.

In addition to the flow behavior, the adsorption behavior was characterized via dissolved organic carbon (DOC) measurements. DOC characterization quantifies the amount of organic carbon present in aqueous samples after filtration [167]. The organic carbon content is determined by complete oxidation, usually either catalytic high-temperature oxidation, chemical oxidation or UV-persulfate oxidation [167]. Subsequently, the released CO_2 amount is determined quantitively, typically via an IR detector [167]. The principle of total organic carbon (TOC) measurement is the same, with the only exception that the sample is not filtered prior to characterization. DOC and TOC measurements are standard tools in the characterization of superplasticizer adsorption in cement pastes [132, 134, 168]. To investigate this adsorption behavior, a cement sample (w/c = 1.2) containing the superplasticizer sample was prepared and thoroughly mixed

(see SI, chapter 10.4.4, p. 159). Subsequently, the particles were removed from the mixture by centrifugation and decantation. As the adsorbed portion of polymer is removed with the particles, the DOC content of the supernatant can be used to calculate the mass of adsorbed polymer if the carbon content of the polymer is known. For a precise result, the inorganic carbon has to be removed prior to DOC characterization. For this purpose, a strong acid like orthophosphoric acid (H_3PO_4) is added, leading to the decomposition of the carbonates to water and CO_2, which is removed via degassing prior to measurement [167].

The DOC data in Figure 45 B) confirms the adsorption of the PCMOxa-comb PCMOxa-100-9x25 on the cement particles. Moreover, the adsorbed mass is in the same range as for the reference BASF VP 14.1. Considering the observed σ_0 reduction as well as the confirmed adsorption of the PCMOxa-combs, we presume that the PCMOxa combs function via the same working mechanism as conventional PCE by adsorption of the polycarboxylate BB and steric hinderance created by the unadsorbed SC.

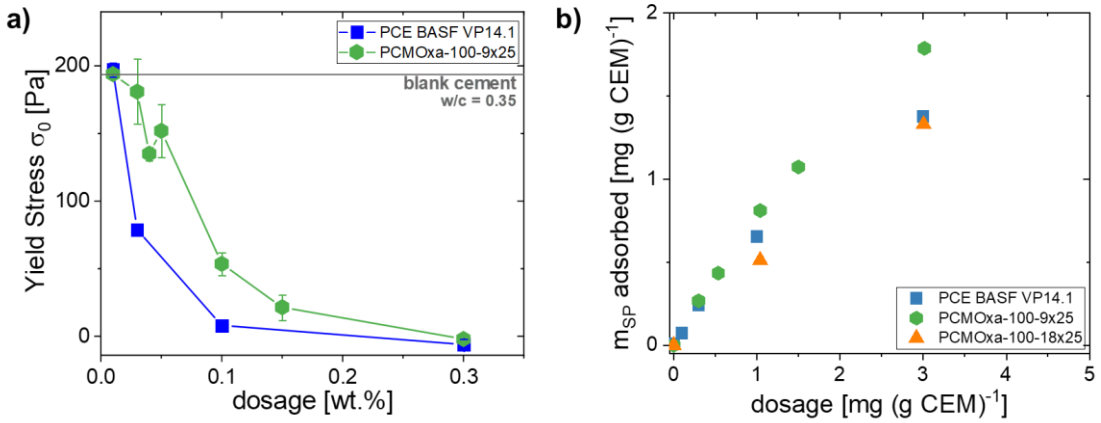

Figure 45: a) Yield stress σ_0 plotted against concentration c for PCMOxa-100-9x25 in comparison to the commercial PCE comb BASF VP14.1. b) Mass of adsorbed comb polymer as function of the initial dosage, both in mg per g of dry cement. Both the σ_0-reduction and the adsoprtion behavior of BASF VP 14.1 can be reproduced by PCMOxa-100-9x25.

4.1.3 Structure-Property Relationship of PCMOxa Combs

The synthesized comb polymer library (compare Table 4) was used to investigate the structure-property-relationship by correlation of the yield stress to the varied structural parameter, as shown in Figure 46. For molecules of the same *B*, we roughly estimate that the number of covered adsorption sites is the same for the same number of macromolecules $N_{polymer}$. Furthermore, we assume that the available surface *S* is proportional to the mass of dry cement. Consequently, we estimate the surface coverage θ to be proportional to the polymer concentration *c* in relation to the used mass of dry cement of 100 g, given in µmol (100 g)$^{-1}$.

$$\theta \sim \frac{N_{polymer}}{S} \text{ given in } \frac{\mu mol}{100 g} \tag{4.2}$$

Under this assumption, the molecules were dosed at the same molar concentration [mol] per 100 g of dry cement [100 g CEM] to investigate the influence of grafting density captured by *N* and SC length *P*. The more common dosage in weight percent per mass of dry cement (wt.%) is given as well.

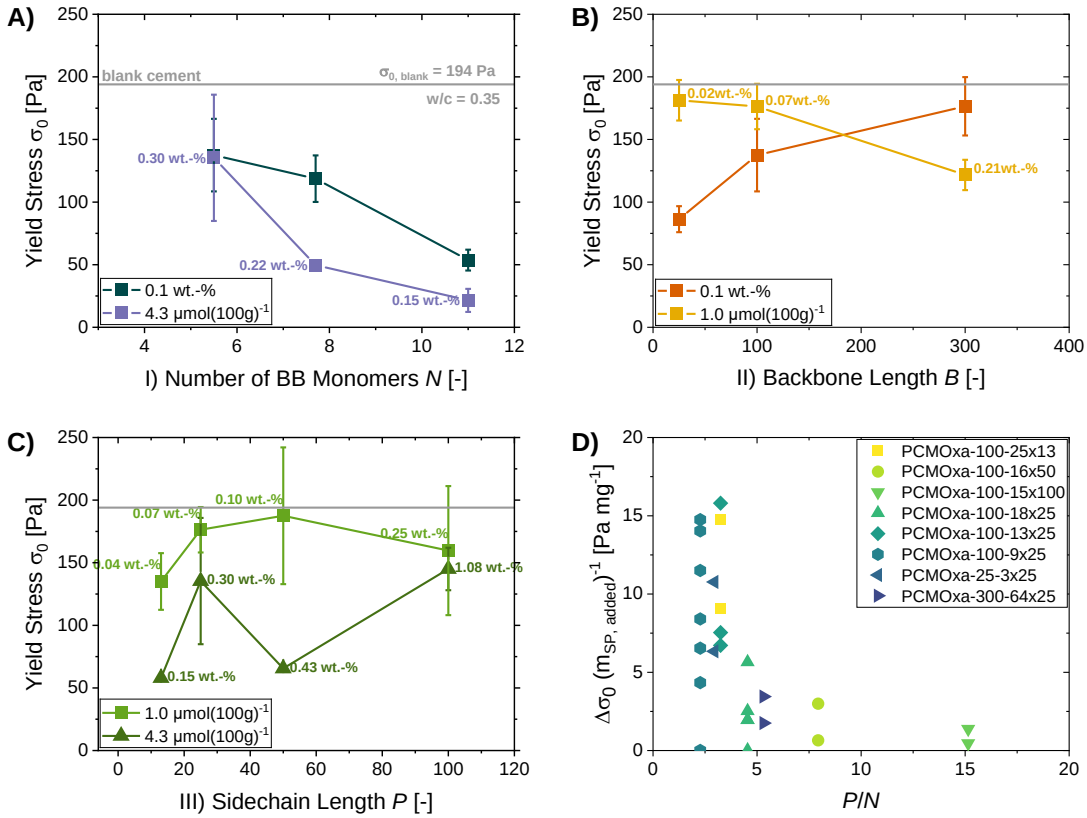

Figure 46: Yield Stress σ_0 plotted against A) number of BB monomers per sidechain N from series I) corresponding to the grafting density of the comb, B) backbone degree of polymerization B from series II), C) sidechain degree of polymerization P from series III) (compare Table 4). For samples added in µmol (100 g)$^{-1}$, the respective wt.% concentration is added next to the data point. Further explanations to the chosen concentrations are given in the text. The grey, horizontal line corresponds to the yield stress of blank cement paste $\sigma_{0,blank}$ = 194 Pa. D) Yield stress difference $\Delta\sigma_0$ per added superplasticizer mass $m_{SP,\,added}$ displayed against P/N which is the ratio of SC length to number of BB monomers per SC. This graph summarizes all measurement data presented in A) to C). $\Delta\sigma_0\, m_{SP,\,added}^{-1}$ corresponds to the dosing efficiency. The highest dosing efficiency is achieved for P/N = 2-5.

In Figure 46 A), σ_0 decreases with increasing *N*. This observation is in agreement with previous studies on PCEs [169, 170]. Microscopically, an increasing value of *N* leads to a lower SC density per BB resulting in a less denser brush topology. Consequently, the sidechains are expected to be less stretched and the average brush height should be decreased [10, 171]. Based on this microscopic picture, the yield stress would be expected to increase with increasing *N*. For polymer brush stabilized nanoparticles, both calculations and experiments suggest the existence of an optimum at medium grafting densities [171–173]. At the optimum grafting density, the brushes can interpenetrate and the steric repulsion between particles is maximized.

For brushes with a higher density than the optimum (low *N*), the brushes cannot interpenetrate and an attractive potential between the polymer covered particles leads to flocculation [171]. In addition, high grafting densities decrease the number of free carboxylate units COO^- per sidechain and therefore reduce the adsorption ability of the comb [9]. Considering the DOC data presented in Figure 45 B), we assume the densest comb of the series PCMOxa-100-18x25 is adsorbed sufficiently. Therefore, the observed trend is presumed to be caused by the high grafting density preventing comb interpenetration. Based on our data, we assume an optimum grafting density at $N \geq 11$ for PMOxa-chains of $P = 25$. Gädt et al. report the highest dosage efficiency for $P/N = 6 - 12$ for conventional PCEs [129]. For $P = 25$, this corresponds to an optimum at $N = 2$-4, which is much lower than the here obtained $N \geq 11$. This difference in the *P*/*N*-optimum between PMOxa and PCE is a result of the higher steric demand of PMOxa in water compared to PEO of the same length, as concluded from the larger hydrodynamic radius of PMOxa compared to PEG at the same degree of polymerization [44]. For series II varying the backbone length *B*, two different additive concentrations were tested as shown in Figure 46 B). For a molar concentration of 1.0 µmol $(100g)^{-1}$, only PCMOxa-300-64x25 reduces the yield stress. Since this comb is significantly larger than the two other tested combs, it can cover more surface area with the same number of molecules resulting in a more efficient σ_0 reduction. Therefore, in addition, this series was investigated with the same mass concentration of 0.1 wt.%. For the mass concentration, the trend is inverted. The yield stress increases with increasing *B*. For conventional PCE, a similar trend has been reported by Yamada et al. [128] while several other studies have observed an increased fluidity for higher *B* values [125, 132, 174]. Based on adsorption theory, combs of high *B* should display an increased adsorption ability [132] and therefore lead to a bigger yield stress reduction. However, in our study, we observe the opposite trend for $\sigma_0(B)$. This could be explained by the higher *N* and thus higher charge density of PCMOxa-25-3x25 in comparison to the other two tested combs as $B = N \cdot n$ (Figure 42). We assume that *N* has a much higher influence on the adsorption ability as the backbone length and therefore *N* is a bigger factor in yield stress reduction than the backbone length *B*. For the influence of sidechain length *P*, many studies on conventional PCE combs suggest that the yield stress reduction per mass of adsorbed polymer is more pronounced for combs with longer sidechains [128, 175]. Microscopically, this can be explained by an increased brush height *h* for increased *P* [10]. Consequently, the yield stress reduction is expected to be more pronounced. However, in our study no clear trend of the σ_0 dependency on *P* was obtained, as displayed in Figure 46 C). All investigated combs reduce the yield stress at a dosage of 4.3 μmol $(100\ g)^{-1}$. PCMOxa-100-16x50 and PCMOxa-100-25x13 reduce σ_0 significantly by $\Delta\sigma_0 \sim 100$ Pa, while the σ_0-reduction of PCMOxa-100-15x100 and PCMOxa-100-18x25 is smaller with $\Delta\sigma_0 \sim 50$ Pa. We assume that the chosen grafting ratios ($4 < N < 6.6$) form dense brushes in which the negative charges along the backbone are shielded by the sidechains and therefore do not adsorb well to the cement particle surface. A lower grafting density is suspected to yield more effective plasticizers.

Combining the results of the three individual series, we can conclude that there is an optimum comb structure at intermediate *P* and *N* values and that the different structural parameters influence each other. Combs with longer sidechains need more space between the chains to be effective, so a higher value of *P* should be accompanied by a higher *N* to achieve the same yield stress reduction. Empirically, it was also found that the yield stress correlates well with *P*/*N*

[129, 132]. Therefore, a simplified view on the question of optimum parameters is given by Figure 46 D). The yield stress reduction $\Delta\sigma_0$ per mass of dosed PCMOxa $m_{SP,\,added}$ is correlated to *P*/*N*. For small *P*/*N*, the highest dosing efficiency $\Delta\sigma_0\, m_{SP,\,added}^{-1}$ can be achieved. The PCMOXa comb design for a maximum in $\Delta\sigma_0\, m_{SP,\,added}^{-1}$ is assumed to be in the range of 2 < P/N < 5, however no definite maximum can be determined from the here presented data without further synthesis and measurements. Gädt et al. report the highest dosing efficiency for conventional PCEs at P/N = 6 - 12 [129], which is substantially higher than the here obtained *P*/*N* range for maximum $\Delta\sigma_0\, m_{SP,\,added}^{-1}$. The difference in the $\Delta\sigma_0\, m_{SP,\,added}^{-1}$ range between PCE and PCMOxa shows that the PCMOxa combs need shorter sidechains or a lower sidechain density than commercial PCEs to achieve their maximum efficiency. This is reasonable since PMOxa has a persistence length of l_p = 1.7 nm and is therefore significantly stiffer than PEO with l_p = 0.38 nm [24, 176, 177]. Additionally, PMOxa also exhibits a higher hydrodynamic volume as PEO for the same degree of polymerization [44]. Therefore, we assume that PCMOxa combs of the same *P* create a higher brush height *h* than a corresponding PCE, resulting in a lower *P*/*N* optimum. Within the uncertainty of the experiment, we find no difference in the efficiency of yield stress reduction for the change in sidechain chemistry between these two types of combs. The presented synthesis would allow to fine tune the molecular properties and would allow a rather simple and more detailed optimization.

4.2 Alternative Synthesis for PCMOxa Combs via Grafting-Through Procedure

The grafting-onto procedure presented in the previous chapter is an elaborate synthetic strategy which is especially useful to obtain highly defined model systems. However, the number of synthetic steps, monomer purities and inert gas atmosphere complicates the potential upscaling of the grafting-onto synthesis route and thus limits its potential future applications. Therefore, a second synthetic strategy based on a grafting-through approach was tested to obtain PCMOxa combs, as displayed in Figure 47. This grafting-through procedure, also referred to as the macromonomer route, is a two-step synthesis. The first step is the synthesis of a poly(2-methyl-2-oxazoline) methacrylate (PMOxa – MA) macromonomer via cationic polymerization and end-capping with methacrylic acid. In the second reaction step, the macromonomer is copolymerized with methacrylic acid (MAA) in a free radical polymerization. The macromonomer route is analogue to the commercial synthesis of PCE [8].

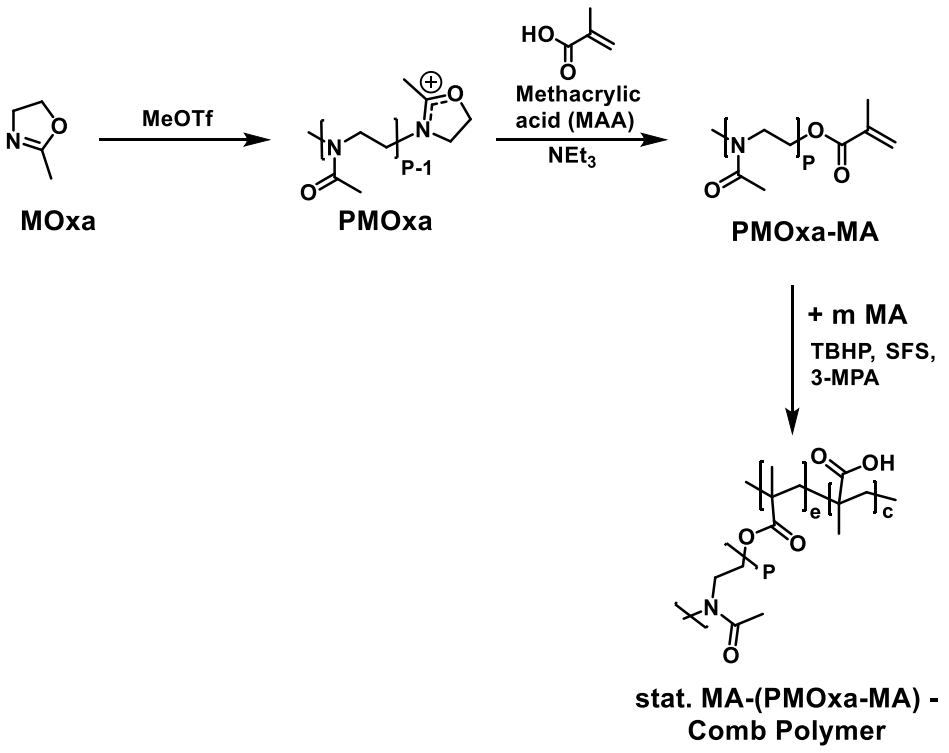

Figure 47: Reaction scheme of the macromonomer route. The first reaction step is the CROP of 2-methyl oxazoline (MOxa). The cationic PMOxa-chains are end-capped with deprotonated methacrylic acid (MAA) to obtain PMOxa-MA macromonomers. The statistic PCMOxa-combs are synthesized via copolymerization of the PMOxa-MA macromonomer and MAA in a free radical polymerization in the presence of the chain transfer agent 3-mercapto propionic acid (3-MPA).

The macromonomer route has the advantage that one macromonomer batch can be stored and then used for the synthesis of several combs within several weeks. In the previously presented

grafting-onto approach, the sidechains are usually synthesized directly before the grafting procedure individually for every comb. Thus, although the same sidechain length was intended, the molecular weights of the sidechains can differ by 10 %. However, it should be noted that this deviation is within the uncertainty of the molecular weight determination by SEC.

4.2.1 Synthesis of PMOxa Macromonomer

The macromonomer synthesis was adapted from literature [53, 162]. Methyl trifluoro-methanesulfonate (methyl triflate, MeOTf) was chosen as an initiator for the ring opening polymerization to ensure a cationic polymerization (see chapter 2.1.1, p. 9). The PMOxa SCs are polymerized in ACN at 80 °C. The reaction is terminated by end-capping of the living cationic PMOxa chains with MAA deprotonated with the non-nucleophilic base triethyl amine (NET_3) dissolved in ACN, as displayed in Figure 48.

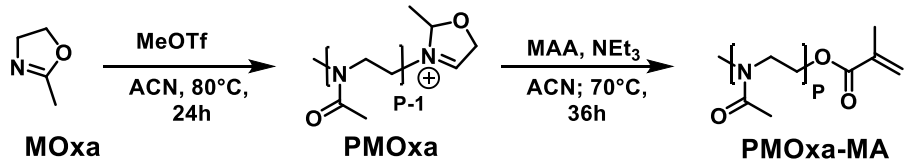

Figure 48: Reaction scheme of PMOxa-MA macromonomer synthesis. 2-methyl oxazoline is polymerized in a living cationic ring opening polymerization (CROP) initiated with methyl trifluoromethanesulfonate (methyl triflate, MeOTf) in acetonitrile (ACN). The reaction is terminated with an end-capping of the living cationic PMOxa with deprotonated methacrylic acid. The synthesis was adapted from [53, 162].

The successful end-capping is confirmed by ^{1}H-NMR, as displayed in Figure 49. The excess of base, methacrylic acid and the methyl triflate was removed during the purification of the crude product by several extraction steps with chloroform. Precipitation in ice-cold diethyl ether yielded the pure PMOxa - macromonomers. The integration of the protons of the main chain (labeled d in Figure 49) yields a degree of polymerization of approximately 22, corresponding to a molecular weight of approximately M_n = 2 000 g/mol.

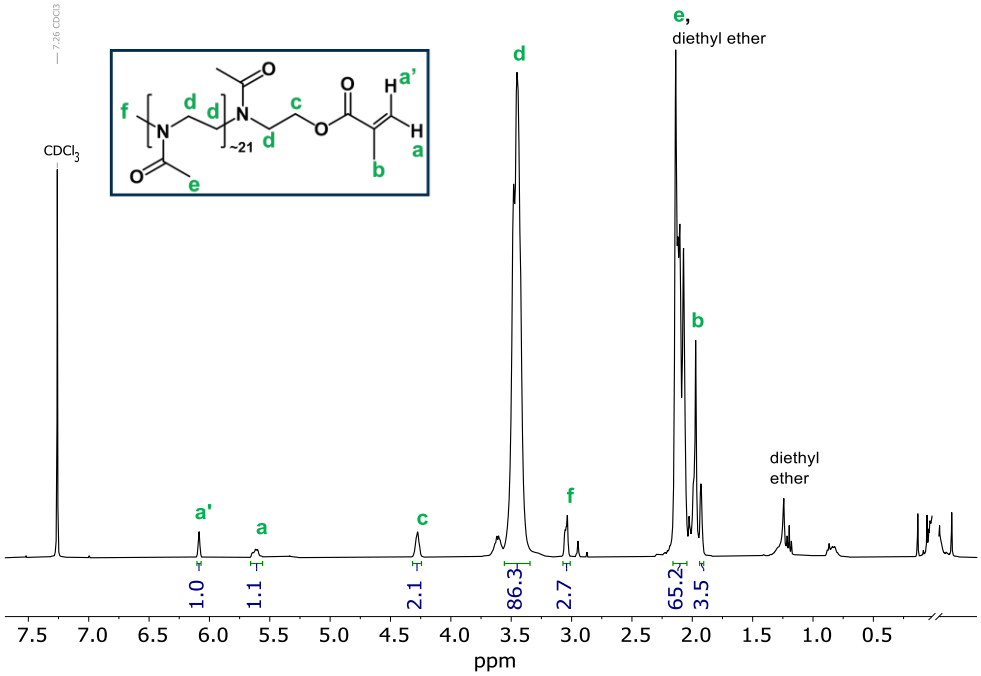

Figure 49: ^{1}H-NMR spectrum (400 MHz, 16 scans, $CDCl_3$) of PMOxa-MA macromonomer.

Two macromonomers of different molecular weights were synthesized via the route presented in Figure 48. The obtained PMOxa-MA products were characterized via ^{1}H-NMR and SEC. The molecular weights and dispersity are summarized in Table 5. The ^{1}H-NMR gives the actual degree of polymerization by the ratio of the integral I_a to I_e and thereby confirms that the intended degree of polymerization was achieved. The samples are labelled as PMOxa-MA-P_n with P_n obtained from the ^{1}H-NMR. A PS and a PMMA SEC calibration were used to characterize the synthesized macromonomers. Both SEC calibrations overestimate the molecular weight of the macromonomers compared to the value obtained from ^{1}H-NMR analysis. The molecular weights obtained with the PMMA calibration deviate 15 % for PMOxa-MA-12 and 44 % for PMOxa-MA-24 from the results of ^{1}H-NMR. The deviations are increased for the PS calibration with 60 % for PMOxa-MA-12 and 83 % for PMOxa-MA-24. Since the results obtained via the PMMA calibration are closer to the actual molecular weight, the PMMA calibration was used for the characterization of all PMOxa-containing samples.

Table 5: Overview on molecular weights and dispersity of the synthesized PMOxa-MA macromonomers.

	M_{theo} (synthesis)		**SEC, PS calibration**			**SEC, PMMA calibration**			**NMR**	
Name	**M_n [g mol^{-1}]**	**P_n**	**M_n [g mol^{-1}]**	**P_n**	**PDI**	**M_n [g mol^{-1}]**	**P_n**	**PDI**	**P_n**	**M_n [g mol^{-1}]**
PMOxa-MA-12	**1000**	**12**	**1600**	**19**	**1.08**	**1150**	**14**	**1.11**	**12**	**1000**
PMOxa-MA-22	**2000**	**24**	**3300**	**39**	**1.07**	**2600**	**31**	**1.10**	**22**	**1900**

4.2.2 Comb Synthesis by Copolymerization of PMOxa Macromonomer and Methacrylic Acid

The comb synthesis was adapted from a typical PCE synthesis [148] and is displayed in Figure 50. The comb synthesis was exemplary performed for PMOxa-MA-21. The macromonomer was copolymerized with 2.5 equivalents of methacrylic acid. In commercial PCE, acrylic acid is often chosen as the comonomer due to its low cost. However, acrylate-type monomers can undergo backbiting reactions which produce mid-chain radicals [34, 178] and would consequently result in combs with branched backbones. Therefore, methacrylic acid was chosen as comonomer in this work since it does not undergo the backbiting reaction [34]. Moreover, the use of methacrylic acid facilitates the comparison between the combs synthesized via the grafting-onto (chapter 4.1, p. 63) and the grafting-trough approaches as the resulting comb polymers are chemically identical.

In the grafting through synthesis, the redox initiation system of tert-butyl hydroperoxide (TBHP) and sodium formaldehyde sulfoxylate (SFS) enables the reaction to be conducted at room temperature. The chain-transfer agent 3-mercapto propionic acid (3-MPA) is added to lower the molecular weight of the obtained combs [34]. Since only one PCMOxa-comb was synthesized via free radical copolymerization (FRP) of PMOxa-MA-22 and MA, it is referred to as FRP-PCMOxa for simplicity.

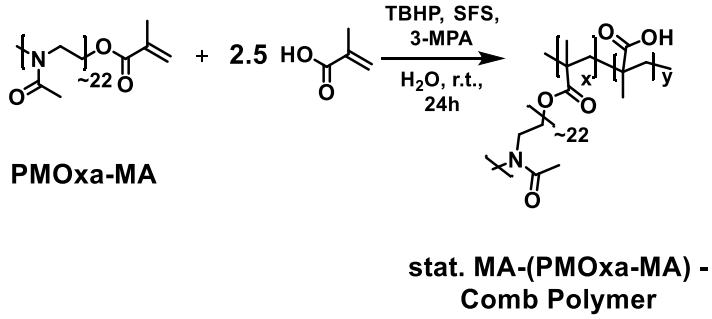

Figure 50: Reaction scheme of free radical copolymerization of PMOxa-MA and MAA in aqueous solution. The reaction is initiated with a redox system (tBHP,SFS) and is conducted in the presence of a chain transfer agent (3-MPA). For the PCE synthesis, the PMOxa-MA macromonomer was exchanged to a commercial poly(ethylene glycol)monomethylethermethacrylate (PEGMA) and the synthesis was conducted as noted.

The successful formation of the PCMOxa-combs is indicated by a shift of the main peak in SEC measurements (DMAc + 0.316 g L^{-1} LiBr) to smaller elution volumes, as displayed in Figure 51. As a reference, the SEC trace of the grafting-onto product PCMOxa-100-18x25 is shown as well. PCMOxa-100-18x25k is assumed to be the closest in sidechain length (P = 25) and number of carboxylic acid per sidechain (N = 5.5) to the FRP comb (P = 21, N = 3.5, see further discussion below). The molecular weight data of the FRP-PCMOxa is presented in Table 6. The SEC trace of the FRP-PCMOxa does not display any remaining sidechain peak at 15 mL, indicating full conversion of the macromonomer.

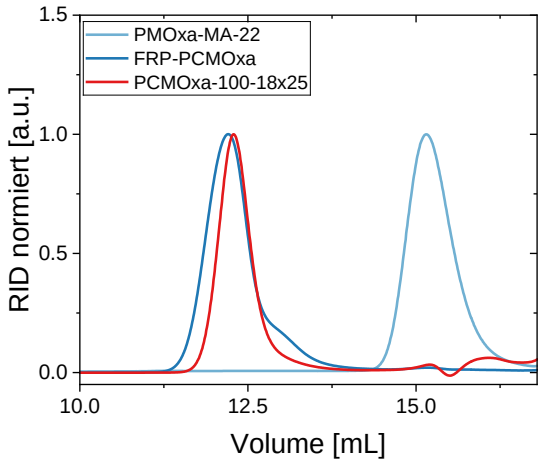

Figure 51: SEC traces of PMOxa-MA macromonomer, the resulting FRP-PCMOxa comb in reference to the grafting-onto product PCMOxa-100-18x25.

In addition to the synthesis of the FRP-PCMOxa, the synthetic strategy presented in Figure 50 was used to synthesize a PCE with PEO sidechains for reference. This PCE compound is referred to as FRP-PCE. In the synthesis, a PEO-methacrylate macromonomer with a degree of polymerization of P = 22 ($M_n \approx 950$ g mol^{-1}) was copolymerized with 2.5 eq. methacrylic acid in the presence of 3-MPA in aqueous solution. The obtained FRP-PCE was characterized via SEC as well and the results are given in Table 6.

Table 6: The FRP-PCMOxa and the FRP-PCE were characterized via SEC (DMAc + 0.316 g L^{-1}, PMMA calibration). The monomer ratio is given as the molar ratio of MAA to methacrylate macromonomer (MM). (*) The molecular weight and the dispersity of the PEO SC were adapted from the manufacturer's specifications.

	SC				**Monomer-ratio**	**Comb**		
Name	**Polymer**	**P**	**M_n [g mol^{-1}]**	**Đ**	**MAA:MM**	**M_n [g mol^{-1}]**	**M_w [g mol^{-1}]**	**Đ**
FRP-PCMOxa	PMOxa	21	2 600	1.10	2.5	48 000	71 000	1.48
FRP-PCE	PEO	22	950*	1.08*	2.5	42 000	73 000	1.76

In contrast to the grafting-onto strategy, the number of backbone monomers per sidechain *N*, the backbone length *B* and consequently the number of repeating units *n* of the two synthesized FRP combs is not well defined (for terminology of structural parameters see Figure 42, p. 65). Since the SEC indicates full conversion, *N* can be estimated from the stochiometric monomer ratio in the polymerization. Since one backbone monomer is already attached to the sidechain, *N(theo)* = (MAA:MM) + 1. The actual *N* can also be derived via integration of the backbone monomers in ^{1}H-NMR, as displayed in Figure 52 for FRP-PCMOxa.

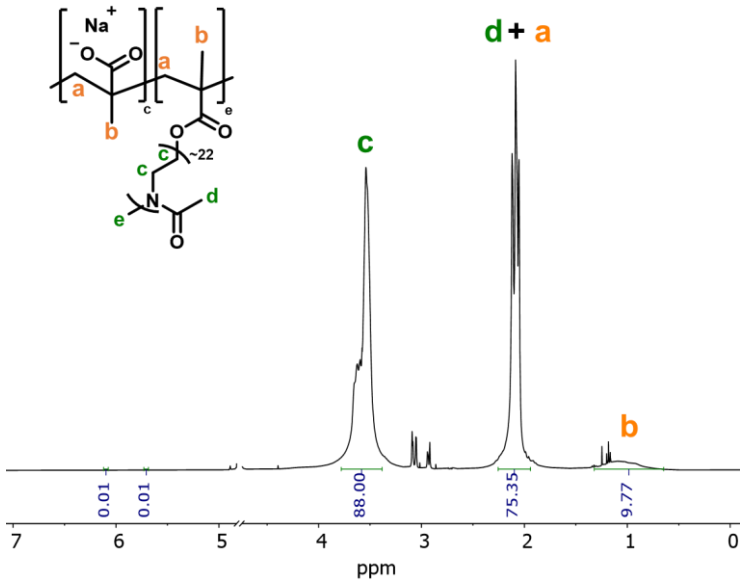

Figure 52: ^{1}H-NMR (400 MHz, 16 scans, D_2O) of FRP-PCMOxa comb. The spectrum was referenced to the residual solvent peak. The integration was referenced to the 88 H of the PMOxa chain (labelled c). The backbone monomer integrals were obtained as b = 10 and a = 75 – d = 75 – 66 =9.

N was calculated from the integrals of the 2 H of the CH_2-group (**a**) and the 3 H of the methyl group (**b**) in the methacrylate repeating units. Since the NMR integrals I are referenced to one sidechain (I_c = 88), *N* can simply be calculated by the integral of I_a or I_b divided by the respective proton number. The results are summarized in Table 7 in comparison to the theoretical $N_{synthesis}$ obtained from the monomer ratio in the synthesis. The number of backbone monomers *N* of the FRP-PCE comb was determined in the same manner also via ^{1}H-NMR, as displayed in Figure 53.

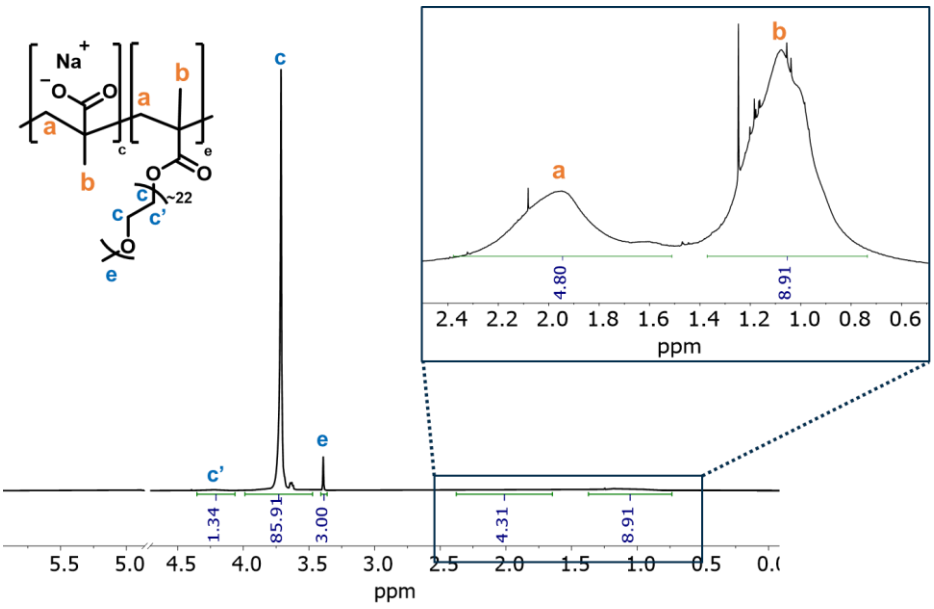

Figure 53: ^{1}H-NMR spectrum (400 MHz, 16 scans, D_2O) of FRP-PCE.

Table 7: Integration of ^{1}H-NMR to obtain backbone monomers per sidechain N. The integrals a and b were divided by their respective proton number (H_a = 2, H_b = 3) to give the grafting densities N_a and N_b. N(NMR) is the average of N_a and N_b.

	N (synthesis)	**Integral a**	N_a	**Integral b**	N_b	***N (NMR)***
FRP-PCMOxa	3.5	9	4.5	10	3.3	3.9
FRP-PCE	3.5	5	2.5	9	3	2.75

The obtained *N* values correspond closely to the values of $N_{synthesis}$ calculated from the stoichiometry in the polymerization. This agrees with the full conversion being indicated by SEC (compare Figure 51) and the ^{1}H-NMR (compare Figure 52). In the master thesis of K. Beier [149], the FRP synthesis (see Figure 50) was used to synthesize three PCE compounds with a high (N = 2), medium (N = 3.8) and low (N = 6) grafting density. The synthesis parameters of the medium comb were the same as for the here presented FRP-PCE. Acid-base titration and ^{1}H-NMR were used to determine the number of free carboxylic acids per PEO sidechain. Beier could show that the number of free carboxylic acids per sidechain corresponds to the stoichiometry of the polymerization with an uncertainty of under 5% (obtained by titration). However, the values for *N* obtained by ^{1}H-NMR showed a much higher deviation of approximately 50 % since the peaks are rather broad and small, therefore the integration has a higher uncertainty than the values obtained by titration. Thus, the value of *N* from stoichiometry is preferred over the *N* calculated from the ^{1}H-NMR spectra in the following.

The backbone length *B* of the FRP combs could not be determined. End-group analysis via ^{1}H-NMR failed as the proton signals of the tert-butyl group (initiator) as well as the proton signals of the 3-MPA (CTA) are expected in the region of 0.5 – 1.5 ppm and are therefore overlapped by the methyl group of the PMAA backbone. Since *N* is known with a comparatively low uncertainty, *B* could be calculated if the molecular weight would be known. However, the molecular weight obtained with the SEC in DMAc equipped with a dRI detector and PMMA calibration is not representative of the actual molecular weight of the FRP combs. To obtain a rough order of magnitude estimate, *B* was calculated on the basis of the master thesis of Beier [149]. Beier performed aqueous SEC in 0.7 M Na_2HPO_4 calibrated with PEO standards (200 – 100 000 g mol^{-1}). He obtained a peak molecular weight of M_p = 56 000 g mol^{-1} for the medium PCE comb, which would correspond to a backbone length of *B* = 42 (MM:MAA of 1:2.8) (compare Table 29, p. 166). The molecular weight obtained from the aqueous SEC calibrated with PEO standards is presumed to be closer to the true molecular weight than the value obtained via SEC in DMAc, since the calibration corresponds at least to the sidechain polymer. Nevertheless, the error of these values remains relatively large due to the polymer's branched and charged structure as well as the unknown refractive index of the PMAA copolymer backbone. Therefore, the calculation of *B* should only be regarded as a rough order-of-magnitude estimate. Static Light Scattering, either with a MALS detector in SEC or as an independent characterization, should be used to determine the actual molecular weight and calculate the correct *B*.

4.2.3 Rheological Characterization of the Grafting-Through PCMOxa Combs

The influence of the grafting-through combs, FRP-PCE and FRP-PCMOxa, onto the yield stress of cement paste was tested in the same procedure as for the grafting-onto PCMOxas (compare chapter 4.1, p. 63). The molecules were dosed at a typical concentration of 0.1 wt.% for superplasticizers. The result of the average yield stress and its standard deviation of three successive flow curves is plotted in Figure 54. For comparison, the yield stress of blank cement paste, the commercial PCE BASF VP14.1 (for characterization see chapter 'Materials' in SI, p. 151) and the grafting-onto comb PCMOxa-100-9x25 were included in the graph. PCMOxa-100-9x25 was chosen as a reference as it is the grafting-onto compound with the biggest yield stress reduction of $\Delta\sigma_0$ = 145 Pa at the dosage of 0.1 wt.%. The structural parameters of the presented combs are summarized in Table 8.

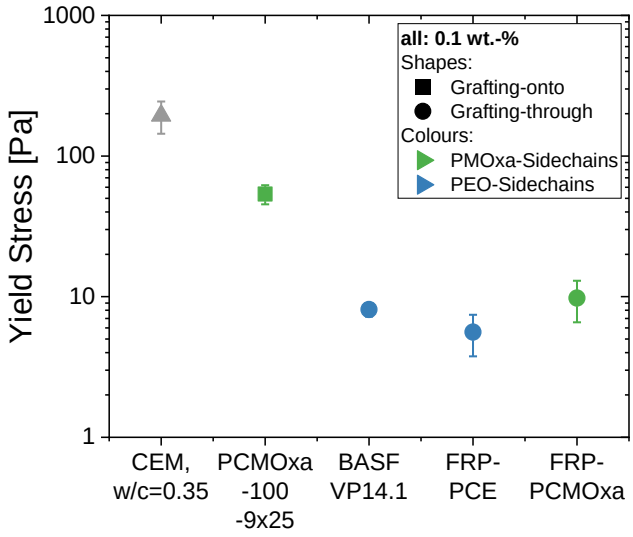

Figure 54: Average yield stress and standard deviation of three independent flow curves for blank cement paste with w/c = 0.35 (grey), the grafting-onto comb PCMOxa-100-9x25 (green rectangle), the commercial PCE BASF VP14.1 (blue circle), the grafting-through comb FRP-PCE (blue circle) and the FRP-PCMOxa (green circle).

Table 8: Structural parameters of compounds compared in the rheological characterization presented in this chapter. The molecular weights and dispersity of the PCMOxa compounds and the FRP-PCE were obtained via SEC in DMAc. The reported values for BASF VP14.1 were determined via aqueous SEC as published [166]. The value of N for BASF VP14.1 was determined in [149].

	Comb							BB		SC	
Name	**B**	**P**	**N**	**n**	**M_n [g mol^{-1}]**	**M_w [g mol^{-1}]**	**Đ**	**M_n [g mol^{-1}]**	**Đ**	**M_n [g mol^{-1}]**	**Đ**
PCMOxa-100-9x25	100	25	11	8	40 000	53 000	1.34	8 500	1.25	3 000	1.09
BASF VP14.1	-	20	2.82	-	11 700	25 000	2.39	-	-	-	-
FRP-PCMOxa	50 ± 25	22	3.5	-	48 000	71 000	1.48	-	-	2 600	1.1
FRP-PCE	50 ± 25	21	3.5	-	42 000	73 000	1.76	-	-	950	1.08

The FRP-PCE and the FRP-PCMOxa reduce the yield stress to the same value of $\sigma_0 \approx 10$ Pa within the uncertainty of the experiment. Consequently, for comparable side-chain lengths and identical FRP synthesis parameters, the yield stress reduction is equivalent for PCMOxa and PCE. Moreover, the yield stress reduction of the FRP combs is comparable to that of the commercial product BASF VP14.1 at the same mass dosage. The FRP combs perform significantly better than the grafting-onto products. The yield stress obtained for FRP-PCMOxa ($\sigma_0 \approx 10$ Pa) is five times lower than the yield stress obtained for the grafting-onto PCMOxa-100-9x25 ($\sigma_0 \approx 50$ Pa) at the same dosage of 0.1 wt.%. This result is unexpected. Based on the findings in chapter 4.1.3 (p. 68), it was anticipated that $N = 3.5$ for the FRP combs would be too small in comparison to the determined optimum of $N \leq 11$, leading to a minor or even no reduction of the yield stress. This raises the question on how well the model systems presented in chapter 4.1 can represent commercial comb-polymer products, due to differences in their dispersity and potential differences in the polymer structures, namely the parameters *B*, *N* and *n*, as a result of the synthesis route.

The expected performance of FRP-PCMOxa was derived based on the structural parameters presented in Table 8. However, both the structural values of the samples as well as the molecular weights and dispersity have high uncertainties for the grafting-through products. Consequently, the predictions for the yield stress reduction may be incorrect. Of the known structural parameters of the FRP combs, *N* has the highest uncertainty, while *P* is well defined since the PMOxa-MA macromonomer was synthesized via the living CROP. As discussed in the previous chapter 4.1.2, *B* and *n* could not be determined. *N* was assumed to be 3.5 based on stoichiometry of the synthesis. Following the findings of chapter 4.1.3 (p. 68), $N = 3.5$ should lead to very dense combs and consequently a small or even no reduction of the yield stress should be observed. This discrepancy between the expected and the observed yield stress reduction could be explained by a false estimation of the value of *N*. However, as discussed in the previous chapter, the indications of complete conversion by two characterization methods are a strong argument for *N* to be close to the stochiometric ratio. However, a branching point on average every 3.5 monomers is a very high grafting ratio which might be unlikely due to the steric demands of the sidechains. Thus, it is assumed that very short backbones with a little number of sidechains are preferably formed over long molecules with a large number of sidechains. This should result in a rather high dispersity and low molecular weight. However, this is not reflected by SEC data presented in Table 8 (p. 80). The obtained $Đ = 1.45$ is small for a free radical polymerization, especially at full conversion. Typical values for a free radical polymerization without a CTA are $Đ \geq 2$ and CTAs are known to further increase the dispersity by initiating additional chain growth [179]. Therefore, it seems that the SEC in DMAc underestimates the true dispersity of the complex branched structures due to the unsuitable calibration or secondary effects, like unfavorable solvent-polymer interactions. It could be that the potentially charged methacrylate backbone is not properly solvated by the aprotic DMAc. It is understood that the dispersity obtained via SEC represents different structural features for the two different synthesis strategies. In the grafting-onto procedure, the BB length and the SC length are known and defined at the moment of grafting. The dispersity in the molecular weight is mainly determined by the variance of the number of sidechains. In the grafting-through procedure, the dispersity incorporates both the dispersity of the backbone length and the variance in number of sidechains. The

variance in backbone length might be much bigger than the cumulative PDI of $Đ = 1.45$ indicates.

In addition, the SEC in DMAc fails to determine the actual molecular weight. For branched structures in general, the calibration obtained with linear standards underestimates the actual molecular weight [180]. The deviation increases for increasing molecular weights and increasing number of branches [181]. This was also shown for PCEs in aqueous SEC calibrated with linear PEO standards [181]. We therefore assume that the molecular weights of the grafting-onto combs are underestimated and the deviation from the actual molecular weight increases with increasing molecular weight. We further assume that the molecular weight of the FRP-PCMOxa is significantly lower than that of the grafting-onto PCMOxa combs. Therefore, it is assumed that the higher efficiency in yield stress reduction for the FRP-PCMOxa compared to PCMOxa-100-9x25 is caused by higher dispersity, the lower backbone length and potentially smaller molecular weight of the FRP comb. We propose that these parameters affect the comb distribution within the cement suspension. Molecules of shorter backbone length, as probably obtained by FRP, lead to a much more homogenous distribution at the same surface coverage θ than molecules with longer backbones, as obtained via the grafting-onto approach. This hypothesis is graphically illustrated in Figure 55.

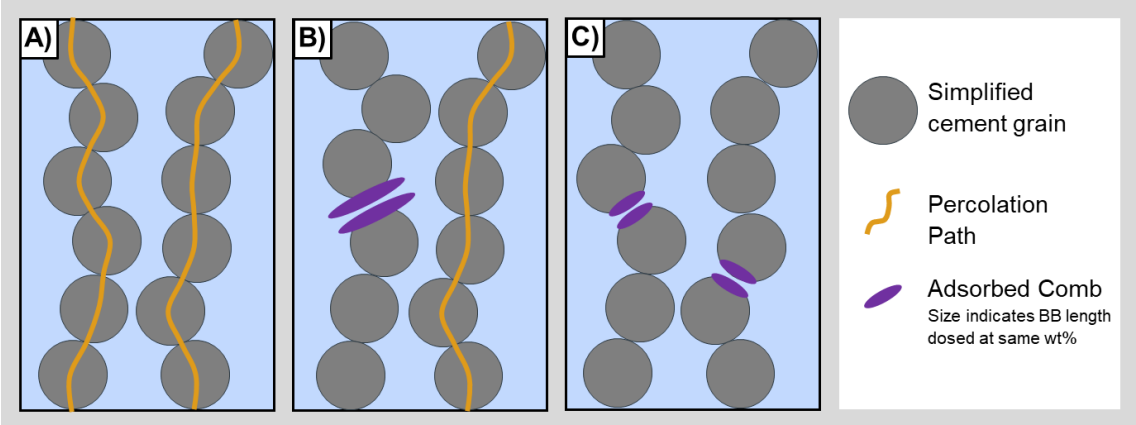

Figure 55: Visualization of proposed influence of molecular weight on the distribution of the comb polymers in a cement suspension. The cement grains are approximated as round particles. The contact between the particles leads to the formation of a percolation path (orange), which increases the macroscopic yield stress. The adsorbed combs (represented by purple ellipses) partly cover the surface of the cement grains and thereby prevent the formation of percolation paths. Molecules of different backbone length and thus different molecular weights (differently sized ellipses) at the same dosage (and same adsorbed mass) cover the same amount of the available cement surface. However, the number of prevented contact points is smaller for the bigger molecules as the distribution is less homogeneous. Consequently, molecules of smaller molecular weight lead to a bigger yield stress reduction macroscopically.

4.3 Conclusions and Outlook

Chapter 4 presents poly(carboxylate methyloxazolines) (PCMOxa, IUPAC: poly(2-methyl-2-oxazoline)-*graft*-poly(methacrylic acid)), which are comb polymers with a polycarboxylate backbone and poly(2-methyl-2-oxazoline) (PMOxa) sidechains. These comb polymers were developed based on the commercial superplasticizer poly(carboxylate ether) PCE, but with substituted sidechain chemistry. PMOxa was chosen as a water-soluble and uncharged alternative to poly(ethylene oxide) (PEO). To the best of our knowledge, this is the first study on the influence of chemical nature of the sidechain on the functionality of defined and low disperse comb-structured superplasticizers (SP). Two different synthetic strategies towards the comb polymers with PMOxa-sidechains were presented: a grafting-onto and a grafting-through. The grafting-through approach is also referred to as macromonomer route. The grafting-onto synthesis combines anionic and cationic synthesis to receive combs with low dispersity and well-defined molecular weights of both backbone (BB) and sidechains (SCs) combined with an average and disperse grafting density. This synthetic strategy allows the individual characterization of BB and SC. Consequently, the structural parameters of the grafting-onto PCMOxa combs can be determined easily with a low uncertainty. Therefore, these combs are suited for comprehensive structure-property investigations.

The influence of the synthesized PCMOxa combs on the workability of cement pastes was investigated by determination of the yield stress via flow curves in steady-shear of OPC pastes with w/c = 0.35 and varying PCMOxa concentrations in the range of 0.01 – 1 wt.%. To verify whether PCMOxa can function as a superplasticizer, its performance was assessed on a selected grafting-onto sample. The investigated PCMOxa reduced the yield stress in a similar manner and amount as the commercial PCE sample. Moreover, a similar yield stress vs polymer concentration correlation was obtained. Dissolved organic carbon (DOC) measurements revealed that the adsorption of PCMOxa combs is similar to conventional PCEs. Therefore, it was concluded that the PCMOxa combs have a similar working mechanism as conventional PCE via the adsorption of their negatively charged BB onto the cement particle surface while the non-adsorbing poly(oxazoline) SCs create steric hinderance between the particles. In a first attempt to understand the structure-property relationship of these new comb-superplasticizers, a library of PCMOxa was synthesized while systematically varying the number of BB monomers per SC *N*, the SC length *P* and the BB length *B*. Thereby, it was shown that PCMOxa exhibits a structure-property relationship of a similar archetype in yield stress reduction as PCE in OPC. However, the parameter set for a maximum in $\Delta\sigma_0\ m_{SP,\,added}^{-1}$ is shifted to lower *P* and *N* values for PCMOxa compared to PCE due to the higher chain stiffness and consequently the increased hydrodynamic radius of the sidechain. Therefore, the correlation of yield stress with *P*/*N* reveals a shift of the dosing efficiency maximum to lower *P*/*N* of 2 < P/N < 5 in comparison to conventional PCE, which show the highest dosing efficiency at P/N = 6 - 12 [129]. As a result, less dense combs or combs with shorter sidechain lengths compared to conventional PCE are the structures for PCMOxa to achieve maximum yield stress reduction in cement paste per added mass of polymer. However, an absolute statement about the dosing efficiency of PCMOxa in comparison to PCE cannot be made at this early stage.

In addition to the grafting-onto procedure, an alternative synthesis route was presented in chapter 4.2. A standard macromonomer route (or grafting-through strategy) originally developed for PCE was transferred to the synthesis of PCMOxa combs [148]. The macromonomer was prepared following a procedure from literature [162] by living cationic ring opening polymerization terminated via an end-capping reaction with methacrylic acid to obtain a PMOxa-methacrylate (PMOxa-MA). ^{1}H-NMR confirmed its structure. The combs were then polymerized in a free-radical polymerization (FRP) in the presence of a chain-transfer agent (CTA) at room temperature. SEC verified the successful comb formation. The grafting-through synthesis has several practical advantages over the grafting-onto approach. Only a single reaction step under Schlenk conditions is required, making the route readily up-scalable. Microwave-assisted CROP could further shorten the macromonomer synthesis time from approximately 24 h to 1 - 5 min [53]. However, the structural parameters obtained via the macromonomer route are poorly defined making it unsuitable for structure-property relationship investigations. The degree of polymerization of the sidechain *P* was obtained from ^{1}H-NMR with a low uncertainty, while the number of backbone monomers per sidechain *N* was estimated from the stoichiometry of the polymerization. The number of repeating units *n* and thus the backbone length *B* remain indeterminate. In addition to the FRP-PCMOxa, the same synthetic strategy was applied to synthesize a PCE with a PEO sidechain for reference. The FRP-PCE and the FRP-PCMOxa reduced the yield stress to essentially the same value of $\sigma_0 \approx 10$ Pa within the uncertainty of the measurement. Consequently, for comparable side-chain lengths and identical synthesis parameters, the yield stress reduction is equivalent for PCMOxa and PCE. Moreover, the yield stress reduction of the FRP combs is comparable to that of the commercial product BASF VP14.1. In addition, the FRP-PCMOxa achieved a five-fold greater yield stress reduction than a grafting-onto comb at the identical dosage of 0.1 wt.%. Although the exact cause of this observation remains unclear, we propose that the higher dispersity and the lower molecular weight of the FRP-PCMOxa leads to a more homogeneous polymer distribution within the cement suspension.

In summary, the macromonomer route enables a simple, up-scalable synthesis of PCMOxa comb polymers that not only reduces the yield stress more effectively than the grafting-onto polymers but also offers practical advantages for industrial applications. This increases the potential of PCMOxa for industrial applications. PCMOxa might be able to address some of the short comings of PCE, especially the functionality loss in the presence of clay, e.g. bentonite. Clays are commonly found in the aggregates used as the fillers in concrete. Moreover, calcined clays are often used as cement replacements in concrete production to reduce the carbon footprint [6]. Therefore, high-range water reducers or superplasticizers are needed which provide control over clay containing mixtures. However, PCE often loses its functionality in the presence of clay due to the formation of intercalations structures of the PEO sidechains in between the aluminosilicate sheets [182]. Comb polymers with alternative sidechains, like the here presented PCMOxa combs, could potentially prevent intercalation and thus be a suitable alternative to PCE. To further investigate the suitability of PCMOxa for practical applications, a holistic assessment of its impact on the cement paste over the whole time frame of hydration is needed. The compressive strength of the hardened paste under the influence of PCMOxa is next to the reduction of the initial fluidity the second criterion to determine its suitability for application. Ideally, the final compressive strength should either be unchanged or increased in the presence of PCMOxa. In addition, slump retention, meaning the ability to maintain the initial

yield stress reduction over time, needs to be investigated. Furthermore, the effect of PCMOxa on the cement hydration, especially on the formation of hydrates at early hydration stages could be investigated in future studies. It should be noted, that the observations on the yield stress reduction of FRP-PCMOxa are based on a single set of structural parameters. To validate these observations, a comprehensive study of a series of polymers with systematically varied synthesis parameters would be needed. In addition, the analytical determination of the molecular weight and the dispersity needs to be improved to get further insight into the difference in the yield stress reduction efficiency of the grafting-onto and the grafting-through combs, for example by using Static Light Scattering, either with a multiangle light scattering (MALS) detector in SEC or as an independent characterization method. Diffusion-ordered spectroscopy (DOSY) is not a suitable method, as a study on branched homopolymer pom-pom structures showed that the molecular weight is underestimated to the same extent as in SEC [180], thus offering no improvement over conventional chromatographic methods for branched polymer structures.

5 Rheo-FTIR – Development and Application of a Versatile Tool to Investigate Chemo-Rheological Relationships

Rheometry is a versatile technique which can be used to characterize the flow behavior for a large variety of applications such as the processing of polymer melts, the flowability of cement pastes or the skin feel of cosmetic products. In the case of e.g. rubber vulcanization, time-dependent changes in the rheological behavior can be observed. To identify the microscopic origins of these rheological changes, different combinations of rheometers with additional analytical methods have been developed. These methods involve dielectric spectroscopy (DES) [11–14], small angle x-ray scattering (SAXS) [15, 16] and nuclear magnetic resonance (NMR) [17–19] amongst others. These types of experimental set-ups have been labelled as '*in-situ'* [183], 'hyphenated' [184] or 'combined' [20] techniques in previous works. These labels are not clearly defined and are therefore often used synonymously. In this work, we call a measurement '*in-situ*' if a single analytical technique is used to follow a chemical reaction in real-time. Rheological techniques which combine rheology with an additional measurement device e.g. spectroscopy, are named 'combined' techniques.

This work focuses on the further development of a combination of rheometry with FTIR spectroscopy, the so-called Rheo-FTIR. In general, FTIR is a method to obtain information about the chemical composition, molecular conformation or crystallinity of materials [142, 138, 185]. In combination with rheometry, it can be used to characterize a wide range of materials, e.g. bring new insights to hydrogel kinetics [20] or shear-induced effects like the denaturation of proteins in silk [186].

A variety of mechano-FTIR combined techniques have been realized in the last decades [187–193]. All of these combinations impose a uniaxial deformation onto the sample, either in elongation or compression. The spectral information is then obtained via transmission FTIR of the sample under deformation. A set-up incorporating ATR via an IRE was realized by Nishikawa et al. [193–196]. Their measurement set-up is also limited to uniaxial deformation. The combination of a rotational rheometer with ATR FTIR has been commercialized by Thermosphere Scientific under the trade name Rhenium. It is available as a modular addition to a stress-controlled Hake-Mars which can be connected to a FTIR spectrometer with side port, e.g. the Thermo Scientific Nicolet iS10. This module has been used to study, e.g. the curing of polyurethane resins [197] or shear-induced denaturation and aggregation of silk proteins [186, 198].

In this working group, we have developed an alternative Rheo-FTIIR set-up as a modular addition to a strain-controlled TA Instruments ARES G2 [20, 21]. Strain-controlled rheometers are equipped with two motors, a lower one to apply sample deformation and the upper to acts as the

transducer. Therefore, the deformation does not interfere with the torque measurement. Thus, induction times are reduced, and the measurement quality is improved. Consequently, strain-controlled rheometers are preferred for FT-Rheology and LAOS investigations.

5.1 Starting Point: The Initial Rheo-FTIR set-up

The Rheo-FTIR set-up used in this work was initially developed by Radebe et al. [20, 21] and is displayed in Figure 56. The set-up combines a high-end strain-controlled TA Instruments ARES G2 and a Bruker Matrix-M FTIR spectrometer. The ARES G2 is equipped with an Advanced Peltier System (APS) for temperature control. The Matrix-M, which features a mid-IR source (4000 – 400 cm^{-1}) and an external MCT detector of the type Bruker LN MCT D316, is optimized for industrial use. Therefore, it is characterized by fast signal averaging, high performance, permanently aligned optics, very compact size (29 × 31 × 24 cm), a relatively low mass (12 kg) and a high insensitivity against mechanical vibrations. The integrated rapid scan option allows scanning velocities of 160 kHz (corresponding to a physical mirror speed of $V' = 5$ cm s^{-1}, equivalent to 15.3 scans/s) (for an explanation of the scanning velocity see chapter 2.5.1, p. 38).

As displayed in Figure 56, the modulated IR-beam is emitted by the Matrix cube. The first off-axis parabolic mirror M1 focuses the beam onto the trapezoid shaped silicon geometry, which acts both as an IRE and the upper plate of a plate-plate geometry. Silicon (Si) was used as ATR crystal material due to its high refractive index, chemical and mechanical robustness, durability and its suitability for precise shaping [20, 138]. Si provides two spectral windows at 8 000 - 1 350 cm^{-1} and 500 – 33 cm^{-1}. Strong phonon absorption bands at 1 350 – 500 cm^{-1} obscure the fingerprint region [143]. After reflection on the surface-sample interface, the light is guided by two additional off-axis parabolic mirrors to the LN2 cooled MCT. The integrated Dewar can contain up to 0.3 L of LN2 corresponding to 6 hrs of maximum measurement time. Compared to standard thermal pyroelectric detectors, i.e. DTGS, the MCT provides up to 10 times higher sensitivity [199]. However, higher sensitivity comes at the cost of spectral range. A typical DTGS detector covers the whole mid-IR range (12 500 – 350 cm^{-1}) while MCT detectors have a cut-off at 800 to 500 cm^{-1}, depending on their bandwidth [142, 200]. The here used Bruker LN MCT D316 covers both the NIR and the MIR region with a spectral range of 12 000 – 600 cm^{-1}.

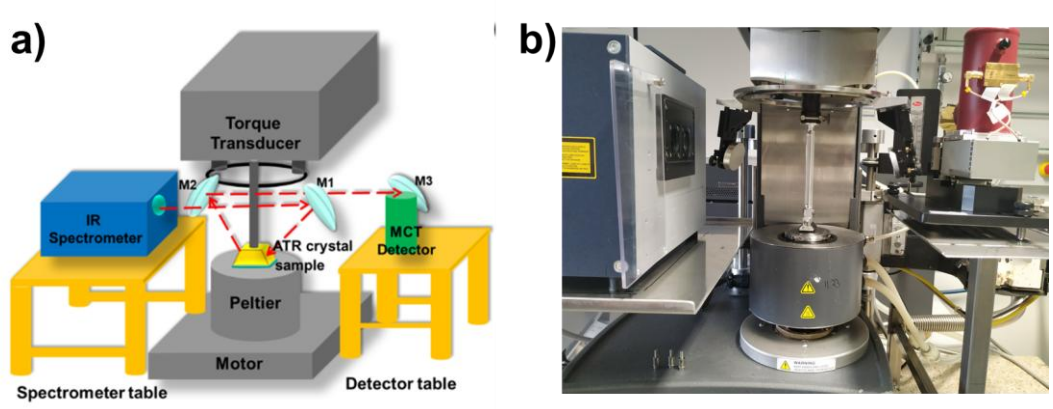

Figure 56: a) Schematic representation of the initial Rheo-FTIR set-up including beam path (red line) b) Picture of the Rheo-FTIR set-up after the initial development in 2021. Both pictures reproduced from [20].

5.2 Modifications to the Rheo-FTIR

With the initial set-up, investigations on hydrogel kinetics were conducted as a proof-of-concept [20]. This confirmed the fundamental working mechanism of the Rheo-FTIR set-up. However, the signal-to-noise ratio (SNR) (see chapter 5.3, p. 97) obtained with this initial set-up was not fully maximized yet. Moreover, the handling was difficult as the spectrometer and the detector were not fixed in place. Therefore, the beam path had to be aligned manually every time the modular FTIR-addition was set-up, resulting in set-up times of up to one hour and compromising the reproducibility of measurement quality. Therefore, several modifications were implemented to the Rheo-FTIR to improve both the SNR and the ease of handling. This chapter summarizes these modifications. The subsequent chapter (chapter 5.3, p. 97) highlights the resulting sensitivity improvements achieved by these modifications. A schematic illustration of the modified set-up is displayed in Figure 57, including the labels given to the individual parts.

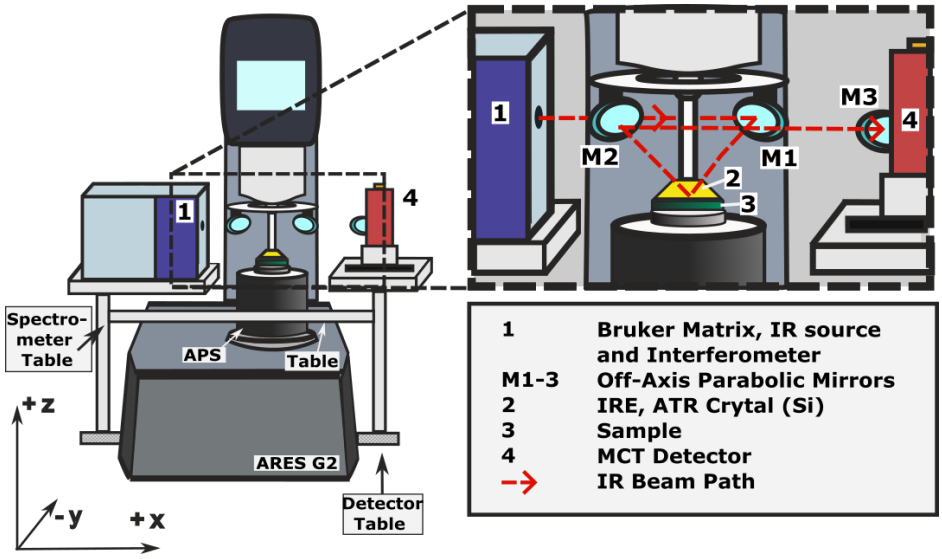

Figure 57: Schematic representation of the modified Rheo-FTIR set-up including labels of the different components.

Reversed beam path. The beam path was reversed from the initial set-up as illustrated in Figure 58. The permanently mounted oven of the ARES G2 restricts the space on the detector side. Reversing the beam path moved the detector position further into the + y-direction, providing additional space to move the detector and introduce adjustment mechanisms.

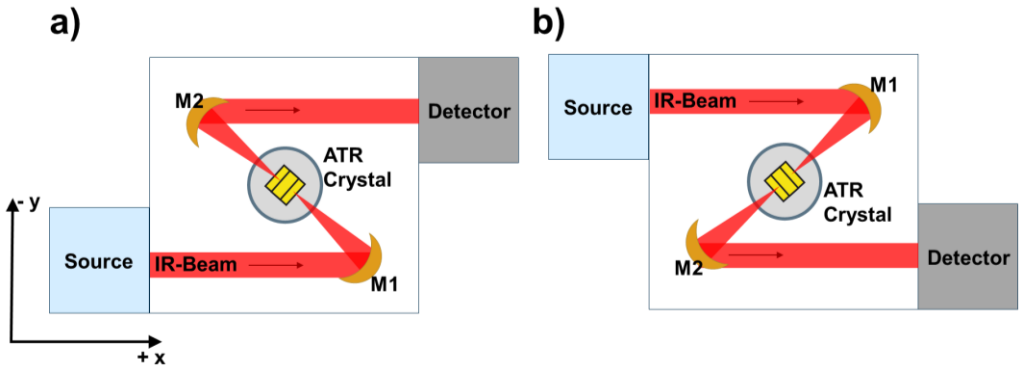

Figure 58: Top view on the beam path. a)The illustration shows the beam path of the initial set-up as published by Radebe et al. [20]. b) The illustration side shows the reversed beam path, which moves the detector further to the front and thus provides additional space.

Additional options for lower geometry. The ATR crystal is implemented to the Rheo-FTIR as the upper geometry. Since the beam path has to be adjusted precisely and is thus fixed in its z - position, the upper geometry has to be fixed in its z - position as well. Technically, this can be easily realized since the rheometer can adjust and hold the geometry position with an uncertainty of 1 µm. However, this fixes the gap height to a pre-set height of 1 mm. This can be a disadvantage in the characterization of soft materials, like hydrogels or elastomers which usually require larger gap heights. Therefore, the lower geometry was redesigned to a set of plates with a cylindric elevation in the middle of a diameter of 25 mm. The standard plate, which was used for the beam path alignment, has an elevation of 10 mm plus a 1 mm gap. To measure samples that require a bigger gap height, the lower plate can be exchanged to plates of smaller elevations, resulting in a larger gap. This concept is illustrated in Figure 59 a). In addition, grooved lower plates are available for materials which are prone to slip, e.g. rubber materials as displayed in Figure 59 b).

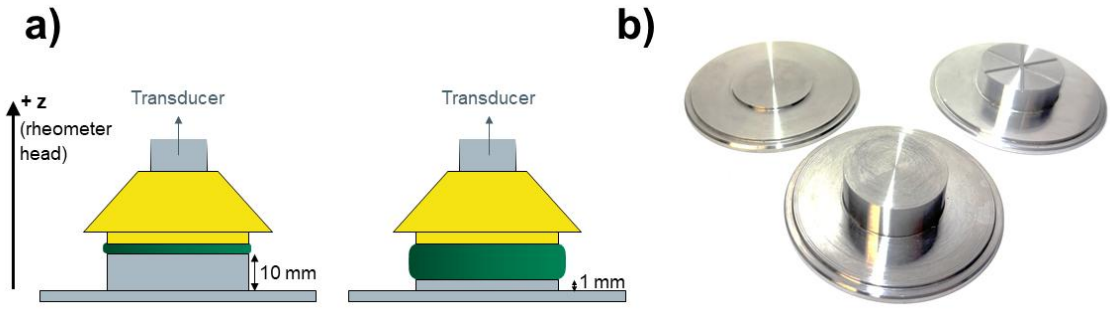

Figure 59: a) Schematic side view of the IRE (yellow), sample (green) with two versions of the exchangeable lower plates. For standard measurements at gap heights of 1 mm, the lower plate with a 10 mm elevation is used. If larger gaps are required, the lower plate can be exchanged to the 1 mm elevation. b) Picture of the available lower plates with elevations of 1 mm, 10 mm and a grooved plate with an 80 mm elevation. An additional picture of the plates in side view is given in the SI (Figure 90, p. 167).

MCT detector. The Dewar size of the MCT detector limits its run time. In the initial set-up, a Dewar volume of 0.3 L corresponding to a maximum run time of 6 h was used. In practice, the maximum run time cannot always be fully utilized. It can be shortened by elevated ambient temperatures in the laboratory (> 25 °C in summer). Moreover, measurements were observed to become unstable at low fill levels, typically within the last hour of the maximum run time. Therefore, a second MCT detector of the same detectivity but with an increased Dewar size was acquired. The new MCT detector has a Dewar volume of 0.5 L, corresponding to a maximum run time of 8 h.

Redesign of table. As shown in Figure 57 (p. 91), the complete assembly supporting both the spectrometer and the detector is referred to as *table*. The table is constructed from the *spectrometer table* on the left and the *detector table* on the right, which are connected by a horizontal crossbar. In the redesign of the table, this crossbar was added to reduce flexing and mechanical vibration between the two units. In addition, the table's fixations were reworked. The initial locking screws were exchanged to precision fastenings. The table positions were further refined by exchanging the rheometer transport handles to longer steel rods equipped with mechanical stops at the optimal positions. These rods and the upgraded fastenings are also shown in Figure 92 (SI, p. 168).

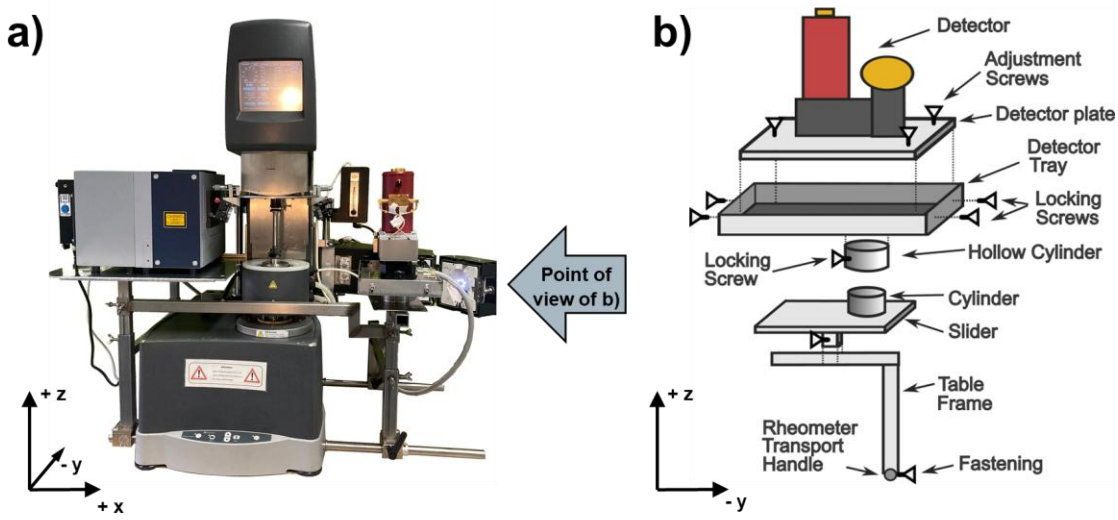

Figure 60: a) Photo of the set-up with the modified table including the horizontal crossbar, the precision fastenings, the steel rods with the positioning stop and the modified spectrometer table. b) Exploded side view of the modified detector table. The detector sits inside a tray, where it can be positioned and fixed via four screws located on the sides of the tray. The tray is mounted to the slider via a 360° joint made from a cylinder shell and a full cylinder. The slider sits on the table frame and defines the y-position.

Additionally, the *detector table* was fully redesigned. In the initial set-up, the detector was placed on a flat table top (see SI, Figure 92, p. 168). Its position in the x-y-plane was not predefined and had to be adjusted manually. Therefore, the measurement quality was dependent on the experience of the user. In the redesigned table, the detector is placed inside a tray, in which it can be positioned precisely and fixed with four screws located on the sides of the tray. A

cylinder shell is attached to the bottom of this tray. A second cylinder is mounted to a flat metal plate, referred to as *slider*. The cylinder shell fits over the full cylinder, creating a joint which allows 360° rotation in the x-y-plane. After alignment, a locking screw in the cylinder shell is used to secure the rotational position. The slider rests on the table frame and can be moved to adjust the position in the y-axis. Locking screws are used to fix the position of the slider on the table frame.

Redesign of ring system holding the mirrors. The mirrors are fixed to *mirror mounts* which are attached to the outside of a *ring system* consisting of an *inner ring* and an *outer ring* as shown in Figure 61. The inner ring is fixed to the rheometer head. The outer ring sits freely on the inner ring which allows 360° rotation in the x-y-plane (compare Figure 62, p. 95). The position of the outer ring can be fixed with a screw. In the initial set-up, the mirrors were mounted to long mirror mounts attached to a rather slim ring system (b_{in} = 18 mm, b_{out} = 58 mm). This initial mirror ring is displayed in Figure 56 (p. 89) and Figure 61 (p. 94). Due to the low structural rigidity of the thin inner ring, the mechanical stresses applied during mounting were sufficient to cause noticeable deformation out of its planar design which compromised its functionality. To address this issue, the ring system was redesigned using rings with greater material thickness (b_{in} = 25 mm, b_{out} = 45 mm) to prevent deformation. The redesigned ring system is displayed in Figure 62 (p. 95).

Additionally, the original mirror mounts were exchanged to shorter mounts. This modification brings the mirrors closer to the center of the ring, reducing the mirror-crystal distance from 18 cm to 15 cm. A distance of approximately 15 cm corresponds to the focal length of the used off-axis parabolic mirrors and therefore improves the signal intensity. Both the initial and the revised mirror mount are displayed in Figure 61.

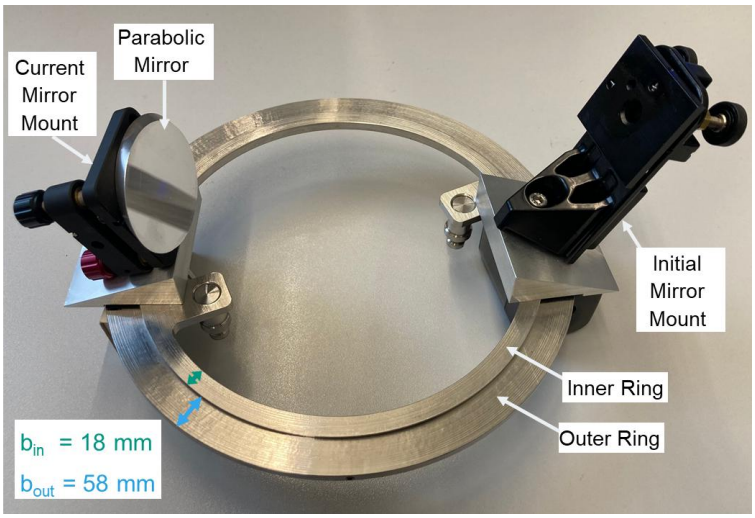

Figure 61: Upside-down picture of the ring system used in the initial set-up equipped with two different mirror mounts: The longer mirror mount on the right side was used in the initial set-up (compare Figure 56, p. 89), while the shorter mirror mount on the left side is used in the current set-up. Exchanging the mirror mounts during the modification process moved the mirrors closer to the center of the ring and consequently to the mirror-crystal distance to the focal length of the off-axis parabolic mirrors.

In addition, a micrometer screw was added to the attachment of the mirror mount as shown in Figure 62 and in Figure 91 (SI, p. 167). This screw allows precise movement of the mirror along the axis perpendicular to the ring system. Thus, it allows the fine adjustment of the mirror-center distance and consequently the mirror-crystal distance. This feature is essential for accurately positioning the focal point to the desired location.

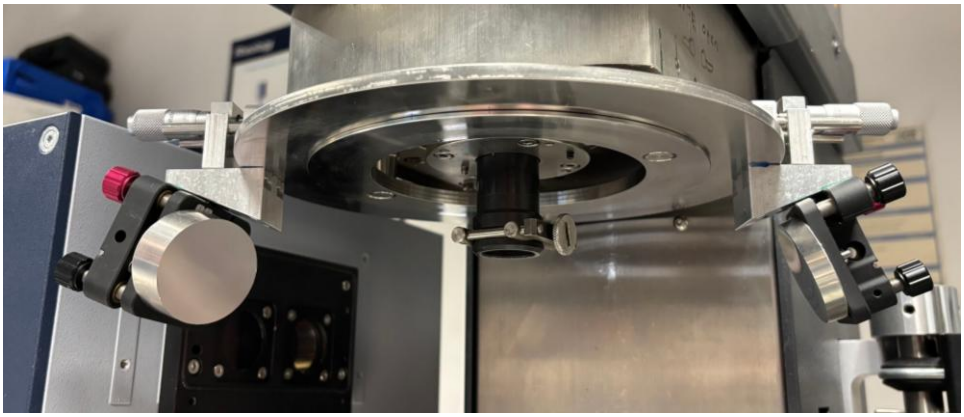

Figure 62: Redesigned ring system featuring increased material thickness and a micrometer screw integrated to the attachment of the mirror mounts. The micrometer screw allows fine adjustment of the mirror position along the axis perpendicular to the ring plane, enabling precise adjustment of the focal length.

Upper Geometry. The reduction in the length of the mirror mounts also required a reduction of the length of the upper geometry. In the initial set-up, the geometry had a length of 16.5 cm. As the length of the mirror mounts was reduced by 3 cm, the length of the upper geometry could be reduced by a similar amount. The current geometry now has a length of L = 12.8 cm, bringing it closer to the dimensions of commercial geometries, e.g. 25 mm PP TA Instruments L ≈ 9 cm. Moreover, the shaft of the upper geometry was redesigned from a cross-hatched cross-section to a hollow cylindrical structure. This redesigned shaft allows the integration of a temperature sensor which is advantageous for temperature sensitive measurements. Moreover, the material of the geometry shaft and clamp was changed. The clamp holding the crystal is now made from titanium, while the shaft has been changed to stainless steel. Stainless steel and titanium have a lower thermal expansion coefficient and a reduced torsion compliance compared to the aluminum used in the initial design, thus improving mechanical stability and reducing thermal expansion.

Table 9: Comparison of the thermal expansion coefficient and the G-Modulus of the materials used for the upper geometry [201–203].

	Aluminum, (old shaft)	**Stainless Steel,** (new shaft)	**Titanium,** (clamp)
Thermal expansion coefficient	$23 \cdot 10^{-6}$ K^{-1}	$12 \cdot 10^{-6}$ K^{-1}	$8.6 \cdot 10^{-6}$ K^{-1}
G-Modulus	25 GPa	62 - 87 GPa	43 GPa

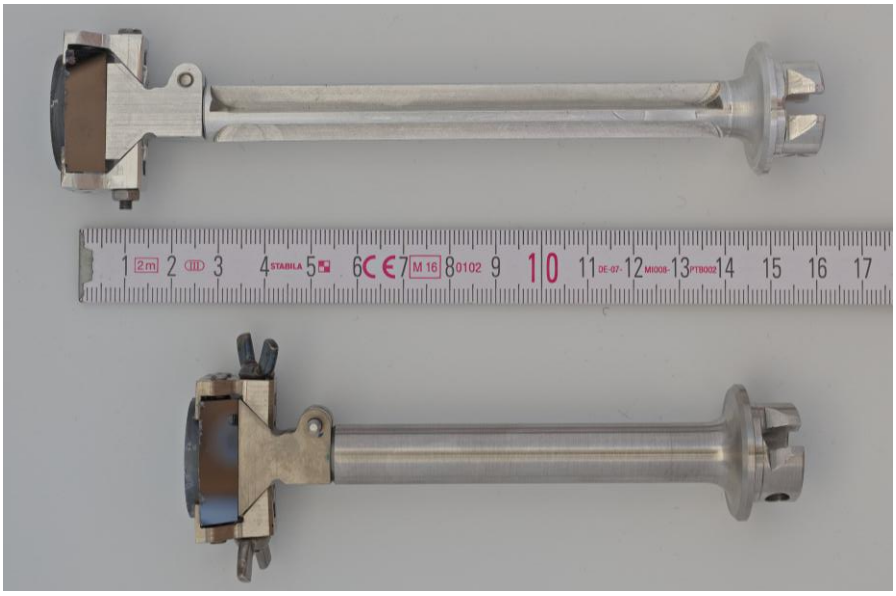

Figure 63: Picture of initial aluminum (top) and current stainless steel (bottom) upper geometry showing the reduction in length and the updated shaft design.

Heat cover. In parallel to the modifications reported in this work, Xu et al. designed a heat cover to improve the heating efficiency of the upper geometry [204]. This allows measurements at temperatures up to the APS limit of T_{max} = 150 °C. This modification is mentioned here for completeness, as the heat cover was used in some measurements discussed in the following chapters.

IR Parameter Optimization. The FITR parameters were optimized following the previous works of Beskers [199] and Radebe [21]. The Bruker Matrix-M is equipped with a rapid scan option. This allows scanning velocities of up to 160 kHz (V' = 5 cm s^{-1}). A thorough comparison of the different scanning velocities revealed the highest $S/N \cdot n^{-1/2}$ for 20 kHz which is equivalent to a scanning speed of 2.3 scans per seconds (see SI, Figure 93, p. 168). These findings are in agreement with literature [142] and the manufacturer recommendations. Therefore, a scanning velocity of 20 kHz is recommended for standard measurements. A higher scanning velocity can be considered when the experiment allows a sensitivity trade-off for reduced measurement time. The used measurement parameters for standard FTIR measurements are summarized in Table 27 (SI, p. 160).

5.3 Improvements in FTIR Sensitivity

The set-up modifications were implemented to increase the measurement quality of the FTIR spectra obtained by the Rheo-FTIR. Many of the modifications on the individual components were performed in parallel. Consequently, the effect of the individual modifications on the measurement quality cannot be examined independently. Moreover, all changes focused on improving the beam path alignment. The effect of an improved alignment on the spectral quality is discussed in the following. A common measure of spectral quality is the signal-to-noise ratio (SNR). The SNR is defined by equation (5.1):

$$\mathrm{SNR} = \frac{Signal}{Noise} \tag{5.1}$$

The SNR is dependent on several measurement parameters, i.e. the number of scans n, the spectral resolution $\Delta\tilde{\nu}$, the specific detectivity D^* and the optical throughput Θ [138, 142].

$$\mathrm{SNR} \sim n^{1/2} \cdot \Delta\tilde{\nu} \cdot D^* \cdot \Theta \tag{5.2}$$

The SNR can be improved by increasing the number of scans (SNR ~ $n^{1/2}$ for stochastic noise) [142], which simultaneously increases the measurement time. Therefore, the time-independent signal-to-noise ratio (SNR · $t^{-1/2}$, t in seconds) is equal to SNR ~ $n^{1/2}$ if the scanning velocity is kept constant. Low resolution (> 8 cm^{-1} for liquids) increases the SNR because shortening the optical path difference restricts the Fourier transform to the region near the intense center burst, while excluding the noise-intense wings of the interferogram [138]. Both the number of scans and the resolution have to be chosen based on the experiment performed. If not stated otherwise, n = 64 and $\Delta\tilde{\nu}$ = 4 cm^{-1} were chosen in this work. A complete overview of the used FTIR parameters is given in Table 27 (SI, p. 160). The detector sensitivity D^* is a figure of merit to characterize the performance of photodetectors. It is specific to the detector used. For the given MCT detector, $D^* > 2 \cdot 10^{10}$ cm $Hz^{1/2}W^{-1}$. The optical throughput Θ characterizes the light transfer efficiency from the source to the detector, which increases the SNR.

The modifications on the Rheo-FTIR (see chapter 5.2, p. 91), especially on the ring system and the detector table, allowed more precise positioning of all components. Therefore, the total alignment of the beam path could be readjusted more precisely which increased the intensity obtained at the detector. This intensity is given by the Bruker Software OPUS in analog-digital-converter (ADC) counts. In OPUS, the signal intensity is displayed for a 16 - bit ADC from -32 768 to +32 768 bits. However, the actual conversion in the Matrix - M is performed with a 24 - bit ADC. In the initial set-up of Radebe et al., ADC counts of 8 000 - 16 000 a.u. were obtained using a preamplification of a factor ten [21]. The modifications and the resulting substantially improved alignment produce reproducible ADC counts of approximately 25 000 a.u. without any preamplification of the signal. This is close to the saturation of the MCT detector at +/-28 000 a.u.. The ADC count reflects the amount of light reaching the detector and therefore is an indirect measure for the optical throughput of the system Θ. It has to be noted that the relationship is only qualitative. However, the substantial increase in the ADC

count indicates that the improved alignment of the beam path leads to a significant increase in the optical throughput of the system.

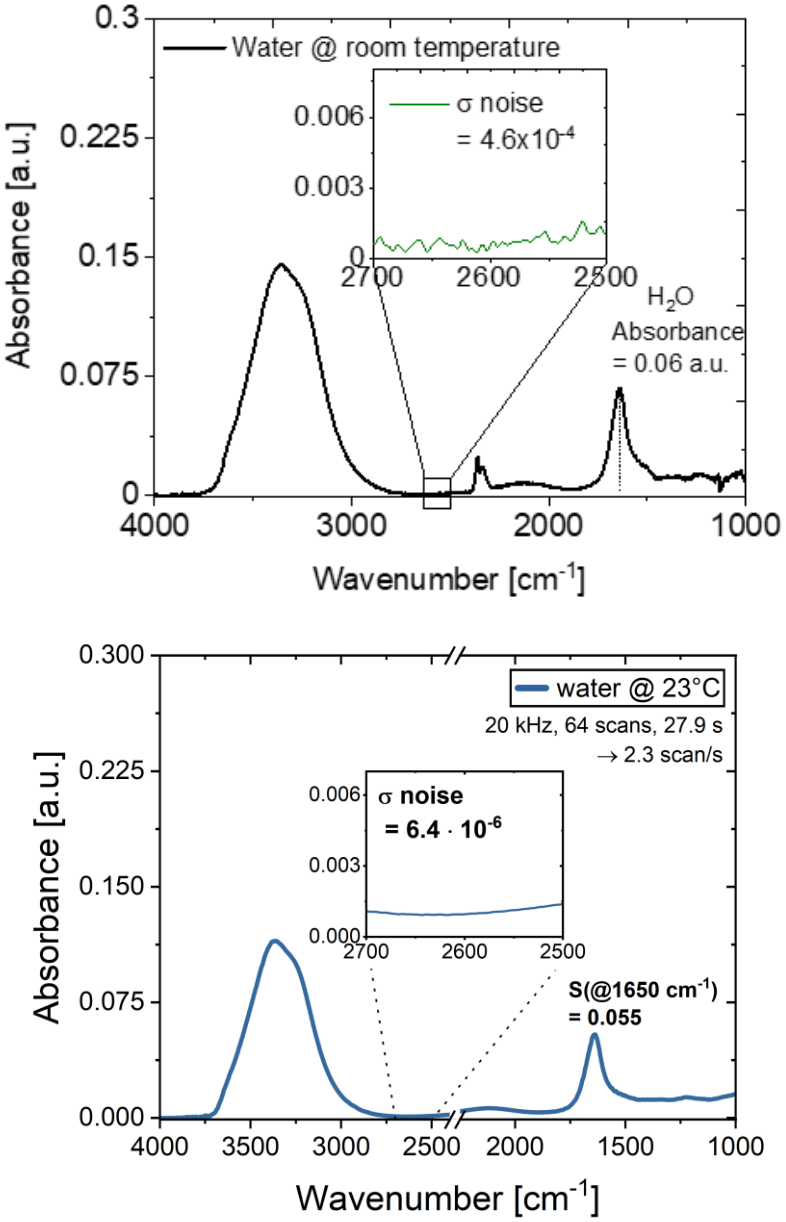

Figure 64: Spectrum of water obtained a) with the initial set-up which was the state of the art in 2021, reproduced from [21] and b) after finalizing the modifications.

As stated in equation 5.2, the optical throughput is proportional to the SNR. Since the modifications increased the optical throughput, they consequently substantially increased the SNR. Figure 64 shows two spectra of water obtained before and after the implementation of the modifications on the set-up. For the calculation of the SNR, the signal intensity of the H_2O-scissoring

vibration at 1640 cm^{-1} is divided by the standard deviation of the noise in the wavenumber region of 2700 cm^{-1} to 2500 cm^{-1}. For the spectrum obtained with the modified set-up, a centered moving average baseline (window size of 15 points, corresponding to $\Delta\tilde{\nu}$ = 30 cm^{-1}) was fitted over the noise wavenumber region and subtracted from the spectrum to eliminate the underlying curvature (compare SI, Figure 94, p. 169). The obtained SNR, $SNR \cdot t^{-1/2}$ and $SNR \cdot t^{-1/2}$ values are summarized in Table 2. For the initial set-up, the values are given based on the spectrum shown in Figure 64 [20, 21]. It should be noted that the values given by Radebe et al. [21] of a scan speed of 40 kHz (equivalent to 4.4 scans/s in forward-backward mode), a number of scans of n = 64 and a measurement time of t = 30s are contradictory. For the calculation of the SNR values, it was assumed that the spectrum was obtained with a scan speed of 40 kHz for a scan time of 30 s (corresponding to n = 132). The SNR for the modified set-up was averaged from 6 independent spectra of water obtained with a scanning velocity of 20 kHz (2.3 scans/s in forward-backward mode), s = 64 and t = 27.9 s. The average and the standard deviation are given in Table 10. The comparison of the $SNR \cdot t^{-1/2}$ before and after the modifications highlights the substantial SNR improvement by a factor of 63, saving approximately a factor 4 000 in measurement time.

Table 10: SNR improvement at room temperature. The spectrum obtained with the initial set-up was recorded for 30 s with a scan speed of 40 kHz and a number of scans n = 132, while the spectrum obtained with the modified set-up was recorded with for 27.9 s with a scan speed of 20 kHz (n = 64).

	Initial set-up 2021	**Modified set-up 2026**	**Improvement factor**	**Time saving factor**
ADC count	8 000-16 000 a.u. At 10x preamplification	25 000 a.u. Without amplification	16 - 32	-
SNR	130	8 200 ± 820	63	-
$SNR \cdot n^{-1/2}$	11.3	1 025	91	-
$SNR \cdot t^{-1/2}$	24 $s^{-1/2}$	1 520 ± 170 $s^{-1/2}$	63	4 000

The increase in sensitivity expands the range of accessible experimental conditions to elevated temperatures (25 - 150 °C). Measurements at elevated temperatures exhibit a considerable loss in sensitivity as shown on two spectra of LDPE recorded at 130 °C with the initial and the modified set-up in Figure 65 [205]. The main reason for the loss of sensitivity is the increase of thermal noise due to black body irradiation of the sample and the set-up components with increased temperature within the detector's view [142]. For the initial set-up with a rather low sensitivity at room temperature, experiments at elevated temperatures resulted in poor spectra and a considerable loss of spectral information, meaning that both sensitivity and selectivity were compromised (see Figure 65).

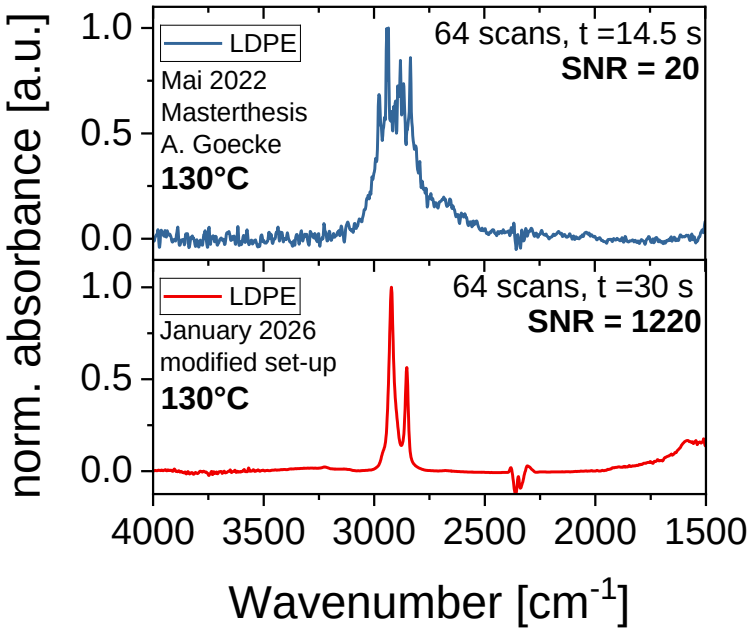

Figure 65: Normalized LDPE spectra in melt state obtained with the initial set-up (blue) [205] and the modified set-up (red). The modifications led to a substantial SNR improvement of a factor 61. It should be noted that the spectra were obtained with different scan speeds (40 kHz for the initial and 20 kHz for the modified set-up), thus the same number of scans results in different measurement times.

To compare the sensitivity improvement at elevated temperatures by the implemented modifications, the SNR was determined in the not-normalized spectra with the intensity of the asymmetric C-H -stretch vibration at 2921 cm^{-1} and the standard deviation in the wavenumber range of 3500 – 3300 cm^{-1} (compare SI, Figure 95 - Figure 97, p. 169 - 170). For the LDPE spectrum obtained with the initial set-up, the peak at 3100 – 2200 cm^{-1} was fitted with two Gaussian functions and a maximum of 0.61 a.u. was determined for the Gaussian peak at 2921 cm^{-1} (compare SI, Figure 97 and Table 30, p. 170). For the spectrum obtained with the modified set-up, a centered moving average baseline (window size of 25 points, corresponding to $\Delta\tilde{\nu}$ = 50 cm^{-1}) was fitted over the noise wavenumber region and subtracted from the spectrum to remove the underlying curvature prior to the calculation of the standard deviation (compare SI, Figure 96, p. 170).

Table 11: SNR values obtained for LDPE in the melt state at 130 °C with the initial set-up in 2022 and the modified set-up in 2026. It should be noted that the spectra were obtained with different scan speeds (40 kHz for the initial and 20 kHz for the modified set-up), thus the same number of scans results in different measurement times. As the SNR values are based on single measurements, no uncertainties are given in the table. The uncertainty is assumed to be in the range of 10 % consistent with the SNR values determined at room temperature.

	Initial set-up 2022	**Modified set-up 2026**	**Improvement factor**
SNR	20	1220	61
SNR · $n^{-1/2}$	2.5	152.5	61
SNR · $t^{-1/2}$	5.3 $s^{-1/2}$	223 $s^{-1/2}$	42

The modifications led to a substantial improvement of the SNR at 130 °C by a factor 61, consistent with the SNR increase obtained for the room temperature measurements. However, the improvement in $SNR \cdot t^{-1/2}$ is only a factor of 42 due to the differences in measurement times resulting from the different applied scan speeds. Anika Goecke obtained the spectrum with a scanning velocity of 40 kHz (4.4 scans/s) [205], whereas a scanning velocity of 20 kHz (2.3 scans/s) was chosen in this work. Interestingly, the sensitivity loss due to thermal noise is substantial: Increasing the temperature from 25 °C to 130 °C leads to a reduction in SNR of approximately 85 % for both the initial set-up and the modified set-up.

In addition to the sensitivity improvement, the modifications on the Rheo-FTIR set-up improved the handling. The redesign of several components reduced the set-up time by a factor of four from about 1 h to 15 min. The main reduction of set-up time was achieved by the simplification of the set-up design and the fixation of the detector position, which eliminated the manual alignment of the beam path.

5.4 Beam-Path Enclosure – Stabilization of Atmosphere to Reduce CO_2 and H_2O Artifacts

The IR beam probes not only the sample but also the atmosphere it passes through on its path from the spectrometer to the detector (length of beam path: L ≈ 95 cm). Atmospheric gases such as carbon dioxide (CO_2) and water vapor ($H_2O_{(g)}$) strongly absorb IR light. This is not problematic per se: If their concentration is constant between acquisition of background single channel scan (BGSC) and sample single channel scan (SSC), their absorption bands cancel out during the spectrum calculation and consequently do not appear in the final spectrum. However, fluctuations in atmospheric concentration can lead to residual bands of CO_2 and $H_2O_{(g)}$. CO_2 absorption produces an intense band at approximately 2400 – 2240 cm^{-1}, while the vibration-rotational lines of water vapor are less intense but cover two broad wavenumber ranges between 4000 – 3400 cm^{-1} and 2000 – 1500 cm^{-1}. These residual bands may appear both with a positive or a negative intensity, depending on whether the concentration increased (+) or decreased (-) relative to the background scan.

Providing a dry purge with a stable composition is critical for high spectral quality in a FTIR spectrometer. In commercial FTIR instruments, this challenge is addressed with enclosing the beam path and purging it with a gas to stabilize the atmosphere. For the Bruker Vertex 70, the instrument is purged with dry, pressurized air of defined and constant composition. In addition, commercial FTIR instruments are often equipped with drying agents to stabilize the atmosphere and to protect hygroscopic optical components, like KBr windows and beam splitters. As an alternative to gas purging, FTIR measurements can also be performed under vacuum to suppress artifacts. In principle, the absorption bands of water vapor and CO_2 can be mathematically removed in the processing of the spectra. Commercial software, like Bruker OPUS, includes built-in algorithms for real-time removal of residual atmospheric absorption bands during spectrum acquisition. However, the mathematical corrections can be incomplete or incorrect and can thus introduce artifacts, which is particularly problematic in quantitative analysis. For these reasons, the suppression of atmospheric bands through a gas purge is generally preferred over mathematical correction.

The modified Rheo-FTIR set-up presented in the previous chapters (p. 91) is not enclosed. Therefore, residual bands of CO_2 and $H_2O_{(g)}$ frequently occur, especially during longtime measurements (> 30 min) in which the laboratory atmospheric conditions in the laboratory may change due to, for example, people walking in the room or breathing near to the FTIR instrument. Figure 66 shows two spectra of high-oleic sunflower oil obtained with the unpurged, open Rheo-FTIR, each exhibiting residual CO_2 and $H_2O_{(g)}$ bands. These two spectra were recorded using BGSC and SSC obtained within two minutes of each other on the same measurement day within 30 min of each other. The comparison demonstrates that atmospheric fluctuations, while more likely during long-term measurements, can also affect individual single spectra, depending on the laboratory environment at the time of acquisition. A complete assignment of the peaks for high-oleic sunflower oil is provided in Figure 98 (SI, p. 171). The CO_2 band only covers a small wavenumber range that does not overlap with any absorption bands of the sample and therefore does not affect the information content of the spectrum. In contrast, the residual bands

of $H_2O_{(g)}$ overlap with several sample bands, even obscuring weaker absorptions as the C=C-vibration at 1653 cm^{-1}.

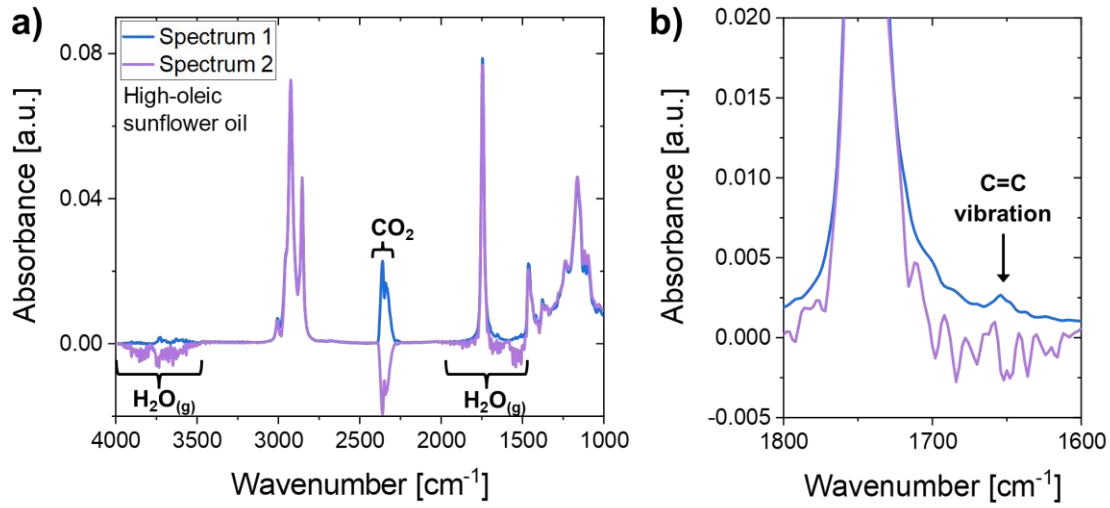

Figure 66: a) Two spectra of high-oleic sunflower oil obtained with the Rheo-FTIR set-up. A complete assignment of the sample peaks is given in Figure 98 (SI, p. 171). Fluctuations in the atmospheric composition during the acquisition of the BGSC and the SSC led to artifactual absorption bands of water vapor $H_2O_{(g)}$ in the two wavenumber ranges between 4000 – 3400 cm^{-1} and 2000 – 1500 cm^{-1}, and CO_2 at 2400 – 2240 cm^{-1}. b) Enlargement of the wavenumber region of 1800 – 1600 cm^{-1} in the two spectra of high-oleic sunflower oil. The H_2O absorption bands in spectrum 2 obscure the weak C=C-vibration band at 1653 cm^{-1}.

In order to eliminate the gas fluctuations in the Rheo-FTIR, a mechanical enclosure was constructed and tested. The development process underwent three successive design steps which are described and discussed in the following subchapters: the cubic enclosure, the beam path purge and the vent addition to the beam path purge.

5.4.1 First Design Approach: Full Enclosure

The first design step was the combination of two cubic metal enclosures connected with a flexible tube, as shown in Figure 67. As this design fully encloses the entire beam path as well as all optical components such as the mirrors and the MCT detector, it is referred to as full enclosure (FE). The FE design is the most straight-forward design of an enclosure with regards to the positioning within the set-up. Cubic enclosure 1 (CE1) covers the sample compartment which includes the off-axis parabolic mirrors M1 and M2 as well as the ATR geometry. CE1 is mounted to the top of the APS and fixed in its position with two screws. The fixation of CE1 allowed the precise positioning of the windows for the IR beam. Two gas inlets are implemented to flush CE1 with dry nitrogen gas (N_2), the main inlet at the back and APS inlet. The gas flow at the main inlet of a diameter of ¼" (6.3 mm) can be adjusted via valve V1. For V1, a needle valve without any flow meter was used. Therefore, the gas flow is given in valve opening (VO) from 0 % (closed) to 100 % (fully opened). The gas inlet at the APS is used to flush

the small gap (< 1 mm) between the lower geometry and the APS. In general, this gas flow is applied for all measurements involving the APS. Its main functions are the improvement of heat transfer between the APS and the lower geometry as well as the prevention of malfunctions caused by sample flowing or falling into the APS gap. In addition, this gas flow contributes to the overall flushing of the sample compartment CE1.

The sample compartment CE1 has been designed with two openings in the front which can be used to change the sample or to remove the upper geometry for cleaning. The sliding door was made from transparent acrylic glass to allow the user to monitor the sample during the measurement. Moreover, the whole metal front side can be opened to e.g. remove the upper geometry or to readjust the mirrors. The front is connected to the main box via hinges at the bottom so that the front functions as a hatch. A picture with the opened front hatch is given in Figure 99 (SI, p. 171).

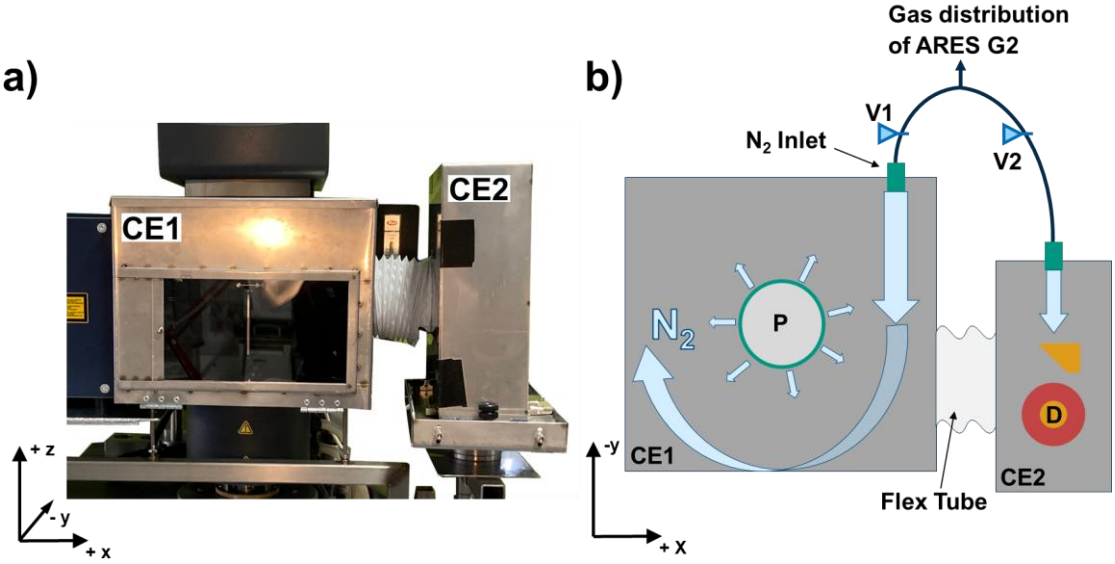

Figure 67: a) Photo of the Rheo-FTIR including the full enclosure (FE) consisting of the two cubic enclosures CE1 and CE2, connected by a flexible tube. b) Schematic illustration of the top view on the FE design. The enclosure can be purged via three N_2 inlets (turquoise), valve V1, valve V2 and the APS inlet surrounding the lower geometry P. V1 and V2 have diameters of ¼" (6.3 mm). The MCT is marked with the letter D for detector. The blue arrows indicate the envisioned N_2 gas flow.

Cubic enclosure 2 (CE2) covers the detector. It is installed by positioning it over the detector. Two metal pins on the detector plate define its position. CE2 has a separate N_2 inlet at the back which can be controlled by valve V2. The gas flow at V2 is controlled by a flow meter and can be varied between 0 L min^{-1} to 25 L min^{-1}. As CE2 is completely closed, it has to be removed to fill the MCT Dewar with LN2. Therefore, the total time of purging plus obtaining measurements is limited by the maximum run time of the MCT detector of approximately 8 h. In practice, the maximum run time cannot always be fully utilized. It can be shortened by elevated temperatures in the laboratory (> 25 °C in summer). Moreover, measurements were observed to

become unstable at low fill levels. Therefore, the purging time was deliberately limited to one hour in order to maximize the measurement window.

The functionality of the FE was tested by purging the system for one hour without any sample and investigating the observed fluctuations. In an attempt to create similar testing conditions, CE1 was completely opened and CE2 was removed for 30 min to achieve a "defined" initial unpurged state. The BGSC was taken in the unpurged state. Afterwards, the enclosure was closed, and the gas flow was started. V2 and the gap purge were set to 5 L min^{-1} and the opening of V1 was varied from 0 % to 100 % to find optimum conditions. The measurement was started immediately after opening the gas flow. A spectrum was recorded every 2 min. The results were compared to an analogue one hour measurement in open atmosphere without any enclosure.

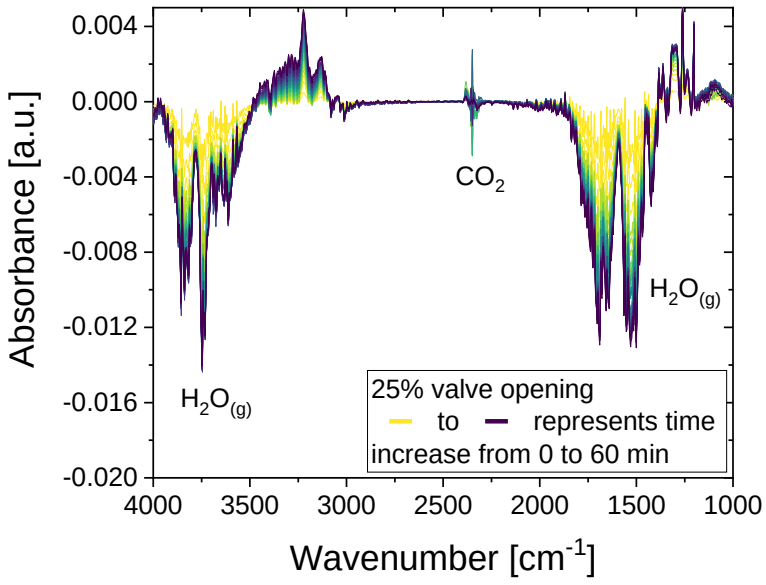

Figure 68: Baseline corrected spectra of atmospheric fluctuations within one hour of purging with a 25 % valve opening (VO) at V1. V2 and the APS inlet were set to 5 L min^{-1}. The color gradient from yellow (t = 0) to dark blue (t = 60 min) indicates the progression of measurement time. A spectrum was recorded every 2 min.

The baseline corrected spectra for a 25 % VO are given in Figure 68. Over the course of time, more water is removed from the beam path, resulting in an increase of the negative intensity of the rotational-vibrational bands of $H_2O_{(g)}$. For CO_2, no clear time-dependent behavior is visible in the spectra. The absolute changes in the spectra were not used for the evaluation for several reasons. First, the purge is not meant to remove all CO_2 and $H_2O_{(g)}$ but to ensure constant atmospheric conditions for the measurement, meaning that no fluctuations are observed. It is consistent with the design of the experiment, that at the beginning of the purge, the change in CO_2 and $H_2O_{(g)}$ is more pronounced than after the purge somewhat stabilizes the atmosphere. Second, it should be noted that the initial state of the measurement is not well defined. The enclosure was opened for 30 min before the experiment to achieve an initial state corresponding to atmospheric conditions. However, these conditions strongly depend on the laboratory atmospheric conditions, e.g. the air humidity or the strength of the room ventilation which both vary

in between measurement days. Therefore, the absolute changes of different measurements cannot be compared as they refer to different initial atmospheric conditions.

Therefore, for further evaluation of the spectra, the successive spectra of each measurement were subtracted from each other resulting in difference spectra that indicate the change of the atmosphere over time. The resulting difference spectra for the example of 25 %VO measurement are shown in Figure 69. The 60 min spectrum (darkest shade of blue) corresponds to the artifacts in a spectrum calculated from a BGSC and a SSC recorded within 2 minutes of each other after a N_2 purge of 60 min.

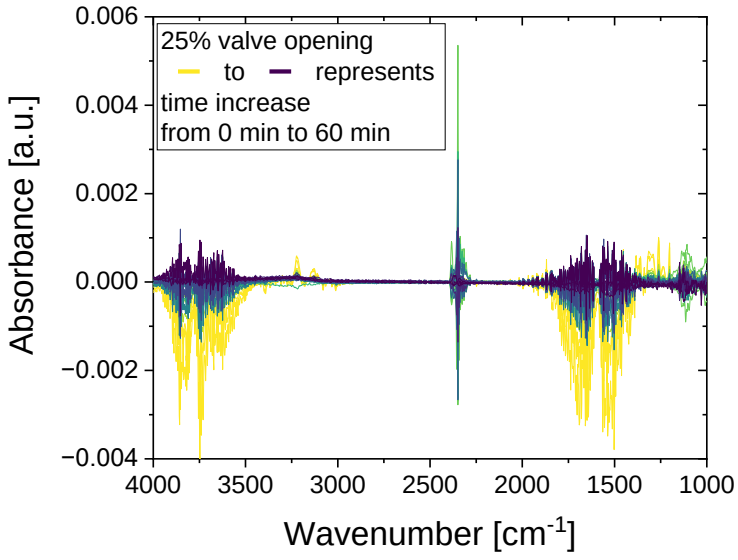

Figure 69: Result of subtraction of subsequent spectra. The absorption bands visible in this graph correspond to the artifacts which after the respective purging time for BGSC and SSC obtained within 2 min of each other. For example, the darkest blue line corresponds to the artifacts after 60 min of N_2 flushing for BGSC and SSC obtained within 2 min of each other.

No residual CO_2 and $H_2O_{(g)}$ bands should be visible in the subtracted spectra when the atmospheric composition is perfectly stable and no fluctuations occur. To simplify the comparison, the three relevant wavenumber regions corresponding to the absorption bands of CO_2 (2400 – 2240 cm^{-1}) and $H_2O_{(g)}$ (4000 – 3400 cm^{-1} and 2000 – 1350 cm^{-1}) were integrated. The line passing through the boundary points of the integration was used as the local baseline. The obtained absolute area was plotted against the time, as shown in Figure 70 for 25 % VO. The absolute area was chosen over the integral because it represents the artifact size. Large artifacts can obscure small peaks thereby complicating their analysis. In the diagram of the absolute area plotted against the measurement time in Figure 70, the trend already indicated by the subtracted spectra can be extracted more easily. The absolute area of the CO_2 fluctuations is not influenced by the N_2 purge. This indicates that the N_2 flow contains enough CO_2 to cause small fluctuations independently of the purge. However, the CO_2 band is limited to a wavenumber region where only a small number of bonds absorb IR light. Therefore, in the following subchapters, the CO_2 fluctuations are not further analyzed. The analysis is concentrated on the water bands, as they

overlap about 41 % of the available spectral range in the Rheo-FTIR (water vapor bands: 4000 – 3400 cm^{-1} and 2000 – 1350 cm^{-1}, spectral range of Rheo-FTIR: 4000 – 1000 cm^{-1}). In Figure 70, the two wavenumber regions of $H_2O_{(g)}$ show differences in their absolute area but exhibit the same trend. The concentration of water vapor changes rapidly in the beginning of the experiment, then levels off and fluctuates around a non-zero value. If a perfectly stable atmosphere would be reached, the integrated absolute area should level-off to zero indicating a constant atmospheric composition. The non-zero value however indicates that no stable atmosphere was reached within 60 min. However, it seems that a steady state of constant change is reached after 20 min meaning that the atmosphere changes at a low, but constant rate. This constant change rate means that after 60 min of N_2 purge, $H_2O_{(g)}$ artifacts are present if a BGSC and a SSC are taken within 2 min of each other. In a long-term measurement of a series of spectra, these artifacts could sum up over the course of time, obscuring more sample peaks. Therefore, if the optimum of a change rate of zero cannot be reached, this plateau value should be minimized to obtain $H_2O_{(g)}$ artifacts which are as small as possible.

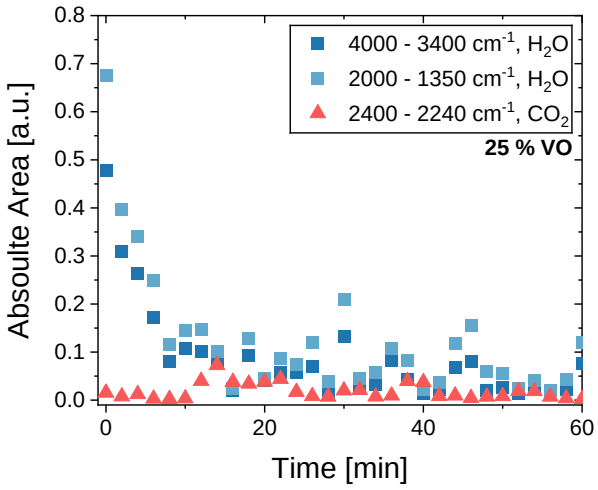

Figure 70: Absolute Area obtained by integration of three different wavenumber regions plotted against the measurement time. The chosen wavenumber regions correspond to the absorbance bands of CO_2 (2400 – 2240 cm^{-1}, red triangle) and $H_2O_{(g)}$ (4000 – 3400 cm^{-1} and 2000 – 1350 cm^{-1}, blue squares).

To compare the quality of different purge parameters, e.g. different flow rates due to different VO, the mean plateau value of the absolute area in the time range of 30 – 60 min and its standard deviation were determined for the $H_2O_{(g)}$ bands at 4000 – 34000 cm^{-1}. These bands are representative of the water vapor concentration change. The mean value represents the average area of the artifacts and is therefore a measure of merit of their size while the standard deviation represents the fluctuation around this value. A small mean value therefore corresponds to small $H_2O_{(g)}$ artifacts.

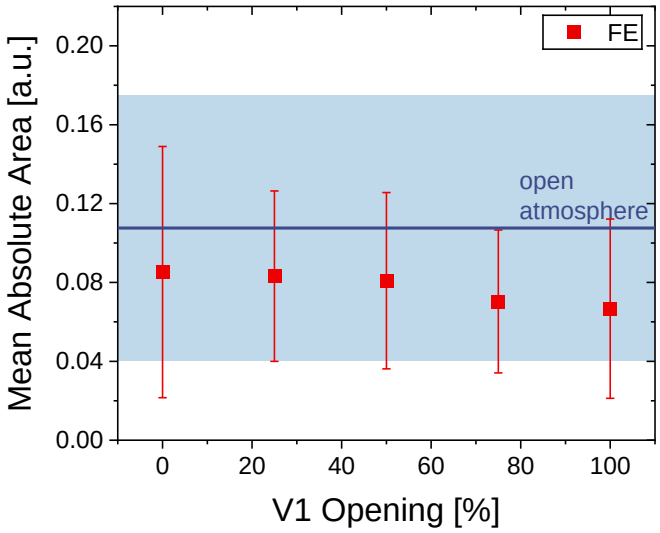

Figure 71: The mean plateau value of the absolute area within the time frame of 30 – 60 min and its standard deviation are plotted against the valve opening of V1 for the first design iteration full enclosure (FE), which was varied between 25 % and 100 % while V2 and the APS inlet were set to 5 L min^{-1}. The V1 opening of 0 % corresponds to a fully closed cubic enclosure without any N_2 flow with all N_2 inlets being closed. As a reference, the mean value of an open atmosphere (no enclosure) is given as a blue line. The light blue box represents its standard deviation.

To optimize the N_2 purge, the opening of V1 was varied between VO = 25 % and VO = 100 % while V2 and the APS inlet were set to 5 L min^{-1}. In addition, the closed cubic enclosure with three closed inlets and consequently no N_2 flow was tested. The results are labelled as V1 opening of 0 % in Figure 71. The obtained values are referenced to an open atmosphere measurement whose mean plateau value is indicated as a blue line in Figure 71. Its standard deviation is represented by the light blue box. This diagram shows that the Rheo-FTIR enclosure without any air flow already stabilizes the atmospheric composition in comparison to the open atmosphere. This is indicated by the reduced plateau value and standard deviation of VO 0 % relative to the results of the open atmosphere measurement. Within the uncertainty of the measurement, the size of the artifacts is not reduced by the N_2 purge in comparison to a closed enclosure without gas flow. However, the fluctuations are reduced by approximately 30 % due to the N_2 flow, indicating that the atmosphere within the enclosure is less fluctuating. However, this effect seems not to correlate with the valve opening. This means that any N_2 flow stabilizes the atmospheric composition the same independently of the flow rate. However, no tested configuration of gas flow parameters achieved a completely stable atmosphere in the beam path.

In conclusion, the FE design is a straight-forward design. The evaluation of different flow parameters shows that the enclosure in general reduces fluctuations in the atmospheric composition. This effect is however independent of the N_2 flow rate. For all tested configurations, the desired constant atmospheric composition could not be achieved within 60 min. This could have several reasons. First, the used N_2 gas might not be completely dry or fluctuate in its composition. It is generated by an N_2 generator within the building (INMATEC, PN1550 OG). PSA technology guarantees dry N_2 - purity of 99,6 % which is monitored by analytical instruments in

the generator. Therefore, it is assumed that possible water impurities in the N_2 gas flow are unlikely to cause the observed, rather strong fluctuations. Second, the FE is constructed from interlocked aluminum sheets. Small gaps (< 1 mm) are left open at the joints. Air from the laboratory might be drawn into the enclosure, causing constant fluctuations in the atmosphere composition inside the enclosure. It is assumed that the N_2 flow creates an overpressure inside the enclosure preventing air from entering the FE. Third, the purging time was chosen too short. The data displayed in Figure 70 can also be interpreted that no true plateau value is reached. This means that the rate of purging is slowed down after 20 min but continues to approach zero and would reach the optimum eventually. Therefore, the gas flow has to be applied long enough to completely purge the entire volume of FE. In order to achieve this, either the purging time could be increased or the volume to be purged can be reduced. The second option was realized in the second design approach: the beam path purge (BPP).

5.4.2 Second Design Approach: Beam Path Purge

In the first design iteration, the straightforward full enclosure (FE), the optimum stable atmosphere could not be reached. The data indicates that after 60 min, substantial fluctuations in the atmosphere composition lead to non-negligible artifacts. As possible cause, it was assumed that a purging time of 60 min is not sufficient to purge the complete volume of the FE and stabilize the atmospheric conditions. One possible solution would be to increase the time of the N_2 purge before the experiment is started. This would be analogue to offline FTIR instruments like the Vertex 70, for example, which has to be purged with dry pressurized air for 12 - 24 h after opening to ensure artifact-free spectra. In the FE design, prolonging the purging time is not possible due to the current design of CE2. CE2 needs to be removed completely to fill the LN2-Dewar of the MCT detector which is necessary for its functionality. That means, that if the FE would e.g. be purged with N_2 for 12 h overnight, the detector cover CE2 would have to be removed to refill the MCT Dewar. This would consequently obliterate all effects of the N_2 purge. A possible solution would be to incorporate an LN2-filling nozzle to CE2 to enable refilling of the MCT Dewar without removing CE2, therefore allowing for longer purging times. However, the incorporation of a filling nozzle to CE2 is complex as it has to guarantee that no LN2 is spilled within CE2. Since the MCT Dewar has no level indicator, overflow of the MCT Dewar indicates that it is filled to its capacity. Spilled LN2 inside CE2 could be trapped within corners or joint lines of CE2. The local temperature reduction could lead to tension and potential failure of the material.

An alternative to prolonging the purging time is to improve the efficiency of the N_2 purge by reducing the volume which has to be purged, thereby reducing the needed purging time. This was realized in the second design iteration, the beam path purge (BPP) which is displayed in Figure 72. In this design, the beam path is enclosed within tubes which each have a N_2 inlet. These tubes are attached to the side walls of CE1. This concentrates the gas flow to the volume of the IR beam which should increase its efficiency. Moreover, the BPP keeps most of the beam path enclosed and purged during sample loading through the acrylic glass door of CE1. Thus, it also reduces the volume for potential fluctuations which in turn should improve the stability of

the N_2 atmosphere. Therefore, the BPP design does not only address the challenge raised in the previous chapter but also conquers the practical challenge of fluctuations caused by opening the enclosure during sample loading.

The volume of the beam path enclosure was reduced by introducing polyvinylchloride (PVC) tubes to CE1 which are purged via direct N_2 inlets. Each tube has a volume of approximately 0.24 L (d = 3.6 cm, L = 24 cm) in comparison to the volume of CE1 of 17.6 L (L = 24.5 cm, W = 30 cm, H = 24 cm). Tube 1 (T1) encloses the beam for the distance from the spectrometer to parabolic mirror M1, while tube 2 (T2) encloses the beam from the parabolic mirror M2 to the window leading to the flexible tube. The beam is not enclosed in between M1 and M2 and is therefore not directly purged in this volume. However, since CE1 is kept closed, it is assumed that this beam path is purged passively by the gas flow from the tubes which is deflected by the mirrors. The proposed gas flow is also incorporated in the scheme in Figure 72.

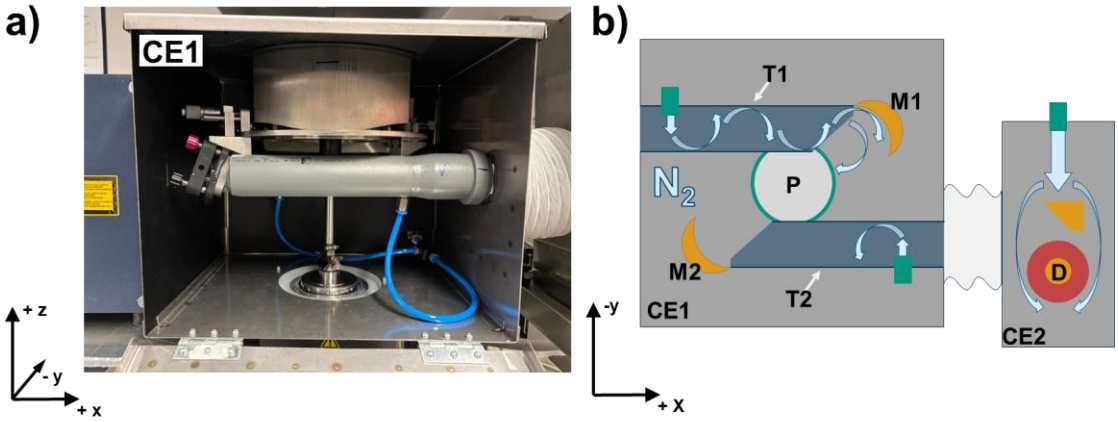

Figure 72: a) Picture of PVC tubes T1 (back) and T2 (front) of the beam path purge (BPP) design. B) Schematic illustration of the BPP in top view. Tube T1 covers the beam path from spectrometer to the parabolic mirror M1, while tube T2 encloses the beam path from the parabolic mirror M2 to the window towards the flexible tube.

Two hoses of the same diameter of 6 mm and length connect the two inlets of T1 and T2 with the inlet in the back of CE1. Consequently, the flow rate in the tubes is controlled with V1. The flow rate in one tube corresponds to half the flow rate at V1. To optimize the gas flow in the BPP design, the V2 and the APS inlet were set to 5 L min^{-1}, while the V1 opening was varied between 25 % and 100 % similarly to the investigations on the FE design in the previous chapter. The data presented in the following was obtained during the bachelor thesis of Yago Rodrigues Melges [206]. The evaluation of the data was revised to be consistent with the other data presented in this chapter. The data was evaluated in the same manner as for the FE design by subtracting the successive spectra of each other, integrating the area corresponding to the absorption bands of $H_2O_{(g)}$ at 4000 – 3400 cm^{-1}, plotting the absolute area against the time and determining the average absolute area and its standard deviation for the time frame of 30 - 60 min. The results are displayed in Figure 73 in comparison to the FE design.

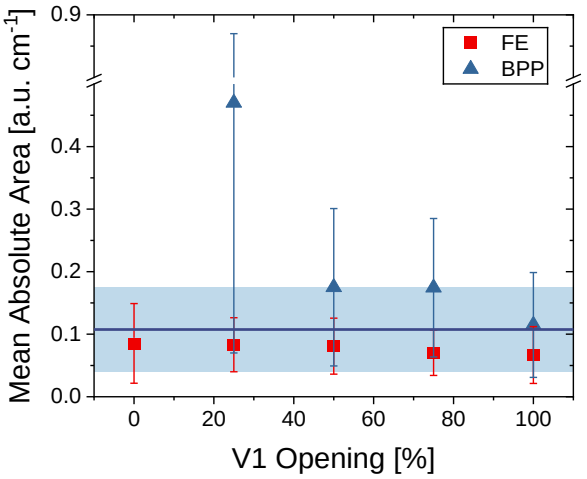

Figure 73: Comparison of the two enclosure designs FE and BPP. The y-axis is discontinued from 0.5 to 0.8 for better readability. The BPP design substantially increases the water fluctuations both in comparison to the FE design as well as to open atmosphere measurements.

As can be seen in Figure 73, the BPP results in considerably larger artifacts on average compared to the FE purging and measurement under open atmospheric conditions. Moreover, the fluctuations around the mean artifact area are significantly higher, which is reflected in the substantially increased standard deviations. The smallest mean absolute area and thus the optimum of the tested gas flow conditions is achieved for a V1 Opening of 100 %. However, the hereby obtained optimum only corresponds open atmospheric conditions. It can be concluded that the BPP design leads to more fluctuations inside the beam path and therefore to more artifacts on average than the FE design. Several hypotheses may account for this observation. The direct gas inlet at the tubes might introduce increased fluctuations by turbulent gas flow directly in the optical beam path, thereby affecting the spectra more strongly than a N_2 inlet that is not located in spatial proximity to the beam like in the FE design. Another explanation could be that the gas flow from the tubes is not sufficient to purge the unpurged volume remaining between M1 and M2. Alternatively, the tube design could facilitate the entrainment of a larger amount of condense water from the exterior of the MCT detector into the beam path, which would likewise result in enhanced fluctuations. This last hypothesis of condensed water being transported into the tubes was addressed in the next design iteration: the introduction of a vent to the BPP design.

5.4.3 Third Design Step: Introduction of a Vent to the Beam Path Purge

The data obtained for the BPP indicates that condensed water from the MCT detector may be entrained within T2, causing stronger fluctuations than in the FE purge. To address this effect, the BPP design was extended by incorporating an orifice at CE2 that serves as a vent. This modification should establish a gas flow that is largely located inside CE2, with N_2 entering at the inlet of CE2 and exciting through the vent. To realize this design concept, three orifices were introduced on the front side of CE2: one at the top, one at mid-height aligned with the mirror as well as the inlet and one at the bottom. A picture of the CE2 front side with the three orifices as well as a schematic illustration of the set-up including the proposed gas flow are given in Figure 74.

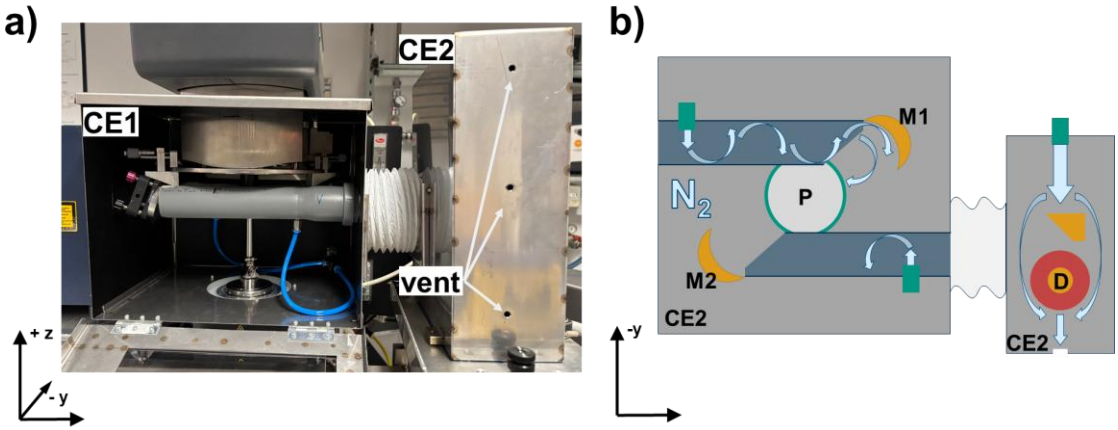

Figure 74: a) Picture of BPP including three vents at CE2. The vents are referred to by their position as top, mid-height and bottom vent. b) Schematic illustration of vBPP. The vent is supposed to create a separate gas flow through CE2, transporting potential condensed water through the vent instead to CE1.

To optimize the position of the vent, one of the orifices was left open while the other two were sealed with tape. With this configuration, a 60 min atmospheric measurement analogue to the experiments in the previous chapters was conducted. These experiments were carried out within the bachelor thesis of Y. Melges [206]. In these measurements, V1 opening was chosen for 75 % and V2 and the APS inlet were set to 5 L min^{-1} which was determined to be the optimum conditions for the BPP set-up in the work of Y. Melges [206]. From the revised data in Figure 73 (p. 112), the minimum artifacts size and therefore the optimum gas flow conditions would be obtained with a V1 Opening of 100 % and a gas flow at V2 and the APS inlet of 5 L min^{-1}. However, the difference between the VO of 75 % and 100 % is within the uncertainty of the measurement, therefore the choice of a V1 opening of 75 % stays valid. A spectrum was obtained every 30 s without any delay in between spectra.

The evaluation of this experimental data was revised to be consistent with the previous chapters. Instead of the artifacts of the whole spectrum, only the H_2O bands at 4000-3400 cm^{-1} were

considered in the evaluation, similar to the previous chapters. Thus, the trends presented here differ from the trends published in [206].

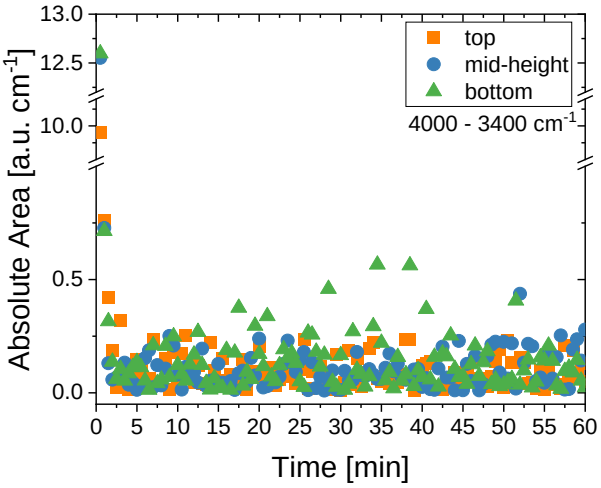

Figure 75: Absolute area of water signal at 4000 – 3400 cm^{-1} plotted against purging time for the three vent positions top (orange square), middle (blue circle) and bottom (green triangle).

The absolute area of the H_2O bands at 4000-3400 cm^{-1} is plotted against the purging time in Figure 75 for the different vent positions. The average of the absolute area in the time frame of 30 - 60 min and its standard deviation for the different vent positions are summarized in Table 12. The smallest artifact size and the least fluctuations were obtained for the top vent position. However, the differences between the different vent positions are within the uncertainty of the experiment. The comparison to the previous design steps FE and BPP shows that the introduction of a vent does not significantly improve the purging efficiency. The FE design still resulted in the smallest artifacts and the least fluctuations.

Table 12: Mean absolute area $A_{30\text{-}60}$ in the time frame of 30 to 60 min in dependence of the vent position. The optimum values obtained for the FE and the BPP design are given for comparison.

	FE, V1 at 75 %	**BPP, V1 at 100 %**	**Top Vent**	**Mid-height Vent**	**Bottom Vent**
$A_{30\text{-}60}$ [a.u. cm^{-1}]	0.07 ± 0.036	0.115 ± 0.084	0.089 ± 0.065	0.116 ± 0.088	0.122 ± 0.117

Due to the difference in data evaluation, in the reference work, the mid-height vent was determined as the optimum position for the vent in [206]. Thus, the optimization of the flow conditions was carried out at the mid-height vent with the other vents sealed. The flow rate at V2 was varied between 5 L min^{-1} and 15 L min^{-1}. The results are summarized in Table 13.

Table 13: Variation of flow rates at V2, revised data from [206].

	FE, V1 at 75 %	**BPP, V1 at 100 %**	**5 Lmin^{-1}, Mid. Vent**	**10 Lmin^{-1}, Mid. Vent**	**15 Lmin^{-1}, Mid. Vent**
$A_{30\text{-}60}$ [a.u. cm^{-1}]	0.07 ± 0.036	0.115 ± 0.084	0.116 ± 0.088	0.115 ± 0.076	0.086 ± 0.062

5.4.4 Next Possible Design Steps

In conclusion, none of the three tested designs maintained a stable atmosphere without H_2O-fluctuations within the 60 min test period. As the FE design is easier to handle during measurements and gives better results in the gas purge experiments, it should be used as the base of future designs optimization. The sealing of all joints in the enclosure should improve the efficiency of the gas flush and help to create a stable atmosphere within a reasonable time frame. Especially the connection of the flex tube between CE1 and CE2 has to be revised. In the current design, the flex tube is simply connected by slotting the ends into a gap between metal sheets. If it is not properly installed, gaps of up to 1 mm can occur. Moreover, the hole in CE1 towards the spectrometer should also be sealed. This can be realized by mounting the side wall of CE1 directly to the spectrometer with a seal in between. Implementing these measures is expected to increase the efficiency of the gas flush and achieve a stable atmosphere more rapidly.

The introduction of a liquid nitrogen filling nozzle is inevitable. The refilling of the MCT Dewar without removing CE2 would allow for purging times exceeding the maximum run time of the MCT detector. Longer purging times could be beneficial for the formation of a stable atmosphere within the enclosure. Commercial instruments like the Vertex are recommended to be purged for 12 – 24 h after opening to ensure a stable atmosphere. It has to be considered, however, that the length of the filling nozzle defines the distance between MCT Dewar and top of CE2. This would limit the set-up to a specific detector size. Moreover, a mechanism to seal the filling nozzle would be needed in case the Rheo-FTIR is to be used with the thermoelectrically cooled MCT (TE-MCT). A sealed set-up and a LN2 filling nozzle would allow the use of drying agents e.g. zeolite or $CaCl_2$ within the enclosure. These drying agents can remove water from the instrument atmosphere. If water is completely removed, fluctuations are eliminated, as shown in the work of T. Beskers [199]. However, the use of a drying agent requires a sealed set-up as air exchange through gaps would lead to H_2O fluctuations because the air exchange with the surrounding laboratory occurs faster than the removal of water from the atmosphere. In addition to improving the FE design, a flow meter could be incorporated to V1 to allow a more precise optimization of the gas flow rate. Moreover, the ratio between the gas inlet and the enclosure size should be revisited and compared to commercial instruments. Furthermore, future investigations on the atmospheric conditions need to consider the surrounding laboratory conditions. The humidity as well as the strength of the laboratory ventilation vary in between measurement days, which has been observed both during IR measurements as well in the studies on cement rheology (compare chapter 3.2, p. 51). Therefore, the atmospheric investigations should be repeated on several measurement days to ensure a stable atmosphere can be achieved inde-

pendently of the surrounding laboratory atmosphere. To address the CO_2 fluctuations, the N_2 purge could be changed from the generator with 99.6 % purity to N_2 gas cylinders of higher purity of 99.999%.

5.5 Time-dependent Investigations on Ettringite Formation Under the Influence of Highly Charged Polymers

The results presented in the following subchapter are part of a publication [22].

5.5.1 Ettringite Formation in Ordinary Portland Cement at early Hydration States Monitored via Rheo-FTIR

In the hydration of ordinary Portland cement (OPC), two reactions dominate: the silicate and the aluminate reaction [59, 63] (see chapter 2.2.2, p. 15). During the early stages of the aluminate reaction, C_3A dissolves rapidly and reacts with sulfate to form ettringite. The continuous precipitation of ettringite during the early hydration of OPC markedly influences rheological properties, such as viscosity and thixotropy [68, 113, 207]. Consequently, both qualitative and quantitative investigations on ettringite formation and its relation to the rheological evolution during cement hydration are of great interest.

In this study, ettringite formation was monitored with our unique *in-situ* Rheo-FTIR set-up. The measurements were conducted in 2023 during an intermediate stage of the modifications on the set-up. Consequently, the sensitivity was not fully maximized yet. The measurements were conducted with a five times improved sensitivity in comparison to the initial set-up [22].

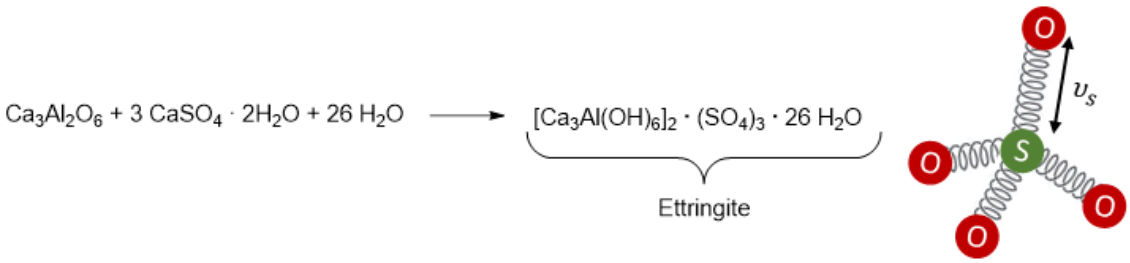

Figure 76: Reaction equation of ettringite formation in sum formula with a schematic representation of the S-O-stretching (ν_s) vibration in a sulfate molecule. It should be noted, that the charge of the sulfate ion (SO_4^{2-}) was neglected in the schematic drawing for simplicity.

During ettringite formation, sulfate from the pore solution is bound within the newly formed mineral. This is expressed in the general chemical formula in Figure 76. The hydration of OPC (w/c = 0.4) was monitored during the first hour of hydration. One FTIR spectrum was recorded every 14.5 seconds (40 kHz, 64 scans). The structural build-up of the cement paste was followed via an oscillatory time sweep. The strain was chosen at $\gamma_0 = 0.01\%$ to obtain a linear deformation, which would not disturb the formation of percolation paths during the structural build-up [114].

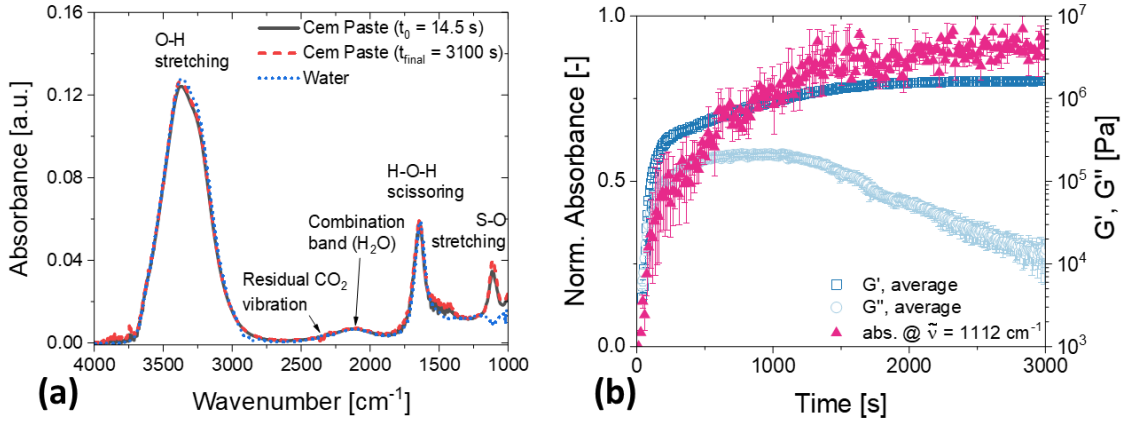

Figure 77: a) IR spectra of pure water as well as two spectra of cement paste, corresponding to the begin of the measurement (t_0 = 14.5 s) and the end of the measurement (t_{end} = 3100 s). b) Absorbance (peak maximum) at 1 112 cm^{-1} averaged over three measurements as well as the averaged loss and storage modulus are plotted as a function of measurement time for cement paste obtained online using the Rheo-FTIR setup.

Figure 77 presents the FTIR spectra of the cement paste measured immediately after mixing and after one hour of hydration, together with a water spectrum used as a reference. The sulfate vibration appears as a characteristic peak at 1 112 cm^{-1} [208, 209]. Sulfate is present in different cement phases such as gypsum or ettringite as well as dissolved in the cement solution. Jakob et al. employed the same CEMI 42.5 R for *in-situ* XRD studies [95]. They observed that, after the initial dissolution, the concentrations of all sulfate containing solid phases remained constant whereas the amount of ettringite increased. The ettringite concentration shows a limited growth behavior in both the aforementioned *in-situ* XRD studies as well as our FTIR investigations [95]. We therefore attribute the change in the sulfate peak intensity to the formation of ettringite. The normalized absorbance at 1 112 cm^{-1} was plotted as a function of time, which is displayed in Figure 77 b), and averaged over three independent measurements. The absorbance increases exponentially at first and reaches a plateau after roughly 1 500 s. In the same figure, the average values of G' and G'' measured during the structural build-up of the cement paste are shown.

In general, the absorbance is directly proportional to the concentration, which is expressed by the Lambert-Beer-law [185]:

$$A = \varepsilon l c \tag{5.3}$$

where A is the absorbance, ε the molar extinction coefficient, c the concentration of the absorbing species and l the optical path length. The molar extinction coefficient is proportional to the absorption cross section of the sample [185]. Due to the accumulation of absorbing molecules in solid state, we assume that ε (ettringite) >> ε ($SO_{4,aq}^{2-}$) and thus interpret changes in the measured absorption as changes in ettringite concentration.

The normalized G' was plotted against the normalized absorbance in Figure 78. This is equivalent to the solidification of the cement paste in dependence of the ettringite content. Two regimes can be identified from the graph. In the first regime, the slope of the G' increase accord-

ing to a power law scaling of 1.5. In this regime, the ettringite build-up is almost proportional to the solidifying of the cement slurry. After a critical concentration of ettringite is reached (in our case at a normalized absorbance for large times, $A_{norm} := A/A(t = \infty) = 0.3$), the solidification is accelerated and G' increases by the power law exponent of 3. This transition is linked to the size of the precipitated ettringite particles. Initially, small nuclei of ettringite are formed which continue to grow during the precipitation [210]. When they exceed a certain size, they act as contact points which are needed to form percolation paths. These percolation paths lead to the accelerated rigidification of the cement sample [97].

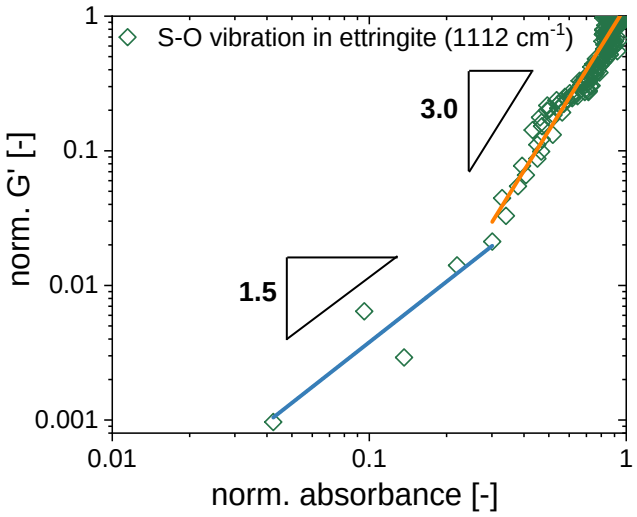

Figure 78: Normalized, time dependent storage modulus as a function of the normalized, time dependent IR absorbance @ 1 112 cm^{-1} of fresh cement paste.

5.5.2 Synthesis of Highly Charged PMAA of Different Topologies

Numerous earlier studies have shown that polymers, most notably the widely used superplasticizer PCE (see chapter 2.4, p. 29), affect the ettringite formation [164, 165, 211, 212]. More recent work suggests that the quantity of ettringite formed is dependent of the charge density in the PCE molecule [113]. To explore this effect, the hydration of cement pastes under the influence of highly charged polymers similar to PCE was investigated. To mimic PCE with a high charge density, two model systems of pure polycarboxylate were synthesized: a linear and a PMAA star as summarized in Figure 79.

The linear PMAA was synthesized via reversible addition-fragmentation chain transfer (RAFT) polymerization, following the work of Pelet and Putnam [213]. The use of a dithio- or trithiocarbonate chain-transfer agent in RAFT ensures an equal distribution of the chain growth probability among all polymer chains. Consequently, RAFT possesses many synthetic advantages, including the ability to synthesize defined structures with a polydispersity (PDI) of 1.3 to <1.1,

as well as a high flexibility in reaction conditions including the use of protic solvents, e.g. water [26]. Therefore, RAFT was chosen for the synthesis of linear PMAA as a simple, straightforward one-step approach with a high control over molecular parameters.

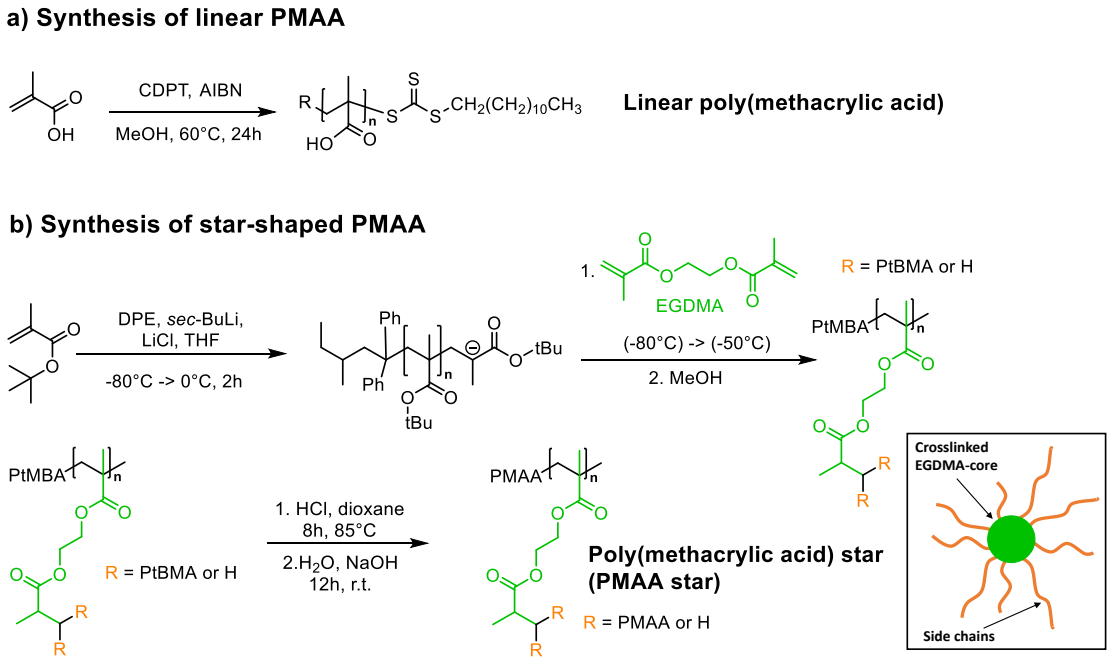

Figure 79: Synthesis of the investigated a) linear and b) star shaped PMAA.

Additionally, a PMAA star was synthesized. A star polymer represents the simplest branched structure and therefore serves as a model system for the more complex branched PCEs. The PMAA star was prepared by living anionic polymerization (see chapter 2.1.2, p. 6). This living polymerization was chosen for the star synthesis because the reaction proceeds without side reactions such as recombination or disproportionation. Consequently, no additional purification of the product was needed as it would be the case for a star synthesis via RAFT polymerization.

Due to the incompatibility of the anionic propagating species with the acidic carboxyl group of PMAA, tBMA was used as a precursor monomer for the polymerization. Living tBMA chains were synthesized and linked by the addition of the crosslinker EGDMA. The polymerization was stopped by the addition of methanol. In a consecutive reaction step, the precursor is hydrolyzed to form the desired free carboxylic groups which is necessary to make the molecule water-soluble. A further addition of base allows to charge the polymer by deprotonation of the carboxylic group. The two PMAA model systems were characterized via size-exclusion chromatography (SEC). The weight average molecular weights as well as the dispersity of the model systems are summarized in Table 14.

Table 14: M_w *and PDI of the PMAA model systems (obtained by SEC;* [1]*PDI =* M_w/M_n *and* M_w *obtained from dRI-detector,* [2]M_w *calculated from MALS detector, calculated with dn/dc(PtBMA) = 0.075 mL/g [214]).*

Polymer	Molecular Weight	PDI[1]
Linear	M_w^1 = 22.000 g/mol	1.30
Star	M_w^2(SC, PtBMA) = 18.000 g/mol	1.05
	M_w^2 (star, PtBMA) = 77.000 g/mol	1.28

5.5.3 Ettringite Formation in the Presence of Highly Charged PMAA

To evaluate the impact of the self-synthesized PCE model systems on the ettringite formation, each polymer was added to ordinary Portland cement (OPC) at a fixed dosage of 0.5 wt.% normalized to the mass of dry cement (compare chapter 4, p. 61). This concentration lies within the typical dosage range for commercial PCEs ≤ 2 wt.% [8]. The PMAA-based polymers were dissolved in the mixing water before the mixing of the cement paste using the direct-addition protocol. Direct addition of PCE is known to have an accelerating effect on the onset of the aluminate reaction [126], which is often accompanied by an increased ettringite precipitation leading to an increase in the specific surface area [211].

All measurement conditions were identical to those applied for plain cement pastes. The time-dependent absorbance of the ettringite peak at 1 112 cm^{-1} was monitored as well as G' and G'' during the structural build-up.

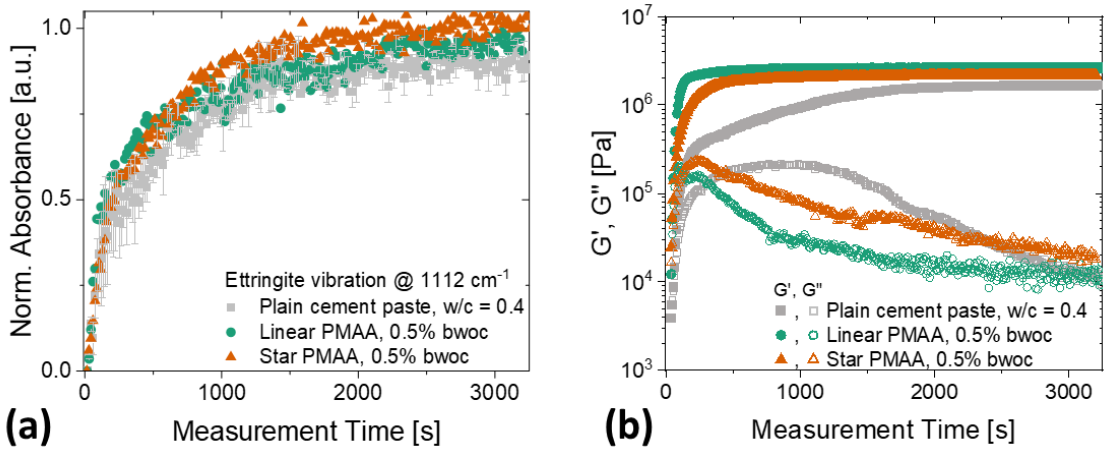

Figure 80: (a) Normalized absorbance of ettringite vibration @ 1 112 cm^{-1} *and (b) Storage modulus (closed symbols) and loss modulus (open symbols) of plain cement paste and the cement paste with added linear and star-shaped PMMA.*

As shown in Figure 80 (a), the normalized adsorption slightly increases in the presence of PMAA polymers. Moreover, the addition of polymer has a prominent effect on the structural build-up of the pastes. G' rises rapidly and reaches its plateau value approximately 1000 s earlier than in polymer-free cement pastes. This shift in the evolution of G' cannot be directly

linked to the absolute amount of ettringite because no internal standard of known concentration was employed. Instead, the ettringite concentration is expressed by the ratio of the sulfate-peak absorption ($\tilde{\nu}$ = 1 112 cm^{-1}) to the peak absorbance related to water ($\tilde{\nu}$ = 3380 cm^{-1}). This ratio was calculated for each recorded spectrum and correlated with the evolution of G' to examine how the structural build-up depends on to the concentration of precipitated ettringite.

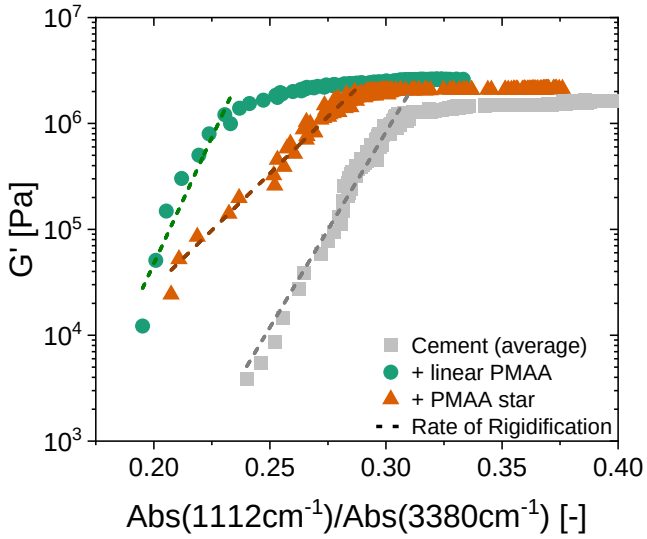

Figure 81: Storage modulus shown as a function of the absorbance @ 1 112 cm^{-1} (ettringite) normalized to the absorbance @ 3380 cm^{-1} (water).

As shown in Figure 81, all samples show a similar behavior in the evolution of G' with increasing ettringite concentration. The storage modulus increases fast until a plateau is reached at 2·10^6 Pa. The increase of G' was fitted with a straight line, its gradient corresponding to the rate of rigidification [40]. The rate of rigidification is the highest for the linear PMAA and lowest for the star. For both samples containing the polymer, G' is increased at lower ettringite concentrations than for plain cement paste. This indicates that less ettringite is necessary in the presence of polymer to form a percolation network that leads to a G' increase [97, 114]. This effect has two possible reasons. Firstly, since rather big polymers were synthesized, one possible explanation for this effect is that the polymers are adsorbed to more than one cement particle. Therefore, they act as bridges between particles and accelerate the formation of a percolation network [215]. Both polymers are assumed to have similar hydration radii due to their similar molecular weights. The linear PMAA has a degree of polymerization P_n of 255 in comparison to 226 of one sidechain in the PMAA star. However, branched structures such as stars have a smaller radius of gyration than linear chains of the same P_n. Thus, the linear polymer is more likely to adsorb to more than one cement grain if compared to the star shaped polymer. Therefore, the rate of rigidification is higher for the linear polymer than for the PMAA star. Second, the G' increase could also be related to the morphology of the precipitated ettringite. In FTIR spectroscopy, the absorbance is proportional to the concentration of the investigated compound. However, no information about the morphology of the precipitated ettringite can be obtained. Differ-

ent studies indicate a change in the morphology of ettringite in the presence of highly-charged PCE [165, 216]. Therefore, the same amount of substance of ettringite could be precipitated in more and finer particles in the presence of polymer than in plain cement pastes. A higher amount of initial fine ettringite increases the number of contact points, resulting in a faster formation of a percolation network [113].

5.6 Conclusions and Outlook

The Rheo-FTIR set-up is a powerful and versatile tool to investigate the correlation of chemical changes and the macroscopic rheological behavior. The experimental set-up was initially developed by Radebe et al. in 2021 within this working group [20, 21]. While this initial set-up proved to be sufficient to investigate the reaction kinetics of poly(acrylic acid) hydrogels [20], its sensitivity was not fully maximized yet. Therefore, several set-up modifications are reported in this work which were implemented to increase the sensitivity of the integrated FTIR spectrometer and facilitate the use of the whole set-up. Technical changes to improve the handling and extend the versatility of the Rheo-FTIR included reversing the beam path and the redesign of the lower geometry. More precise positioning of optical components and improved beam path alignment were achieved through reconstruction of the table and incorporation of an additional adjustment screw in the redesigned mirror ring system. In addition, the upper geometry was shortened, and the cross-hatched shaft was replaced with a cylindrical shaft to minimize the torsion compliance of the geometry. Moreover, the new upper geometry allows the use of an additional temperature sensor within the cylindrical shaft.

The reported modifications lead to a substantial sensitivity ($SNt^{-1/2}$) increase by a factor of 63 by improving the optical throughput θ. The increase in θ was indicated by an increase in the ADC count, which is a measure included in the OPUS software reflecting the intensity obtained at the detector. In the previous work of Radebe et al., ADC counts of 8 000 – 16 000 a.u. with ten times preamplification were reported [21]. The improved set-up now allowed for reproducible ADC counts of 25 000 a.u. without preamplification. Moreover, the modifications reduced the set-up time of the modular Rheo-FTIR from approximately 1 h to 15 min. The sensitivity can probably be further increased by redesigning the ATR crystal to reduce its size. Reduction of the path length within the silicon would reduce the loss of signal by IR absorption of the crystal's phonon vibrations [142]. Moreover, reducing the size would lead to a decrease in cost, which in turn would allow to explore other possible ATR crystal materials such as ZnSe, Ge, or diamond, which are transparent in the whole mid-IR range (4000 – 400 cm^{-1}). While advantageous, their application needs to be considered with regard to possible safety implications, as e.g. ZnSe releases toxic fumes at pH values below five and above nine [142]. Moreover, the addition of a mechanism to precisely position and fix the orientation of the spectrometer is expected to further increase the sensitivity and the reproducibility of spectral quality. As highlighted in chapter 5.3 (p. 97), the SNR improvement extends the applicability of the Rheo-FTIR to investigations at elevated temperatures up to the Advanced Peltier System (APS) temperature limit of 150 °C. The heat cover developed by Xu et al. [204] improved the temperature stability of both sample and upper geometry. Future work will focus on investigations of reaction kinetics at elevated temperatures, like rubber curing. To further extend the scope of applications, polarization filters could be added to the beam path of the Rheo-FTIR. These filters would enable investigations of shear-induced effects, such as the orientation of functional groups [198].

Gases like carbon dioxide (CO_2) and water vapor ($H_2O_{(g)}$) strongly absorb IR light. Fluctuations in their concentration within the beam path can lead to artifactual absorption bands which can obscure sample peaks. This is especially challenging in long-term measurements in which these

artifacts can sum up over time, creating large absorption bands. Commercial FTIR spectrometers usually address this challenge by enclosing the beam path and purging the instrument with dry pressurized air of defined composition or nitrogen to stabilize the atmosphere within the instrument. In chapter 5.6, this concept was implemented to the Rheo-FTIR with three different enclosure designs for the Rheo-FTIR: the full enclosure (FE), the beam path purge (BPP) and the vented Beam Path Purge (vBPP). The three designs were tested for their efficiency in stabilizing the atmosphere within 60 min of purging time. The time frame was chosen due to the limits of the MCT Dewar size. In conclusion, none of the tested designs enables the formation of a stable atmosphere within 60 min. However, the FE design gave the most promising results. Therefore, this design needs to be improved by sealing the joints, installing a flow meter at V1, and most importantly, incorporating an LN2 filling nozzle to improve the efficiency of the purge. In addition, drying agents like zeolite or $CaCl_2$ could be used to remove water from the instrument's atmosphere.

The Rheo-FTIR set-up was applied to investigate the chemical changes in cement pastes in early hydration stages. The experiments on plain cement pastes showed that the Rheo-FTIR set-up was suitable for conducting *in-situ* studies of ettringite formation. Moreover, the increase in the storage modulus was correlated with ettringite content, indicating that solidification is affected by increasing ettringite concentration. To investigate the influence of PCE-like polymers, two highly charged model systems were synthesized from PMAA via RAFT and living anionic polymerization. Their effect on the ettringite formation was investigated within the first hour of hydration. It was found that the cement pastes containing polymer showed a steeper increase of G' at lower ettringite concentrations. The linear polymer has a more pronounced effect compared to the star-shaped polymer topology. This is consistent with the hypothesis that the polymer leads to an increase in contact points without increasing the ettringite content. These contact points might be formed by the polymer itself, which adsorbs to multiple cement particles and thus act as molecular bridges between them. Moreover, the polymer might alter the morphology of the precipitated ettringite, which leads to more, but smaller sized ettringite particles. To conclude, physical interactions such as particle interactions are more dominant in the structural build-up than the formation of ettringite during the first few minutes to the first hour of cement paste hydration.

6 Conclusions and Outlook

This work addresses the effect of superplasticizers in cement pastes at early hydration states, with a focus on their influence on rheological properties and formation of ettringite. The three main parts concentrate on the development of a measurement procedure for a reproducible rheological characterization of cement pastes, the synthesis of a series of Poly(carboxylate methyl-oxazoline) (PCMOxa, IUPAC: poly(2-methyl-2-oxazoline)-*graft*-poly(methacrylic acid)) comb polymers as an alternative to the most prominent superplasticizer poly(carboxylate ether), as well as the sensitivity improvement and the application of a homebuilt Rheo-FTIR set-up for an investigation on the early hydration of cement paste in the presence of highly-charged poly(methacrylic acid) (PMAA).

In chapter 3, a reproducible and reliable rheological protocol for determining the yield stress of cement pastes by rotational rheometry was developed. Five different geometries were systematically compared. Among these, a 50 mm plate-plate (PP) geometry with a 600-grit sandpaper glued to the surface with cyanoacrylate glue delivered a yield-stress value of 46 ±7 Pa, which was closest to the reference spread-flow result of 42 Pa while maintaining laminar flow conditions. Key experimental parameters were systematically optimized to improve the reproducibility, resulting in a final measurement procedure that includes a sample age of 15 min, using an IKA stirrer to homogenize the sample prior to the measurement, application of a pre-shear of 100 s^{-1} for 60 s, strict control of water (10 ± 1 °C) and ambient temperature (22 ± 1 °C), and an increase of the prepared sample mass from 10 g to 100 g of dry cement per measurement. The validity of this optimized procedure was confirmed by its ability to reproduce characteristic cement paste flow curves. Moreover, the inverse-fifth-power correlation between yield stress and spread-flow diameter [107, 108] could be confirmed for a series of different water-to-cement mass ratios (w/c-ratio). The protocol also successfully captured the characteristic S-shaped reduction in yield stress with increasing superplasticizer dosage. In summary, the optimized rheological protocol provides accurate and reproducible yield stress values that are consistent with spread-flow reference methods and reliably reflect variations in mix design. Consequently, this procedure was used in all rheological characterizations of cement pastes presented in this work.

Understanding the structure-property relationship of comb superplasticizers is central to design the molecules for future challenges like low-carbon concrete formulations, which is addressed in chapter 4. To gain a further understanding of the structure-property relationship, a potential model system for the commercial poly(carboxylate ether) (PCE) was developed in chapter 4. PCMOxa consist of a polycarboxylate backbone and poly(2-methyl-2-oxazoline) (PMOxa) sidechains. PMOxa was chosen as a water-soluble and uncharged alternative to the typical sidechain polymer poly(ethylene oxide) (PEO). Two different synthetic strategies towards the comb polymers with PMOxa-sidechains were presented: a grafting-onto and a grafting-through. The grafting-through approach is also referred to as macromonomer route.

In the grafting-onto procedure, the backbone is synthesized via anionic polymerization of tert-butylmethacrylate (tBMA) and successive hydrolysis to obtain linear poly(methacrylic acid) (PMAA). The living PMOxa sidechains synthesized via cationic ring opening polymerization (CROP) are grafted to the PMAA backbone via the formation of an ester bond. To verify whether PCMOxa can function as a superplasticizer, its performance was assessed on a selected grafting-onto sample. It was shown that PCMOxa can reduce the yield stress in a similar manner and amount as commercial PCE samples. Moreover, a similar yield stress vs polymer concentration correlation was obtained. Dissolved organic carbon (DOC) measurements revealed that the PCMOxa adsorb similarly to conventional PCEs. Consequently, it was concluded that PCMOxa combs have a similar working mechanism as conventional PCE via the adsorption of their negatively charged backbone (BB) onto the cement particle surface while the non-adsorbing sidechains (SCs) create steric hinderance between the particles [8]. The grafting-onto synthesis combines anionic and cationic synthesis to receive combs with low dispersity and well-defined molecular weights of both BB and SCs. Therefore, these combs are especially suited for comprehensive structure-property investigations. In a first attempt to understand the structure-property relationship of these new comb-superplasticizers, a library of eight PCMOxa comb polymers was synthesized while systematically varying the number of BB monomers per sidechain *N*, the SC length *P* and the BB length *B* (for terminology of structural parameters see Figure 42, p. 65). Thereby, it was shown that PCMOxa exhibits a structure-property relationship of a similar archetype as PCE. However, the parameter set for a maximum in $\Delta\sigma_0\ m_{SP,\,added}^{-1}$ is shifted to lower *P* and *N* values for PCMOxa compared to PCE. This shift might be attributed to the higher chain stiffness and consequently the increased hydrodynamic radius of the sidechain. Consequently, PCMOxa combs with shorter or less densely grafted sidechains should exhibit the highest dosing efficiency. While a direct quantitative comparison of the overall efficiency of PCMOxa and PCE cannot yet be made, this study represents, to the best of our knowledge, the first systematic investigation on the influence of sidechain chemistry on the performance of highly defined, low-dispersity comb-structured superplasticizers.

In addition to the grafting-onto synthesis, a standard grafting-through synthesis or macromonomer route developed for PCE [148] was transferred to the synthesis of PCMOxa combs. A macromonomer was prepared by living cationic ring opening polymerization terminated via an end-capping reaction with methacrylic acid to obtain a PMOxa-methacrylate (PMOxa-MA) [162]. ^{1}H-NMR confirmed its structure. Subsequent free-radical copolymerization (FRP) of PMOxa-MA with $P = 22$ and methacrylic acid (MAA) in the presence of the chain-transfer agent (CTA) 3-mercapto propionic acid (3-MPA) at room temperature yielded the FRP-PCMOxa comb, as verified by SEC. As a reference, a FRP-PCE comb with PEO sidechains of a similar length ($P = 22$) was synthesized using the same synthetic conditions. Rheological characterization revealed that FRP-PCMOxa and FRP-PCE reduced the yield stress to a comparable value of $\sigma_0 \approx 10$ Pa, similar to the commercial reference PCE BASF VP14.1. Notably, FRP-PCMOxa achieved a fivefold greater yield stress reduction than PCMOxa-100-9x25, which was chosen as a reference because it is the best-performing grafting-onto compound with a yield stress reduction of $\Delta\sigma_0 = 145$ Pa at the dosage of 0.1 wt.% (100 mg polymer per 100 g of dry cement). Although the exact cause of the increased yield stress reduction of the FRP-PCMOxa remains unclear, we propose that the higher dispersity and the lower molecular weight of FRP-PCMOxa lead to a more homogeneous polymer distribution within the cement

suspension. While the grafting-through approach offers limited control over molecular architecture and is therefore less suited for detailed structure-property investigations, it provides significant practical advantages, such as synthetic simplicity and reduction of reaction time. Since only a single reaction step under Schlenk conditions is required, the route is readily up-scalable. Microwave-assisted CROP could further shorten the macromonomer synthesis from approximately 24 h to 1 – 5 min [53]. Importantly, PCMOxa combs may address shortcomings of conventional PCEs, particularly their loss of efficiency in the presence of clay minerals such as bentonite. PCEs can suffer from sidechain intercalation into clay layers, resulting in a loss of dispersing efficiency. The alternative sidechain chemistry of PCMOxa might suppress intercalation, making these polymers promising candidates or clay-containing systems, including concrete incorporating calcined clays as low-carbon supplementary cementitious materials (SCM).

In chapter 5, the final part of this work, the home-built Rheo-FTIR was further developed and applied to investigate early cement hydration. Several modifications on the set-up were implemented prior to the investigations to improve the alignment of the infrared (IR) beam path and increase the mechanical stability of the set-up. The modifications included the redesign of the mirror ring system, the detector table and the upper geometry, all of which contributed to a more robust and reproducible IR beam alignment. These changes resulted in a substantial 63-fold increase in signal-to-noise ratio (SNR) and significant reduction in set-up time from ca. 1 h to 15 min. Further modifications, such as the reduction of the crystal depth and the addition of a mechanism to position and fix the spectrometer orientation are expected to further enhance the sensitivity and the reproducibility of spectral quality.

The fluctuations in concentrations of gases like carbon dioxide (CO_2) and water vapor ($H_2O_{(g)}$) within the open beam path can lead to artifacts in the spectrum. This is especially challenging in long-term measurements such as investigations on the cement hydration kinetics in which these artifacts can sum up over time, creating large absorption bands which can obscure sample peaks. Three different enclosure designs were implemented to the Rheo-FTIR to purge the sample compartment with dry nitrogen to stabilize the atmosphere: the full enclosure (FE), the beam path purge (BPP) and the vented Beam Path Purge (vBPP). While none of the tested designs was able to stabilize the atmospheric composition within 60 min of purging, the FE design gave the most promising results. However, further improvements are needed such as sealing the joints, implementation a flow meter at valve V1 and most importantly, the incorporation of a liquid nitrogen (LN2) filling nozzle for the MCT-detector to prolong the accessible purging time. In addition, drying agents like zeolite or $CaCl_2$ could be used to remove water from the instrument's atmosphere. Although further improvements are still required, the modified set-up proved suitable for *in-situ* studies of ettringite formation within the first hour of hydration. Rheo-FTIR measurements on plain cement pastes demonstrated a clear correlation between increasing ettringite content indicated by the SO_4^{2-} - stretching vibration at 1 112 cm^{-1} and the rise in storage modulus, indicating that ettringite contributes to early structural build-up. Experiments with highly charged PCE-like model polymers of poly(methacrylic acid) (PMAA) showed that polymer-containing pastes exhibit a steeper increase in the time-dependent storage modulus G'(t) at lower ettringite concentrations, with the linear polymer having a more pronounced effect than the star-shaped analogue. These findings suggest that physical particle interactions, such as polymer-mediated bridging or changes in ettringite morphology, dominate

early structural development, particularly within the first minutes to the first hour of hydration [215].

7 References

1. Monteiro, P.J.M., Miller, S.A., Horvath, A.: Towards sustainable concrete. Nature Mater. 16, 698–699 (2017). https://doi.org/10.1038/nmat4930.
2. Activity Report 2024, https://www.cembureau.eu/media/sblceede/cembureau-activity-report-2024.pdf, last accessed 2026/01/22.
3. Shivaprasad, K.N., Yang, H.-M., Singh, J.K.: A path to carbon neutrality in construction: An overview of recent progress in recycled cement usage. J. CO2 Util. 83, 102816 (2024). https://doi.org/10.1016/j.jcou.2024.102816.
4. Beumelburg, C.: Weltpremiere bei Heidelberg Materials: Eröffnung der CCS-Anlage in Norwegen läutet neue Ära des nachhaltigen Bauens ein | Heidelberg Materials Deutschland, https://www.heidelbergmaterials.de/de/media/baufachpresse/eroeffnung-ccs-anlage-brevik, last accessed 2026/01/23.
5. CCS: Risiken statt Klimaschutz, https://www.bund.net/klimawandel/ccs/, last accessed 2026/01/23.
6. Snellings, R., Suraneni, P., Skibsted, J.: Future and emerging supplementary cementitious materials. Cem. Concr. Res. 171, 107199 (2023). https://doi.org/10.1016/j.cemconres.2023.107199.
7. Marandi, N., Shirzad, S.: Sustainable cement and concrete technologies: a review of materials and processes for carbon reduction. Innov. Infrastruct. Solut. 10, 408 (2025). https://doi.org/10.1007/s41062-025-02213-5.
8. Aïtcin, P.-C., Flatt, R.J. eds: Science and technology of concrete admixtures. Woodhead Publishing, Cambridge, UK (2015).
9. Marchon, D., Boscaro, F., Flatt, R.J.: First steps to the molecular structure optimization of polycarboxylate ether superplasticizers: Mastering fluidity and retardation. Cem. Concr. Res. 115, 116–123 (2019). https://doi.org/10.1016/j.cemconres.2018.10.009.
10. Flatt, R.J., Schober, I., Raphael, E., Plassard, C., Lesniewska, E.: Conformation of Adsorbed Comb Copolymer Dispersants. Langmuir. 25, 845–855 (2009). https://doi.org/10.1021/la801410e.
11. Hyun, K., Höfl, S., Kahle, S., Wilhelm, M.: Polymer motion as detected via dielectric spectra of 1,4-cis-polyisoprene under large amplitude oscillatory shear (LAOS). J. Non-Newton. Fluid Mech. 160, 93–103 (2009). https://doi.org/10.1016/j.jnnfm.2009.03.002.
12. Watanabe, H., Matsumiya, Y., Horio, K., Masubuchi, Y., Uneyama, T.: Rheo-Dielectric Behavior of Soft Matters. In: Non-Equilibrium Soft Matter Physics. pp. 37–87. World Scientific (2012). https://doi.org/10.1142/9789814360630_0002.
13. Watanabe, H., Matsumiya, Y., Inoue, T.: Rheo-dielectrics in oligomeric and polymeric fluids: a review of recent findings. J. Phys.: Condens. Matter. 15, S909 (2003).
14. Hager, N.E., Domszy, R.: Monitoring of Hydration Processes in Cement Materials by Broadband Time-Domain-Reflectometry Dielectric Spectroscopy. J. Appl. Phys. 96, 5117–5128 (2004). https://doi.org/10.1063/1.1797549.
15. Struth, B., Hyun, K., Kats, E., Meins, T., Walther, M., Wilhelm, M., Grübel, G.: Observation of New States of Liquid Crystal 8CB under Nonlinear Shear Conditions as Observed via a Novel and Unique Rheology/Small-Angle X-ray Scattering Combination. Langmuir. 27, 2880–2887 (2011). https://doi.org/10.1021/la103786w.
16. Meins, T., Hyun, K., Dingenouts, N., Fotouhi Ardakani, M., Struth, B., Wilhelm, M.: New Insight to the Mechanism of the Shear-Induced Macroscopic Alignment of Diblock Copolymer Melts by a Unique and Newly Developed Rheo–SAXS Combination. Macromolecules. 45, 455–472 (2012). https://doi.org/10.1021/ma201492n.

17. Ratzsch, K.-F., Friedrich, C., Wilhelm, M.: Low-field rheo-NMR: A novel combination of NMR relaxometry with high end shear rheology. J. Rheol. 61, 905–917 (2017). https://doi.org/10.1122/1.4991513.
18. Al-kaby, R.N., Jayaratne, J.S., Brox, T.I., Codd, S.L., Seymour, J.D., Brown, J.R.: Rheo-NMR of transient and steady state shear banding under shear startup. J. Rheol. 62, 1125–1134 (2018). https://doi.org/10.1122/1.5037594.
19. Callaghan, P.T.: Rheo-NMR: A new window on the rheology of complex fluids. Encyclopedia of nuclear magnetic resonance. 9, 737–750 (2002).
20. Radebe, N.W., Fengler, C., Klein, C.O., Figuli, R., Wilhelm, M.: Rheo-IR: A combined setup for correlating chemical changes via FTIR spectroscopy and rheological properties in a strain-controlled rheometer. Journal of Rheology. 65, 681–693 (2021). https://doi.org/10.1122/8.0000251.
21. Radebe, N.W.: Combination of a Strain-Controlled Rheometer with an IR Spectrometer for in-situ Mechanical and Chemical Analysis of Cement Paste, (2021).
22. Meyer, T., Klein, C.O., Figuli, R., Wilhelm, M.: The development of a unique Rheo-FTIR set-up to monitor ettringite formation in the presence of highly charged polymers. In: Opus Fluidum Futurum—Rheology of Reactive, Multiscale, Multiphase Construction Materials (in press).
23. Koltzenburg, S., Maskos, M., Nuyken, O.: Polymere: Synthese, Eigenschaften und Anwendungen. Springer Berlin Heidelberg, Berlin, Heidelberg (2014). https://doi.org/10.1007/978-3-642-34773-3.
24. Seiffert, S., Kummerlöwe, C., Vennemann, N. eds: Lechner, Gehrke, Nordmeier - Makromolekulare Chemie: Ein Lehrbuch für Chemiker, Physiker, Materialwissenschaftler und Verfahrenstechniker. Springer Berlin Heidelberg, Berlin, Heidelberg (2020).
25. Tieke, B. ed: Makromolekulare Chemie: eine Einführung. Wiley, Hoboken (2014).
26. Chong, Y.K., Le, T.P.T., Moad, G., Rizzardo, E., Thang, S.H.: A More Versatile Route to Block Copolymers and Other Polymers of Complex Architecture by Living Radical Polymerization: The RAFT Process. Macromolecules. 32, 2071–2074 (1999). https://doi.org/10.1021/ma981472p.
27. Kohut-Svelko, N., Pirri, R., Asua, J.M., Leiza, J.R.: Redox initiator systems for emulsion polymerization of acrylates. J. Polym. Sci. A Polym. Chem. 47, 2917–2927 (2009). https://doi.org/10.1002/pola.23362.
28. Lamb, D.J., Fellows, C.M., Gilbert, R.G.: Radical entry mechanisms in redox-initiated emulsion polymerizations. Polymer. 46, 7874–7895 (2005). https://doi.org/10.1016/j.polymer.2005.06.078.
29. Odian, G.G.: Principles of polymerization. Wiley-Interscience, Hoboken N.J. (2004).
30. Bevington, J.C., Melville, H.W., Taylor, R.P.: The termination reaction in radical polymerizations. Polymerizations of methyl methacrylate and styrene at 25°. J. Polym. Sci. 12, 449–459 (1954). https://doi.org/10.1002/pol.1954.120120136.
31. Fischer, E., Storti, G., Cuccato, D.: Aqueous Free-Radical Polymerization of Non-Ionized and Fully Ionized Methacrylic Acid. Processes. 5, 23 (2017). https://doi.org/10.3390/pr5020023.
32. Ibarra-Montaño, E.L., Rodríguez-Laguna, N., Sánchez-Hernández, A., Rojas-Hernández, A.: Determination of pKa Values for Acrylic, Methacrylic and Itaconic Acids by 1H and 13C NMR in Deuterated Water. J. Appl. Sol. Chem. Model. 4, 7–18 (2015). https://doi.org/10.6000/1929-5030.2015.04.01.2.
33. Beuermann, S., Buback, M., Hesse, P., Kuchta, F.-D., Lacík, I., van Herk, A.M.: Critically evaluated rate coefficients for free-radical polymerization Part 6: Propagation rate coefficient of methacrylic acid in aqueous solution (IUPAC Technical Report). Pure and Applied Chemistry. 79, 1463–1469 (2007). https://doi.org/10.1351/pac200779081463.

34. Wittenberg, N.F.G., Buback, M., Stach, M., Lacík, I.: Chain Transfer to 2-Mercaptoethanol in Methacrylic Acid Polymerization in Aqueous Solution. Macromol. Chem. Phys. 213, 2653–2658 (2012). https://doi.org/10.1002/macp.201200484.
35. Rizzardo, E., Chen, M., Chong, B., Moad, G., Skidmore, M., Thang, S.H.: RAFT Polymerization: Adding to the Picture. Macromolecular Symposia. 248, 104–116 (2007). https://doi.org/10.1002/masy.200750211.
36. Hadjichristidis, N., Hirao, A.: Anionic Polymerization. Springer, Tokyo (2015). https://doi.org/10.1007/978-4-431-54186-8.
37. Szwarc, M.: 'Living' Polymers. Nature. 178, 1168–1169 (1956). https://doi.org/10.1038/1781168a0.
38. Baskaran, D., Müller, A.: Anionic vinyl polymerization—50 years after Michael Szwarc. Prog. Polym. Sci. 32, 173–219 (2007). https://doi.org/10.1016/j.progpolymsci.2007.01.003.
39. Saldívar-Guerra, E., Vivaldo-Lima, E. eds: Handbook of Polymer Synthesis, Characterization, and Processing. John Wiley & Sons, Inc, Hoboken, NJ, USA (2013). https://doi.org/10.1002/9781118480793.
40. Mori, H., Müller, A.H.E.: New polymeric architectures with (meth)acrylic acid segments. Prog. Polym. Sci. 28, 1403–1439 (2003). https://doi.org/10.1016/s0079-6700(03)00076-5.
41. Gaballa, S.A., Naguib, Y.W., Mady, F.M., Khaled, K.A.: Polyethylene glycol: Properties, applications, and challenges. J. Adv. Biomedical Pharm. Sci. 7, 26–36 (2024).
42. Kobayashi, S.: Polymerization of Oxazolines. In: Polymer Science: A Comprehensive Reference. pp. 397–426. Elsevier (2012). https://doi.org/10.1016/B978-0-444-53349-4.00110-2.
43. Hoogenboom, R.: The future of poly(2-oxazoline)s. Eur. Polym. J. 179, 111521 (2022). https://doi.org/10.1016/j.eurpolymj.2022.111521.
44. Grube, M., Leiske, M.N., Schubert, U.S., Nischang, I.: POx as an Alternative to PEG? A Hydrodynamic and Light Scattering Study. Macromolecules. 51, 1905–1916 (2018). https://doi.org/10.1021/acs.macromol.7b02665.
45. Nemati Mahand, S., Aliakbarzadeh, S., Moghaddam, A., Salehi Moghaddam, A., Kruppke, B., Nasrollahzadeh, M., Khonakdar, H.A.: Polyoxazoline: A review article from polymerization to smart behaviors and biomedical applications. Eur. Polym. J. 178, 111484 (2022). https://doi.org/10.1016/j.eurpolymj.2022.111484.
46. Kobayashi, S.: Polymerization of Oxazolines. In: Polymer Science: A Comprehensive Reference. pp. 397–426. Elsevier (2012). https://doi.org/10.1016/B978-0-444-53349-4.00110-2.
47. Lorson, T., Lübtow, M.M., Wegener, E., Haider, M.S., Borova, S., Nahm, D., Jordan, R., Sokolski-Papkov, M., Kabanov, A.V., Luxenhofer, R.: Poly(2-oxazoline)s based biomaterials: A comprehensive and critical update. Biomaterials. 178, 204–280 (2018). https://doi.org/10.1016/j.biomaterials.2018.05.022.
48. Weber, C., Hoogenboom, R., Schubert, U.S.: Temperature responsive bio-compatible polymers based on poly(ethylene oxide) and poly(2-oxazoline)s. Prog. Polym. Sci. 37, 686–714 (2012). https://doi.org/10.1016/j.progpolymsci.2011.10.002.
49. Aquazol | Polymer Company, https://www.polychemistry.com/products/aquazol/, last accessed 2026/01/26.
50. Jäger, M., Schubert, S., Ochrimenko, S., Fischer, D., Schubert, U.S.: Branched and linear poly(ethylene imine)-based conjugates: synthetic modification, characterization, and application. Chem. Soc. Rev. 41, 4755 (2012). https://doi.org/10.1039/c2cs35146c.
51. Legros, C.: Engineering of Poly(2-oxazoline)s for a potential Use in biomedical Applications, (2015).

52. Sedlacek, O., Monnery, B.D., Hoogenboom, R.: Synthesis of defined high molar mass poly(2-methyl-2-oxazoline). Polym. Chem. 10, 1286–1290 (2019). https://doi.org/10.1039/C9PY00013E.
53. Weber, C., Becer, R.C., Baumgaertel, A., Hoogenboom, R., Schubert, U.S.: Preparation of Methacrylate End-Functionalized Poly(2-ethyl-2-oxazoline) Macromonomers. Des. Monomers Polym. 12, 149–165 (2009). https://doi.org/10.1163/156855509X412090.
54. Weber, C., Remzi Becer, C., Guenther, W., Hoogenboom, R., Schubert, U.S.: Dual Responsive Methacrylic Acid and Oligo(2-ethyl-2-oxazoline) Containing Graft Copolymers. Macromolecules. 43, 160–167 (2010). https://doi.org/10.1021/ma902014q.
55. Meier-Merziger, M., Fickenscher, M., Hartmann, F., Kuttich, B., Kraus, T., Gallei, M., Frey, H.: Synthesis of phase-separated super-H-shaped triblock architectures: poly(L -lactide) grafted from telechelic polyisoprene. Polym. Chem. 14, 2820–2828 (2023). https://doi.org/10.1039/D3PY00230F.
56. Lei, L., Hirata, T., Plank, J.: 40 years of PCE superplasticizers - History, current state-of-the-art and an outlook. Cem. Concr. Res. 157, 106826 (2022). https://doi.org/10.1016/j.cemconres.2022.106826.
57. Ordinary Portland Cement. In: Dictionary of Concrete Technology. pp. 955–957. Springer, Singapore (2025). https://doi.org/10.1007/978-981-97-2998-2_522.
58. DIN EN 197-1:2011-11, Zement- Teil 1: Zusammensetzung, Anforderungen und Konformitätskriterien von Normalzement; Deutsche Fassung EN_197-1:2011, https://www.dinmedia.de/de/-/-/140246044. https://doi.org/10.31030/1758792.
59. Scrivener, K.L., Juilland, P., Monteiro, P.J.M.: Advances in understanding hydration of Portland cement. Cem. Concr. Res. 78, 38–56 (2015). https://doi.org/10.1016/j.cemconres.2015.05.025.
60. Kurdowski, W.: Cement and concrete chemistry. Springer, Dordrecht (2014).
61. Benedix, R.: Bauchemie: Einführung in die Chemie für Bauingenieure und Architekten. Springer Fachmedien, Wiesbaden (2015). https://doi.org/10.1007/978-3-658-04144-1.
62. Flatt, R.J., Bowen, P.: Yodel: A Yield Stress Model for Suspensions. J. Am. Ceram. Soc. 89, 1244–1256 (2006). https://doi.org/10.1111/j.1551-2916.2005.00888.x.
63. Bullard, J.W., Jennings, H.M., Livingston, R.A., Nonat, A., Scherer, G.W., Schweitzer, J.S., Scrivener, K.L., Thomas, J.J.: Mechanisms of cement hydration. Cem. Concr. Res. 41, 1208–1223 (2011). https://doi.org/10.1016/j.cemconres.2010.09.011.
64. Scrivener, K., Ouzia, A., Juilland, P., Kunhi Mohamed, A.: Advances in understanding cement hydration mechanisms. Cem. Concr. Res. 124, 105823 (2019). https://doi.org/10.1016/j.cemconres.2019.105823.
65. John, E., Lothenbach, B.: Cement hydration mechanisms through time – a review. J Mater Sci. 58, 9805–9833 (2023). https://doi.org/10.1007/s10853-023-08651-9.
66. Scrivener, K.L., Nonat, A.: Hydration of cementitious materials, present and future. Cem. Concr. Res. 41, 651–665 (2011). https://doi.org/10.1016/j.cemconres.2011.03.026.
67. Nonat, A.: The structure and stoichiometry of C-S-H. Cem. Concr. Res. 34, 1521–1528 (2004). https://doi.org/10.1016/j.cemconres.2004.04.035.
68. Jakob, C., Jansen, D., Ukrainczyk, N., Koenders, E., Pott, U., Stephan, D., Neubauer, J.: Relating Ettringite Formation and Rheological Changes during the Initial Cement Hydration: A Comparative Study Applying XRD Analysis, Rheological Measurements and Modeling. Materials. 12, 2957 (2019). https://doi.org/10.3390/ma12182957.
69. Scrivener, K., Snellings, R., Lothenbach, B. eds: A Practical Guide to Microstructural Analysis of Cementitious Materials. CRC Press (2016). https://doi.org/10.1201/b19074.
70. Kirchberger, I., Goetz-Neunhoeffer, F., Neubauer, J.: Enhancing the aluminate reaction during OPC hydration by combining increased sulfate content, triethanolamine and tartaric acid. Cem. Concr. Res. 170, 107188 (2023). https://doi.org/10.1016/j.cemconres.2023.107188.

71. Hesse, C., Goetz-Neunhoeffer, F., Neubauer, J.: A new approach in quantitative in-situ XRD of cement pastes: Correlation of heat flow curves with early hydration reactions. Cem. Concr. Res. 41, 123–128 (2011). https://doi.org/10.1016/j.cemconres.2010.09.014.
72. Jansen, D., Goetz-Neunhoeffer, F., Stabler, C., Neubauer, J.: A remastered external standard method applied to the quantification of early OPC hydration. Cem. Concr. Res. 41, 602–608 (2011). https://doi.org/10.1016/j.cemconres.2011.03.004.
73. Zunino, F., Scrivener, K.: Factors influencing the sulfate balance in pure phase C3S/C3A systems. Cem. Concr. Res. 133, 106085 (2020). https://doi.org/10.1016/j.cemconres.2020.106085.
74. Münstedt, H., Schwarzl, F.R.: Deformation and Flow of Polymeric Materials. Springer Berlin Heidelberg, Berlin, Heidelberg (2014). https://doi.org/10.1007/978-3-642-55409-4.
75. Osswald, T.A., Rudolph, N.S.: Polymer rheology: Fundamentals and applications. Hanser Publications, Cincinnati (2015).
76. Mezger, T.G.: The Rheology Handbook: 4th Edition. Vincentz Network, Hanover (2012). https://doi.org/10.1515/9783748600367.
77. Dealy, J.M.: Structure and rheology of molten polymers: From structure to flow behavior and back again. Hanser Publishers, Cincinnati (2018).
78. Carreau, P.J., Kee, D.C.R., Chhabra, R.P.: Rheology of Polymeric Systems: Principles and applications. Carl Hanser Verlag GmbH & Co. KG, München (2021). https://doi.org/10.3139/9781569907238.
79. Tadros, T.F.: Rheology of Dispersions: Principles and Applications. Wiley-VCH, Weinheim (2010). https://doi.org/10.1002/9783527631568.
80. colloidal, https://goldbook.iupac.org/terms/view/C01172, (2025). https://doi.org/10.1351/goldbook.C01172.
81. Roussel, N. ed: Understanding the rheology of concrete. Woodhead Publishing, Cambridge (2012).
82. Coussot, P.: Rheophysics: Matter in all its States. Springer International Publishing, Cham (2014). https://doi.org/10.1007/978-3-319-06148-1.
83. Mewis, J., Wagner, N.J.: Colloidal suspension rheology. Cambridge Univ. Press, Cambridge (2012).
84. Einstein, A.: Eine neue Bestimmung der Moleküldimension. Annalen der Physik. 19, 289–306 (1906).
85. Einstein, A.: Berichtigung zu meiner Arbeit: Eine neue Bestimmung der Moleküldimension. Annalen der Physik. 39, 591–592 (1911).
86. Ovarlez, G., Cohen-Addad, S., Krishan, K., Goyon, J., Coussot, P.: On the existence of a simple yield stress fluid behavior. J. Non-Newton. Fluid Mech. 193, 68–79 (2013). https://doi.org/10.1016/j.jnnfm.2012.06.009.
87. Coussot, P.: Fifty shades of yield stress fluids: rheological challenges and engineering perspectives. Rheol. Acta. 64, 167–193 (2025). https://doi.org/10.1007/s00397-025-01488-w.
88. Yahia, A., Khayat, K.H.: Analytical models for estimating yield stress of high-performance pseudoplastic grout. Cem. Concr. Res. 31, 731–738 (2001). https://doi.org/10.1016/s0008-8846(01)00476-8.
89. Feys, D., Cepuritis, R., Jacobsen, S., Lesage, K., Secrieru, E., Yahia, A.: Measuring Rheological Properties of Cement Pastes: Most common Techniques, Procedures and Challenges. RILEM Technical Letters. 2, 129–135 (2017). https://doi.org/10.21809/rilemtechlett.2017.43.
90. Feys, D., Verhoeven, R., Schutter, G.: Evaluation of Time Independent Rheological Models Applicable to Fresh Self-Compacting Concrete. Appl. Rheol. 17, 56244-1-56244–10 (2007). https://doi.org/10.1515/arh-2007-0018.

91. Mewis, J., Wagner, N.J.: Thixotropy. Adv. Colloid Interface Sci. 147–148, 214–27 (2009). https://doi.org/10.1016/j.cis.2008.09.005.
92. Coussot, P.: Rheometry of pastes, suspensions, and granular materials: applications in industry and environment. Wiley-Interscience, Hoboken, NJ (2005).
93. Vogel, C., Coenen, M., Schack, T., Beyer, D., Haist, M.: Image-based analysis of fresh concrete flow - determining the correlation between flow behavior and rheological properties. ce papers. 6, 621–627 (2023). https://doi.org/10.1002/cepa.2916.
94. Link, J., Sowoidnich, T., Pfitzner, C., Gil-Diaz, T., Heberling, F., Lützenkirchen, J., Schäfer, T., Ludwig, H.-M., Haist, M.: The Influences of Cement Hydration and Temperature on the Thixotropy of Cement Paste. Materials. 13, (2020). https://doi.org/10.3390/ma13081853.
95. Jakob, C., Jansen, D., Dengler, J., Neubauer, J.: Controlling ettringite precipitation and rheological behavior in ordinary Portland cement paste by hydration control agent, temperature and mixing. Cem. Concr. Res. 166, 107289 (2023). https://doi.org/10.1016/j.cemconres.2023.107095.
96. Sha, S., Mantellato, S., Weckwerth, S.A., Zhang, Z., Shi, C., Flatt, R.J.: Do superplasticizers work the way we think? New insights from their effect on the percolation threshold of limestone pastes. Cem. Concr. Res. 172, 107235 (2023). https://doi.org/10.1016/j.cemconres.2023.107235.
97. Roussel, N., Ovarlez, G., Garrault, S., Brumaud, C.: The origins of thixotropy of fresh cement pastes. Cem. Concr. Res. 42, 148–157 (2012). https://doi.org/10.1016/j.cemconres.2011.09.004.
98. Hayek, M., El Bitouri, Y., Bouarab, K., Yahia, A.: Structural Build-Up of Cement Pastes: A Comprehensive Overview and Key Research Directions. Constr. Build. Mater. 5, 31 (2025). https://doi.org/10.3390/constrmater5020031.
99. Roussel, N., Bessaies-Bey, H., Kawashima, S., Marchon, D., Vasilic, K., Wolfs, R.: Recent advances on yield stress and elasticity of fresh cement-based materials. Cem. Concr. Res. 124, 105798 (2019). https://doi.org/10.1016/j.cemconres.2019.105798.
100. DIN EN 1015-3:2007-05 Prüfverfahren für Mörtel für Mauerwerk - Teil 3: Bestimmung der Konsistenz von Frischmörtel (mit Ausbreittisch);, https://www.dinmedia.de/de/-/-/95365414, (2007). https://doi.org/10.31030/9832047.
101. Haist, M., Link, J., Nicia, D., Leinitz, S., Baumert, C., Bronk, T., Cotardo, D., Eslami Pirharati, M., Fataei, S., Garrecht, H., Gehlen, C., Hauschildt, I., Ivanova, I., Jesinghausen, S., Klein, C., Krauss, H.-W., Lohaus, L., Lowke, D., Mazanec, O., Pawelczyk, S., Pott, U., Radebe, N.W., Riedmiller, J.J., Schmid, H.-J., Schmidt, W., Secrieru, E., Stephan, D., Thiedeitz, M., Wilhelm, M., Mechtcherine, V.: Interlaboratory study on rheological properties of cement pastes and reference substances: comparability of measurements performed with different rheometers and measurement geometries. Mater. Struct. 53, 1–26 (2020). https://doi.org/10.1617/s11527-020-01477-w.
102. Lange, A., Plank, J.: Optimization of comb-shaped polycarboxylate cement dispersants to achieve fast-flowing mortar and concrete. J. Appl. Polym. Sci. 132, (2015). https://doi.org/10.1002/app.42529.
103. Dhar, S., Liberto, T., Barentin, C., Divoux, T., Robisson, A.: Discrepancies in dynamic yield stress measurements of cement pastes. Rheol. Acta. (2024). https://doi.org/10.1007/s00397-024-01465-9.
104. Matos, P.R., Pilar, R., Casagrande, C.A., Gleize, P.J.P., Pelisser, F.: Comparison between methods for determining the yield stress of cement pastes. J Braz. Soc. Mech. Sci. Eng. 42, (2020). https://doi.org/10.1007/s40430-019-2111-2.
105. Kantro, D.: Influence of Water-Reducing Admixtures on Properties of Cement Paste—A Miniature Slump Test. Cem. Concr. Aggreg. 2, 95–102 (1980). https://doi.org/10.1520/CCA10190J.

106. Gao, J., Fourie, A.: Spread is better: An investigation of the mini-slump test. Minerals Engineering. 71, 120–132 (2015). https://doi.org/10.1016/j.mineng.2014.11.001.
107. Roussel, N., Coussot, P.: "Fifty-cent rheometer" for yield stress measurements: From slump to spreading flow. J. Rheol. 49, 705–718 (2005). https://doi.org/10.1122/1.1879041.
108. Murata, J.: Flow and deformation of fresh concrete. Matériaux et Constructions. 17, 117–129 (1984). https://doi.org/10.1007/BF02473663.
109. Qian, Y., Kawashima, S.: Distinguishing dynamic and static yield stress of fresh cement mortars through thixotropy. Cem. Concr. Compos. 86, 288–296 (2018). https://doi.org/10.1016/j.cemconcomp.2017.11.019.
110. Haist, M.: Zur Rheologie und den physikalischen Wechselwirkungen bei Zementsuspensionen, (2009).
111. Bala, M., Zentar, R., Boustingorry, P.: Comparative study of the yield stress determination of cement pastes by different methods. Mater Struct. 52, 102 (2019). https://doi.org/10.1617/s11527-019-1403-4.
112. Yuan, Q., Zhou, D., Khayat, K.H., Feys, D., Shi, C.: On the measurement of evolution of structural build-up of cement paste with time by static yield stress test vs. small amplitude oscillatory shear test. Cem. Concr. Res. 99, 183–189 (2017). https://doi.org/10.1016/j.cemconres.2017.05.014.
113. Nicia, D., Jakob, C., Jansen, D., Ivanov, D., Mazanec, O., Dengler, J., Neubauer, J., Lowke, D.: Thixotropy of superplasticized cement pastes – Underlying mechanisms considering the polycarboxylate molecular structure, interparticle interactions and hydration kinetics. Cem. Concr. Res. 173, 107289 (2023). https://doi.org/10.1016/j.cemconres.2023.107289.
114. Mostafa, A.M., Yahia, A.: Physico-chemical kinetics of structural build-up of neat cement-based suspensions. Cem. Concr. Res. 97, 11–27 (2017). https://doi.org/10.1016/j.cemconres.2017.03.003.
115. Michel, L., Reiter, L., Sanner, A., Flatt, R.J., Kammer, D.S.: Structural build-up at rest in the induction and acceleration periods of Portland Cement. Cem. Concr. Res. 186, 107665 (2024). https://doi.org/10.1016/j.cemconres.2024.107665.
116. Jiao, D., Schutter, G.: Insights into the viscoelastic properties of cement paste based on SAOS technique. Constr. Build. Mater. 357, 129320 (2022). https://doi.org/10.1016/j.conbuildmat.2022.129320.
117. Ukrainczyk, N., Thiedeitz, M., Kränkel, T., Koenders, E., Gehlen, C.: Modeling SAOS Yield Stress of Cement Suspensions: Microstructure-Based Computational Approach. Materials. 13, (2020). https://doi.org/10.3390/ma13122769.
118. Yuan, Q., Lu, X., Khayat, K.H., Feys, D., Shi, C.: Small amplitude oscillatory shear technique to evaluate structural build-up of cement paste. Mater Struct. 50, 112 (2016). https://doi.org/10.1617/s11527-016-0978-2.
119. El Bitouri, Y.: Rheological Behavior of Cement Paste: A Phenomenological State of the Art. Eng. 4, 1891–1904 (2023).
120. Thiedeitz, M., Kränkel, T., Gehlen, C.: Viscoelastoplastic classification of cementitious suspensions: transient and non-linear flow analysis in rotational and oscillatory shear flows. Rheol. Acta. 61, 549–570 (2022). https://doi.org/10.1007/s00397-022-01358-9.
121. Habel, K., Viviani, M., Denarié, E., Brühwiler, E.: Development of the mechanical properties of an Ultra-High Performance Fiber Reinforced Concrete (UHPFRC). Cement and Concrete Research. 36, 1362–1370 (2006). https://doi.org/10.1016/j.cemconres.2006.03.009.
122. Schiefer, C., Plank, J.: CO_2 emission of polycarboxylate superplasticizers (PCEs) used in concrete. J. Clean. Prod. 427, 138785 (2023). https://doi.org/10.1016/j.jclepro.2023.138785.

123. Kujawa, W., Olewnik-Kruszkowska, E., Nowaczyk, J.: Concrete Strengthening by Introducing Polymer-Based Additives into the Cement Matrix—A Mini Review. Materials. 14, 6071 (2021). https://doi.org/10.3390/ma14206071.
124. Karakuzu, K., Kobya, V., Mardani-Aghabaglou, A., Felekoğlu, B., Ramyar, K.: Adsorption properties of polycarboxylate ether-based high range water reducing admixture on cementitious systems: A review. Constr. Build. Mater. 312, 125366 (2021). https://doi.org/10.1016/j.conbuildmat.2021.125366.
125. Sha, S., Wang, M., Shi, C., Xiao, Y.: Influence of the structures of polycarboxylate superplasticizer on its performance in cement-based materials-A review. Constr. Build. Mater. 233, 117257 (2020). https://doi.org/10.1016/j.conbuildmat.2019.117257.
126. Marchon, D., Juilland, P., Gallucci, E., Frunz, L., Flatt, R.J.: Molecular and submolecular scale effects of comb-copolymers on tri-calcium silicate reactivity: Toward molecular design. J. Am. Ceram. Soc. 100, 817–841 (2017). https://doi.org/10.1111/jace.14695.
127. Hanehara, S., Yamada, K.: Rheology and early age properties of cement systems. Cem. Concr. Res. 38, 175–195 (2008). https://doi.org/10.1016/j.cemconres.2007.09.006.
128. Yamada, K., Takahashi, T., Hanehara, S., Matsuhisa, M.: Effects of the chemical structure on the properties of polycarboxylate-type superplasticizer. Cem. Concr. Res. 30, 197–207 (2000). https://doi.org/10.1016/S0008-8846(99)00230-6.
129. Wagner, T., Lange, T., Gädt, T.: Meta-Analysis of PCE Structures as Dispersants in Cementitious Materials. ACI SP. 354, 61–74 (2022).
130. Mantellato, S., Flatt, R.J.: Shifting factor—A new paradigm for studying the rheology of cementitious suspensions. J. Am. Ceram. Soc. 103, 3562–3574 (2020). https://doi.org/10.1111/jace.17040.
131. Mantellato, S.: Flow Loss in Superplasticized Cement Pastes, https://www.research-collection.ethz.ch/entities/publication/60d26af4-3a78-44e0-9df7-425ae6eaf318, (2017).
132. Weckwerth, S.A., Temme, R.L., Flatt, R.J.: Experimental method and thermodynamic model for competitive adsorption between polycarboxylate comb copolymers. Cem. Concr. Res. 151, 106523 (2022). https://doi.org/10.1016/j.cemconres.2021.106523.
133. Gay, C., Raphaël, E.: Comb-like polymers inside nanoscale pores. Advances in Colloid and Interface Science. 94, 229–236 (2001). https://doi.org/10.1016/S0001-8686(01)00062-8.
134. Marchon, D., Sulser, U., Eberhardt, A., Flatt, R.J.: Molecular design of comb-shaped polycarboxylate dispersants for environmentally friendly concrete. Soft Matter. 9, 10719 (2013). https://doi.org/10.1039/c3sm51030a.
135. Atkins, P., de Paula, J.: Physikalische Chemie. Wiley-VCH, Weinheim (2013).
136. Plank, J., Hirsch, C.: Impact of zeta potential of early cement hydration phases on superplasticizer adsorption. Cem. Concr. Res. 37, 537–542 (2007). https://doi.org/10.1016/j.cemconres.2007.01.007.
137. Sha, S., Sirajuddin, M., Flatt, R.J.: D3 method: Direct and delayed dosing: New insights into specific surface area modification by superplasticizers. Cem. Concr. Res. 181, 107541 (2024). https://doi.org/10.1016/j.cemconres.2024.107541.
138. Smith, B.C.: Fundamentals of Fourier Transform Infrared Spectroscopy. CRC Press, Boca Raton (2011).
139. Hoffmann, G. ed: Infrared and Raman spectroscopy: Principles and applications. De Gruyter, Boston (2023).
140. Larkin, P.J.: Infrared and Raman spectroscopy: principles and spectral interpretation. Elsevier, Amsterdam (2018).
141. Günzler, H., Gremlich, H.-U.: IR-Spektroskopie: Eine Einführung. Wiley-VCH, Weinheim (2003).
142. Griffiths, P.R., De Haseth, J.A.: Fourier transform infrared spectrometry. Wiley-Interscience, Hoboken, NJ (2007).

143. Choosing the right ATR crystal for FTIR analysis, https://specac.com/theory-articles/choosing-the-right-atr-crystal/, last accessed 2026/02/02.
144. Wallevik, O.H., Feys, D., Wallevik, J.E., Khayat, K.H.: Avoiding inaccurate interpretations of rheological measurements for cement-based materials. Cem. Concr. Res. 78, 100–109 (2015). https://doi.org/10.1016/j.cemconres.2015.05.003.
145. Mechtcherine, V., Muthukrishnan, S., Mikhalev, D. eds: Opus Fluidum Futurum—Rheology of Reactive, Multiscale, Multiphase Construction Materials. (2026).
146. Meyer, T.: Synthesis and Characterization of Polyelectrolytes and their Influence on the Hardening of Cement Pastes, (2022).
147. Mechtcherine, V., Khayat, K., Secrieru, E.: Rheology and Processing of Construction Materials: RheoCon2 & SCC9. Springer Nature (2019).
148. Wagner, T., Gädt, T.: Rheological Investigation of a Set of PCE Superplasticizers in Cement. ce papers. 6, 607–613 (2023). https://doi.org/10.1002/cepa.2850.
149. Beier, K.: Adsorption Properties of Polycarboxylate Ethers and their Influence on the Workability of Cement Pastes, (2024).
150. Manneville, S.: Recent experimental probes of shear banding. Rheol. Acta. 47, 301–318 (2008). https://doi.org/10.1007/s00397-007-0246-z.
151. Link, J., Strybny, B., Divoux, T., Sowoidnich, T., Coenen, M., Gstöhl, S., Schlepütz, C.M., Zuber, M., Hellmann, S., Rößler, C., Lützenkirchen, J., Heberling, F., Manneville, S., Schäfer, T., Ludwig, H.-M., Haist, M.: Mechanisms of thixotropy in cement suspensions considering influences from shear history and hydration. ce/papers. 6, 698–704 (2023). https://doi.org/10.1002/cepa.2810.
152. Juilland, P., Gallucci, E., Flatt, R., Scrivener, K.: Dissolution theory applied to the induction period in alite hydration. Cem. Concr. Res. 40, 831–844 (2010). https://doi.org/10.1016/j.cemconres.2010.01.012.
153. Zhang, K., Mezhov, A., Schmidt, W.: Effect of agitation during the early-age hydration on thixotropy and morphology of cement paste. Mater Struct. 57, 226 (2024). https://doi.org/10.1617/s11527-024-02504-w.
154. Almakhadmeh, M., Soliman, A.M.: Effects of mixing water temperatures on properties of one-part alkali-activated slag paste. Constr. Build. Mater. 266, 121030 (2021). https://doi.org/10.1016/j.conbuildmat.2020.121030.
155. Dalas, F., Pourchet, S., Nonat, A., Rinaldi, D., Sabio, S., Mosquet, M.: Fluidizing efficiency of comb-like superplasticizers: The effect of the anionic function, the side chain length and the grafting degree. Cem. Concr. Res. 71, 115–123 (2015). https://doi.org/10.1016/j.cemconres.2015.02.001.
156. Stecher, J., Plank, J.: Novel concrete superplasticizers based on phosphate esters. Cem. Concr. Res. 119, 36–43 (2019). https://doi.org/10.1016/j.cemconres.2019.01.006.
157. Liu, X., Guan, J., Lai, G., Zheng, Y., Wang, Z., Cui, S., Lan, M., Li, H.: Novel designs of polycarboxylate superplasticizers for improving resistance in clay-contaminated concrete. J. Ind. Eng. Chem. 55, 80–90 (2017). https://doi.org/10.1016/j.jiec.2017.06.031.
158. Glassner, M., Vergaelen, M., Hoogenboom, R.: Poly(2-oxazoline)s: A comprehensive overview of polymer structures and their physical properties. Polym. Int. 67, 32–45 (2018). https://doi.org/10.1002/pi.5457.
159. Meyer, T., Wilhelm, M.: Poly(2-methyl-2-oxazoline) based Polycarboxylate Superplasticizers: a new perspective on the structure-property relationship of Polycarboxylate Ethers (PCE). in writing.
160. Fayt, R., Forte, R., Jacobs, C., Jerome, R., Ouhadi, T., Teyssie, Ph., Varshney, S.K.: New initiator system for the living anionic polymerization of tert-alkyl acrylates. Macromolecules. 20, 1442–1444 (1987). https://doi.org/10.1021/ma00172a058.
161. Arens, L.: Polyelectrolyte hydrogels with various network architectures: Synthesis, characterisation and use in membrane-free desalination, (2018).

162. Bai, L., Tan, L., Chen, L., Liu, S., Wang, Y.: Preparation and characterizations of poly(2-methyl-2-oxazoline) based antifouling coating by thermally induced immobilization. J. Mater. Chem. B. 2, 7785–7794 (2014). https://doi.org/10.1039/c4tb01383b.
163. Gay, C., Raphaël, E.: Comb-like polymers inside nanoscale pores. Adv. Colloid Interface Sci. 94, 229–236 (2001). https://doi.org/10.1016/S0001-8686(01)00062-8.
164. Sha, S., Ma, Y., Lei, L., Zhang, Y., Liu, Y., Xiao, Y., Shi, C.: Effect of polycarboxylate superplasticizers on the growth of ettringite in deionized water and synthetic cement pore solution. Constr. Build. Mater. 341, 127602 (2022). https://doi.org/10.1016/j.conbuildmat.2022.127602.
165. Schönlein, M., Plank, J.: Influence of PCE kind and dosage on ettringite crystallization performed under terrestrial and microgravity conditions. J. Am. Ceram. Soc. 101, 3575–3584 (2018). https://doi.org/10.1111/jace.15513.
166. Lei, L., Chomyn, C., Schmid, M., Plank, J.: Characterization data of reference industrial polycarboxylate superplasticizers used within Priority Program DFG SPP 2005 “Opus Fluidum Futurum - Rheology of reactive, multiscale, multiphase construction materials.” DIB. 31, 106026 (2020). https://doi.org/10.1016/j.dib.2020.106026.
167. Bisutti, I., Hilke, I., Raessler, M.: Determination of total organic carbon – an overview of current methods. TrAC Trends in Analytical Chemistry. 23, 716–726 (2004). https://doi.org/10.1016/j.trac.2004.09.003.
168. Fang, X., Shi, Y., Yan, C., Wang, H., Hui, J.: Polycarboxylate ether superplasticizer with gradient structure: excellent dispersion capability and sulfate resistance. Colloid Polym Sci. 300, 1113–1127 (2022). https://doi.org/10.1007/s00396-022-04994-y.
169. Zhang, L., Miao, X., Kong, X., Zhou, S.: Retardation effect of PCE superplasticizers with different architectures and their impacts on early strength of cement mortar. Cem. Concr. Compos. 104, 103369 (2019). https://doi.org/10.1016/j.cemconcomp.2019.103369.
170. Winnefeld, F., Becker, S., Pakusch, J., Götz, T.: Effects of the molecular architecture of comb-shaped superplasticizers on their performance in cementitious systems. Cem. Concr. Compos. 29, 251–262 (2007). https://doi.org/10.1016/j.cemconcomp.2006.12.006.
171. Brittain, W.J., Minko, S.: A structural definition of polymer brushes. J. Polym. Sci. A Polym. Chem. 45, 3505–3512 (2007). https://doi.org/10.1002/pola.22180.
172. Gast, A.P., Leibler, L.: Interactions of sterically stabilized particles suspended in a polymer solution. Macromolecules. 19, 686–691 (1986). https://doi.org/10.1021/ma00157a035.
173. Hasegawa, R., Aoki, Y., Doi, M.: Optimum Graft Density for Dispersing Particles in Polymer Melts. Macromolecules. 29, 6656–6662 (1996). https://doi.org/10.1021/ma960365x.
174. Bessaies-Bey, H., Massoussi, N., Mulik, S., Baumann, R., Schmitz, M., Radler, M., Gelardi, G., Flatt, R.J., Roussel, N.: Polycarboxylate ester adsorption on cement grains: Influence of polydispersity. Cem. Concr. Res. 143, 106383 (2021). https://doi.org/10.1016/j.cemconres.2021.106383.
175. Uchikawa, H., Hanehara, S., Sawaki, D.: The Role of Steric Repulsive Force in the Dispersion of Cement Particles in Fresh Paste Prepared with Organic Admixture. Cem. Concr. Res. 27, 37–50 (1997).
176. Gubarev, A.S., Lezov, A.A., Podsevalnikova, A.N., Mikusheva, N.G., Fetin, P.A., Zorin, I.M., Aseyev, V.O., Sedlacek, O., Hoogenboom, R., Tsvetkov, N.V.: Conformational Parameters and Hydrodynamic Behavior of Poly(2-Methyl-2-Oxazoline) in a Broad Molar Mass Range. Polymers. 15, 623 (2023). https://doi.org/10.3390/polym15030623.
177. Kienberger, F., Pastushenko, V.Ph., Kada, G., Gruber, H.J., Riener, C., Schindler, H., Hinterdorfer, P.: Static and Dynamical Properties of Single Poly(Ethylene Glycol) Molecules Investigated by Force Spectroscopy. Single Mol. 1, 123–128 (2000).

https://doi.org/10.1002/1438-5171(200006)1:2%253C123::AID-SIMO123%253E3.0.CO;2-3.
178. Nikitin, A.N., Castignolles, P., Charleux, B., Vairon, J.-P.: Determination of Propagation Rate Coefficient of Acrylates by Pulsed-Laser Polymerization in the Presence of Intramolecular Chain Transfer to Polymer. Macromol. Rapid Commun. 24, 778–782 (2003). https://doi.org/10.1002/marc.200350025.
179. Furuncuoğlu, T., Uğur, İ., Değirmenci, İ., Aviyente, V.: Role of Chain Transfer Agents in Free Radical Polymerization Kinetics. Macromolecules. 43, 1823–1835 (2010). https://doi.org/10.1021/ma902803p.
180. Sprado, M.: Investigation of branched polymers using DOSY on a low field NMR-spectrometer, (2025).
181. Gelardi, G., Sanson, N., Nagy, G., Flatt, R.J.: Characterization of Comb-Shaped Copolymers by Multidetection SEC, DLS and SANS. Polymers. 9, (2017). https://doi.org/10.3390/polym9020061.
182. Ng, S., Plank, J.: Interaction mechanisms between Na montmorillonite clay and MPEG-based polycarboxylate superplasticizers. Cem. Concr. Res. 42, 847–854 (2012). https://doi.org/10.1016/j.cemconres.2012.03.005.
183. Fengler, C., Keller, J., Ratzsch, K.-F., Wilhelm, M.: In Situ RheoNMR Correlation of Polymer Segmental Mobility with Mechanical Properties during Hydrogel Synthesis. Adv. Sci. 9, 2104231 (2022). https://doi.org/10.1002/advs.202104231.
184. Räntzsch, V., Özen, M.B., Ratzsch, K.-F., Stellamanns, E., Sprung, M., Guthausen, G., Wilhelm, M.: Polymer Crystallization Studied by Hyphenated Rheology Techniques: Rheo-NMR, Rheo-SAXS, and Rheo-Microscopy. Macromol. Mater. Eng. 304, 1800586 (2019). https://doi.org/10.1002/mame.201800586.
185. Skoog, D.A., Holler, F.J., Crouch, S.R.: Instrumentelle Analytik: Grundlagen - Geräte - Anwendungen. Springer Spektrum, Berlin ; Heidelberg (2013). https://doi.org/10.1007/978-3-642-39726-4.
186. Boulet-Audet, M., Vollrath, F., Holland, C.: Rheo-attenuated total reflectance infrared spectroscopy: a new tool to study biopolymers. Phys. Chem. Chem. Phys. 13, 3979 (2011). https://doi.org/10.1039/c0cp02599b.
187. Siesler, H.W.: Rheo-optical Fourier transform IR spectroscopy of polyurethane elastomers. Polym. Bull. 9, 382–389 (1983). https://doi.org/10.1007/BF00265317.
188. Wang, H., Palmer, R.A., Manning, C.J.: Study of Impulse Polymer Rheo-Optics by Step-Scan FT-IR Time-Resolved Spectroscopy. Appl. Spectrosc. 51, 1245–1250 (1997). https://doi.org/10.1366/0003702971941827.
189. Scherzer, T.: Rheo-optical FTIR spectroscopy of epoxy resins. J. Appl. Polym. Sci. 58, 501–514 (1995). https://doi.org/10.1002/app.1995.070580303.
190. Scherzer, T.: Molecular orientation in novolac cured epoxy resins as studied by rheo-optical FTIR spectroscopy. J. Appl. Polym. Sci. 70, 247–259 (1998). https://doi.org/10.1002/(SICI)1097-4628(19981010)70:2%253C247::AID-APP5%253E3.0.CO;2-U.
191. Budevska, B.O., Manning, C.J., Griffiths, P.R., Roginski, R.T.: Step-Scan Fourier Transform Infrared Study on the Effect of Dynamic Strain on Isotactic Polypropylene. Appl. Spectrosc. 47, 1843–1851 (1993). https://doi.org/10.1366/0003702934065920.
192. Hofmann, G.R., Sevegney, M.S., Kannan, R.M.: A Rheo-Optical FTIR Spectrometer for Investigating Molecular Orientation and Viscoelastic Behavior in Polymers. Int. J. Polym. Anal. Ch. 9, 245–274 (2004). https://doi.org/10.1080/10236660490920237.
193. Nishikawa, Y., Nakano, T., Noda, I.: Two-Dimensional Correlation Study of Uniaxially Drawn Poly(Ethylene Terephthalate) Films by Using Attenuated Total Reflection Based Dynamic Compression Modulation Step-Scan Fourier Transform Infrared in Combination

with Spectral Simulation Analysis by Density Functional Theory. Appl. Spectrosc. 60, 145–154 (2006). https://doi.org/10.1366/000370206776023386.
194. Nishikawa, Y., Nakano, T., Noda, I.: Impulse-Induced Compression Rheo-Optics Study of Polymers Using Attenuated Total Reflection Based Step-Scan Fourier Transform Infrared Time-Resolved Spectroscopy. Appl. Spectrosc. 62, 948–955 (2008). https://doi.org/10.1366/000370208785793353.
195. Nishikawa, Y., Nakano, T., Noda, I.: Rheo-Optical Study of Polymers by Using Time-Resolved Soft-Pulse Compression Attenuated Total Reflection Step-Scan Fourier Transform Infrared Spectroscopy. Appl. Spectrosc. 63, 1204–1210 (2009). https://doi.org/10.1366/000370209789806939.
196. Nishikawa, Y., Nakano, T., Noda, I.: Detection of Reversible Nonlinear Dynamic Responses of Polymer Films by Using Time-Resolved Soft-Pulse Compression Attenuated Total Reflection Step-Scan Fourier Transform Infrared Spectroscopy. Appl. Spectrosc. 66, 312–318 (2012). https://doi.org/10.1366/11-06481.
197. Feustel, M., Küchenmeister, C.: Detailed analysis of curing reactions of polyurethane resins using the Rheonaut technology for simultaneous rheometry and FTIR. Application Note 247. 1–4 (2010).
198. Boulet-Audet, M., Terry, A.E., Vollrath, F., Holland, C.: Silk protein aggregation kinetics revealed by Rheo-IR. Acta Biomater. 10, 776–784 (2014). https://doi.org/10.1016/j.actbio.2013.10.032.
199. Beskers, T.F.: Entwicklung eines chemisch sensitiven Detektors für die Gelpermeationschromatographie auf Basis von Infrarotspektroskopie, (2014).
200. Kempfert, K.D., Jiang, E.Y., Oas, S., Coffin, J.: Detectors for Fourier Transform Spectroscopy. AN-00125. (2001).
201. Overview of materials for Stainless Steel, https://matweb.com/search/DataSheet.aspx?MatGUID=71396e57ff5940b791ece120e4d563e0, last accessed 2026/02/11.
202. Titanium, Ti, https://matweb.com/search/DataSheet.aspx?MatGUID=66a15d609a3f4c829cb6ad08f0dafc01&ckck=1, last accessed 2026/02/11.
203. Aluminum, Al, https://matweb.com/search/datasheet.aspx?MatGUID=0cd1edf33ac145ee93a0aa6fc666c0e0, last accessed 2026/02/11.
204. Xu, X., Klein, C.O., Figuli, R., Wilhelm, M.: Investigations on rubber curing with novel Rheo-IR. in writing.
205. Goecke, A.: Recycling of Polyolefins, (2022).
206. Melges, Y.R.: Hydrogel Synthesis from Polyacrylic Acid and Analysis of its chemo-mechanical Properties via Rheo-IR, (2026).
207. Kißling, P.A., Link, J., Heinemann, M., Lübkemann-Warwas, F., Rieck genannt Best, F., Sowoidnich, T., Mundstock, A., Ludwig, H.-M., Haist, M., Bigall, N.C.: Influence of in situ ettringite formation on the rheological properties of quartz suspensions. Constr. Build. Mater. 408, 133678 (2023). https://doi.org/10.1016/j.conbuildmat.2023.133678.
208. Horgnies, M., Chen, J.J., Bouillon, C.: Overview about the use of Fourier Transform Infrared spectroscopy to study cementitious materials. Presented at the Materials Characterisation 2013 June 4 (2013). https://doi.org/10.2495/MC130221.
209. Ylmén, R., Jäglid, U., Panas, I.: Monitoring Early Hydration of Cement by Ex Situ and In Situ ATR-FTIR – a Comparative Study. J. Am. Ceram. Soc. 97, 3669–3675 (2014). https://doi.org/10.1111/jace.13186.
210. Poupelloz, E., Gauffinet, S., Nonat, A.: Study of nucleation and growth processes of ettringite in diluted conditions. Cem. Concr. Res. 127, 105915 (2020). https://doi.org/10.1016/j.cemconres.2019.105915.

211. Dalas, F., Pourchet, S., Rinaldi, D., Nonat, A., Sabio, S., Mosquet, M.: Modification of the rate of formation and surface area of ettringite by polycarboxylate ether superplasticizers during early C_3A–$CaSO_4$ hydration. Cem. Concr. Res. 69, 105–113 (2015). https://doi.org/10.1016/j.cemconres.2014.12.007.
212. Winnefeld, F., Zingg, A., Holzer, L., Pakusch, J., Becker, S.: The ettringite-superplasticizer interaction and its impact on the ettringite distribution in cement suspensions. Superplasticizers and other chemical admixtures. Proceedings ninth ACI international conference. Sevilla Spain, (2009).
213. Pelet, J.M., Putnam, D.: High Molecular Weight Poly(methacrylic acid) with Narrow Polydispersity by RAFT Polymerization. Macromolecules. 42, 1494–1499 (2009). https://doi.org/10.1021/ma801433g.
214. Carletto, A., Cardozo, A.F., Suriano, R., Manoury, E., Turri, S., Poli, R.: Core Cross-Linked Amphiphilic Star-Block Copolymers with (Meth)acrylic Acid Shells Prepared by Atom Transfer Radical Polymerization. Isr. J. Chem. 52, 328–338 (2012). https://doi.org/10.1002/ijch.201100125.
215. Özen, S., Altun, M.G., Mardani-Aghabaglou, A.: Effect of the polycarboxylate based water reducing admixture structure on self-compacting concrete properties: Main chain length. Constr. Build. Mater. 255, 119360 (2020). https://doi.org/10.1016/j.conbuildmat.2020.119360.
216. Wang, J., Yin, J., Kong, X.: Influences of PCE superplasticizers with varied architectures on the formation and morphology of calcium hydroxide crystals. Cem. Concr. Res. 152, 106670 (2022). https://doi.org/10.1016/j.cemconres.2021.106670.
217. Lu, Z.C., Haist, M., Ivanov, D., Jakob, C., Jansen, D., Leinitz, S., Link, J., Mechtcherine, V., Neubauer, J., Plank, J., Schmidt, W., Schilde, C., Schröfl, C., Sowoidnich, T., Stephan, D.: Characterization data of reference cement CEM I 42.5 R used for priority program DFG SPP 2005 “Opus Fluidum Futurum - Rheology of reactive, multiscale, multiphase construction materials.” DIB. 27, 104699 (2019). https://doi.org/10.1016/j.dib.2019.104699.
218. Pott, U., Crasselt, C., Fobbe, N., Haist, M., Heinemann, M., Hellmann, S., Ivanov, D., Jakob, C., Jansen, D., Lei, L., Li, R., Link, J., Lowke, D., Mechtcherine, V., Neubauer, J., Nicia, D., Plank, J., Reißig, S., Schäfer, T., Schilde, C., Schmidt, W., Schröfl, C., Sowoidnich, T., Strybny, B., Ukrainczyk, N., Wolf, J., Xiao, P., Stephan, D.: Characterization data of reference materials used for phase II of the priority program DFG SPP 2005 “Opus Fluidum Futurum – Rheology of reactive, multiscale, multiphase construction materials.” DIB. 47, 108902 (2023). https://doi.org/10.1016/j.dib.2023.108902.
219. Ezzat, M., Xu, X., El Cheikh, K., Lesage, K., Hoogenboom, R., Schutter, G.: Structure-property relationships for polycarboxylate ether superplasticizers by means of RAFT polymerization. Journal of Colloid and Interface Science. 553, 788–797 (2019). https://doi.org/10.1016/j.jcis.2019.06.088.
220. Kobayashi, S., Masuda, E., Shoda, S., Shimano, Y.: Synthesis of acryl- and methacryl-type macromonomers and telechelics by utilizing living polymerization of 2-oxazolines. Macromolecules. 22, 2878–2884 (1989). https://doi.org/10.1021/ma00197a002.
221. Efstratiadis, V., Tselikas, G., Hadjichristidis, N., Li, J., Yunan, W., Mays, J.W.: Synthesis and characterization of poly(methyl methacrylate) star polymers. Polym. Int. 33, 171–179 (1994). https://doi.org/10.1002/pi.1994.210330208.
222. Aouichat, B.S., Hosseinpoor, M., Yahia, A., Dupuis, M.: Dispersion of cellulose nanocrystals and cellulose nanofibers in aqueous suspensions: synergistic effect of concrete superplasticizers. Mater Struct. 58, 289 (2025). https://doi.org/10.1617/s11527-025-02811-w.

8 Acknowledgements

I would like to thank:

- **Prof. Manfred Wilhelm** for the opportunity to do a PhD in your working group. Moreover, I would like to thank you for all the possibilities you provide us with. Especially your encouragement to visit conferences and do a research stay abroad cannot be taken for granted. Travelling was one of my favorite parts of PhD, so thank you deeply for making it possible.
- **Dr. Christopher O. Klein** for the many hours we spent in front of the Rheo-FTIR, the shared laughter, the confusion and the Eureka-Moments. I had so much fun building this set-up with you. I am proud of our creation.
- **Dr. Roxana Figuli** for your patience and your open ear when I needed it. I knew I could always come to you and ask for help.
- **Dr. Max Schußmann**, my favorite person in and outside of the lab. I would like to thank you for your scientific contribution to this work, for our fruitful discussions and your great ideas on where to take this project. Moreover, thank you for being there for me all the time, through the good and the bad, the tears of despair and the celebrations of success. Every day, I am grateful to have you in my life.
- **Anika Goecke**, the best office partner I could wish for. Thank you for all the numerous discussions on data, slides and mental health. You helped me so many times when I felt stuck, both scientifically and mentally. I wouldn't have made it without you.
- **My students Yago and Klaus**. I thank both of you for trusting me to be your supervisor, for bringing my ideas to live and developing them into independent works. I am happy to have contributed to your academic career, wherever it may take you. Klaus, I thank you for your amazing master thesis on linear superplasticizers. Your results have contributed substantially to chapters 3.1 und 4.2.2 in this dissertation. Also, thank you for proof-reading parts of my thesis. Yago, I thank you for your great bachelor thesis on hydrogel kinetics observed via Rheo-FTIR. Your work has contributed substantially to chapter 5.4.
- **Melvin Herzog**. Thank you for your help with the million (I might exaggerate) cement paste measurements we performed together. With your exact execution of the measurement protocol, you were one of the best lab assistants I had. The data we obtained together basically makes up chapter 4! I wish you all the best for the rest of your training to a laboratory technician.
- **Matthias Weber** from the **Engler-Bunte-Institute** (EBI) in Karlsruhe. Thank you for performing the DOC measurements.
- **Jan Pesek** from **AK Grunwaldt**. Thank you for your expertise and technical support with the gas purge at the Rheo-FTIR.
- **The Workshop, especially Andreas Wagner**. Thank you for all your work on the Rheo-FTIR. The set-up would not look the same without our discussions and all of your ideas.

I will forever appreciate how you elevated my wonky prototypes made from cardboard, tape and a crazy idea to beautiful, well thought-through designs.

- **Prof. Patrick Théato and his group**, who were so generous to let me use their laboratory infrastructure. A big thanks goes to **Birgit Huber**, my hero, who measured so many aqueous SECs for me. Although none of them made it to my final thesis (I'm sorry), your help will forever be appreciated. In a time when the complex characterization of comb copolymers was making me feel helpless and alone, you and your support was the silver lining on the horizon. You probably don't know how your simple "I can help you with that" had me floating for weeks. Moreover, I would like to deeply thank **Klara Urbschat** for helping me with the DMAc SEC and **Alexandra Orlova, Dr. Sven Schneider and Dr. Nico Zuber** for the many, many 400 MHz NMR spectra.
- All my **friends and colleagues in AKW**. I thank all of you for accompanying me on this journey. I think we did a great job bringing AKW back to life after the pandemic, even if some traditions changed. Also, I am grateful for the friends I found in this group. We will forever share the memories we made here! I would like to thank **Dr. Lea Fischer, Sarah Palloks, Tobias Schwan, Xiaohe Xu, Sandunika Perera, Anne-Sophie Mollenkopf and Tim Schülein** for proof-reading parts of my thesis.
- All my **SPP2005 friends and colleagues**. Thank you**, Silvia Reißig, Dr. Ursula Pott, Dr. David Nicia, Daniil Mikhalev, Moritz Kluwe, Dr. Julian Link, Bastian Strybny, Christian Vogel** and all others for answering my million questions on cement and concrete. Without you, I couldn't have navigated this large research field. Thank you for helping me to understand the civil engineering community and pointing me in the right directions. Also, thank you for all the amazing memories made at the winter school and during the long nights in Dresden;) I am so glad, I was a part of SPP and met all of you!
- My **friends from AKT: Dr. Nico Zuber, Dr. Sven Schneider, Dr. Alexander Grimm and Dr. Daniel Döpping**. Thank you for all the fun memories, the legendary 322 Abende, the bullshit discussions during lunch time and all the answers to my confused synthesis questions. Your expertise on RAFT and PEO helped me out a lot. And I promise, I will never say that poly(vinyl alcohol) is a water-soluble polymer :D
- **Daniel Zimmermann**, **Ingrid Zeller** and **Sabine Weiland**, who silently keep AKW running. Thank you for all your support and your help with all the complicated bureaucracy during ordering processes and travel bookings. Without you, we would be lost.
- The friends I made in Sherbrooke, Canada, **Dr. Valentin Roux** and **Yousra Bouatam**. I will forever be grateful for all the effort you made to make me feel integrated and welcome.
- Last but certainly not least, I would like to thank **my family**. Danke an Euch, dass ihr mir immer den Rücken freigehalten habt und alle meine Entscheidungen unterstützt habt. Ohne Euch wäre ich nicht so weit gekommen.

9 Publications and Conference Contributions

Publications

1) Tamara Meyer, Christopher O. Klein, Roxana Figuli, and Manfred Wilhelm. "The Development of a Unique Rheo-FTIR Set-up to Monitor Ettringite Formation in the Presence of Highly Charged Polymers." in *Opus Fluidum Futurum—Rheology of Reactive, Multiscale, Multiphase Construction Materials*, Springer, 978-3-032-15391-3, https://doi.org/10.1007/978-3-032-15391-3_3

2) Tamara Meyer, and Manfred Wilhelm. "Poly(2-Methyl-2-Oxazoline) Based Polycarboxylate Superplasticizers: A New Perspective on the Structure-Property Relationship of Polycarboxylate Ethers (PCE)." *Cement and Concrete Research, Under Review*

3) Tamara Meyer, Christopher O. Klein, Roxana Figuli, Nonkululeko W. Radebe and Manfred Wilhelm. "Improving spectral sensitivity of recently developed, unique Rheo-FTIR set-up." *In Writing*

4) Silvia Reißig, Carolin Bedolla, Tamara Meyer, and Viktor Mechtcherine. "Rheologisches Verhalten von Faserbewehrtem LC3-Feinkornbeton Im Kontext Der Additiven Fertigung." *ce/papers* 6, no. 6 (2023): 755–63. https://doi.org/10.1002/cepa.2820.

5) SPP2005 'Opus Fluidum Futurum' collaboration, Viktor Mechtcherine, Tamara Meyer et al., Rheology of Reactive Multiscale, Multiphase Building Material Systems: New Findings and Research Needs, *Progress in Materials Science, Under Review*

Conference Contributions

International Congress on Rheology 2023
Athens, Greece, 29.07.-04.08.2023
T. Meyer, M. Wilhelm
Rheological studies on the influence of different PCE superplasticizers on cement paste
Poster

Grand Final SPP2005 "Opus Fluidum Futurum" 2024
Dresden, Germany, 03.06.-04.06.2025
T. Meyer, C. O. Klein, R. Figuli, M. Wilhelm
Combined Methods for Characterization of Cement Pastes

Oral

Annual European Rheology Conference AERC 2025
Lyon, France, 14.04.-17.04.2025
T. Meyer, Christopher O. Klein, M. Wilhelm
An investigation on the sensitivity and temporal resolution limitations of a recently self-developed Rheo-FTIR set-up
Oral

International Conference on the Chemistry of Construction Materials, 5th ICCM 2025
Garching, Germany, 08.09.-10.09.2025
T. Meyer, M. Wilhelm
Synthesis and Rheological Characterisation of Poly(2-Methyl-2-Oxazoline) - PCEs in Ordinary Portland Cement Pastes
Oral

10 Appendix

10.1 List of Abbreviations

ACN	Acetonitrile
ADC	Analog-Digital-Converter
APS	Advanced Peltier System
ATR	Attenuated Total Reflectance
BB	Backbone
BGSC	Background Single Channel Spectrum
BPP	Beam Path Purge, second design iteration in chapter 5.4
CE1	Cubic Enclosure 1, part of full enclosure (FE) design, enclosing sample compartment of Rheo-FTIR
CE2	Cubic Enclosure 2, part of full enclosure (FE) design, enclosing Rheo-FTIR detector
CROP	Cationic Ring Opening Polymerization
DTGS	Deuterated Triglycin Sulfate, IR-detector at room temperature
FE	Full Enclosure, first design iteration in chapter 5.4
FT	Fourier-Transform
FTIR	Fourier-Transform Infrared Spectroscopy
IR	Infrared Spectroscopy
IRE	Internal Reflectance Element
LAOS	Large Amplitude Oscillatory Shear
LN2	Liquid Nitrogen
MAA	Methacrylic Acid
MALS	Multi-Angle Light Scattering
MCT	Mercury-Cadmium-Telluride, IR-detector, cooled with liquid nitrogen
NMR	Nuclear Magnetic Resonance
OPC	Ordinary Portland Cement

PAA	Poly(acrylic acid)
PCE	Poly(carboxylate ether)
PCMOxa	Poly(carbxyolate methyloxazolines)
PEtOxa	Poly(2-ethyl-2-oxazoline)
PMAA	Poly(methacrylic acid)
PMOxa	Poly(2-methyl-2-oxazoline)
POxa	Poly(2-alky-2-oxazoline)
PP	Plate-Plate Geometry
RAFT	Radical Addition-Fragmentation Transfer Polymerization
SAOS	Small amplitude oscillatory shear
SC	Sidechain
SEC	Size-Exclusion Chromatography
SI	Supporting Information
SSC	Sample Single Channel Spectrum
vBPP	Beam Path Purge including vent at CE2, second design iteration in chapter 5.4
VO	Valve Opening

10.2 Materials

The following chemicals were used as received: 2',2-Azobis(isobutyronitrile) (AIBN, Sigma Aldrich), chloroform ($CHCl_3$, 99.8 %, Fisher scientific), 2-Cyano-2-propyldodecyltrithiocarbonat (CDTP, 97%, TCI Chemicals), dichloromethane (DCM, p.a., HPLC grade, Thermo scientific), diethyl ether (99.5 %, Fisher scientific), n,n-dimethylformamide (DMF, 99 % extra dry, Thermo scientific), 1,4-dioxane (>98 %, Sigma Aldrich), potassium hydroxide (KOH, p.a., Thermo scientific), *sec*-butyl lithium (*s*-BuLi, 1.3 M in cyclohexane, Thermo scientific), trifluoroacetic acid (TFA, > 99 %, Apollo Scientific).

Tert-butyl methacrylate (tBMA, 98 %, Sigma-Aldrich), ethylene glycol methacrylate (EGDMA, 97,5 %, Merck) and 2-methyl-2-oxazoline (MOxa, 99%, Thermo scientific) were dried over calcium hydride (CaH_2, 92 %, Alfa Aesar) overnight and distilled under reduced pressure. The distilled monomers were stored under an argon atmosphere at -20 °C for maximum 14 days. Acetonitrile (ACN, HPLC grade, Thermo scientific) was dried over CaH_2 overnight and freshly distilled before use. 1,1-diphenylethylene (DPE, 98 %, Alfa Aesar) was titrated with *n*-butyl lithium (*n*-BuLi, solution in hexane, 1.6 M) until the formation of a persistent red color, then distilled under reduced pressure. Tetrahydrofuran (THF, > 99.5 %, Carl Roth) was distilled twice, first from CaH_2, then from sodium benzophenone (99 %, Acros Organics) directly to the reaction flask. Lithium chloride (LiCl, > 98 %, Alfa Aesar) was dried at 120 °C for a week and heated in the reaction flask to 600 °C under reduced pressure prior to synthesis. Methanol (MeOH, 99 %, Carl Roth) was degassed via freeze-pump-thaw. Methyl trifluoromethanosulfonate (MeOTf, 98 %, Apollo Scientific) was distilled under reduced pressure and stored under argon at - 20 °C. Triethyl amine (NEt_3, 99 %, Thermo Scientific) was dried over KOH and distilled before use. Methacrylic acid (MAA, Fisher Scientific) was purified by passing over a basic aluminum oxide column prior to use. For the synthesis of PCMOxa-macromonomer, MAA was distilled under reduced pressure prior to use. Poly(ethylene glycol)monomethylether-methacrylate (PEGMA) of two molecular weights M_n = 500 g mol^{-1} (PEGMA500, Sigma-Aldrich, batch Nr.:MKCP1470) and M_n = 950 g mol^{-1} (PEGMA950, Sigma-Aldrich, batch Nr.: MKCP5234) were used. PEGMA500 was purified by passing over a basic aluminum oxide column prior to use. PEGMA950 was used as received.

The commercial PCE superplasticizer BASF VP14.1 or BASF 2018/VP14.1 was provided by BASF within the framework of the Priority Programm SPP2005 'Opus Fluidum Futurum – Rheology of reactive, multiphase construction materials' (abb.: SPP2005). This product is an aqueous solution of a comb polymer [166]. Typically, superplasticizers are synthesized via copolymerization of a PEO-macromonomer and a charge-bearing monomer, e.g. acrylic acid, and sold in the reaction mixture without removal of unreacted sidearms [8]. This means that the main component of the superplasticizer solution is the comb polymer shown in Figure 82, but the solution also contains unreacted macromonomers, the amount of which is given in Table 15. Although not specified in [166], since BASF VP 14.1 is a formulated product, it can be assumed that in addition to the comb polymer it also contains further performance enhancing components to fine-tune its properties precisely to the intended application [8]. As BASF VP 14.1 is designed for ready-mix concrete, which is manufactured in batch and then delivered to the job site "ready to use", it requires both a high initial fluidity and also slump retention for the time span

of transportation, and thus could potentially contain a retarder [8]. Moreover, it can be assumed that it contains a defoamer to reduce the uncontrolled formation of air bubbles during mixing [8]. A full characterization of the physical properties of BASF VP14.1 is given in the study of Lei et al. [166].

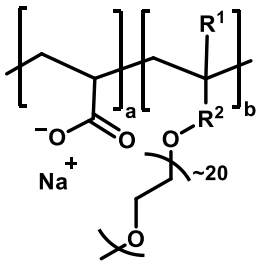

Figure 82: Chemical structure of BASF VP 14.1, reproduced from [166]. The acrylic acid backbone is drawn in its deprotonated form as sodium salt. In the product, the poly(acid) is only partially deprotonated, with an anionic charge amount of 1.3 meq/g [166]. R^1, R^2 are not specified in the reference [166]. The macromonomer most probably was either poly(ethylene glycol) methacrylate (PEGMA) or isoprenyl-terminated PEO (IPEG), which are the most commonly used PEO macromonomers in superplasticizer synthesis, with PEGMA being more common in Europe and IPEG being more common in China [56].

Table 15: Physical properties of BASF VP14.1, reproduced from [166]. The molecular weights and dispersity were obtained via SEC in 0.1 M $MaNO_3$ and 0.3 g L^{-1} NaN_3 adjusted to pH = 12 equipped with a dRI detector and a three-angle static light scattering detector [166]. The refractive index increment of PEO dn/dc = 0.135 mg L^{-1} was used for the calculation of the molecular weight [166].

Property	BASF VP 2018/14.1
Solid content	19.5 wt.%
Density	1.04 kg L^{-1}
M_n	11 770 g mol^{-1}
M_w	28 090 g mol^{-}
PDI	2.39
Macromonomer Conversion	84.4 %

The cement used in this work is an ordinary Portland cement (OPC) of the type CEMI 42.5 R which was provided by Heidelberg Materials within the framework of SPP 2005 “Opus Fluidum Futurum”. Two separate batches of cement were used in this work, which were provided in the first (2018) and the second funding period (2021), respectively. In chapter 5.5 (p. 117), CEMI 42.5 R of the first funding period (2018) was used, while all other experiments involving cement were conducted with CEMI 42.5 R of the second funding period (2021). A few central values of the two cement batches are given in the following. A full characterization of the cement of the first funding period (2018) is given in the study of Lu et al. [217], while Pott et al. give a complete characterization of the cement used in the second funding period [218].

CEMI 42.5 R – First Funding Period

Table 16: Part I of oxide composition of CEM I 42.5R of the first funding period in 2018. Table was split for readability. Reproduced from [217].

	CaO	SiO_2	Al_2O_3	Fe_2O_3	MgO	K_2O	Na_2O	TiO_2
Composition (wt.%)	64.4	20.4	5.4	2.6	1.4	0.77	0.22	0.29
Standard deviation	0.85	0.16	0.19	0.21	0.15	0.09	0.01	0.02

Table 17: Part II of oxide composition of CEM I 42.5R (first funding period, 2018). Reproduced from [217]. Loss on ignition (LOI) is a standard measure to determine cement quality. LOI quantifies the loss of weight after heating the cement to 950 – 1 000 °C due to evaporation of water and organic compounds. Typically, LOI should be ≤ 4 % for OPC.

	P_2O_5	Mn_2O_3	SO_3	LOI	Cl^-	Insoluble residue	Sum
Composition (wt.%)	0.14	0.07	2.7	1.87	0.02	1.04	100.12
Standard deviation	0.04	0.02	0.35	0.05	0.003	0.12	0.25

Table 18: Part I of phase contents of CEM I 42.5R (first funding period, 2018). Table was split for readability. Reproduced from [217].

	C_3S	C_2S	C_3A (orth.)	C_3A (cub.)	C_4AF	Anhydrite	Basanite	Arcanite
Composition (wt.%)	55.8	14.6	3.6	7.3	7.4	2.2	2.7	0.5
Standard deviation	1.79	0.45	0.58	0.50	0.97	0.27	0.45	0.23

Table 19: Part II of phase contents of CEM I 42.5R (first funding period, 2018). Reproduced from [217].

	Calcite	Quartz	Periclase	Sum
Composition (wt.%)	3.7	0.9	0.4	99.5
Standard deviation	0.19	0.21	0.11	0.50

Table 20: Particle size of CEM I 42.5R (first funding period, 2018). Reproduced from [217]. The table summarizes the percentiles, with d10 denoting that 10 % of the sample is smaller than the given value. d50 and d90 denote that 50 % and 90 % of the sample are smaller than the given value, respectively. As the particle size was determined with laser diffraction, the percentiles are vol.%.

	d10	d50	d90
Average particle size [µm]	1.5	14.8	44.6
Standard deviation	0.66	1.03	1.29

CEMI 42.5 R – Second Funding Period

Table 21: Part I of oxide composition of CEM I 42.5R of the second funding period in 2021. Table was split for readability. Reproduced from [218].

	CaO	SiO_2	Al_2O_3	Fe_2O_3	MgO	K_2O	Na_2O	TiO_2
Composition (wt.%)	61.79	21.14	5.53	2.27	1.39	0.77	0.21	0.32
Standard deviation	2.17	1.34	0.42	0.08	0.22	0.08	0.08	0.06

Table 22: Part II of oxide composition of CEM I 42.5R (second funding period, 2021). Reproduced from [218]. Loss on ignition (LOI) is a standard measure to determine cement quality. LOI quantifies the loss of weight after heating the cement to 950 – 1000 °C due to evaporation of water and organic compounds. Typically, LOI should be ≤ 4 % for OPC.

	P_2O_5	Mn_2O_3	SO_3	LOI	Cl^-	Insoluble residue	Sum
Composition (wt.%)	0.14	0.03	2.84	2.48	0.030	0.82	98.94
Standard deviation	0.08	0.03	0.69	0.10	0.0007	0.30	-

Table 23: Part I of phase contents of CEM I 42.5R (second funding period, 2021). Table was split for readability. Reproduced from [218].

	C_3S	C_2S	C_3A (orth.)	C_3A (cub.)	C_4AF	Sulfate carrier
Composition (wt.%)	54.45	18.07	3.28	7.55	5.17	4.82
Standard deviation	4.15	0.34	1.10	0.89	2.66	1.12

Table 24: Part II of phase contents of CEM I 42.5R (second funding period, 2021). Reproduced from [218].

	Calcite	Quartz	Periclase	Sum
Composition (wt.%)	4.08	0.42	0.75	98.59
Standard deviation	1.87	0.17	0.21	-

Table 25: Particle size of CEM I 42.5R (second funding period, 2021). Reproduced from [218]. The table summarizes the percentiles, with d10 denoting that 10 % of the sample is smaller than the given value. d50 and d90 denote that 50 % and 90 % of the sample are smaller than the given value, respectively. As the particle size was determined with laser diffraction, the percentiles are vol.%.

	d10	d50	d90
Average particle size [µm]	1.92	14.10	41.49
Standard deviation	0.64	1.91	4.33

10.3 Experimentals of Chapter 3

Preparation of cement pastes: To prepare the paste, 100 g of OPC was added to 34 mL of deionized water over the span of 15 s while simultaneously stirring the paste with an IKA stirrer equipped with a 4-blade mixer at a rotational speed of 200 rpm. After complete addition, the mixture was stirred for additional 15 s before a 30 s pause for returning the caking material was made. Subsequently, the paste was stirred for 2 min at 550 rpm. In the following 9 min rest time, the paste was covered with a wet paper towel to prevent evaporation. Subsequently, the paste was homogenized for one minute at 550 rpm and then transferred to a TA Instruments ARES G2 strain-controlled rheometer equipped with 50 mm parallel plates with wet-sanding sandpaper (600 grit) glued to the surface. The rheological characterization started exactly 15 minutes after initial water-to-cement contact. For the yield stress determination, steady shear experiments were performed utilizing shear rates starting from high shear rate to low shear rate in the range of $\dot{\gamma}$ = 100 s^{-1} to 0.1 s^{-1} following a similar procedure as [101].

Figure 83: Mixing set-up (left) including the IKA stirrer used for the preparation of cement pastes in this work. The samples were mixed in plastic containers, similar to the one shown in the left picture. The material of the mixing container as well as the container size (volume and aspect ratio) should be kept constant within a measurement series to ensure a constant temperature evolution within the paste. The IKA stirrer is equipped with a 4-blade mixer (right). The used IKA stirrer shows the rotations per minute (rpm) in a display above the rotary control, which is calculated from the applied force.

Table 26: Protocol for the preparation of cement paste, developed on the basis of [101].

0:00 - 0:15 min	**Addition of water (T = 10 °C) to cement powder at 200 rpm (lowest position at IKA stirrer). Do a bit of dry homogenization before. At the beginning of measurement day remix the large container of cement. t=0 at first water to cement contact**
0:15 - 0:30 min	**Continue at 200rpm**
0:30 – 1:00 min	**Pause to return caking material from the side of the beaker**
1:00 – 3:00 min	**Mixing at 550rpm**
3:00 -12:00 min	**Pause, covering beaker with wet paper towel to prevent evaporation**
12:30 – 13:30 min	**Homogenization at 550rpm**
13:30-15:00 min	**Sample Loading Temperature of paste needs to be checked, should be room temperature (22 °C or 23 °C) ± 1 °C**
15:00 min	**Start of measurement**

Synthesis of RAFT PCE: The synthesis of RAFT PCE (referenced in Figure 39, p. 56) was adapted from literature [219]. For the synthesis, MAA (2 g, 2 mL, 24 mmol), PEGMA500 (3 g, 2.8 mL, 6 mmol), CDPT (0.35 g, 1 mmol), AIBN (0.033 g, 0.2 mmol) and 1,4 – dioxane (25 mL) were added to a dry glass flask with a magnetic stirring bar. The reaction mixture was purged with Argon for 15 min while the solution was stirred. Subsequently, the reaction mixture was heated to 85 °C and stirred overnight. After 16 h, the reaction was stopped by rapid cooling upon immersing the flask in an ice bath. The product was precipitated into cold diethyl ether. The RAFT PCE product was obtained as a highly-viscous, yellow liquid. SEC characterization in aqueous 0.1 M Na_2HPO_4 gave M_n = 500 g mol^{-1}, M_w = 1 800 g mol^{-1}, and $Đ$ = 3.54.

10.4 Experimentals of Chapter 4

10.4.1 Synthetic Procedures

Synthesis of PMAA Backbone: The linear PtBMA BB precursor was synthesized via anionic polymerization following established procedures [36, 160]. For the backbone of $B = 100$, LiCl (350 mg, 8.3 mmol) is added to a glass flask and dried under vacuum at 600 °C. Subsequently, dry THF (300 mL) is distilled into the flask. After cooling the reaction flask to -80 °C, DPE (2.2 mL, 12.5 mmol) and *sec*-BuLi (2 mL, 1.3 M in cyclohexane, 2.6 mmol) are added. The persistent dark red color indicated the successful formation of the initiator 1,1-diphenylhexyllithium. Subsequently, tBMA (35 mL, 30.6 g, 0.22 mol) was added and the solution was stirred at -80 °C for 2 h. The polymerization was terminated by the addition of degassed MeOH (ca. 2 mL). The polymer was precipitated in a MeOH/water mixture (80/20-vol.%) and dried at 70 °C under reduced pressure. For the hydrolysis, 25 g PtBMA BB-precursor were dissolved in 350 mL DCM and 40 mL TFA (60 g, 0.42 mol, 3 eq. to tBMA) was added. The reaction mixture was stirred overnight. After the reaction was completed, the solvent was removed under reduced pressure. TFA was removed by three successive cycles of co-evaporation with DCM. The complete hydrolysis was confirmed by ^{1}H-NMR. The product was dried in vacuo to yield 12 g of white solid PMAA backbone.

Synthesis of PCMOxa via grafting-onto synthesis: The comb synthesis was adapted from the literature [54, 162, 220]. For the synthesis of i.e. PCMOxa-100-15x100, freshly distilled ACN (125 mL), MOxa (10 g, 10 mL, 0.12 mol) and MeOTf (0.19 g, 0.13 mL, 1.2 mmol) were added to a dry flask and stirred at 80 °C for 24 h. In a separate dry glass flask, 0.4 g PMAA backbone was dissolved in a mixture of DMF (1.5 mL) and NEt_3 (1 mL, 0.72 g, 7.1 mmol). The mixture was added to the flask containing the living PMOxa sidechains and stirred at 70 °C for 36 h. After the reaction mixture was cooled to room temperature, the solvent was removed under reduced pressure. 20 mL of saturated, aqueous $NaHCO_3$-solution were added to the mixture and stirred for 30 min. The water was removed under reduced pressure. Subsequently, 500 mL $CHCl_3$ were added to the solid residue and stirred overnight. The solution was dried over sodium sulfate, filtered and concentrate under reduced pressure. The product was precipitated into cold diethyl ether. The precipitate was dried in vacuo to yield 9 g of a white solid PCMOxa-100-15x100, which was stored under argon at -20 °C.

Synthesis of PMOxa-Macromonomer: The macromonomer was synthesized according to a procedure adapted from literature [162]. For PMOxa-MA-22, ACN (125 mL), MOxa (15 g, 15 mL, 0.18 mol) and MeOTf (0.1.23 g, 0.85 mL, 7.5 mmol) were sequentially added to a dry flask and stirred at 80 °C for 24 h. For the end capping, MAA (0.8 mL, 0.97 g, 11 mmol) and NEt_3 (1.8 mL, 1.3 g, 18 mmol) were mixed in a second dry flask for at least 15 min before being transferred to the reaction vessel. The end capping reaction was carried out at 70 °C for 36 h. After cooling to room temperature, the solvent was removed under reduced pressure. Saturated aqueous $NaHCO_3$-solution (60 mL) was added and stirred for 30 min. The solvent was again removed under reduced pressure, and the solid residue was stirred in 250 mL $CHCl_3$ overnight. The solution was dried over sodium sulfate, filtered and concentrated under reduced pressure. The product was precipitated in 800 mL cold diethyl ether. The product was collected and dried

in vacuo to yield 10 g of a white solid PCMOxa-MA-22. The product was stored under argon at -20 °C.

Synthesis of FRP-PCMOxa and FRP-PCE via grafting-through synthesis: The FRP comb synthesis was adapted from literature [148, 149]. For FRP-PCE, PEGMA950 (1.62 g, 15 mmol) and MAA (0.32 g, 3.8 mmol) were dissolved in deionized water (2 mL) and 0.2 mL of an aqueous solution of 3-MPA (0.53 mol/L), 0.33 mL of an aqueous solution of SFS (0.35 mol/L) and 0.33 mL of an aqueous solution of TBHP (0.32 mol/L) were sequentially added. For FRP-PCMOxa, PMOxa-MA-21 (1.5 g, 7.5 mmol) and MAA (0.16 g, 1.9 mmol) were dissolved in deionized water (2 mL) and 0.1 mL of an aqueous solution of 3-MPA (0.53 mol/L), 0.16 mL of an aqueous solution of SFS (0.35 mol/L) and 0.16 mL of an aqueous solution of TBHP (0.32 mmol/mL) were sequentially added. The reaction mixtures were stirred overnight at room temperature. The product was obtained via freeze-drying the reaction mixture over night.

10.4.2 Characterization of Synthesized Compounds

SEC of PtBMA precursor: The linear PtBMA was characterized with an Agilent 1200 series SEC, equipped with an isocratic pump, a differential refractive index detector (dRI), a UV/Vis detector, a multi-angle light scattering detector (SEC-MALS, Polymer Standards Service, PSS Mainz, Germany) and a PSS SDV-Lux-1000 Å, whereby tetrahydrofuran (SEC grade, 0.025 % BHT) was used as an eluent at 1 mL min^{-1} flow rate at 25 °C. The system was calibrated with poly(methyl methacrylate) (800 - 110 000 g mol^{-1}) standards.

SEC of PMOxa sidechains and combs: Size exclusion chromatography in dimethyl acetamide (DMAc, HPLC grade) was performed with an Agilent Technologies 1260 Infinity II system, equipped with both a differential refractive index (dRI) detector as well as a UV/Vis detector. The system was calibrated with ReadyCal standards, using PMMA standards with molecular weights ranging from 800 to 2 200 000 g mol^{-1}. The columns used were a front Mixed-C and a Mixed-E column from Agilent. The eluent was DMAc with 0.79 g of LiBr per 2.5 L of solvent (0.316 g L^{-1}). Typically, 50 µL of a filtered 2.0 mg mL^{-1} sample solution was injected onto the columns. The system operated at a temperature of 50 °C with a flow rate of 1 mL min^{-1}. The structural parameters *N* and *n* were calculated from integration of the remaining sidechain peak.

NMR: ^{1}H-spectra were recorded on a Bruker Avance lll Microbay 400 MHz spectrometer at room temperature in deuterium oxide (D_2O, 99.8 %, Acros Organics) and deuterated chloroform ($CDCl_3$, 99.8 %, Acros Organics). The signals were referenced to the residual solvent peak.

10.4.3 Rheological Characterizations of PCMOxa-Modified Cement Pastes

Preparation of cement pastes: For the cement samples, ordinary Portland cement (OPC) of the type CEM I 42.5 provided by Heidelberg Materials within the framework of SPP 2005 “Opus

Fluidum Futurum" was used. A full characterization of the used cement is given elsewhere [218]. All cement pastes were prepared with a w/c-ratio of 0.35. Prior to cement paste preparation, different stock solutions of PCMOxa polymer in deionized water were prepared. PCMOxa was added using 1 mL of solution with varying concentrations. To measure e.g. a concentration of 0.1 wt-% by weight of dry cement, a stock solution was prepared by dissolving 310 mg of PCMOxa-100-18x25 in 3.1 mL deionized water. To prepare the paste, 100 g of OPC was added to 34 mL of deionized water over the span of 30 s while simultaneously stirring the paste with an IKA stirrer equipped with a 4-blade mixer at a rotational speed of 200 rpm. After complete addition, the mixture was stirred for additional 1.5 min at 550 rpm. Two minutes after first water-to-cement-contact, 1 mL of the PMOxa-comb stock solution (corresponding to 100 mg of PCMOxa-100-18x25) were added and the paste was stirred for another minute. The paste was covered with a wet paper towel for additional 9.5 min. Subsequently, the paste was homogenized for one minute and then transferred to a TA Instruments ARES G2 strain-controlled rheometer equipped with 50 mm parallel plates with wet-sanding sandpaper (600 grit) glued to the surface. The rheological characterization started exactly 15 min after initial water-to-cement contact. For yield stress determination, steady shear experiments were performed utilizing shear rates starting from high shear rate to low shear rate in the range of $\dot{\gamma}$ = 100 s^{-1} to 0.1 s^{-1} following a similar procedure as [101].

10.4.4 Characterization of PCMOxa Adsorption

Dissolved organic carbon (DOC) analysis: For the DOC analysis, the procedure was adapted from literature [132]. Cement pastes of w/c = 1.2 were prepared by mixing 20.0 g of cement and 23.0 g of water in a glass beaker using an IKA stirrer with a four bladed stainless-steel turbine agitator. The dispersion was first stirred at 200 RPM for one minute, then at 550 RPM. Afterwards, 1 mL of PCMOxa stock solution was added 2 min after initial mixing. After further 9 min of stirring, the cement dispersion was transferred into a centrifuge tube. The mixture was centrifuged at 4000 RPM (resulting in an acceleration of 2415 g) using a Hettich 320 universal table centrifuge for 15 minutes, beginning exactly 15 min after first water contact. After centrifugation, 2 mL of the supernatant were taken, filtrated through a 0.45 µm syringe filter and diluted by a factor of 10. The syringe filters were pre-washed using 80 mL of deionized water. The obtained samples were acidified by addition of 0.1 mL of concentrated orthophosphoric acid (85 %). The dissolved organic carbon was analyzed in the Engler-Bunte-Institute (EBI) using a Shimadzu TOC-Analyzer (Model TOC-L CPH). All samples were prepared by using freshly tapped deionized water. DOC of the blank cement paste without any superplasticizer should be determined to consider the organic carbon contained in the cement due to e.g. grinding aids, etc. The carbon content of the superplasticizer sample, which is necessary to calculate the adsorbed mass correctly, can either be calculated from the molecular structure or, more precisely, can be obtained by directly measuring DOC or TOC of a superplasticizer solution of known concentration.

10.5 Experimentals of Chapter 5

10.5.1 FTIR Parameters

If not mentioned otherwise, the following measurement parameters were chosen in the OPUS software:

Table 27: Optimized settings in OPUS software in all performed FTIR measurements.

Parameter	Settings
Resolution	**4 cm^{-1}**
Background scan time	**64 scans**
Sample scan time	**64 scans**
Wavenumber region	**4 000 cm^{-1} – 1 000 cm^{-1}**
Aperture	**“Open” (corresponds to 4 mm)**
Preamplification gain	**Ref. (no amplification)**
Scanning velocity	**20 kHz**
Background and sample signal gain	**Automatic**
Wanted high frequency limit	**8 000**
Wanted low frequency limit	**0**
High pass filter	**Open**
Lowpass filter	**Automatic**
Acquisition mode	**Double-Sided, Forward-Backward**
Phase resolution	**32**
Phase correction mode	**Mertz**
Apodization function	**Blackman-Harris 3-Term**
Zero filling factor	**2**

10.5.2 Synthesis and Characterization of PMAA Polymers

Linear Poly(methacrylic acid) (PMAA): The synthesis of linear PMAA was performed following the work of Pelet and Putnam [213]. MAA (5 g, 58 mmol), CDPT (80.3 mg, 0.2 mmol) and AIBN (3.8 mg, 0.02 mmol) were dissolved in 20 mL MeOH. The reaction mixture was purged with Argon for 10 mins, then heated to 60 °C and stirred for 24 h. The polymer was

precipitated in cold diethyl ether and dried under vacuum overnight. The product was obtained as a yellow solid.

PMAA Star: The synthesis was performed following the work of Efstratiadis [221]: LiCl (100 mg, 2.4 mmol) in dry THF (150 mL) cooled to -80 °C with an acetone/liquid nitrogen cooling bath. DPE (5.6 mL, 0.24 mol/L in dry THF, 1.25 mmol) and *sec*-BuLi (0.18 mL, 1.4 M in cyclohexane, 0.25 mmol) were added. The persistent dark red color indicated the successful formation of the initiator 1,1-diphenylhexyllithium (DPHLi). tBMA (5.7 mL, 5 g, 35.2 mmol) was added and the temperature was kept at -80 °C for 1 h. Subsequently, EGDMA (0.5 mL, 2 M in THF, 1.00 mmol) was added to the living PtBMA anions at -80 °C and the reaction mixture was stirred for 2 h. The reaction was terminated with an excess of degassed MeOH (2 mL). The polymer was precipitated in a MeOH/water mixture (80/20 - vol.%) and dried at 70 °C under reduced pressure. For the hydrolysis, the obtained polymer was dissolved in 1,4-dioxane (50 mL) and a 10-fold excess of HCl (6.5 mL, 12 M in water, 15.5 mmol) was added. The reaction mixture was stirred for 6 h at 85 °C. Subsequently, the solution was diluted with water (500 mL) and neutralized with NaOH (typically about 2 mL, 33 wt.% in water). The polymer was obtained after freeze-drying as a white powder.

SEC of PtBMA precursor: The linear PtBMA was characterized with an Agilent 1200 series SEC, equipped with an isocratic pump, a differential refractive index detector (dRI), a UV/Vis detector, a multi-angle light scattering detector (SEC-MALS, Polymer Standards Service, PSS Mainz, Germany) and a PSS SDV-Lux-1000 Å, whereby tetrahydrofuran (SEC grade, 0.025 % BHT) was used as an eluent at 1 mL min^{-1} flow rate at 25 °C. The system was calibrated with poly(methyl methacrylate) (800 - 110 000 g mol^{-1}) standards.

NMR. ^{1}H-spectra were recorded on a Bruker Avance lll Microbay 400 MHz spectrometer at room temperature in deuterium oxide (D_2O, 99.8 %, Acros Organics) and deuterated chloroform ($CDCl_3$, 99.8 %, Acros Organics). The signals were referenced to the residual solvent peak.

10.5.3 Rheological Measurements

Preparation of cement pastes: For the cement samples, ordinary Portland cement (OPC) of the type CEM I 42.5 provided by SPP2005 “Opus Fluidum Futurum” was used. The cement characteristics are summarized in this previous work [217]. All samples were prepared with a w/c-ratio of 0.4: 50g of OPC were added to 20 mL of deionized water over the span of 30 s while stirring with an IKA stirrer equipped with a 4-blade mixer at a rotational speed of 200 rpm. After complete addition, the mixture was stirred for additional two minutes at 500 rpm. Subsequently, the sample was placed into the geometry and the measurement was started 3.5 min after first water-to-cement contact. For the experiments with PMAA, the polymer was dissolved in the mixing water prior to mixing. The concentration was 0.5% bwoc (by weight of cement = m(dry polymer) / m(dry cement)).

Rheo-FTIR Measurements: Rheo-FTIR measurements were performed on a strain-controlled ARES G2 (TA Instruments) rheometer combined with a Bruker Matrix-MF. The FTIR device

was equipped with a mid-infrared source and a MCT detector. The measurements were performed at 22 °C using a self-designed silicon ATR crystal geometry, which is equivalent to a 25 mm parallel plate geometry, and a gap of 1 mm. A pre-shear at 100 s^{-1} for 60 s was performed for all measurements. Oscillatory time sweeps were conducted by recording the time-dependent response of the material deformed with a fixed strain amplitude of γ_0 = 0.01% and a fixed frequency of $\omega_1/2\pi$ = 1 Hz.

10.6 Supplementary Information

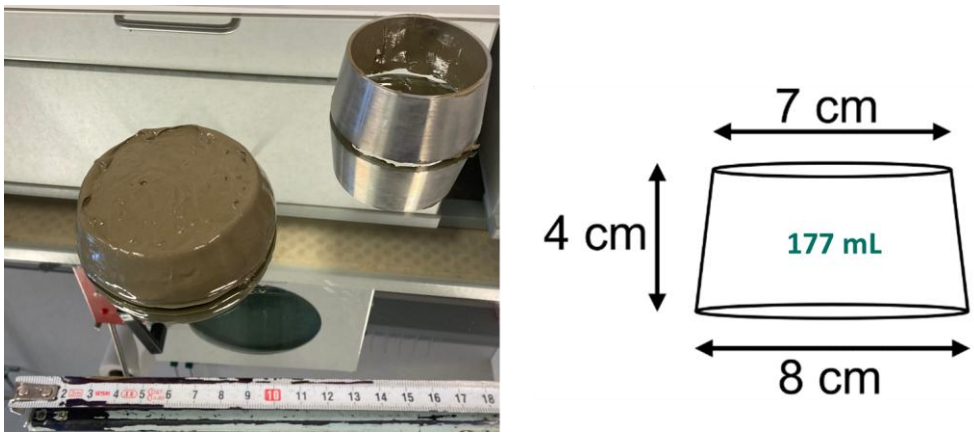

Figure 84: Spread flow test conducted with a Vicat cone and a cement paste of w/c = 0.35. The measures of a Vicat cone are given in the schematic on the right side. This spread flow experiment was conducted on a dry glass plate (in this case a mirror).

10.6.1 Chapter 3

Figure 85: Photo of grooved concentric cylinder and grooved cup. The cylinder has a diameter of 26.6 mm and a length of 50 mm, while the cup has a diameter of 28.9 mm, resulting in a gap of 1.126 mm [222]. This geometry was used with a stress-controlled Anton Paar MCR 302 for all rheometric experiments conducted at Université de Sherbrooke, Sherbrooke, Kanada.

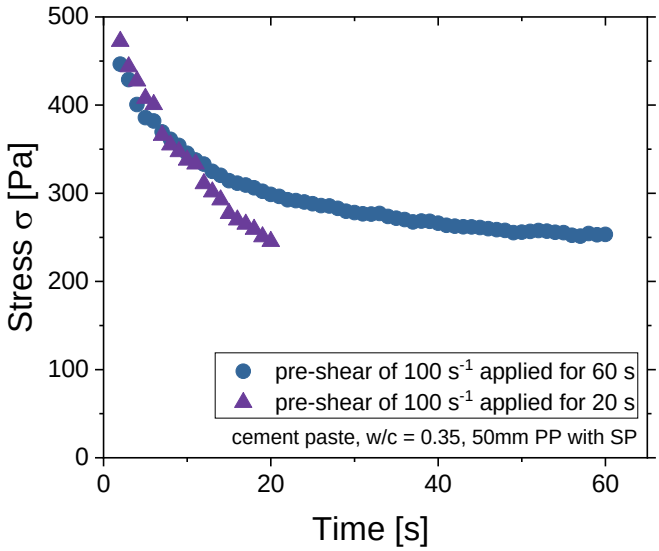

Figure 86: Effect of pre-shear duration in the rheometer. The pre-shear duration of 20 s was applied following the reference study [101]. However, it was observed that the duration of 20 s was not sufficient to obtain a steady state. Therefore, the duration of the pre-shear step was prolonged to 60 s which was observed to be sufficient to reach a steady state and thus erase the shear history imposed during sample loading.

10.6.2 Chapter 4

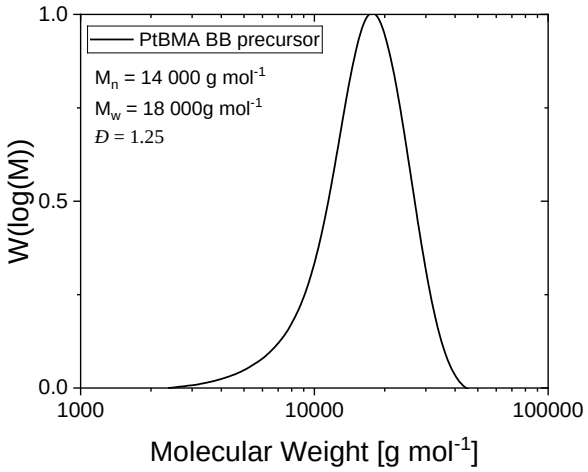

Figure 87: Molecular Weight distribution of PtBMA BB precursor, obtained via SEC in THF. The molecular weight M_n = 14 000 g mol^{-1} corresponds to B ≈ 100 (M(tBMA) = 142 g mol^{-1}).

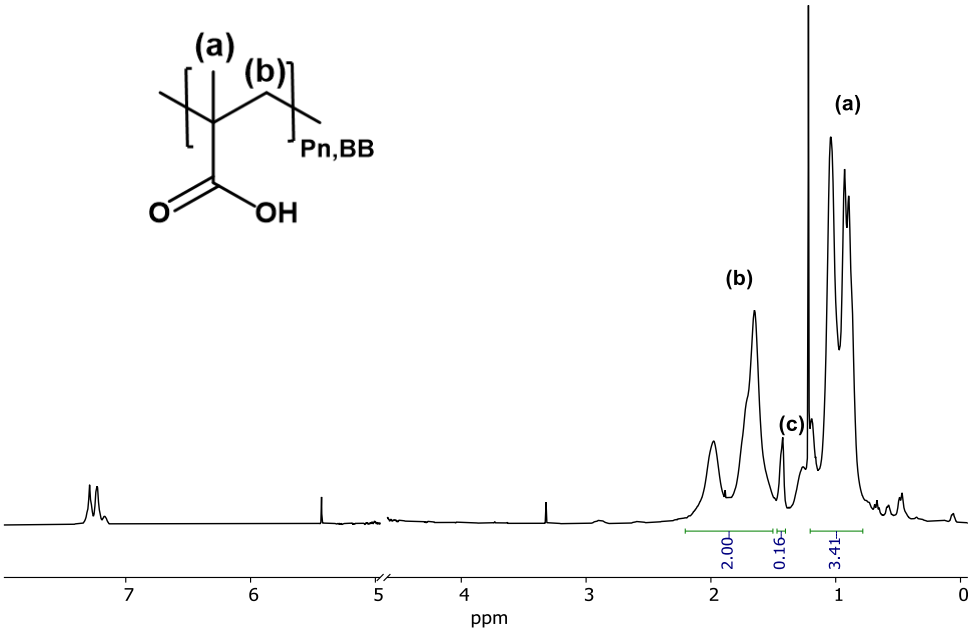

Figure 88: ^{1}H-NMR spectrum of fully hydrolyzed PMAA backbone in D_2O (400 MHz). The Peak labelled with (a) corresponds to the protons of the methyl group, while (b) marks the peak of the backbone protons. The label (c) marks the remaining protons of the tert-butyl group, which either from non-hydrolyzed tert-butyl esters or of the cleavage product tert-butanol which was not removed by the purification steps. The integral of 0.16 for 9 H corresponds to tert-butyl content of ~1.5 mol-%. The acidic proton is not visible in D_2O.

Table 28: Fit parameters of Bingham-Fits displayed in Figure 44 (p. 67).

concentration	σ_0	η_p
0.03	**164**	**0.81**
0.05	**138**	**1.03**
0.1	**51**	**0.82**
0.15	**15**	**0.72**
0.3	**-2**	**0.09**

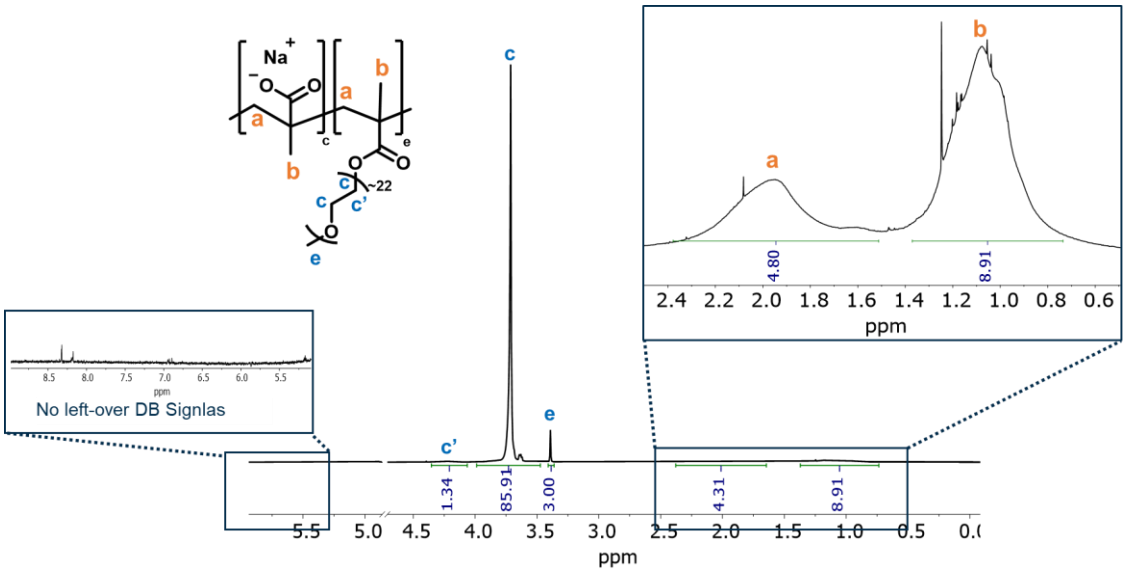

Figure 89: [1]H-NMR of FRP-PCE (D_2O, 400 MHz). The enlargement from 9 – 5 ppm shows no leftover double-bond (DB) signals.

Table 29: SEC results (0.7 M $NaHPO_4$, PEO standards 200 – 100 000 g mol^{-1}, RI detector) for the medium comb from [149]. The ratio of macromonomer to methacrylic acid was 1:2.8 as confirmed by titration. Thus, the average structural repeating unit has a molecular weight of 1 076 g mol^{-1} + (2.8 · 86 g mol^{-1}) = 1 317 g mol^{-1}. The backbone length B was obtained as $B = M_x$ / 1 317 g mol^{-1}

	dRI-Signal	***B*** = M_x / 1 317 g mol^{-1}
M_n	38 000 g mol^{-1}	29
M_w	90 000 g mol^{-1}	68
M_p	56 000 g mol^{-1}	43
Đ	2.37	

10.6.3 Chapter 5

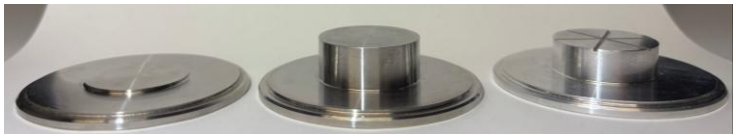

Figure 90: Sideview of lower plate options. The grooved plate designed for rubber analysis has an elevation of 8 mm height.

Figure 91: Close up of M2, with additional adjustment screw at the mirror mount attachment to precisely adjust the mirror-crystal distance to the focal length of the off-axis parabolic mirror.

Figure 92: Picture of old detector table (left) and redesigned table (right) including the fastenings and the exchanged rods used for the installment of the table.

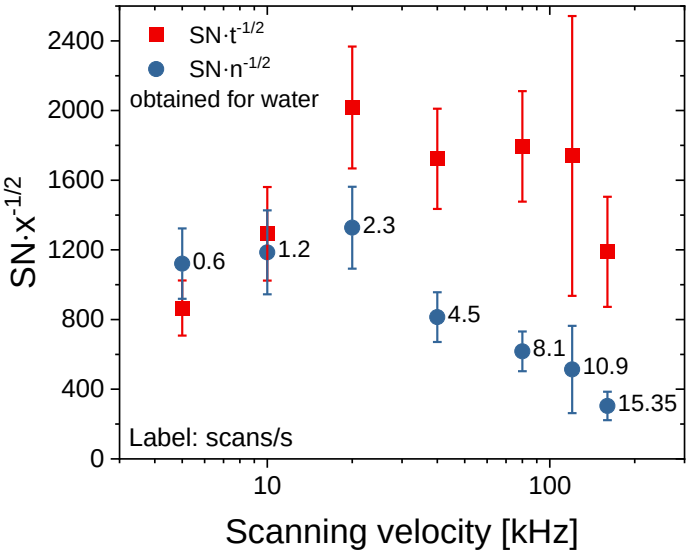

Figure 93: Signal-to-noise ratio $SNx^{-1/2}$ normalized to the number of scans n (blue circles) and the measurement time t (red squares) plotted against the scanning velocity given kHz. Since the scanning speed was varied, the number of scans is no longer proportional to the measurement time. Consequently, the $SNn^{-1/2}$ values were used to determine the optimum scan speed. The highest $SNn^{-1/2}$ was obtained for a scanning velocity of 20 kHz. The labels correspond to the scan speed given in scans/s. The Bruker Matrix-M can obtain spectra with a scan speed of up to 15.35 scans/s. In the double-sided, forward-backward mode used in this work, two interferograms are recorded during one scan. As half an interferogram is needed to calculate one spectrum, two interferograms correspond to 4 spectra. Consequently, in the double-sided, forward-backward mode, the scan speed of 2.3 scans/s is equivalent to 9.2 spectra/s. The maximum scan speed of 160 kHz provided by the Matrix-M thus corresponds to 15.35 scans/s · 4 = 61.4 spectra/s.

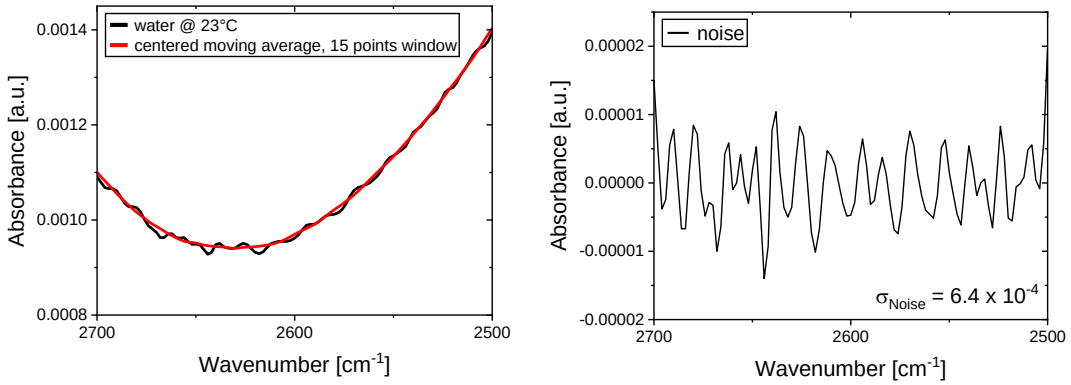

Figure 94: Noise Region of water spectrum obtained with revised Rheo-FTIR set-up. A centered moving average (window size of 15 points, corresponding to $\Delta\tilde{\nu}$ = 30 cm^{-1}) was used to remove the underlying curvature before obtaining the standard deviation to calculate the SNR.

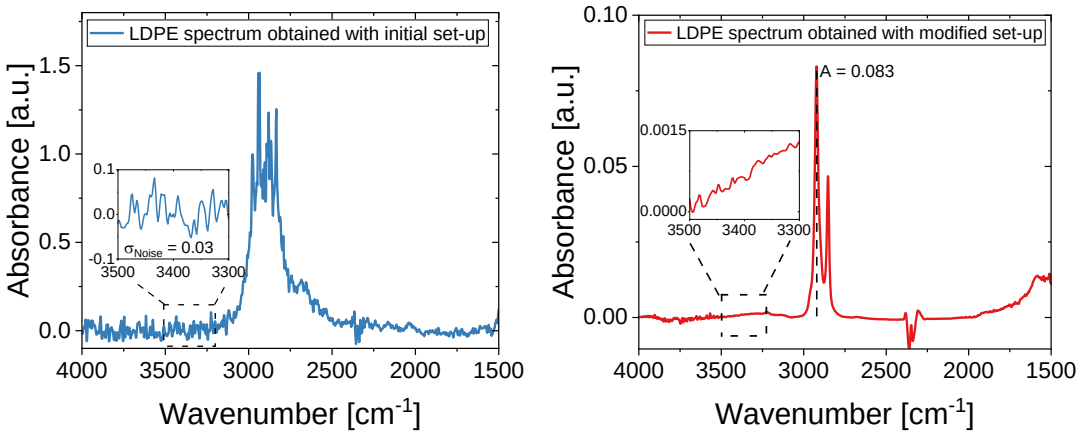

Figure 95: Spectra of LDPE at 130 °C obtained with the initial set-up in the year 2022 (blue) and the modified set-up in January 2026 (red). In the spectrum obtained with the initial set-up, the comparatively high absorbance values in combination with the unexpected peak shape indicate a measurement artifact, potentially a digital overcompensation of a poor signal. The SNR was calculated from the baseline corrected spectra with the intensity of the asymmetric C-H -stretch vibration at 2921 cm^{-1} and the standard deviation in the wavenumber range of 3500 – 3300 cm^{-1}. In the spectrum obtained with the modified set-up (red), the peak at 2921 cm^{-1} has a maximum absorbance of 0.083 a.u.. The noise region shows a curvature, which had to be removed prior to noise calculation, as further shown in Figure 96, p. 170. For the initial set-up (blue), the noise could be calculated directly from the baseline corrected data and the standard deviation in the wavenumber range of 3500 – 3300 cm^{-1} was obtained as σ_{Noise} = 0.03. The peak at 3100 – 2200 cm^{-1} was fitted with two Gaussian functions to obtain the maximum of the asymmetric C-H -stretch vibration at 2921 cm^{-1}, as displayed in Figure 97, p. 170.

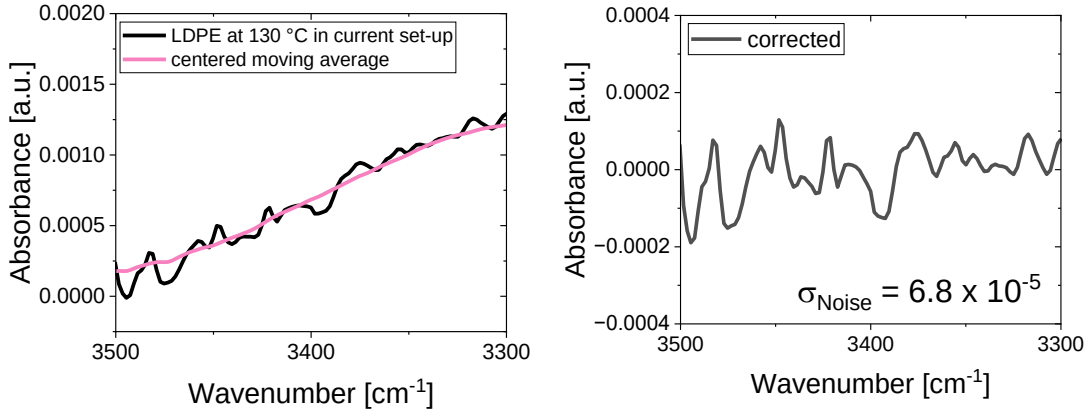

Figure 96: Wavenumber region used to determine the noise in the LDPE spectrum obtained with the modified set-up. To remove the underlying curvature, a centered moving average (window size of 25 points, corresponding to $\Delta\tilde{\nu}$ = 50 cm^{-1}) was fitted and subtracted prior to the calculation of the standard deviation, which was obtained as σ_{Noise} = 6.8 · 10^{-5}.

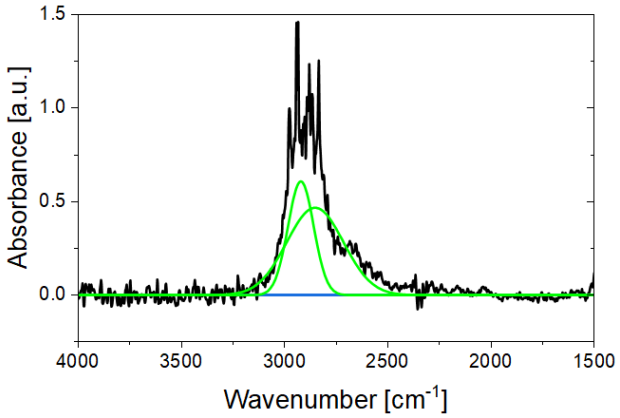

Figure 97: Peak Deconvolution performed on LDPE spectrum obtained with the initial set-up to obtain the peak intensity of the asymmetric C-H – stretch vibration. The fit parameters are summarized in the following table.

Table 30: Fit parameters obtained for peak deconvolution. The Peak maximum of 0.61 a.u. was used to calculate the SNR ratio given in Figure 65 (p. 100)

Peak	Center Position	Peak Shape	Peak Maximum	FWHM
Asym. C-H stretch	**2921 cm^{-1}**	**Gaussian**	**0.61 a.u.**	**146 cm^{-1}**
Sym. C-H stretch	**2852 cm^{-1}**	**Gaussian**	**0.47 a.u.**	**323 cm^{-1}**

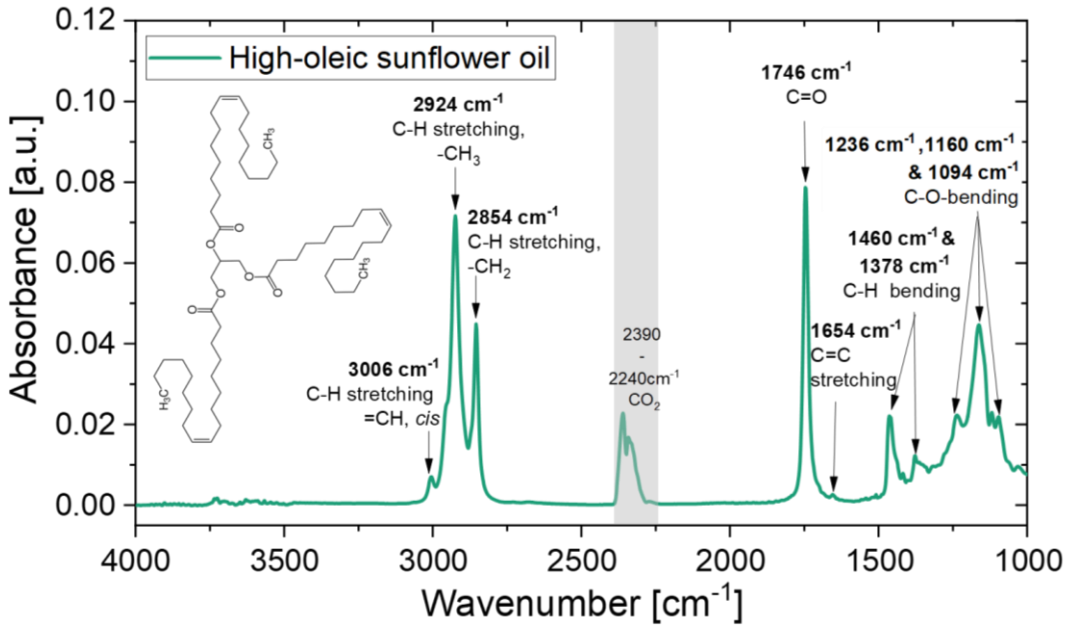

Figure 98: Spectrum of high-oleic sunflower oil including peak assignments.

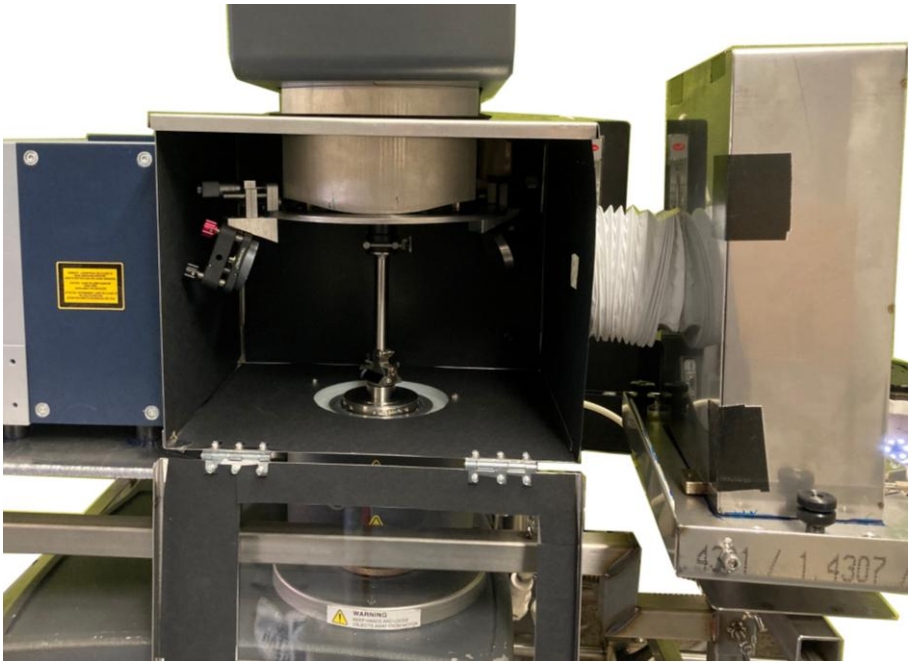

Figure 99: Rheo-FTIR enclosure with opened CE1 front hatch.